

---

# Composite and Adiabatic Techniques for Efficient EIT Light Storage in $\text{Pr}^{3+}:\text{Y}_2\text{SiO}_5$

---

Komposite und adiabatische Techniken zur effizienten EIT-basierten  
Lichtspeicherung in  $\text{Pr}^{3+}:\text{Y}_2\text{SiO}_5$   
Dissertation von Daniel Schraft, Oktober 2016



TECHNISCHE  
UNIVERSITÄT  
DARMSTADT

Fachbereich Physik  
Institut für Angewandte Physik  
Nichtlineare Optik und  
Quantenoptik

Bitte zitieren Sie dieses Dokument als:  
URN: urn:nbn:de:tuda-tuprints-65069  
URL: <http://tuprints.ulb.tu-darmstadt.de/id/eprint/6506>

Dieses Dokument wird bereitgestellt von tuprints,  
E-Publishing-Service der TU Darmstadt.  
<http://tuprints.ulb.tu-darmstadt.de>



Die Veröffentlichung steht unter folgender Creative Commons Lizenz:  
Namensnennung - Keine kommerzielle Nutzung - Keine Bearbeitung 4.0  
Deutschland  
<https://creativecommons.org/licenses/by-nc-nd/4.0/>



# Composite and Adiabatic Techniques for Efficient EIT Light Storage in $\text{Pr}^{3+}:\text{Y}_2\text{SiO}_5$

Vom Fachbereich Physik  
der Technischen Universität Darmstadt

zur Erlangung des Grades  
eines Doktors der Naturwissenschaften  
(Dr. rer. nat.)

genehmigte Dissertation  
von M.Sc. Daniel Schraft  
aus Frankfurt am Main

Referent: Prof. Dr. Thomas Halfmann  
Korreferent: Prof. Dr. Thomas Walther

Tag der Einreichung: 19. 10. 2016  
Tag der Prüfung: 5. 12. 2016

Darmstadt 2017

D17



---

# Abbreviations

<b>AOM</b>	acousto-optic modulator
<b>CAP</b>	composite adiabatic passage
<b>CP</b>	composite pulse
<b>CPMG</b>	Carr-Purcell-Meiboom-Gill (sequence)
<b>DD</b>	dynamical decoupling
<b>DDC</b>	dynamic decoherence control
<b>DSB</b>	dark state beating
<b>EIT</b>	electromagnetically induced transparency
<b>EIT-LS</b>	light storage based on electromagnetically induced transparency
<b>FWHM</b>	full width at half maximum
<b>HSE</b>	Hahn spin echo
<b>KDD</b>	Knill dynamical decoupling (sequence)
<b>NMR</b>	nuclear magnetic resonance
<b>OPO</b>	optical parametric oscillator
<b>PrYSO</b>	praseodymium-doped yttrium orthosilicate ( $\text{Pr}^{3+} : \text{Y}_2\text{SiO}_5$ )
<b>RAP</b>	rapid adiabatic passage
<b>REIDS</b>	rare-earth ion-doped solids
<b>RF</b>	radio-frequency
<b>RHD</b>	Raman heterodyne detection
<b>RWA</b>	rotating wave approximation
<b>SSSP</b>	single-shot shaped pulse
<b>TDSE</b>	time-dependent Schrödinger equation
<b>UCP</b>	universal composite pulse
<b>UR</b>	universal robust (sequence)

# Contents

<b>Introduction</b>	<b>1</b>
<b>1 Rare-Earth Ion-doped Solids</b>	<b>3</b>
1.1 Praseodymium-doped Yttrium Orthosilicate Crystal . . . . .	3
1.2 Spectroscopic Properties of $\text{Pr}^{3+}:\text{Y}_2\text{SiO}_5$ . . . . .	4
1.2.1 Fine Structure and Crystal Field Interaction . . . . .	5
1.2.2 Hyperfine Structure . . . . .	6
1.3 Line Broadening Mechanisms . . . . .	8
<b>2 Coherent Wave Matter Interactions</b>	<b>11</b>
2.1 Coherent Interactions in a Two-Level System . . . . .	11
2.1.1 Rabi Oscillations and Pulsed Excitation . . . . .	12
2.1.2 Description of Macroscopic Systems . . . . .	13
2.1.3 Composite Pulses . . . . .	14
2.2 Coherent Interactions in a Three-Level System . . . . .	17
2.3 Adiabatic Light Storage in a Three-Level System . . . . .	18
2.3.1 Electromagnetically Induced Transparency . . . . .	18
2.3.2 EIT-based Light Storage . . . . .	21
2.3.3 Limitations on the Efficiency of the EIT Light Storage Protocol	23
2.3.4 Limitations on the Efficiency due to the Storage Medium . . .	29
2.4 Raman Heterodyne Detection in a $\Lambda$ -System . . . . .	30
<b>3 Experimental Setup</b>	<b>32</b>
3.1 Optical Setup . . . . .	32
3.2 Crystal and Cryostat Setup . . . . .	34
3.3 Radio-frequency Magnetic Field System and Mounts . . . . .	35
3.4 Detection of Light Storage Signals . . . . .	37
3.5 Raman Heterodyne Detection . . . . .	37
<b>4 Optimization of the EIT Light Storage Efficiency</b>	<b>38</b>
4.1 Preparation of a $\Lambda$ -System for EIT Light Storage . . . . .	39
4.2 Experimental Observation of EIT in PrYSO . . . . .	40
4.3 Determination of the Light Storage Efficiency . . . . .	42
4.4 Optimization of the Light Storage Efficiency . . . . .	43
4.5 Concepts to Increase the Optical Depth . . . . .	44
4.5.1 Multipass Geometry to Increase the Optical Depth . . . . .	45
4.6 EIT Light Storage in a Multipass Setup . . . . .	47
4.6.1 Maximum Light Storage Efficiency for Variable Optical Depths	50
4.7 Conclusion . . . . .	52

<b>5</b>	<b>Rephasing of Atomic Coherences by Composite/Adiabatic Techniques</b>	<b>53</b>
5.1	Introduction to Rephasing of Atomic Coherences . . . . .	54
5.1.1	Generation and Detection of an RF-induced Coherence . . . . .	54
5.1.2	Atomic Coherences in Inhomogeneous Broadened Transitions	55
5.1.3	Diabatic Rephasing of Atomic Coherences . . . . .	56
5.1.4	Rephasing Efficiency of Imperfect $\pi$ -Pulses . . . . .	58
5.2	Universal Composite Pulses . . . . .	61
5.2.1	Theory of Universal Composite Pulses . . . . .	61
5.2.2	Experimental Results on Universal Composite Pulses . . . . .	62
5.3	Composite Adiabatic Passage . . . . .	67
5.3.1	Adiabatic Passage Processes . . . . .	67
5.3.2	Theory on Composite Adiabatic Passage . . . . .	71
5.3.3	Experimental Results on Composite Adiabatic Passage . . . . .	72
5.3.4	Conclusion . . . . .	80
5.4	Single-Shot Shaped Pulses . . . . .	80
5.4.1	Derivation of Single-Shot Shaped Pulses . . . . .	81
5.4.2	Experimental Results on Single-Shot Shaped Pulses . . . . .	84
5.4.3	Conclusion . . . . .	86
<b>6</b>	<b>Composite Pulses for Dynamic Decoherence Control</b>	<b>87</b>
6.1	Implementation of Dynamical Decoupling Sequences . . . . .	87
6.2	DDC for Coherences prepared by RF-Pulses . . . . .	88
6.3	DDC for EIT-LS Coherences . . . . .	96
6.4	Conclusion . . . . .	98
	<b>Conclusion and Prospects for Future Work</b>	<b>99</b>
	<b>Zusammenfassung</b>	<b>101</b>
<b>A</b>	<b>Additional Experimental Results on SSSP</b>	<b>104</b>
<b>B</b>	<b>Investigations on Stimulated Photon Echos</b>	<b>106</b>
<b>C</b>	<b>Determination of HF Transition Frequencies</b>	<b>108</b>
<b>D</b>	<b>Derivation of the Linear Susceptibility <math>\chi^{(1)}</math></b>	<b>109</b>
	<b>Bibliography</b>	<b>111</b>
	<b>Publications and Conference Contributions</b>	<b>125</b>
	<b>Supervisions and Contributions to Teaching</b>	<b>128</b>
	<b>Curriculum Vitae</b>	<b>129</b>
	<b>Acknowledgment</b>	<b>130</b>



## Introduction

Reliable and efficient quantum memories are of crucial relevance for current, and future applications in quantum computation, and quantum as well as classical communication networks. Such applications rely on fault tolerant, highly efficient, long term storage memories. However, these requirements can currently only be well satisfied by classical electronic storage media, which on the other hand are unsuitable to store an arbitrary quantum state. Only the properties of a quantum state, capable to carry a coherent superposition of states, enables the realization of quantum information processing [1], and the development of quantum repeaters [2] for quantum networks [3,4]. Most approaches investigate quantum memories based on the interaction between photons and matter [5]. Photons represent a reliable carrier of quantum information. The rather strong interaction between photons and matter permits an efficient transfer of information.

In the last decade a number of different optical storage protocols [5–7] suitable for quantum information storage by photon-matter interactions have been proposed. In particular, storage techniques based on atomic frequency combs (AFC) [8], controlled reversible inhomogeneous broadening (CRIB) [9], gradient echo memories (GEM) [10] and electromagnetically induced transparency (EIT) [11,12] have been investigated. These protocols transfer the information of the photon into an atomic coherent superposition of a storage medium, aiming for high storage efficiency, large storage capacity and long storage duration. This work focuses on EIT-based optical data storage [13,14], which preserves the quantum state of a input photon (light) pulse as an atomic coherence between two states. Next to different storage protocols, there also exists a number of different media in which quantum storage can be achieved. For example, EIT-based light storage was first experimentally realized in vapors [14,15] and cold atomic gases [16] because of their well defined spectral structures and potential high optical depth, necessary to achieve high storage efficiencies. However, the main disadvantage of such gaseous media is, that prepared coherences suffer from diffusion and collision processes, which limit the achievable storage time to the  $\mu\text{s}$ -regime. In contrast, solid state media, like NV centers [17], quantum dots [18,19], and rare-earth ion-doped solids (REIDS) [20] can provide atom-like spectroscopic properties with the advantages of localized interaction centers, simpler scalability and handling. Such media provide exceptionally long coherence lifetimes [21], and therefore excellent properties for long term EIT-based light storage [22]. However, the storage efficiency in such EIT-driven solid state media is usually rather low, i.e. a few % only, in contrast to vapors, where storage efficiencies of 87 % had been achieved using GEM [10]. The purpose of this work is to improve an previously demonstrated

EIT-based solid state memory, realized in a praseodymium-doped yttrium orthosilicate (PrYSO) crystal. In particular, we optimize the EIT-based light storage, and increase the optical depth, in order to maximize the storage efficiency in PrYSO. We further investigate a number of diabatic and adiabatic techniques, based on composite pulses (CP), to efficiently preserve atomic coherences prepared by the EIT light storage protocol in order to improve the storage time of the memory.<sup>1</sup>

This thesis is structured as follows: In **Chapter 1** we give an introduction on REIDS, in particular PrYSO. We focus on the spectroscopic structure, relevant for this work. Mechanisms and processes defining these spectroscopic properties are described and the relevance of PrYSO as a possible medium for quantum information storage is pointed out. In **Chapter 2** we introduce coherent wave-matter interactions in two-state and three-state systems. First, we describe diabatic excitations in single and inhomogeneously broadened two-state systems. We discuss their robustness with regard to inhomogeneities and variations of experimental parameters, and introduce CP as a common technique to enhance diabatic excitations. Second, we describe the theory on EIT-based light storage in a three-state system, including theoretical and experimental limitations of the storage efficiency. We find the optical depth of the medium limiting the achievable light storage efficiency. **Chapter 3** introduces the experimental setup, the optical setup and the radio-frequency magnetic field system. In **Chapter 4** we show the experimental results on the optimization of the EIT light storage efficiency. The storage efficiency is limited by the rather low optical depth of the PrYSO crystal. We thus present the concept of a probe multipass setup to increase the effective optical depth of the storage medium. We use this multipass setup to optimize the EIT light storage efficiency for different optical depths. We will see that it is possible to drastically increase the efficiency of our solid state memory. **Chapter 5** presents the experimental results on diabatic and adiabatic techniques for rephasing of atomic coherences. We discuss the differences between coherences prepared by the EIT-based light storage, and by direct excitation in an inhomogeneous hyperfine transition of PrYSO. We investigate universal composite pulses [24], composite adiabatic passage [25] and single-shot shaped pulses [26] with respect to their capability to rephase atomic coherences prepared in PrYSO. Furthermore, we compare the robustness of these rephasing protocols with well known techniques such as diabatic  $\pi$ -pulses and rapid adiabatic passage (RAP). We will find that composite techniques can feature an enhanced robustness with regard to variations of experimental parameters. In **Chapter 6** we discuss CP to prolong the storage time in PrYSO. The maximal storage time is limited by the lifetime of the atomic coherences. Decoherence effects usually restrict this lifetime to values much shorter than the theoretical limit given by twice the population lifetime. We apply dynamic decoherence control (DDC) techniques, consisting of a series of driving pulses, to minimize the effect of system-environment interactions leading to decoherence. We investigate the performance of CP for DDC to prolong the storage time in PrYSO, and compare with state of the art dynamical decoupling sequences. We will see that CP can be used to enhance DDC in PrYSO.

---

<sup>1</sup>An overview on the progress made by research teams in the last years is given by Cho *et al.* [23], comparing maximal storage efficiencies and storage times of different media and protocols.



# Chapter 1

## Rare-Earth Ion-doped Solids

For many decades rare-earth ion-doped solids (REIDS) have been of general scientific interest in fundamental research fields and of significant relevance for many basic applications. Today the most prominent example might be the neodymium-doped yttrium aluminum garnet crystal, which is used as a active medium in solid-state laser systems, in research and industrial applications. In the last years REIDS also aroused interest as media for optical data storage [27], as well as for their usage in quantum information processing [28–32], because in contrast to most solid state media, REIDS feature very narrow optical linewidth, and therefore favorable long coherence lifetimes, caused by the weak interaction of the dopant ions with the crystal environment. Most experiments in quantum optics require such precise spectroscopic properties. Thus, the majority of experiments in the past have been performed in atomic or molecular systems, with their spectrally narrow transitions, e.g. warm gases, cold gases, and Bose-Einstein condensates [33–36]. Apart from these gaseous media a group of atom-like solids, like nitrogen-vacancy centers in diamond [37–43], quantum dots [18, 19, 44–46], or REIDS [47–50] exist. In contrast to gases these solid media are easy to handle, scalable and can feature high optical depth. All experiments in this work are performed in a praseodymium-doped yttrium orthosilicate crystal,  $\text{Pr}^{3+}:\text{Y}_2\text{SiO}_5$ , (hereafter referred to as PrYSO). In this chapter a general overview of rare-earth ion-doped solids for coherent optical data storage is given. Particular emphasis is put on the praseodymium-doped yttrium orthosilicate crystal and its spectroscopic properties that are important for optical data storage. Additional information on REIDS can be found in [47–49].

### 1.1 Praseodymium-doped Yttrium Orthosilicate Crystal

The term "rare-earth metals" includes the elements scandium, yttrium and the 15 lanthanides including praseodymium (Pr). A special subgroup of these elements are the 3 times ionized lanthanides cerium to ytterbium, featuring a partially populated 4f orbital, while the 5s and 5p orbitals are fully populated. This electronic configuration leads to a electronic shielding of the electrons in the 4f orbital. Though the transitions in the 4f orbital are usually dipole forbidden in free atoms, they can be weakly driven when lanthanides are embedded as dopants in inorganic crystals. The optical transitions of the 4f orbital in such doped solids feature remarkably narrow homogeneous linewidth [51, 52].

In this work the only stable isotope of praseodymium,  $^{141}\text{Pr}$ , is used. The electronic configuration of  $\text{Pr}^{3+}$ -ion is  $[\text{Xe}]4f^2$ , with two free electrons in the 4f orbital. Figure 1.1 shows the absolute square of the radial wave functions of

the 4f, 5s and 5p orbitals for the free  $\text{Pr}^{3+}$ -ion and the electronic shielding of the 4f orbital. The yttrium orthosilicate crystal is of monoclinic biaxial form with a  $C_2^6h$  (C2/c) space group symmetry, including four  $\text{Y}_2\text{SiO}_5$  molecules per unit cell [53, 54]. Each molecule holds two  $\text{Y}^{3+}$ -ions in two different crystallographic sites. Thus, a doping with  $\text{Pr}^{3+}$  by replacing some of the  $\text{Y}^{3+}$ -ions in the host crystal can occur at different crystallographic sites. These sites show only  $C_1$  symmetry [55], and thus feature different crystal environments, which results in slightly different spectroscopic properties for each site. In addition, the ions in each crystallographic site can be further distinguished by two possible magnetic orientations, as a result of the alignment of the nuclear magnetic spins with respect to the  $C_2$  crystal axis. Because of the larger transition dipole moment, all experiments in this work are realized in ions of site 1, with a transition at a wavelength of  $\lambda = 605.98$  nm [56] to the first optical excited state. Using  $\text{Y}_2\text{SiO}_5$  as a host crystal for  $\text{Pr}^{3+}$  is favorable, as  $\text{Y}^{3+}$  and  $\text{Pr}^{3+}$  have similar ion radii, resulting in only small crystal deformations. Due to the weak nuclear magnetic moments of  $\text{Y}^{3+}$  and  $\text{Pr}^{3+}$ , there is only a small interaction between  $\text{Pr}^{3+}$  and the host crystal environment [49]. These properties lead to an exceptionally long population lifetime of up to 100 s [49, 58]. Typically in optical data storage and quantum optics experiments rather low dopant concentrations in the order of 0.01 – 0.1at.% are used. Much larger dopant concentrations can lead to additional line broadening [59, 60] in such a way, that favorable properties of long lifetimes and decoherence times are lost. Materials with carefully selected atomic radii of the dopant [61], can avoid these problems.

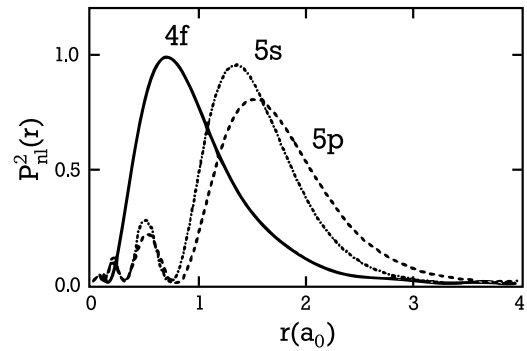


Figure 1.1: Absolute square of the radial wave functions of the 4f, 5s and 5p orbitals for the free  $\text{Pr}^{3+}$ -ion of the ground configuration  $4f^2 5s^2 5p^6$ . Figure taken from [57].

## 1.2 Spectroscopic Properties of $\text{Pr}^{3+}:\text{Y}_2\text{SiO}_5$

The relevant optical transitions used in this work are driven in the 4f orbital. The electronic ground state in Russell-Saunders notation is  $^3\text{H}_4$ . For site 1 this state can be coupled to the optical excited state  $^1\text{D}_2$  with a wavelength of 605.98 nm [56]. In general this optical spectrum is modified by a number of effects. We can describe the system by a simplified Hamilton operator [49]:

$$\hat{H}_{ion} = \underbrace{[\hat{H}_0 + \hat{H}_C + \hat{H}_{SO}]}_{\text{free ion}} + \underbrace{\hat{H}_{CF}}_{\text{crystal field}} + \underbrace{[\hat{H}_{HF} + \hat{H}_Q + \hat{H}_Z + \hat{H}_z]}_{\text{hyperfine structure}} \quad (1.1)$$

Here the level structure of a free ion is described by its potential and kinetic energy ( $\hat{H}_0$ ), the Coulomb interaction ( $\hat{H}_C$ ), and the spin-orbit interaction ( $\hat{H}_{SO}$ ). The interaction of  $\text{Pr}^{3+}$  with the crystal field, when used as a dopant in a host crystal,

is described by  $\hat{H}_{CF}$ . Additionally, hyperfine interactions lead to a further splitting of the levels, primarily caused by magnetic hyperfine interaction ( $\hat{H}_{HF}$ ), and the electric quadrupole interaction ( $\hat{H}_Q$ ). In the presence of an external magnetic field additional splitting by electronic Zeeman effect ( $\hat{H}_Z$ ) and nuclear Zeeman effect ( $\hat{H}_z$ ) occurs. In the following, the different interactions and their effects on the level structure will be explained. A detailed description can be found in [47–49].

### 1.2.1 Fine Structure and Crystal Field Interaction

The primary terms of the Hamilton operator for an ion with  $N$  free electrons without external fields are:

$$\begin{aligned}\hat{H}_0 &= -\frac{\hbar^2}{2m} \sum_{i=1}^N \nabla_i^2 - \sum_{i=1}^N \frac{Ze^2}{r_i} \\ \hat{H}_C &= \sum_{i<j}^N \frac{e^2}{r_{ij}} \\ \hat{H}_{SO} &= \sum_{i=1}^N \xi(r_i) \vec{l}_i \cdot \vec{s}_i\end{aligned}\tag{1.2}$$

In Equation 1.2 the first term of  $\hat{H}_0$  is the kinetic energy and the second term the potential energy of the 4f electrons in the field of the nucleus. As  $\hat{H}_0$  is purely radial the energy shifts are the same for all levels, thus level structure is not changed. The Coulomb and spin-orbit interactions however are radial but non symmetric, affecting the level structure, which leads to a splitting of the energy levels (fine structure). We can usually describe a system in Russell-Saunders notation (LS-coupling), if the interaction between the electrons in the 4f orbital is stronger than the spin-orbit coupling, i.e.  $\hat{H}_C \gg \hat{H}_{SO}$ . If the spin-orbit interaction becomes much stronger than the Coulomb interaction, i.e. ( $\hat{H}_{SO} \gg \hat{H}_C$ ), the jj-coupling can be used to describe the system. In rare-earth ions, Coulomb interaction and spin-orbit interaction are comparable, thus both coupling schemes are inappropriate. However, starting from the LS-coupling an intermediate coupling scheme can be developed [49]. Nevertheless, energy levels of rare-earth ions are mostly labeled in Russell-Saunders notation. The fine structure is defined by the total angular momentum  $J$  with typical energy level splittings of  $\approx 1000 \text{ cm}^{-1}$  [47]. These levels are in general degenerated by  $(2J + 1)$  with regard to  $m_J$ , i.e.  $J$ -multiplets. This degeneracy is lifted by the crystal field interaction ( $\hat{H}_{CF}$ ) due to low symmetry, leading to internal Stark shifts of the levels. The  $J$ -multiplets split into  $(2J+1)$  energy levels with energy differences in the order of  $100 \text{ cm}^{-1}$  [48]. In addition, the crystal field causes a mixing of alternative electron configurations of different parity, e.g. of the [Xe]4f5d and [Xe]4f<sup>2</sup> configuration. Due to this mixing the selection rules are no longer valid. This results in weak allowed electric dipole transitions within the 4f<sup>*N*</sup> configuration. Regarding Pr<sup>3+</sup> doped into Y<sub>2</sub>SiO<sub>5</sub>, this fact allows to drive the transition between the lowest crystal field states <sup>3</sup>H<sub>4</sub> ↔ <sup>1</sup>D<sub>2</sub>. However, the mixing of electronic configurations in PrYSO is rather small, which leads to a weak transition moment, but on the other hand exceptionally long population lifetime for the first optically excited state <sup>1</sup>D<sub>2</sub>( $m_j = -2$ ) in the order of  $\sim 100 \mu\text{s}$ . Populations in higher  $m_j$ -states relax much faster ( $\sim 1 \text{ ns}$ ) into the lowest state of the corresponding  $J$ -multiplet by phonon interactions (see blue arrows in Figure 1.2). However, phonon interactions can also excite electrons into

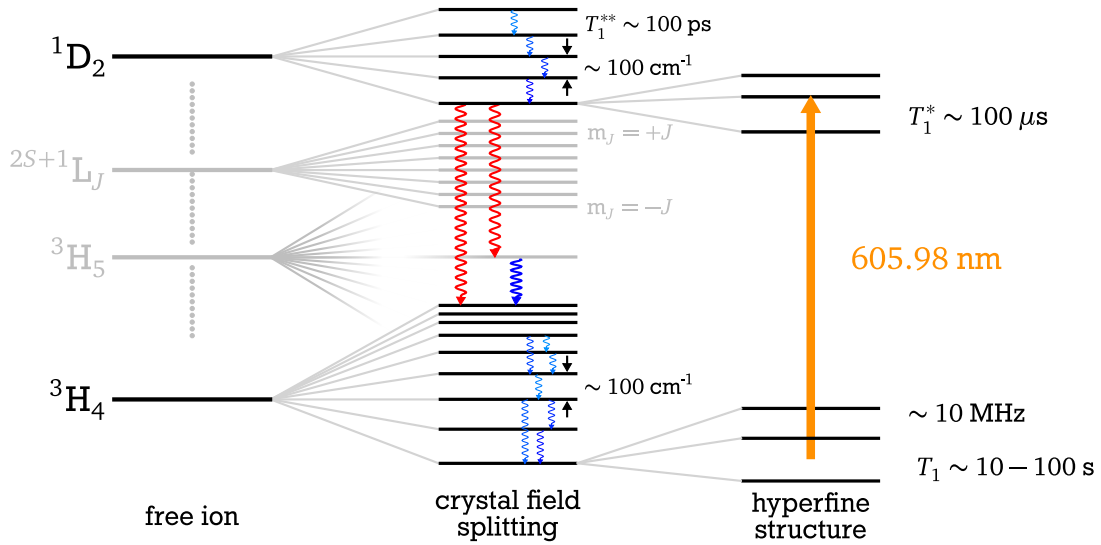


Figure 1.2: (left) Relevant level structure of free  $\text{Pr}^{3+}$ . (center) When used as dopant in a rare-earth crystal, the interaction with the crystal field introduces a splitting of the levels. (right) Hyperfine structure of the lowest crystal field levels. Figure based on [48].

higher crystal field levels or  $J$ -multiplet states by absorption. These excitations can be suppressed by cooling the crystal to temperatures below 4 K. Relaxation from the lowest excited state  $^1\text{D}_2(m_j = -2)$  into  $^3\text{H}_4(m_j = -4)$  occurs mainly via higher crystal field levels ( $^3\text{H}_4(m_j > -4)$  and  $^3\text{H}_5$ ) by fluorescence at wavelength  $\lambda > 610$  nm and from there by a non-radiative decay due to phonon interactions. The level structure due to the crystal field interaction is shown in Figure 1.2.

## 1.2.2 Hyperfine Structure

Rare-earth ions doped in solids, with a nuclear spin  $I \neq 0$ , feature an additional hyperfine structure in the range from MHz to GHz. This structure can be observed, because the homogeneous linewidth of the crystal field levels, when cooled to cryogenic temperatures, is well below 1 MHz.  $\text{Pr}^{3+}$  has a nuclear spin of  $I = 5/2$ . In the following, the different contributions to the hyperfine structure, as described by the Hamilton operator (see Equation 1.1), are discussed. In the case of no external magnetic field two effects contribute to the hyperfine splitting. First, the magnetic hyperfine interaction  $\hat{H}_{HF}$ , which is based on the interaction between nuclear spin  $I$  and the effective magnetic field induced by the electronic angular momentum  $J$ . However, for electronic singlet states, like the  $\text{Pr}^{3+}$ -ion with its two free electrons, the total angular momentum  $J$  vanishes. Thus, in first order, as  $\hat{H}_{HF} \propto \vec{I} \cdot \vec{J}$ , the splitting due to this interaction is zero. In second order, when taking into account also higher crystal field levels of the corresponding  $J$ -multiplet, e.g. states  $^3\text{H}_4(m_j > -4)$  for the ground state  $^3\text{H}_4(m_j = -4)$ , a contribution to the hyperfine structure can be calculated. A second, nuclear electric contribution to the hyperfine structure is mainly given by the electric quadrupole interaction ( $\hat{H}_Q$ ), as the expectation value of the nuclear electric dipole moments vanish. The  $\text{Pr}^{3+}$ -nucleus shows a electric quadrupole moment which interacts with the inhomogeneous crystal field. We can combine the magnetic hyperfine interaction and

the electric quadrupole interaction into an effective pseudo-quadrupole Hamiltonian operator

$$\hat{H}_{HF,Q} = D \left[ I_z^2 - \frac{1}{3} I(I+1) \right] + E (I_x^2 + I_y^2) \quad (1.3)$$

with effective hyperfine constants  $D$  and  $E$ . Written in this form, one can see that this leads to a twofold degenerated hyperfine structure. An additional splitting of the hyperfine structure can occur by taking into account the interaction of the nuclear magnetic moment of the dopant ion with the nuclei of the surrounding atoms in the host material [62]. This so-called, superhyperfine interaction or transferred hyperfine interaction, usually leads to energy splittings of a few kHz.

When additional external magnetic fields are applied the degeneracy of the hyperfine levels is suspended and a further splitting by magnetic Zeeman shifts occurs. This can be described by the electronic Zeeman interaction ( $\hat{H}_z$ ) and the nuclear Zeeman interaction ( $\hat{H}_z$ ). However, as in this present work no external magnetic fields are applied, the magnetic Zeeman shifts are insignificant to the total hyperfine structure. Due to the nuclear spin of  $I = 5/2$  of  $\text{Pr}^{3+}$  each crystal field level splits up into three hyperfine levels, typically labeled with the quantum number  $m_I$ , i.e.  $|\pm 1/2\rangle$ ,  $|\pm 3/2\rangle$  and  $|\pm 5/2\rangle$ .

Figure 1.3 shows the hyperfine structure of the relevant optical transition  ${}^3\text{H}_4(m_J = -4) \leftrightarrow {}^1\text{D}_2(m_J = -2)$  without external magnetic field. Note that the energetic ordering of the excited state hyperfine levels is inverted compared to the ground state hyperfine levels. Due to the low crystal field symmetry the selection rule  $\Delta m_I = 0$  is no longer valid. Thus, all nine transitions between the ground state hyperfine levels and excited state hyperfine levels are allowed. However, the transition moments are quite different. In particular, it is possible to identify an effective 4-level system and an effective 2-level system with only a weak coupling between the systems. Table 1.1 depicts the transition moments  $\mu$  and relative oscillator strength  $f$  between the hyperfine levels of the electronic ground state  ${}^3\text{H}_4(m_J = -4)$  and the excited state  ${}^1\text{D}_2(m_J = -2)$ . These still rather weak transition moments lead to a relatively long population lifetime of the excited state of  $T_1^* = 164 \mu\text{s}$  [56]. The relaxation time of the ground state hyperfine levels is limited by spin flips, and phononic interactions with a strong temperature dependence [63]. At temperatures below 4 K the relaxation times are in the order of 10 – 100 s, depending on the specific hyperfine transition [58]. These relaxation properties, in combination with the unequal transition moments of the hyperfine levels, give rise to population redistribution by optical pumping [63]. The spectroscopic properties of PrYSO of relevance for the present work are summarized in Table 1.2.

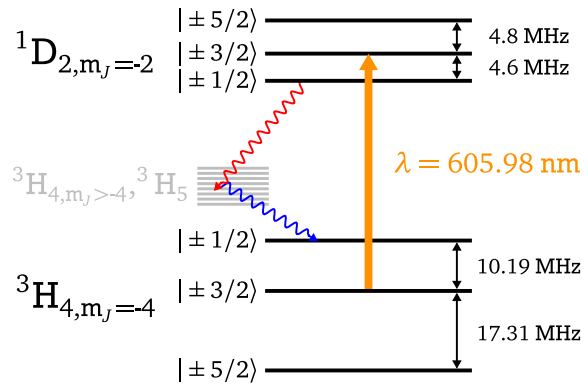


Figure 1.3: Hyperfine structure of the relevant crystal field transition  ${}^3\text{H}_4(m_J = -4) \leftrightarrow {}^1\text{D}_2(m_J = -2)$  of Site 1 of the PrYSO crystal.

Table 1.1: Relative oscillator strength  $f$  and transition moments  $\mu$  between the hyperfine levels of the electronic ground state  $^3H_4(m_J = -4)$  and the excited state  $^1D_2(m_J = -2)$  of PrYSO (Site 1) taken from [64,65]. The effective 4- and 2-level systems are marked in green.

		$^1D_2$		
		$ \pm 1/2\rangle$	$ \pm 3/2\rangle$	$ \pm 5/2\rangle$
$^3H_4$	$ \pm 1/2\rangle$	$f = 0.55$ $\mu = 2.0 \cdot 10^{-32} \text{ Cm}$	$f = 0.38$ $\mu = 1.7 \cdot 10^{-32} \text{ Cm}$	$f = 0.07$ $\mu = 0.7 \cdot 10^{-32} \text{ Cm}$
	$ \pm 3/2\rangle$	$f = 0.4$ $\mu = 1.7 \cdot 10^{-32} \text{ Cm}$	$f = 0.6$ $\mu = 2.1 \cdot 10^{-32} \text{ Cm}$	$f = 0.01$ $\mu = 0.3 \cdot 10^{-32} \text{ Cm}$
	$ \pm 5/2\rangle$	$f = 0.05$ $\mu = 0.6 \cdot 10^{-32} \text{ Cm}$	$f = 0.02$ $\mu = 0.4 \cdot 10^{-32} \text{ Cm}$	$f = 0.93$ $\mu = 2.6 \cdot 10^{-32} \text{ Cm}$

### 1.3 Line Broadening Mechanisms

The set of REIDS feature a broad range of different spectral linewidths. From  $\sim 100$  Hz in trivalent rare-earth ions in host materials with negligible small nuclear moments, to  $\sim 1$  THz in systems at room temperature, strongly coupled by phonons. The nature of REIDS spectral linewidths requires to distinguish between homogeneous and inhomogeneous contributions to the total linewidth. While homogeneous effects contribute equally to all ions in the host crystal, an inhomogeneous broadening arises due to the fact that each dopant ion in the crystal experiences a different local crystal field environment.

#### Homogeneous Linewidth

The homogeneous linewidth  $\Gamma_{hom}$ , i.e. the spectral broadening within a single ion, is determined by the coherence time  $T_2$ , with  $\Gamma_{hom} = 1/\pi T_2$ . Even at very low temperatures, dynamic interaction processes, driving transitions between the electronic states, contribute to this broadening. The total homogeneous linewidth [49, 56] is thus given by:

$$\Gamma_{hom} = \Gamma_{nat} + \Gamma_{ion-spin} + \Gamma_{ion-ion} + \Gamma_{phonon} \quad (1.4)$$

The natural linewidth is caused by the population decay of the excited state and can be calculated by  $\Gamma_{nat} = 1/(2\pi T_1)$ , using the population relaxation time  $T_1$  of the transition. Hence, without any additional interaction, the theoretical maximum coherence time  $T_2$  is limited by the population decay time  $T_1$  with  $T_2 = 2T_1$  only. However, in REIDS in addition to population decay, other effects contribute to the total homogeneous linewidth. Moreover, the interaction between ions and fluctuating atomic nuclei spins and electron spins in the environment lead to  $\Gamma_{ion-spin}$ . A second contribution results from the ion-ion interaction  $\Gamma_{ion-ion}$  between the excited  $\text{Pr}^{3+}$ -ions by electrostatic dipole-dipole interaction. A third contribution ( $\Gamma_{phonon}$ ) is given by phonon excitation and relaxation processes to and from higher crystal field states. In general, the coherence time  $T_2$  is reduced due to these interactions, and thus is much smaller than  $T_1$ . In a PrYSO crystal, cooled



Table 1.2: Relevant relaxation times and corresponding linewidth of PrYSO.

**Excited state  $^1D_2(m_J = -2) \leftrightarrow$  Ground state  $^3H_4(m_J = -4)$  transition**

Population lifetime	$T_1^* = 164 \mu\text{s}$ [56]	$\leftrightarrow$	$\Gamma_{nat}^* \approx 970 \text{ Hz}$
Coherence time	$T_2^* \approx 111 \mu\text{s}$ [56]	$\leftrightarrow$	$\Gamma_{hom}^* \approx 2.9 \text{ kHz}$
Theoretical dephasing time	$T_{deph}^* \approx 45 \text{ ps}$	$\leftrightarrow$	$\Gamma_{inhom}^* \approx 7 \text{ GHz}$

**Ground state  $^3H_4(m_J = -4)$  hyperfine transitions**

Relaxation time $ 3/2\rangle \leftrightarrow  5/2\rangle$	$T_1 = 109.5 \text{ s}$ [58]	$\leftrightarrow$	$\Gamma_{nat}^* = 1.5 \text{ mHz}$
Relaxation time $ 1/2\rangle \leftrightarrow  3/2\rangle$	$T_1 = 8.7 \text{ s}$ [58]	$\leftrightarrow$	$\Gamma_{nat}^* = 18.3 \text{ mHz}$
Coherence time	$T_2 \approx 500 \mu\text{s}$	$\leftrightarrow$	$\Gamma_{hom} \approx 640 \text{ Hz}$ [27]
Dephasing time $ 3/2\rangle \leftrightarrow  5/2\rangle$	$T_{deph} \approx 4.5 \mu\text{s}$	$\leftrightarrow$	$\Gamma_{inhom} \approx 70 \text{ kHz}$ [63]
Dephasing time $ 1/2\rangle \leftrightarrow  3/2\rangle$	$T_{deph} \approx 10 \mu\text{s}$	$\leftrightarrow$	$\Gamma_{inhom} \approx 30 \text{ kHz}$ [63]

to cryogenic temperatures to reduce phononic interactions, the resulting homogeneous linewidth of the excited state  $^1D_2(m_J = -2)$  is  $\Gamma_{hom}^* \approx 2.9 \text{ kHz}$ , and thus much larger than  $\Gamma_{nat}^* \approx 970 \text{ Hz}$ . The homogeneous linewidth of the ground state hyperfine levels is  $\Gamma_{hom} \approx 640 \text{ Hz}$ , leading to a coherence time of  $T_2 \approx 500 \mu\text{s}$ .

## Inhomogeneous Linewidth

The homogeneous linewidth usually can not be measured directly by spectroscopic techniques, due to a large additional inhomogeneous broadening even at very low temperatures. The broadening of the optical transition arises from inhomogeneities in the crystal lattice environment due to defects, like mechanical stress and chemical impurities from the crystal growing process and different atomic radii to the praseodymium ions that substitute the yttrium ions [61]. This leads to local variations in the crystal field for different ions. Thus, ions at different locations feature different crystal field, i.e. optical, transition frequencies. As a result a broadened optical transition is measured. We group all ions with the same transition frequency and label them as a *frequency ensemble*. The inhomogeneous broadening of the optical transition in REIDS are usually in the order of  $\Gamma_{inhom}^* \sim 10 \text{ GHz}$  [49]. Likewise, the transitions within the hyperfine states feature a inhomogeneous broadening  $\Gamma_{inhom}$  of a few kHz, leading to dephasing times  $T_{deph}$  in the order of  $\mu\text{s}$ , with its origin also due to variations in the crystal field environment. We note, that the inhomogeneous broadening in general strongly depends on the dopant concentration [59, 60]. Higher dopant concentrations lead to additional mechanical stress, due to the different atomic radii of the dopant ions and as a result to larger values of  $\Gamma_{inhom}^*$ , and  $\Gamma_{inhom}$ , respectively [60]. In addition, with an increase of the dopant concentration the ground state hyperfine splittings is reduced, and a slight dependence of the ground state hyperfine splitting with

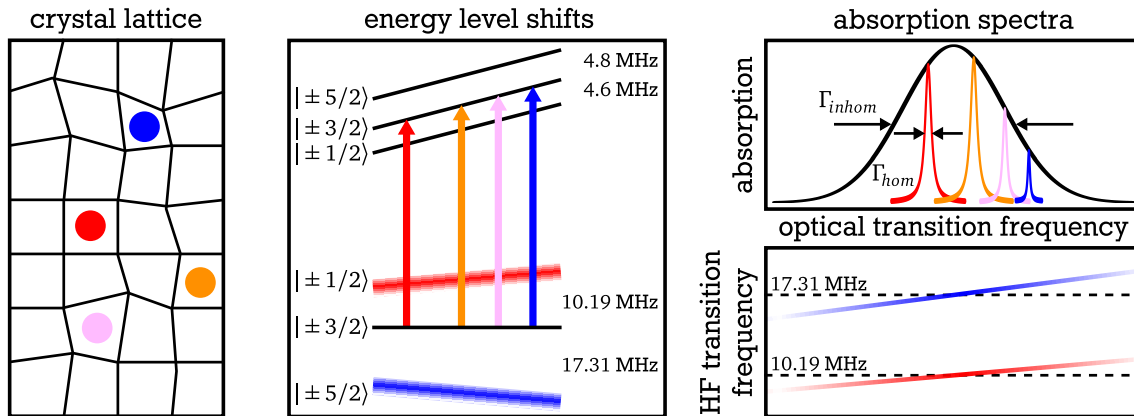


Figure 1.4: Origin of the inhomogeneous broadening of the optical and hyperfine transitions. (Left) Several  $\text{Pr}^{3+}$ -ions (colored dots) experience different crystal field environments. (Center) This leads to variations in the optical and hyperfine transition frequencies. (Right) The superposition of all homogeneously broadened transitions result in a inhomogeneously broadened transition. The center of the hyperfine transition frequencies slightly depend on the position within the inhomogeneous optical line. Figure taken from [58], modified.

respect to the optical transition frequency, i.e. the position within the inhomogeneous broadening of the optical transition was identified [60]. In order to reduce these effects typical dopant concentrations should be well below 1 %.

## Dynamic Effects on the Inhomogeneous Linewidth and Transitions

The inhomogeneous linewidth described in the previous section was introduced as a static phenomena, in which each  $\text{Pr}^{3+}$  exhibits a temporally constant, though from ion to ion slightly different, crystal field environment. However, in general, the crystal field represents a dynamically changing, open-bath environment for  $\text{Pr}^{3+}$ . The  $\text{Pr}^{3+}$ -ions interact with the surrounding yttrium ions of the host crystal via dipole-dipole interaction. Thus, if a stochastic yttrium spin flips occurs, the crystal field environment, and therefore the level structure of the close-by ions changes. The small change of the ions transition frequency can be understood as a spectral movement within the inhomogeneous line. The overall width of the inhomogeneous line is not changed due to this effect. The  $\text{Pr}^{3+}$  ions, with their homogeneous linewidth, just diffuse within the inhomogeneous line, thus this effect is also known as *spectral diffusion* [48, 49, 66]. In addition, also the interaction between  $\text{Pr}^{3+}$ -ions can result in a shift of the transition frequencies. The  $\text{Pr}^{3+}$ -ions feature a state dependent, electric dipole moment. Thus, a  $\text{Pr}^{3+}$ -ion, excited by an external field, changes the transition frequency of the surrounding  $\text{Pr}^{3+}$ -ions. This field induced transition frequency change is called *instantaneous spectral diffusion* [67]. Both effects strongly depend on the interaction strengths and distances between the interacting ions. Static and dynamic inhomogeneous linewidths represent the major obstacles for highly efficient, long-term data storage in REIDS. Thus, in the past years, intensive efforts have been put in the development of techniques to either minimize or compensate these effects. Also the present work deals with advanced compensation techniques, to achieve such a highly efficient, long-term quantum storage device, known as dynamic decoherence control (DDC).



## Chapter 2

# Coherent Wave Matter Interactions

The experiments, conducted in the scope of this work, are based on the interaction of coherent radiation, in the optical regime and radio-frequency regime, with an atom-like solid, the praseodymium ions in the yttrium orthosilicate host crystal. In particular, light storage based on EIT and the techniques applied to preserve the stored information are based on coherent interactions. Thus, in this chapter the basics on coherent wave matter interactions, relevant for this work are described.

We discuss the interactions of an ideal two-state quantum system driven by a coherent field in the diabatic picture. We saw in Chapter 1, that PrYSO exhibits rather large inhomogeneous broadened transitions. We thus introduce a two-state system including a inhomogeneous broadening of the transition and inhomogeneities of the driving field, to describe the hyperfine transitions of PrYSO. We show the population dynamics in such a inhomogeneous two-state system, and introduce composite pulses for robust two-state manipulations. An extensive discussion on coherent dynamics in a two-state system can be found in [68].

The description of the EIT light storage protocol is based on the interaction of a three-state system with two coherent fields. We introduce the adiabatic light storage in a three-state system based on electromagnetically induced transparency (EIT) and discuss limiting effects of the efficiency of the storage protocol and of the storage medium. A detailed description on EIT and light storage by EIT is given in [69, 70].

## 2.1 Coherent Interactions in a Two-Level System

In this section the coherent interactions in a two-state quantum system driven by a coherent field are discussed in a semi-classical description. We assume the coherent driving field, to be a classical electric field. The description holds true for classical magnetic dipole transitions as well. We describe the changes induced by a coherent driving field in a two-state quantum system, as depicted in Figure 2.1, using the time-dependent Schrödinger equation (TDSE):

$$i\hbar \frac{\partial}{\partial t} |\Psi(t)\rangle = \hat{H}(t) |\Psi(t)\rangle \quad (2.1)$$

The Hamilton operator  $\hat{H}(t)$  consists of  $\hat{H}_0$ , the Hamilton operator describing the eigenstates of the unperturbed two-state system, and the operator  $\hat{V}(t)$  describing the time-dependent interaction between the electric field and the two-state system.

We define the electric field with the angular frequency  $\omega$  and the real amplitude  $\vec{\mathcal{E}}_0(t)$  as

$$\vec{\mathcal{E}}(t) = \frac{1}{2} \vec{\mathcal{E}}_0(t) (e^{-i\omega t} + e^{i\omega t}), \quad (2.2)$$

leading to the total Hamilton operator

$$\hat{H}(t) = \hat{H}_0 + \hat{V}(t) = \begin{pmatrix} E_1 & -\vec{\mu}_{12} \vec{\mathcal{E}}(t) \\ -\vec{\mu}_{21} \vec{\mathcal{E}}(t) & E_2 \end{pmatrix}, \quad (2.3)$$

with  $E_1$  and  $E_2$  the energies of levels  $|1\rangle$ , and  $|2\rangle$ , respectively. The interaction of the coherent field with the system is described by  $\vec{\mu}_{ij} \vec{\mathcal{E}}(t)$  with the transition dipole moments defined by  $\vec{\mu}_{ij} = -e \langle i | \vec{r} | j \rangle = \vec{\mu}_{ji}^*$ . After a transformation into the rotating wave picture [68], we define the detuning  $\Delta = \omega - \omega_{12}$ , and the Rabi frequency as

$$\Omega(t) = -\frac{\vec{\mu}_{12} \vec{\mathcal{E}}_0(t)}{\hbar}, \quad (2.4)$$

If the angular carrier frequency  $\omega$  of the driving electric field is much faster than the dynamics of the system, i.e.  $\Omega(t)$ ,  $\dot{\Omega}(t)$ , and  $\Delta(t) \ll \omega$ , we can apply the *rotating wave approximation* (RWA), and write

$$\hat{H}_{\text{RWA}}(t) = \frac{\hbar}{2} \begin{pmatrix} \Delta & \Omega(t) \\ \Omega^*(t) & -\Delta \end{pmatrix}. \quad (2.5)$$

### 2.1.1 Rabi Oscillations and Pulsed Excitation

Solving the Schrödinger Equation 2.1 with the RWA Hamilton operator 2.5 one can calculate the dynamics of the probability amplitudes  $c_1(t)$  and  $c_2(t)$ , and using  $P_n(t) = |c_n(t)|^2$ , the corresponding populations  $P_1(t)$ , and  $P_2(t)$ . If we assume the system is initially prepared in state  $|1\rangle$ , i.e.  $c_1(0) = 1$  and  $c_2(0) = 0$ , the population dynamics are given by

$$P_1(t) = \frac{\Omega^2}{2\Omega_{\text{eff}}^2} [1 + \cos(\Omega_{\text{eff}} t)] + \frac{\Delta^2}{\Omega_{\text{eff}}^2}, \quad \text{and} \quad P_2(t) = \frac{\Omega^2}{2\Omega_{\text{eff}}^2} [1 - \cos(\Omega_{\text{eff}} t)] \quad (2.6)$$

Here, we introduced the effective Rabi frequency given by  $\Omega_{\text{eff}}(t) = \sqrt{\Omega^2(t) + \Delta^2(t)}$ . From Equation 2.6 we see that the populations oscillate with the effective Rabi frequency between the states  $|1\rangle$  and  $|2\rangle$  with an amplitude  $\Omega^2/\Omega_{\text{eff}}^2$ . Only in the case of resonant driving ( $\Delta = 0$ ) a total population inversion is achieved. In this case we define the *pulse area* as  $A = \int_0^\tau \Omega(t) dt$ , with the duration of interaction  $\tau$ . We find population inversion for  $A \equiv (2n + 1)\pi$  with  $n \in \mathbb{N}$  and complete population return for  $A \equiv (2n)\pi$ . Note that  $A$  can in principle be positive, negative, or even zero, depending on the pulse shape of the complex

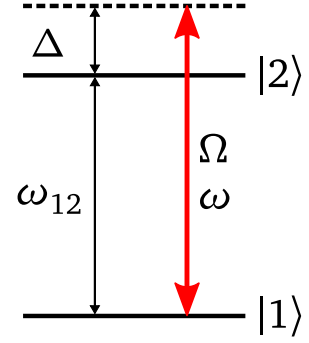


Figure 2.1: Two-state system with transition frequency  $\omega_{12}$  coherently driven by a field of (angular) frequency  $\omega$ , Rabi frequency  $\Omega$ , with a detuning of  $\Delta$ .

Rabi frequency  $\Omega(t)$ . With a pulse area of  $A \equiv (2n + 1)\pi/2$  the system is excited into a maximal coherent superposition of states  $|1\rangle$  and  $|2\rangle$ . Note that all pulses of pulse areas  $0 < A < \pi$  excite the system into a coherent superposition, however not in any case a maximal superposition. Figure 2.2 (top) depicts the Rabi oscillations in a single two-state system for different detuning  $\Delta$  from the resonance frequency  $\omega_{12}$ . In the case of an off-resonant driving the maximal possible population inversion reduces and the oscillation frequency increases.

This effect becomes of special interest, in situations involving an ensemble of two-state systems, where each ensemble  $\epsilon$  experiences a different environment, e.g. a different Rabi frequency  $\Omega_\epsilon(t)$  or a different detuning  $\Delta_\epsilon$ . In this case each individual ensemble has to satisfy the TDSE with its specific detuning  $\Delta_\epsilon$  and Rabi frequency  $\Omega_\epsilon(t)$ . We assume an ensemble of two-state systems with different detunings, i.e. an inhomogeneous broadening  $\Gamma_{12} = -\Delta_\epsilon \dots \Delta_\epsilon$  of the transition  $|1\rangle \leftrightarrow |2\rangle$  and an ensemble driven by different Rabi frequencies, i.e.  $\delta\Omega = -\Omega_\epsilon \dots \Omega_\epsilon$ . We evaluate the probabilities of the ensemble of two-state systems as weighted sums of the individual probabilities,  $P_n(t) = \sum_\epsilon p(\epsilon) |c_n(\epsilon, t)|^2$ , with the weighting factor  $p(\epsilon)$  defining the shape of the inhomogeneous broadening and the distribution of Rabi frequencies. The Rabi oscillation of an ensemble of different detunings, with  $\Gamma_{12} = -\Omega \dots \Omega$ , and with different Rabi frequencies with  $\delta\Omega = -0.15\Omega \dots 0.15\Omega$  is depicted in Figure 2.2 (bottom). We find in both cases that the inhomogeneities lead to a damping of the Rabi oscillations and for the case of  $\Gamma_{12}$  also to an increase of the effective Rabi frequency. Thus, in order to efficiently drive an ensemble of two-state systems the Rabi frequency  $\Omega$  has to be much larger than the inhomogeneous broadening  $\Gamma_{12}$  and inhomogeneities in the Rabi frequency have to be avoided.

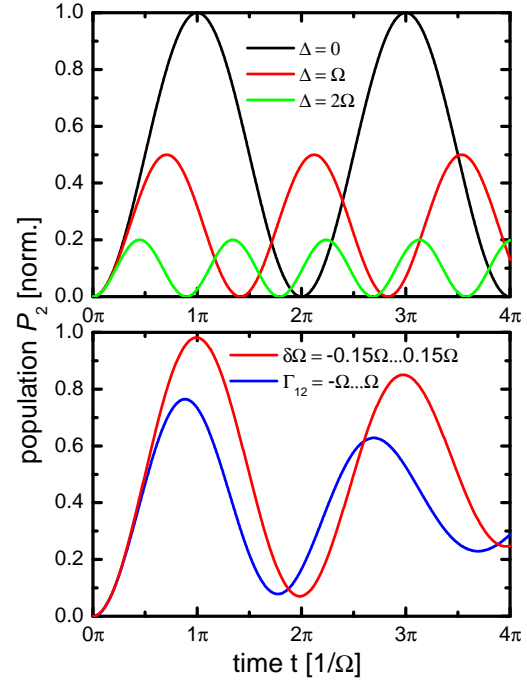


Figure 2.2: (Top) Rabi oscillations for different detunings  $\Delta$  in units of  $\Omega$  from the resonance  $\omega_{12}$  of the single two-state system. (Bottom) Averaged Rabi oscillations in an ensemble of two-state systems with an inhomogeneous broadening  $\Gamma_{12}$  and an inhomogeneity of the driving field  $\delta\Omega$ .

## 2.1.2 Description of Macroscopic Systems

The previous section treated a single, idealized quantum system in a pure state  $|\Psi\rangle = \sum_n c_n |\psi_n\rangle$ , with  $|\psi_n\rangle = e^{-i\zeta_n(t)} |\psi'_n\rangle$ , using the state vectors  $|\Psi\rangle$  to describe the system. Alternatively, the state of the system can be described in the density matrix formalism, with the density matrix of a single, pure system given by

$$\hat{\rho} = |\Psi\rangle\langle\Psi|. \quad (2.7)$$

Thus, in the basis  $\{|\psi_n\rangle\}$  the density matrix can be written as

$$\hat{\rho} = \sum_{i,j} c_i c_j^* |\psi_i\rangle \langle \psi_j|. \quad (2.8)$$

Here, the product of the probability amplitudes  $c_i c_j^*$  gives the density matrix element  $\rho_{ij} = \rho_{ji}^*$ . The diagonal elements  $\rho_{ii}$  correspond to the populations of states  $|\psi_i\rangle$ . Any kind of coherent superposition is described by the off-diagonal elements  $\rho_{ij} (i \neq j)$ . This formalism can also be used to describe a macroscopic system, consisting of a number of single quantum systems with different probabilities  $p_\epsilon$  and states  $|\Psi_\epsilon\rangle$ . The density matrix of such a macroscopic system can thus be written as

$$\hat{\rho} = \sum_{\epsilon} p_{\epsilon} |\Psi_{\epsilon}\rangle \langle \Psi_{\epsilon}|. \quad (2.9)$$

A collective coherent superposition is then described by

$$\rho_{ij} = \sum_{\epsilon} p_{\epsilon} |\rho_{ij}^{\epsilon}| e^{i\Delta_{\epsilon} t}, \quad (2.10)$$

with the individual transition frequency  $\omega_{\epsilon} = \omega_{ij} + \Delta_{\epsilon}$ . We thus find that the individual coherences  $\epsilon$  of a macroscopic collective coherence created in an inhomogeneous broadened system feature different time evolutions of the coherence phases. Hence, the collective coherence is reduced for  $t > 0$ . This effect is called dephasing. In both cases, single quantum systems and macroscopic systems, the dynamics can be described by the Liouville-von-Neumann equation, given by

$$i\hbar \frac{\partial}{\partial t} \hat{\rho} = [\hat{H}, \hat{\rho}] + i\hbar \hat{D}, \quad (2.11)$$

with the dissipator  $\hat{D}$  including relaxations of populations and coherences by spontaneous emission and decoherence effects. For a two-state system we find the dissipator given by

$$\hat{D} = \begin{pmatrix} \Gamma_{21}\rho_{22} & -\gamma_{12}\rho_{12} \\ -\gamma_{21}\rho_{21} & -\Gamma_{21}\rho_{22} \end{pmatrix} \text{ with } \gamma_{12} = \gamma_{21} = \frac{1}{2}\Gamma_{21} + \gamma'_{21}. \quad (2.12)$$

The spontaneous decay rates  $\Gamma_{21}$ , is given by the natural lifetime  $T_1 = 1/\Gamma_{21}$ . The decoherence is described by the decoherence rates  $\gamma_{ij}$  and decays with half the rate of spontaneous decay  $\Gamma_{21}$ . Additional decoherence effects are summarized in  $\gamma'_{21}$ . In PrYSO spectral diffusion gives a large contribution to  $\gamma'_{21}$  in which usually also the reversible effect of dephasing is included.

### 2.1.3 Composite Pulses

We saw in Section 2.1.1 that an efficient diabatic driving of a inhomogeneously broadened two-state system from a initial state into a precisely defined final state becomes ambitious if  $\Gamma_{inhom} \gg \Omega$ . One possible solution to overcome the inefficient driving of a single excitation pulse is the application of pulse sequences, i.e. a series of pulses of possibly different durations  $\tau$  and phases  $\phi$ . Such *composite pulses*

(CP) are usually designed to perform a defined system excitation, e.g. a population inversion as it is achieved by a single  $\pi$ -pulse, while compensating for pulse errors of a single pulse and inhomogeneities of the driven system. CP were first proposed in the mid 70's by Redfield *et al.* [71] and Levitt *et al.* [72] in the field of nuclear magnetic resonance. Today there are an enormous number of different CP, especially designed for their specific application goals and the type of errors involved [73, 74]. One can categorize them into narrowband and broadband CP, i.e. operating for a smaller, or larger bandwidth of parameter variations compared to a single pulse and one can group them regarding their type of error compensation. There are two major types of errors. First, pulse area errors, which can arise e.g. from field inhomogeneities across the sample dimensions, or fluctuations in the driving field. Second, errors induced due to a detuned driving, as it exists in ensemble systems featuring an inhomogeneous broadening. The effect of driving a two-state system using a CP can be understood intuitively in the Bloch sphere picture, represented in a rotating frame with the transition frequency of the two-state system, see Figure 2.3. The Bloch vector (green arrow) describes the state of the system, defined by

$$\vec{r} = (2\text{Re}(\rho_{12}), 2\text{Im}(\rho_{12}), |\rho_{22}| - |\rho_{11}|). \quad (2.13)$$

The z-axis represents the population difference between state  $|1\rangle$  and  $|2\rangle$ . The x- and y-axis depict the coherence  $\rho_{12} = |\rho_{12}^\epsilon| e^{i(\Delta_\epsilon t + \gamma_\epsilon)}$  with  $\gamma_\epsilon = \arctan(\text{Im}(\rho_{12})/\text{Re}(\rho_{12}))$ . The driving of the two-state system is described by rotations of the Bloch vector on the Bloch sphere. The driving field can be translated into a torque vector  $\vec{T}$  driving the Bloch vector  $\vec{r}$  with

$$\vec{T} = (\text{Re}(\Omega), \text{Im}(\Omega), \Delta), \quad \text{and} \quad \dot{\vec{r}} = \vec{T} \times \vec{r}. \quad (2.14)$$

Figure 2.3 depicts the motion (green line) of the Bloch vector (green arrow) by the torque vector (red arrow) on the Bloch sphere for different driving pulses. The system is initially prepared in state  $|1\rangle$ , i.e. the Bloch vector is pointing into the -z-direction. A driving with a perfect  $\pi$ -pulse, yielding a total population transfer from state  $|1\rangle$  into  $|2\rangle$ , would rotate the Bloch vector from the -z direction through the equatorial plane into the z-direction. However, depicted here are driving pulses with pulse area errors (top row) with a reduced Rabi frequency  $\Omega = 0.9\Omega_0$  from the optimal Rabi frequency, here denoted  $\Omega_0$ , and detuning error, i.e. off-resonant driving of the two-state system (bottom row), with a detuning  $\Delta = -0.1\Omega_0$ . We find that a single pulse (left column) can not drive a total population inversion in the presence of pulse area or detuning errors. In both cases the final Bloch vector is not pointing completely into the z-direction. In our example, the population in state  $|2\rangle$  is 95 % with the pulse area error, respectively 98 % with a off-resonant driving. The most intuitive CP consists of three pulse components with pulse areas  $\pi/2$ ,  $\pi$  and  $\pi/2$ . The relative phases between the pulses are  $0^\circ$ ,  $90^\circ$  and  $0^\circ$ . These phases are imprinted on the complex Rabi frequency  $\Omega$ . In the following, we will use the common notation from NMR with the pulse areas  $A$  and phases  $\phi$  as subscripts, i.e.  $A_\phi$ . For this example it leads to  $(\pi/2_0 - \pi_{90} - \pi/2_0)$ . This CP is capable of compensating pulse area errors as one can see in Figure

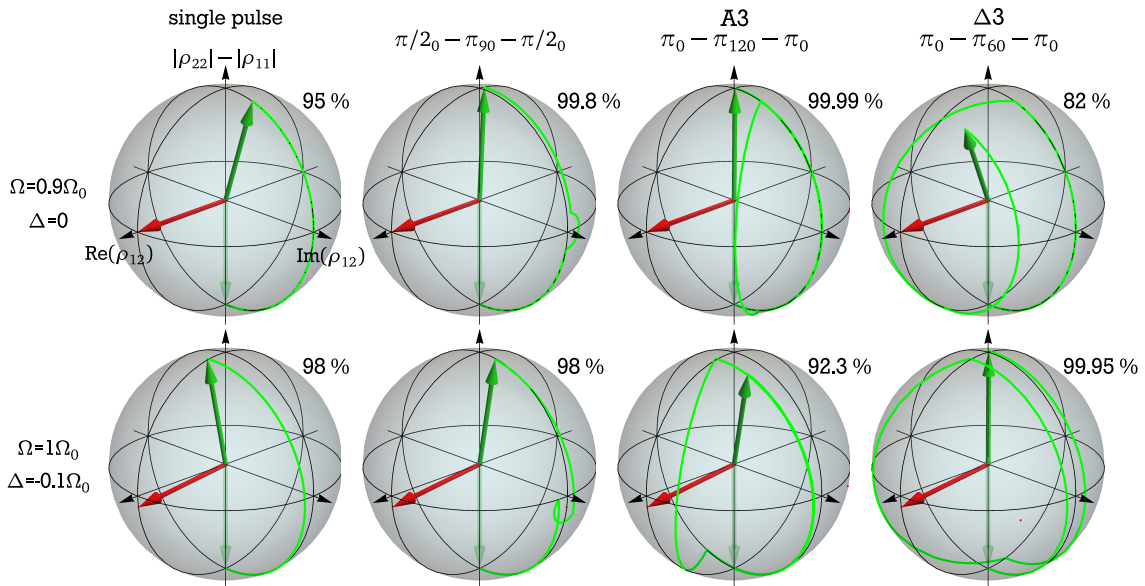


Figure 2.3: Motion (green line) of the Bloch vector (green arrow) on the Bloch sphere for a single pulse and CP of three components, for a pulse area error (top row) and a detuning error (bottom row), i.e. off-resonant driving of the two-state system. The pulses are applied to drive the system from state  $|2\rangle$  to state  $|2\rangle$ . The initial torque vector (red arrow) indicates the first axis of rotation of the pulses. The transfer efficiency, i.e. the population in state  $|2\rangle$  after the pulses, is given next to the Bloch spheres.

**2.3.** The Bloch vector driven by this CP first performs a  $\pi/2_0$  rotation around the  $\text{Re}(\rho_{12})$ -axis. Due to the pulse area error the Bloch vector stops slightly below the equatorial plane of the Bloch sphere. Second, a  $\pi_{90}$  rotation is applied, i.e. the direction of the torque vector is shifted by  $90^\circ$ , rotating the Bloch vector around the  $\text{Im}(\rho_{12})$ -axis. Note that only the torque vector of the first component of the CP is depicted. The Bloch vector is now slightly above the equatorial plane. Finally another  $\pi/2_0$ -pulse is applied, rotating the Bloch vector almost into the z-axis, i.e. achieving a population transfer of 99.8 %. Hence, we saw that this CP is able to compensate for pulse area errors, achieving a better population inversion compared to a single pulse excitation. However, the performance in the case of a detuning error is not improved by this type of CP, compare with Figure 2.3 (bottom row). Additionally, as an example, the performance of two other CP (A3 and  $\Delta 3$ ) are depicted in Figure 2.3. Note that these pulses feature only the phases as free control parameters, i.e. the pulse area of all components of the CP is fixed. We find that the CP A3 is capable of compensating pulse area errors very efficiently (99.99 %), while in the case of detuning errors the population transfer drops to 92.3 %. In the other hand detuning errors can be compensated by using the CP  $\Delta 3$ . However, this CP is very sensitive to pulse area errors. Most CP are designed for quite special tasks, driving the system from a defined initial state into a final state while compensating for one specific type of error. However, we will see in Section 5.2 that it is possible to design robust CP without any knowledge of the type of errors involved in the system and pulses. Note that CP can, however not all do, perform well for any initial state, e.g. a arbitrary coherent superposition.



## 2.2 Coherent Interactions in a Three-Level System

We define a three-state quantum system in  $\Lambda$ -configuration containing two metastable ground states  $|1\rangle$  and  $|3\rangle$ , and an excited state  $|2\rangle$ , see Figure 2.4. The transition frequencies are given by  $\omega_{ij}$ . Optical driving fields, in the following labeled as probe (p) and control (c) field, couple the transitions  $|1\rangle \leftrightarrow |2\rangle$  and  $|3\rangle \leftrightarrow |2\rangle$  of the system, respectively. In dipole approximation the probe and control field can be described by

$$\begin{aligned}\vec{\mathcal{E}}_p(t) &= \frac{1}{2}\vec{\mathcal{E}}_p^0(t)(e^{i\omega_p t} + e^{-i\omega_p t}), \\ \vec{\mathcal{E}}_c(t) &= \frac{1}{2}\vec{\mathcal{E}}_c^0(t)(e^{i\omega_c t} + e^{-i\omega_c t}),\end{aligned}\quad (2.15)$$

with the frequencies of probe and control field labeled  $\omega_p$  and  $\omega_c$ , respectively. The single-photon detunings are given by  $\Delta_p = \omega_p - \omega_{12}$ , and  $\Delta_c = \omega_c - \omega_{23}$ . Following the arguments of Section 2.1 we write the full RWA Hamiltonian as,

$$\hat{H}_{RWA} = \frac{\hbar}{2} \begin{pmatrix} 0 & \Omega_p & 0 \\ \Omega_p & 2\Delta_p & \Omega_c \\ 0 & \Omega_c & 2\delta \end{pmatrix}, \quad (2.16)$$

with the two-photon detuning  $\delta = \Delta_p - \Delta_c$  and real Rabi frequencies  $\Omega_p$ , and  $\Omega_c$  of probe, and control field, respectively. Note that we will no longer explicitly write the time dependance of the Rabi frequencies. In the following we assume two-photon resonance of probe and control field with the transition  $|1\rangle \leftrightarrow |3\rangle$ , i.e.  $\Delta_p = \Delta_c \equiv \Delta \Rightarrow \delta = 0$ . In this case the RWA Hamiltonian of Equation 2.16 can be diagonalized, leading to a new set of eigenstates, called instantaneous, adiabatic, or dressed eigenstates [68]:

$$\begin{aligned}|\psi_0\rangle &= \cos\theta|1\rangle && -\sin\theta|3\rangle \\ |\psi_-\rangle &= \sin\theta\cos\phi|1\rangle - \sin\phi|2\rangle + \cos\theta\cos\phi|3\rangle \\ |\psi_+\rangle &= \sin\theta\sin\phi|1\rangle + \cos\phi|2\rangle + \cos\theta\sin\phi|3\rangle\end{aligned}\quad (2.17)$$

The so-called mixing angles  $\theta$  and  $\phi$  are calculated by

$$\tan\theta = \frac{\Omega_p}{\Omega_c} \quad \text{and} \quad \tan 2\phi = \frac{\sqrt{\Omega_p^2 + \Omega_c^2}}{\Delta}, \quad (2.18)$$

and define the projection of the bare states of the three-state system onto the dressed states. The eigenstates  $|\psi_{\pm}\rangle$  share a contribution of the excited state  $|2\rangle$  with its radiative decay. Thus, these states are usually called bright states. In contrast state  $|\psi_0\rangle$  has no contribution of the excited state  $|2\rangle$ , and is hence referred to as dark state. Therefore, if the system is initially prepared in the dressed dark state  $|\psi_0\rangle$ , it can not be excited to the radiatively decaying state  $|2\rangle$ . In addition,

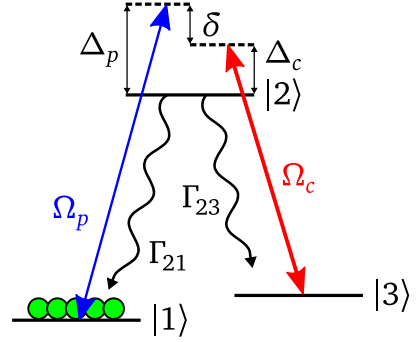


Figure 2.4: Three-state system in  $\Lambda$ -configuration, with probe field (p) and control field (c). The system is driven with Rabi frequencies  $\Omega_p$  and  $\Omega_c$ , with detunings  $\Delta_p$  and  $\Delta_c$ . Population in state  $|2\rangle$  decays with rates  $\Gamma_{21}$  and  $\Gamma_{23}$ .

by a proper choice of the mixing angle  $\theta$ , i.e. the ratio between control and probe Rabi frequency, the dark state  $|\psi_0\rangle$  can hold a superposition of the bare states  $|1\rangle$  and  $|3\rangle$ . However, variations of control and probe Rabi frequency have to be sufficiently slow, i.e. adiabatic, to stay completely in the adiabatic states. These properties allow one to create and store atomic coherences by adiabatic variations of the control and probe Rabi frequencies.

As described in Section 2.1.2 one can treat a single, idealized quantum system, as well as macroscopic systems, by using the density matrix formalism. The dynamics can be described by the Liouville-von-Neumann Equation 2.11. In the case of a three-state  $\Lambda$ -system, we find the dissipator  $\hat{D}$  given by

$$\hat{D} = \begin{pmatrix} \Gamma_{21}\rho_{22} & -\gamma_{12}\rho_{12} & -\gamma_{13}\rho_{13} \\ -\gamma_{21}\rho_{21} & -(\Gamma_{21} + \Gamma_{23})\rho_{22} & -\gamma_{23}\rho_{23} \\ -\gamma_{13}\rho_{13} & -\gamma_{32}\rho_{32} & \Gamma_{23}\rho_{22} \end{pmatrix}, \quad (2.19)$$

with the spontaneous decay rates  $\Gamma_{ij}$ , given by the natural lifetime  $T_1 = 1/\Gamma_{ij}$  and the decoherence rates given by  $\gamma_{ij} = \frac{1}{2}(\sum_k \Gamma_{ik} + \sum_k \Gamma_{jk}) + \gamma'_{ij}$ .

## 2.3 Adiabatic Light Storage in a Three-Level System

Adiabatic light storage is based on the transformation of optical information, i.e. an optical pulse, into a coherent atomic superposition state. There are a number of different light storage protocols, which are able to perform this transformation [5, 7]. This present work uses a storage protocol based on electromagnetically induced transparency (EIT). EIT enables a direct manipulation of the dispersion properties of a medium. The following sections will give an overview on the basic EIT theory and the EIT-based light storage protocol. Finally, we discuss the experimental and theoretical limits and constraints, regarding the maximal achievable storage efficiency.

### 2.3.1 Electromagnetically Induced Transparency

EIT is based on a quantum interference effect between different excitation pathways in an atomic medium. In this way it is possible to eliminate the absorption and refraction at the resonance frequency of a transition. We will describe the EIT effect here in a three-state  $\Lambda$ -type system. Nevertheless, also other coupling schemes, such as ladder- and V-type systems are possible. Assuming a strong control and a weak probe field ( $\Omega_c \gg \Omega_p$ ) and the system initially prepared in state  $|1\rangle$ ,  $|\psi_0\rangle$  if  $\Omega_p = 0$  respectively, we can solve the Liouville-von-Neumann Equation 2.11 using the RWA Hamilton operator, Equation 2.16, and the dissipator  $\hat{D}$ , Equation 2.19, see Appendix D. In the steady-state ( $\dot{\rho} = 0$ ) and for small changes of the initial population, i.e.  $\rho_{11} \cong 1$  we find the linear susceptibility  $\chi^{(1)}$  given by [70]

$$\chi^{(1)} = \frac{|\mu_{12}|^2 \rho}{\epsilon_0 \hbar} \frac{(4\delta (|\Omega_c|^2 - 4\delta\Delta_p) - 16\Delta_p\gamma_{13}^2) + i(16\delta^2\gamma_{12} + 4\gamma_{13}(|\Omega_c|^2 + 4\gamma_{13}\gamma_{12}))}{|\Omega_c|^2 + (2\gamma_{12} + i2\Delta_p)(2\gamma_{13} + i2\delta)} \quad (2.20)$$



with the atomic density  $\varrho$ . Note the  $\chi^{(1)}$  given here slightly differs from [70] due to different definitions of the decoherence rates, see also Appendix D. In order to connect the linear susceptibility  $\chi^{(1)}$  to the absorption coefficient  $\alpha$  and the index of refraction  $n$  we use the following relations:

$$\alpha = 2k_0 \text{Im} \sqrt{1 + \chi^{(1)}} \approx k_0 \text{Im} \chi^{(1)} \quad (2.21)$$

$$n = \text{Re} \sqrt{1 + \chi^{(1)}} \approx 1 + \frac{1}{2} \text{Re} \chi^{(1)} \quad (2.22)$$

Here,  $k_0 = 2\pi/\lambda_0$  is the angular wave number. Thus, it is possible to calculate absorption and dispersion spectra, with respect to the probe field detuning  $\Delta_p$ . Figure 2.5 shows the imaginary part of  $\chi^{(1)}$ , proportional to the absorption coefficient  $\alpha$ , and the real part of  $\chi^{(1)}$ , proportional to the index of refraction  $n$ , for different sets of parameters  $\Omega_c$ ,  $\gamma_{13}$  and  $\Delta_c$ . If no control field is applied ( $\Omega_c = 0$ ), and the relaxation rate of the coherence  $\rho_{13}$  is negligible ( $\gamma_{13} = 0$ ), we find the expected absorption and dispersion profile of the homogeneously broadened transition  $|1\rangle \leftrightarrow |2\rangle$ , see dashed lines in Figure 2.5 (bottom, center). If the control field is switched on, i.e.  $\Omega_c > 0$  the absorption on resonance ( $\Delta_p$ ) vanishes, and we find total transmission (solid red line) for the probe field. The previous single absorption line splits with a separation  $\Delta_{\text{peak}} = \Omega_c$ . Note that this splitting is not due to a linear Stark effect, which would result in an Autler-Townes splitting [75], but can not explain the vanishing absorption on resonance [76]. This zero absorption can only be explained by the destructive interference of the different excitation pathways of the dressed three-state system (Fano interference). The system is initially prepared in the dark state  $|\psi_0\rangle = |1\rangle$ . Thus, coupling states  $|1\rangle$  and  $|2\rangle$  with a resonant probe field leads to two possible transitions in the dressed state picture, i.e.  $|\psi_0\rangle \leftrightarrow |\psi_+\rangle, |\psi_-\rangle$  respectively. The destructive interference of these excitation pathways results in a vanishing absorption of the probe field on resonance. This effect is called *electromagnetically induced transparency* (EIT) [11–13, 70, 77]. A strong control field also changes the dispersive behavior ( $\text{Re} \chi^{(1)}$ ) of a system, see Figure 2.5 (center column). Without a control field applied, we find an anomalous dispersion on resonance (black dashed line). With a control field (solid black line) the system shows a strong normal dispersion. We will see that this changed dispersive behavior will be of importance for EIT-based light storage (see Section 2.3.2). Figure 2.5 (center column) shows that the width  $\Gamma_{\text{EIT}}$  of the EIT feature depends on the control Rabi frequency  $\Omega_c$ . In order to calculate the dependence of  $\Gamma_{\text{EIT}}$  with respect to  $\Omega_c$ , we assume an optically thick medium of length  $L$ . Thus, the response of the entire medium, i.e. the transmission  $T$ , can be calculated from the formula

$$T = e^{-\alpha L} = e^{-2k_0 \text{Im} \sqrt{1 + \chi^{(1)}} L}. \quad (2.23)$$

In order to determine the width  $\Gamma_{\text{EIT}}$ , we further assume  $\gamma_{13} = 0$  and a resonant control field, which leads to  $\delta = \Delta_p$ . We thus can calculate the absorption coefficient  $\alpha$  by a series expansion of  $\chi^{(1)}$  around  $\Delta_p = 0$ . We find

$$\alpha = \frac{4\alpha_0 \gamma_{12}^2 \Delta_p^2}{\Omega_c^4} + \mathcal{O}\left(\frac{\Delta_p^4}{\Omega_c^8}\right), \quad \text{with} \quad \alpha_0 = \frac{2k_0 |\mu_{12}|^2 \varrho}{\gamma_{12} \epsilon_0 \hbar} \quad (2.24)$$

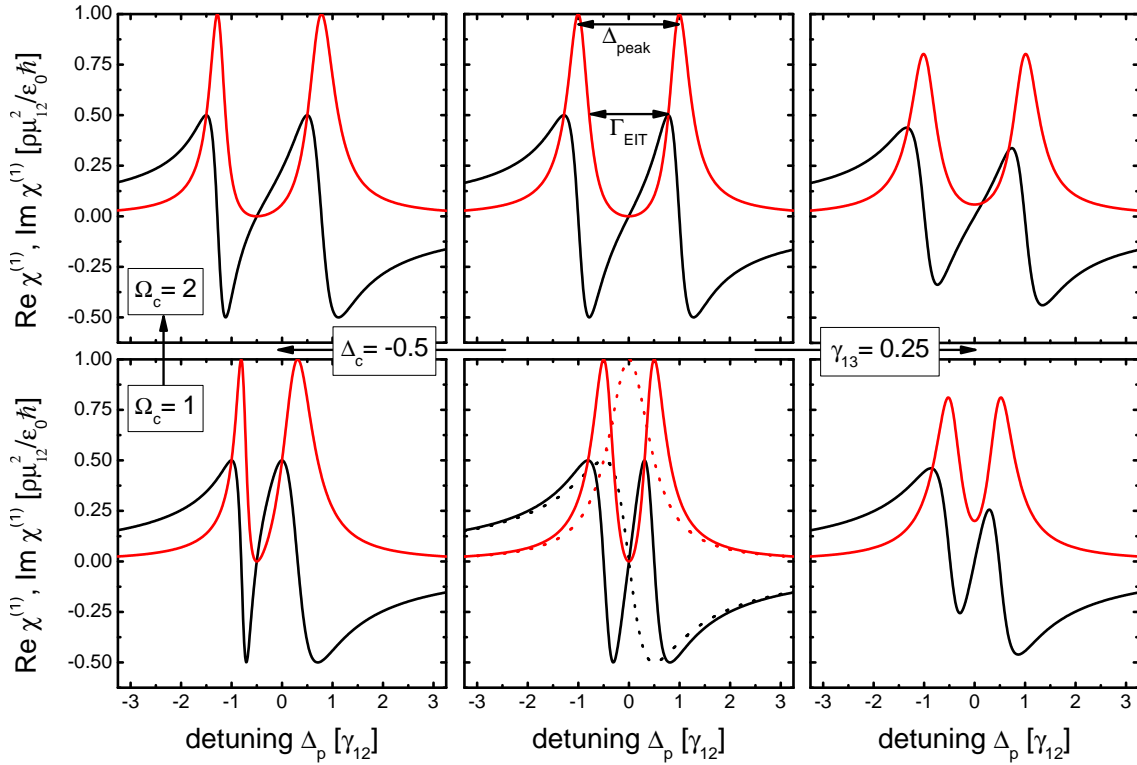


Figure 2.5: Absorption ( $\text{Im}\chi^{(1)}$ , red) and dispersion ( $\text{Re}\chi^{(1)}$ , black) versus the single photon probe field detuning  $\Delta_p$ . All values are given in units of  $\gamma_{12}$ . (Center column) The control field is resonant to the  $|1\rangle \leftrightarrow |2\rangle$  transition ( $\Delta_c = 0$ ) and the relaxation rate of the ground state coherence is  $\gamma_{13} = 0$ . From bottom to top the control Rabi frequency increases from  $\Omega_c = 1$  to 2. (Left column) A control field detuning is added ( $\Delta_c = -0.5$ ). (Right column) A additional ground state relaxation rate is added ( $\gamma_{13} = 0.25$ ). The dotted lines represent the case of no control field, i.e.  $\Omega_c = 0$ .

the absorption on resonance ( $\Delta_p = 0$ ) without a control field applied. We define the optical depth of the medium as  $d = \alpha_0 L$  and determine a Gaussian shape of the EIT window for small probe detunings, using Equation 2.23:

$$T(\Delta_p) = \exp\left[-\frac{4d\gamma_{12}^2\Delta_p^2}{\Omega_c^4}\right] \quad (2.25)$$

We find the width  $\Gamma_{\text{EIT}}$  of the EIT window (FWHM) is a quadratic function of the control Rabi frequency  $\Omega_c$ , given by

$$\Gamma_{\text{EIT}} = \frac{\Omega_c^2}{\gamma_{12}} \frac{\sqrt{\ln 2}}{\sqrt{d}}. \quad (2.26)$$

Previously we described the effect of EIT without taking into account any detuning  $\Delta_c$  of the control field, and coherence decay rate  $\gamma_{13}$  of the ground states. Figure 2.5 (left column) depicts  $\text{Im}\chi^{(1)}$  and  $\text{Re}\chi^{(1)}$  for a control field detuning of  $\Delta_c = -0.5$ . The EIT feature becomes asymmetric, with its center shifted towards  $\Delta_p =$

–0.5. However, total transmission is still achieved. An additional coherence decay rate  $\gamma_{13} = 0.25$  is added in Figure 2.5 (right column). This leads to a residual absorption ( $\text{Im}\chi^{(1)} \neq 0$ ) in the center of the EIT window ( $\Delta_p = 0$ ). We can calculate the transmission for  $\Delta_p = 0$ , and non vanishing decay rates  $\gamma_{ij}$ , using Equations 2.23, and 2.20. We find the transmission

$$T = \exp\left[-\frac{d\gamma_{13}\gamma_{12}}{\gamma_{13}\gamma_{12} + \Omega_c^2}\right]. \quad (2.27)$$

Thus, we find absorption ( $T \neq 0$ ) for values  $\gamma_{ij} \neq 0$ . This residual absorption in the center of the EIT window can be reduced by using higher control Rabi frequency  $\Omega_c$ , see Figure 2.5. For  $\Omega_c^2 \gg \gamma_{13}\gamma_{12}$  almost total transmission is achieved. A coherence decay rate  $\gamma_{13} \neq 0$  also changes the dispersive behavior of the system. With an increase of  $\gamma_{13}$  the dispersion becomes less steep, i.e.  $\frac{dn}{d\omega_p}$  is reduced.

So far we discussed EIT and the effects related to it in the context of a homogeneously broadened medium. However, as we want to use EIT for light storage in PrYSO, we can not neglect its inhomogeneous broadenings of the optical and hyperfine transitions. An inhomogeneous broadening of the hyperfine transition, i.e. the  $|1\rangle \leftrightarrow |3\rangle$  transition, leads to dephasing of the collective coherence, thus causing a residual absorption in the center of the EIT window. An inhomogeneous broadening of the optical transition leads to a variety of different single photon detunings  $\Delta_{p,c}$  of the probe and control field. In PrYSO the broadening of the hyperfine transition is  $\Gamma_{inhom} \approx 30 - 70$  kHz (here labeled  $\Gamma_{13}$ ), see also Table 1.2. The effective inhomogeneous broadening of the optical transition  $\Gamma_{inhom}^*$  (here labeled  $\Gamma_{12}$ ) strongly depends on the preparation of the medium due to optical pumping. As the inhomogeneous broadenings in PrYSO are rather large, i.e.  $\Gamma_{12} \gg \gamma_{12}, \gamma_{13}$  and  $\Gamma_{13} \gg \gamma_{13}$ , we find an altered condition for total transmission in the EIT window [78]. The condition then reads  $\Omega_c^2 \gg \Gamma_{13}\Gamma_{12}$ , which means the Rabi frequency must exceed the inhomogeneous linewidth. Thus, in a medium like PrYSO, the EIT properties are mainly defined by the inhomogeneous broadenings of its transitions.

### 2.3.2 EIT-based Light Storage

In the previous Section 2.3.1 we saw that the control field does not only change the absorption properties ( $\text{Im}\chi^{(1)}$ ), but also the index of refraction  $n$  ( $\text{Re}\chi^{(1)}$ ) and therefore the dispersion  $\frac{dn}{d\omega_p}$  of the medium. EIT-based light storage (EIT-LS) uses this changed dispersion properties of the medium [13, 70, 79]. Instead of anomalous dispersion in the case of no control field applied, we find with a control field normal dispersion for the probe field close to the two photon resonance, see also Figure 2.5. This leads to a modified group velocity  $v_{gr}$  of the probe field inside the medium. For single- and two-photon resonance, i.e.  $\Delta_c = \Delta_p = 0$ , the group velocity of the probe field reads

$$v_{gr} = \frac{d\omega_p}{dk_p} = \frac{c_0}{n + \omega_p \left(\frac{dn}{d\omega_p}\right)} = \frac{c_0}{1 + c_0\alpha_0\gamma_{12}/\Omega_c^2} \approx \frac{\Omega_c^2}{\alpha_0\gamma_{12}}. \quad (2.28)$$

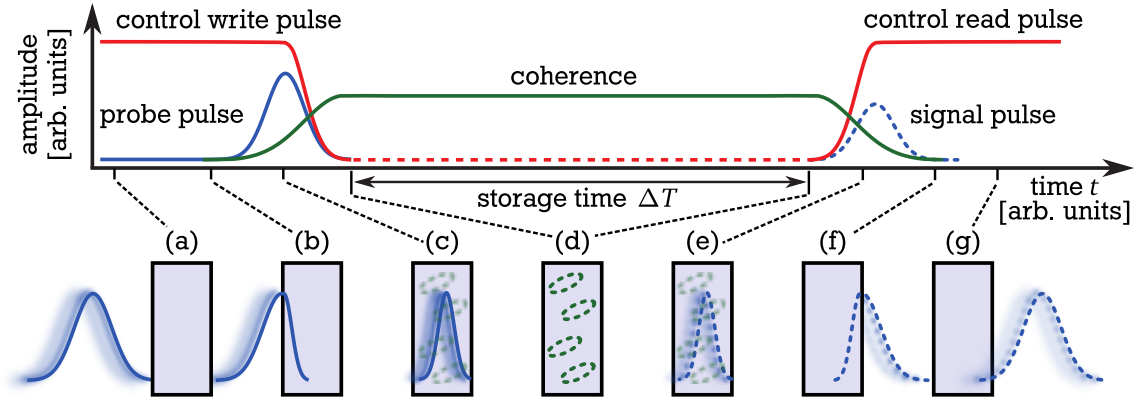


Figure 2.6: (Top) Temporal sequence of the EIT-LS protocol. Control write and control read pulses depicted by red lines. The probe (input) pulse (blue line) is transformed into a coherence (green line). After a storage time  $\Delta T$  a signal pulse (dashed blue line) is retrieved. (Bottom) Probe (input) pulse entering a medium (PrYSO crystal) in EIT conditions. The probe pulse is compressed as it enters the medium and a coherence (green dashed lines) is created. While the probe pulse travels inside the medium with a reduced group velocity, the control write pulse is turned off. The probe pulse is fully transformed into a coherence. After applying a control read pulse this coherence is converted back into a signal pulse. Figure taken from [58], modified.

Thus, a large positive dispersion close to the two-photon resonance, i.e.,  $\Delta_p \approx \Delta_c$  leads to a reduced group velocity of the probe field compared to the vacuum speed of light  $c_0$ . This effect is called *slow light* [16, 80]. Equation 2.28 holds true if we assume slowly varying probe and control fields, i.e. in the adiabatic limit, and no coherence decay, i.e.  $\gamma_{13} = 0$ . Thus, the group velocity of the probe field (i.e. probe pulse) can be controlled by the Rabi frequency  $\Omega_c$  of the control field. In the following the storage and readout process of the EIT-LS protocol is described (compare also with 2.6):

- (a) The medium is initially prepared in state  $|1\rangle$ . A control write pulse prepares the medium in EIT configuration before a probe (input) pulse enters, i.e.  $\Omega_p = 0$  and  $\Omega_c > 0$ . Thus, in the dressed state picture the mixing angle is  $\theta = 0$ , and we find the dressed state  $|\psi_0\rangle = |1\rangle$ . Compare with Equations 2.17 and 2.18.
- (b) As the probe (input) pulse enters the medium, its group velocity is reduced and the pulse is compressed. As  $\Omega_p$  becomes greater zero the mixing angle  $\theta$  increases. Thus, the dressed state  $|\psi_0\rangle$  holds a coherent superposition of bare states  $|1\rangle$  and  $|3\rangle$ .
- (c) While the probe (input) pulse is fully inside the medium the control write pulse is switched off, fulfilling the condition  $\Omega_p/\Omega_c \approx \text{const.}$ , thus preserving the mixing angle  $\theta$ , i.e. the coherence during the storage process. As the control Rabi frequency decreases the probe pulse is further compressed. In the limit of zero control field, the probe pulse is fully transformed into a collective coherent superposition of atomic states. We call this transformation process *stored light*. However, the EIT theory in general assumes weak probe

fields, i.e.  $\Omega_c \gg \Omega_p$ , thus no maximal superposition between states  $|1\rangle$  and  $|3\rangle$  is prepared. In fact, under perfect EIT conditions only a weak coherence can be generated. The spatial distribution of amplitude and phase of the coherence in the crystal, along the axis of the probe pulse, is called *spin wave* [81, 82].

- (d) During the storage time  $\Delta T$  the information (state) of the probe pulse is preserved in a collective superposition state, i.e. spin wave in the storage medium. However, dephasing, decoherence and population relaxation can lead to a decay of the coherence (see Section 2.3.4).
- (e) A control read pulse, equivalent to the write pulse, to achieve an undistorted transformation, transfers the spin wave back into a light pulse, in the following called *signal pulse*. In the ideal case input probe pulse and signal pulse are identical, in particular in frequency, phase and pulse shape.
- (f) The control read pulse renders the medium transparent again, and the signal pulse travels with its reduced group velocity.
- (g) As the signal pulse leaves the EIT medium, it accelerates and is stretched to the original pulse width of the input pulse.

The EIT-LS protocol allows the total transformation and storage of optical information in an atomic superposition, with the possibility of an on-demand readout. Thus, this technique can be used as a quantum-memory protocol [5, 6, 83]. First experiments on EIT-based light storage were carried out by Phillips *et al.* [14] and Liu *et al.* [15].

### 2.3.3 Limitations on the Efficiency of the EIT Light Storage Protocol

In this section we discuss the major effects limiting the efficiency of the EIT-LS protocol. In particular, a rather basic condition for a proper matching of the probe pulse and EIT window properties to a given optical depth  $d$  of a storage medium is introduced. Afterwards, the pulse propagation through an EIT medium and the generation of an optimal spin wave is described. Finally, the proper phase matching of probe and control fields is discussed. We define the total efficiency  $\eta_{\text{EIT}}$  of the EIT-LS protocol as

$$\eta_{\text{EIT}} = \frac{E_{\text{out}}^0}{E_{\text{in}}^0}, \quad (2.29)$$

with the pulse energies of the input probe pulse  $E_{\text{in}}^0$  and of the signal pulse  $E_{\text{out}}^0$  after a storage time  $\Delta T = 0$ . This definition only describes the efficiency of the EIT-LS protocol, not taking into account any decoherence and relaxation processes during a storage time  $\Delta T$ . Also, losses regarding a specific experimental setup, e.g. optics, detectors, are not taken into account. We further define the experimental efficiency of the EIT-LS protocol in our PrYSO crystal after a storage time  $\Delta T$  as

$$\eta_{\text{EXP}}(\Delta T) = \frac{E_{\text{out}}}{E_{\text{in}}}, \quad (2.30)$$

taking into account dephasing, decoherence, population relaxation processes, and the efficiency of rephasing techniques applied. However, for comparability, losses due to the components of the specific optical setup are not considered.

### Spatial and Spectral Condition

Fulfilling the spatial and spectral conditions represents a basic requirement for efficient EIT-LS, which can be already derived from the simple EIT picture described in Section 2.3.1. Of course, a storage of a probe pulse of duration  $\tau_p$  is only possible if the pulse is completely compressed into the medium of length  $L$  during the storage process. If we assume a rectangular probe pulse of  $\tau_p$  with the group velocity  $v_{gr}$ , the spatial dimension of the pulse inside the medium is given by  $\tau_p v_{gr}$ . Using the approximation for the group velocity, see Equation 2.28, we find the spatial condition for the probe pulse fitting into the medium,

$$L \geq \tau_p v_{gr} \approx \tau_p \frac{\Omega_c^2}{\alpha_0 \gamma_{12}}. \quad (2.31)$$

Furthermore, for efficient storage the probe pulse has to fit spectrally into the EIT window  $\Gamma_{\text{EIT}}$ , because spectral components outside the EIT window would be absorbed. The full width at half maximum of the spectrum of a rectangular probe pulse is given by  $\Gamma_p = 5.566/\tau_p$ . With Equation 2.26 we define the spectral condition  $\Gamma_{\text{EIT}} \gg \Gamma_p$  as:

$$\Gamma_{\text{EIT}} = \frac{\Omega_c^2}{\gamma_{12}} \frac{\sqrt{\ln 2}}{\sqrt{d}} \gg \frac{5.566}{\tau_p} = \Gamma_p \quad (2.32)$$

Using  $d = \alpha_0 L$ , we can combine the spatial and spectral conditions, Equations 2.31 and 2.32. In terms of  $\Gamma_{\text{EIT}}$  we obtain the following condition necessary to be fulfilled for an efficient light storage:

$$\sqrt{\ln 2} d \geq \Gamma_{\text{EIT}} \tau_p \sqrt{d} \gg 5.566 \sqrt{d} \quad (2.33)$$

For a rough estimation we can write  $\sqrt{d} \geq \Gamma_{\text{EIT}} \tau_p \gg 1$ . This condition can be fulfilled for a high optical depth  $d$  only. In terms of the control Rabi frequency  $\Omega_c$  Equation 2.33 reads:

$$d \geq \frac{\Omega_c^2 \tau_p}{\gamma_{12}} \gg \frac{5.566}{\sqrt{\ln 2}} \sqrt{d} \quad (2.34)$$

We find that for a given optical depth  $d$ , the combination of control Rabi frequency  $\Omega_c$  and probe pulse duration  $\tau_p$  has to be chosen appropriately to fulfill Equation 2.34. However, for low optical depth it is difficult to fulfill Equation 2.34 at all. Figure 2.7 (left) shows two EIT spectra for different control Rabi frequencies (black dashed and solid lines), and two probe pulse spectra for different pulse durations (red and green solid lines). The corresponding compression of the probe pulses in a storage medium are depicted in 2.7 (right). For the higher control Rabi



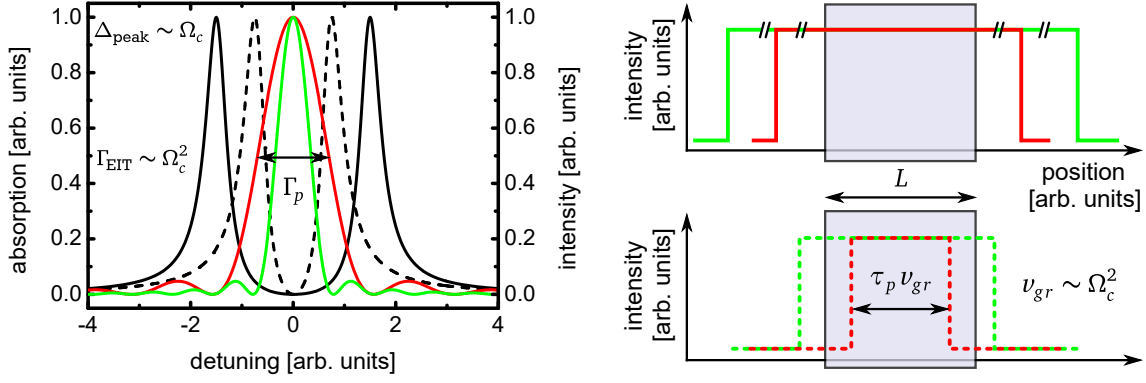


Figure 2.7: (Left) EIT absorption spectra for two control Rabi frequencies (solid and dashed black lines), and the frequency spectra of two rectangular probe pulses (red and green solid lines). (Right) The corresponding probe pulses propagating through the EIT medium, prepared with a strong (solid lines) and weak (dashed lines) control Rabi frequency.

frequency the probe pulses fit into the EIT spectrum (solid black line). However, the probe pulse compression is not strong enough to compress the probe pulse below the length of the storage medium. If the control Rabi frequency is reduced, the pulse compression increases. Thus, the spatial condition is fulfilled better (see dashed red and green lines in Figure 2.7 (right)). However, the corresponding EIT window width is too small to fully cover the bandwidth of the probe pulses. With an increase of the optical depth  $d$  the condition (Equation 2.34) can be fulfilled better. The derivation of this basic condition for efficient light storage by EIT is based on [84, 85].

### Optimal Spin Wave Generation for Maximum EIT Storage Efficiency

This section summarizes the generation of an optimal spin wave in an EIT medium. We follow the arguments of Gorshkov *et al.* [81, 82, 86]. We derive the Heisenberg equations of motions given in [82] from the equations of motion calculated for a weak probe field from the Liouville-von-Neumann Equation 2.11 and the Maxwell-wave equation. We assume  $\gamma_{13} = 0$ ,  $\delta = 0$ , i.e. two-photon resonance,  $\rho_{11} \approx 1$ , and  $\dot{\rho}_{jj} = 0$ . We thus can write in a rotating frame:

$$\begin{aligned}\dot{\rho}_{12} &= \frac{i}{2}\Omega_p + \frac{i}{2}\Omega_c\rho_{13} + i\Delta_p\rho_{12} - \gamma_{12}\rho_{12}, \\ \dot{\rho}_{13} &= \frac{i}{2}\Omega_c\rho_{12}, \\ E' &= i\frac{\omega_p}{c}\frac{\mu_{12}}{\epsilon_0}\varrho\rho_{12},\end{aligned}\tag{2.35}$$

with the particle density  $\varrho = N/V$ . Gorshkov considers a single-photon probe field. We calculate the single-photon electric field to  $E = \sqrt{(2\hbar\omega_p)/(\epsilon_0V)}$ , yielding a single-photon Rabi frequency of  $\Omega_p = \mu_{12}E/\hbar = \mu_{12}\sqrt{(2\omega_p)/(\hbar\epsilon_0V)}$ . For simplification Gorshkov defines the single-photon Rabi frequency including a factor 1/2, yielding  $g \equiv \Omega_p/2 = \mu_{12}\sqrt{\omega_p/(2\hbar\epsilon_0V)}$ . Further a normalized function  $\mathcal{E}(z, t)$  is used to describe the time-dependent shape of the input probe pulse. In

order to use dimensionless variables we define:

$$\rho_{12} = \frac{P}{\sqrt{N}}, \quad \rho_{13} = \frac{S}{\sqrt{N}}, \quad \frac{\Omega_p}{2} = g\mathcal{E}, \quad \frac{\Omega_c}{2} \rightarrow \Omega_c, \quad E = \frac{2\hbar}{\mu_{12}}g\mathcal{E} \quad (2.36)$$

with the total atom number  $N$ . Using the dimensionless variables  $\mathcal{E}$ ,  $P$ ,  $S$ , the definition of  $g$ , and  $\varrho$ , we can write the Heisenberg equations of motion as

$$\begin{aligned} (\partial_t + c\partial_z)\mathcal{E}(z, t) &= ig\sqrt{N}P(z, t) \\ \partial_t P(z, t) &= -(\gamma + i\Delta)P(z, t) + ig\sqrt{N}\mathcal{E}(z, t) + i\Omega_c(t - z/c)S(z, t) \\ \partial_t S(z, t) &= i\Omega_c^*(t - z/c)P(z, t). \end{aligned} \quad (2.37)$$

Here, the first equation describes the propagation of a probe field mode amplitude  $\mathcal{E}$  through a polarizable medium with the effective coupling constant  $g\sqrt{N}$ . The second and third equation describe the time-dependent change of the polarization  $P(z, t)$  and the spin wave  $S(z, t)$ . The polarization decays with  $\gamma$ . We find the source of the spin wave  $S(z, t)$  to be the polarization  $P(z, t)$ . However, the spin wave also depends on the applied control field Rabi frequency  $\Omega_c$ . When the storage is performed the normalized probe field mode  $\mathcal{E}$  is mapped onto the spin wave  $S(z, t)$ . The efficiency of the storage process is given by  $\eta_s = \frac{1}{L} \int_0^L |S(z, T)|^2 dz$ , with  $T$  the time when the storage process is finished. Here,  $S(z, T)$  gives the shape of the spin wave in the medium after the storage process. The readout of the spin wave can be achieved in two schemes. In the forward readout scheme the retrieved probe field mode will propagate in the same direction as before. In contrast, in the backward readout scheme, when the direction of the control field is changed, the retrieved probe field mode will propagate opposite to the input probe field mode. The pure retrieval efficiency can be calculated by  $\eta_r = \frac{c}{L} \int_{T_r}^{\infty} |\mathcal{E}(L, t)|^2 dt$  if the spin wave  $S(z, t)$  has been normalized before retrieval. Without normalization the total efficiency of the storage protocol can be calculated by  $\eta_{\text{EIT}} = \eta_s \eta_r$ . The storage and retrieval in forward and backward readout scheme is depicted in Figure 2.8. Gorshkov *et al.* [81, 82] suggest an iterative procedure to determine the

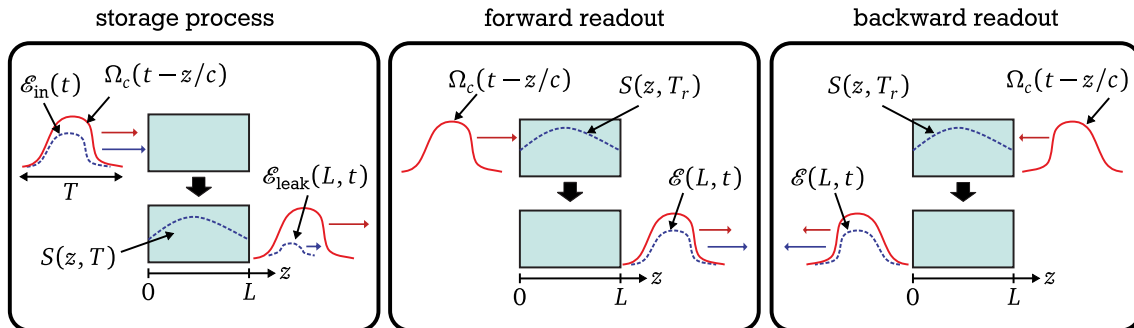


Figure 2.8: Storage process of a probe field  $\mathcal{E}$  into a spin wave  $S$ . During an imperfect storage a part of the probe pulse leaks through the storage medium ( $\mathcal{E}_{\text{leak}}$ ). The retrieval of the spin wave can be performed in forward readout and backward readout scheme. Figure modified from [82].



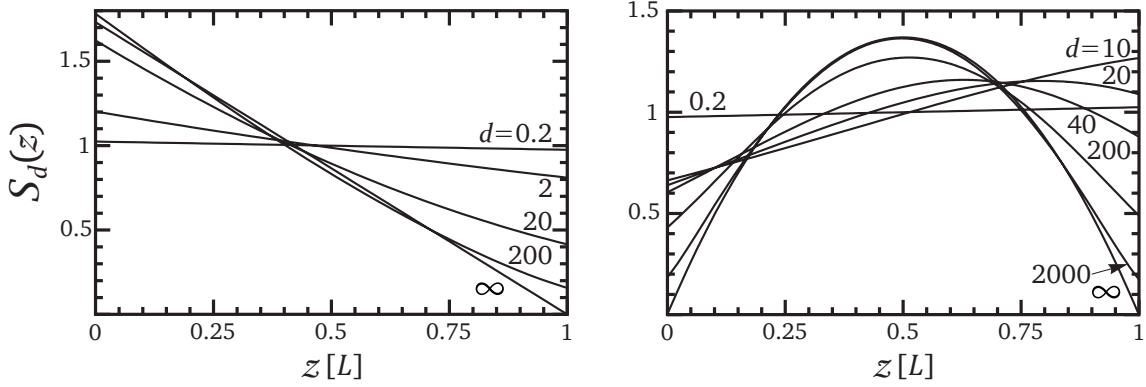


Figure 2.9: Calculated optimal spin waves  $S_d(z)$  for backward readout (left), and forward readout (right) for different optical depth  $d$ . Figure modified from [82].

optimal spin wave, hence the optimal input probe pulse shape for a given control pulse shape. As the readout of the spin wave can be described as a time reversed storage process, the optimal spin wave is achieved if the signal pulse shape is identical to the input probe pulse shape. Thus, an iterative procedure using the signal pulse shape as a new input probe pulse shape can be designed. After a few iterations the pulse shapes converge, and the spin wave which is stored is optimal. As an important result we find that the optimal spin wave  $S(z)$  only depends on the optical depth  $d$  of the medium and is independent of any other parameters such as  $\Omega_c$  or  $\Delta$ . The first experimental implementation of this iterative procedure was performed by Novikova *et al.* [87, 88] to optimize the EIT-LS in Rb vapor.

Figure 2.9 shows the optimal spin wave  $S(z)$  in a storage medium of normalized length for different optical depths  $d$  in backward readout (left) and forward readout (right). Here, the signal pulse is read out to the left. The optimal spin wave strongly depends on the optical depth of the medium. At low optical depth the optimal spin wave is almost constant for both readout schemes. For high optical depth the optimal spin wave in the backward readout becomes a linear function, and tends to zero at the end of the storage medium. In this way the probe (signal) pulse propagation length through the medium is minimized. In the forward readout scheme the optimal spin wave converges towards a symmetric function for high optical depth, as in this case either the probe input pulse or the signal pulse has to propagate fully through the medium. The spin wave tends to zero at both ends of the storage medium, minimizing the leakage. The maximum efficiency of the EIT-LS protocol is achieved if an optimal spin wave is stored and retrieved from the medium. As discussed, this process is optimal if the retrieval is a time

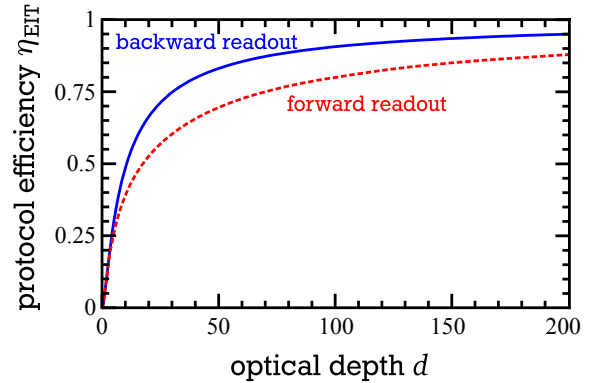


Figure 2.10: Theoretical maximum efficiency of the EIT-LS protocol  $\eta_{\text{EIT}}$  versus the optical depth  $d$  in the forward readout (red dashed line) and in backward readout scheme (solid blue line) as calculated in [82].

inversion of the storage process. In this optimal case the storage and retrieval efficiencies are equal. Figure 2.10 shows the maximal EIT-LS protocol efficiency  $\eta_{\text{EIT}}$  versus the optical depth  $d$  for forward readout (dashed red line) and backward readout (solid blue line). Note the different definitions of the optical depth, here  $d = \alpha L$ , whereas in [81, 82] the optical depth is  $\tilde{d} = 2\alpha L$ . The maximal storage efficiency increases with increasing optical depth. An ideal storage, i.e. 100% efficiency, can only be achieved in the limit of infinite optical depth. The maximal storage efficiency in the forward readout scheme is slightly lower because it does not correspond to full reversal of the storage process. Note that the description given here is drastically shortened, and holds true only in the adiabatic limit, in a system of collinear probe and control fields, and nearly degenerate metastable states  $|1\rangle$  and  $|3\rangle$ . In the case of a non-degeneracy between these states, as in PrYSO, and a small angle between probe and control pulse, as in our experimental setup, an additional phase factor  $e^{-ikz}$  is imprinted on the stored spin wave  $S(z, T)$ . A full description of weak adiabaticity, and non degenerate states can be found in [82]. In the following section the necessity of a proper phase matching of probe and control pulse is discussed in detail.

### Phase Matching Condition

In the previous section we assumed (anti-)collinear probe and control pulses, which coupled a  $\Lambda$ -system with degenerate ground states. Thus, phase matching was intrinsically fulfilled, because probe and control pulses were applied with the same frequency  $\omega$ . However, usually one can not assume degenerate states, and a collinear setup. For example, in the PrYSO crystal used in this work, the embedded  $\Lambda$ -system features non degenerate ground states with a splitting of  $\omega_{13} = 2\pi \cdot 10.191$  MHz. In addition, the optical setup uses an angle of  $\sim 1^\circ$  between probe and control beam. In this case the generated spin wave  $S(z)$  features an additional phase factor  $e^{-ikz}$ . The readout process is optimal only if this phase factor is taken into account, otherwise the readout efficiency is reduced [89]. Phase matching in a general  $\Lambda$ -scheme requires  $\vec{k}_p - \vec{k}_{c,\text{write}} + \vec{k}_{c,\text{read}} - \vec{k}_s = 0$ , with the wave vectors of probe pulse, control write pulse, control read pulse, and signal pulse, respectively. We find for EIT-LS the wave vector  $\vec{k}$  for the spin wave after the storage process to be  $\vec{k} = \vec{k}_p - \vec{k}_{c,\text{write}}$ . During the reading,  $\vec{k}_s = \vec{k} + \vec{k}_{c,\text{read}}$ , has to be fulfilled. Figure 2.11 (top) depicts a general phase matching scheme. Due to the different length of the wave vectors  $\vec{k}_p$  and  $\vec{k}_c$  the phase matching is only fulfilled for specific angles between the wave vectors of probe, control write and control read. Thus, the

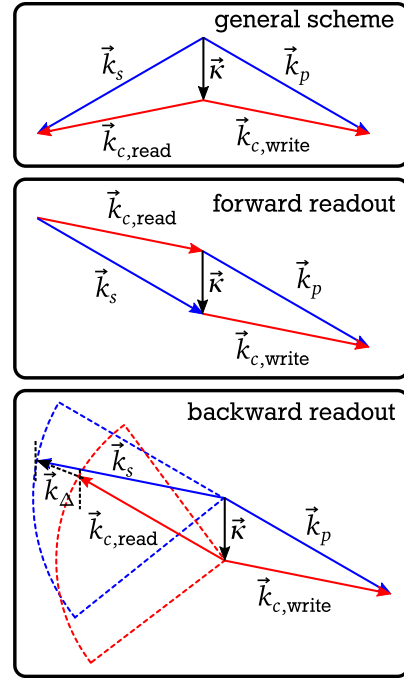


Figure 2.11: Phase matching schemes for light storage. General scheme (top), forward readout (center), and backward readout (bottom).

signal wave vector  $\vec{k}_s$  points into a direction which does not correspond to any wave vector  $\vec{k}_p, \vec{k}_{c,\text{read}}, \vec{k}_{c,\text{write}}$ . This leads to a generally difficult detection of the signal pulse. The only simple case of phase matching is achieved for co-propagating control write and read pulses, i.e.  $\vec{k}_{c,\text{read}} = \vec{k}_{c,\text{write}}$ , see Figure 2.11 (center). Then we find that the signal wave vector is equal to the probe wave vector, i.e.  $\vec{k}_s = \vec{k}_p$ , i.e. the signal pulse propagates into the same direction as the stored probe pulse. We call this scheme forward readout. A possible backward readout scheme, with an easily detectable signal pulse, is depicted in Figure 2.11 (bottom). Here, the control read wave vector  $\vec{k}_{c,\text{read}}$  points opposite to the probe wave vector  $\vec{k}_p$ . This results in a signal wave vector  $\vec{k}_s$  pointing opposite to the direction of the control write wave vector  $\vec{k}_{c,\text{write}}$ . However, the readout in this configuration is not optimal, because of the phase mismatch  $\vec{k}_\Delta$ , due to the non degenerate ground states. We find, that in a  $\Lambda$ -system with non degenerate ground states, an optimal backward readout configuration, reading the spin wave  $S(z)$  in a reversed direction, as described by Gorshkov *et al.* [82], can not be achieved.

### 2.3.4 Limitations on the Efficiency due to the Storage Medium

In the previous section effects limiting the EIT-LS protocol efficiency, assuming an ideal storage medium, were described. However, in a real storage medium during the storage time  $\Delta T$  the created spin wave, i.e. collective atomic coherence, suffers due to decoherence. Thus, the storage is limited by the coherence lifetime  $T_2$ . In PrYSO a number of effects contribute to the decoherence, e.g. population relaxation, stochastic spin flips, and the inhomogeneous linewidth. The population relaxation  $\Gamma$  (compare with Section 2.1.2) in PrYSO is mainly given by radiative decay and phononic interactions. In the ideal case the lifetime  $T_2$  of a coherence is limited by the natural linewidth, i.e.  $T_2 = 2T_1$ . However, in most systems this can not be achieved, and additional decoherence effects ( $\gamma'$ ) further reduce the lifetime  $T_2$  of the coherence. In PrYSO the main source of this additional decoherence are stochastic yttrium spin flips in the host crystal. Since the Pr ions interact with the surrounding yttrium ions via dipole-dipole interaction, an yttrium spin flip changes the level structure of the nearby Pr ions (see also Chapter 1). Especially the hyperfine structure is altered, i.e. the transition frequencies between the hyperfine levels are slightly changed. Thus, a single coherence, present between two hyperfine levels in a Pr ion, experiences an ad hoc change in its phase evolution, i.e. phase velocity. This effect can be understood as temporally varying stochastic inhomogeneous broadening, also known as *spectral diffusion* [48, 49, 66]. Thus, simple rephasing, as described in Chapter 5 can not be applied. In addition, the Pr ions feature a state dependent, electric dipole moment. Thus, a Pr ion, excited by an optical field, changes the transition frequency of the surrounding Pr ions. This field induced transition frequency change is called *instantaneous spectral diffusion* [67]. To minimize decoherence effects due to spectral diffusion several techniques exist. All techniques rely on the idea of decoupling the system from perturbations of the environment. First, dynamic decoherence control (DDC) [90–93], a technique based on pulse trains applied on a time scale shorter than the spectral diffusion correlation time, to minimize

the effect of random phase changes. This technique is also applied in the present work, compare with Chapter 6. Second, static techniques, which use strong 3D static magnetic fields to reduce the effects of decoherence [21, 53]. Recently in a combination of both techniques, EIT-based light storage times of up to one minute in PrYSO [22] and spin coherence times of six hours in  $\text{Eu}^{3+}:\text{Y}_2\text{SiO}_5$  [21] were achieved.

## 2.4 Raman Heterodyne Detection in a $\Lambda$ -System

In order to investigate composite and adiabatic techniques for rephasing of atomic coherences, we create a coherence in the hyperfine transition  $|\pm 1/2\rangle \leftrightarrow |\pm 3/2\rangle$  of the ground state  $^3\text{H}_4$  of PrYSO. This is either done by the application of a RF pulse to directly generate a coherence between the hyperfine ground states, or optically using the EIT-LS protocol, described in the previous Section 2.3.2. In order to measure a coherence, induced by a RF pulse,

we use a technique based on coherent, stimulated Raman scattering [94, 95], called Raman heterodyne detection (RHD). This technique is well established in REIDS spectroscopy [96, 97]. The idea is to use an optical detection field to convert an RF coherence into a coherent, scattered light field. Figure 2.12 shows the detection realized in the hyperfine structure of PrYSO. The states  $|1\rangle$  and  $|3\rangle$  correspond to the hyperfine levels  $|\pm 3/2\rangle$  and  $|\pm 1/2\rangle$  of the ground state  $^3\text{H}_4$ . The state  $|2\rangle$  corresponds to any hyperfine level of the excited state  $^1\text{D}_2$ . Let's assume a coherence  $\rho_{13}$  has already been prepared by an RF pulse.

Then a resonant detection (pump) field of frequency  $\omega_p = \omega_{12}$  on the optical transition  $|1\rangle \leftrightarrow |2\rangle$  will be Raman scattered on the coherence  $\rho_{13}$ . In our system this leads to a coherent, directed Stokes field with a frequency of  $\omega_s = \omega_p - \omega_{13}$ . In general, the pump field can also couple off-resonant to the transition  $|2\rangle \leftrightarrow |3\rangle$ , generating a weak Anti-Stokes field at a frequency  $\omega_{as} = \omega_p + \omega_{13}$ . However, due to the inhomogeneous broadening of the optical transition, there are ensembles in the PrYSO crystal in which the pump field couples again resonant transitions, i.e.  $\omega_p = \omega_{23}$ . Thereby it generates a notable Anti-Stokes field. The intensity of the (Anti-)Stokes field strongly depends on the optical coherence  $\rho_{23}$ . We can calculate the Stokes field  $\vec{E}_s$  using the nonlinear Maxwell wave equation in slowly varying envelope approximation  $\partial \vec{E}_s / \partial z = i\omega_s / (2n\epsilon_0 c) \vec{P}$  and the time-dependent polarization of the medium  $\vec{P}_{23}(t) = \varrho \vec{\mu}_{23} \rho_{23} \exp(i\omega_s t)$ , with the particle number density  $\varrho$  and the transition dipole moment  $\mu_{23}$  to

$$\vec{E}_s(t) = \frac{i\omega_s L}{2n\epsilon_0 c} \varrho \vec{\mu}_{23} \rho_{23} \exp(i\omega_s t). \quad (2.38)$$

Here  $L$  is the length of the medium,  $\epsilon_0$  the vacuum permittivity,  $n$  the refractive index of the medium. The time evolution of the coherences and the populations

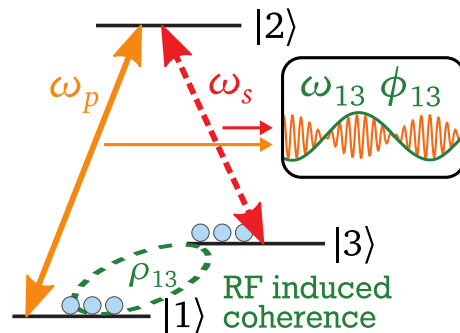


Figure 2.12: RHD scheme realized in the hyperfine structure of PrYSO.

in the  $\Lambda$ -system can be described using the Liouville-von-Neumann Equation 2.11 of six coupled differential equations [95]. Note that here optical pumping effects are not taken into account. After a transformation into the pump field rotating frame and applying the rotating wave approximation (RWA) the set of differential equations can be solved analytically [95]. In the case of a pump field with Rabi frequency  $\Omega_p$  and no RF field applied, the set of differential equations further simplifies. The equation of motion for the optical coherence  $\rho_{23}$ , and the RF coherence  $\rho_{13}$  can thus be written as

$$\dot{\rho}_{23} = \frac{i}{\hbar} \left[ (\Delta_p + i\gamma_{23})\rho_{23} + \frac{\Omega_p}{2}\rho_{13} \right] \text{ and } \dot{\rho}_{13} = \frac{i}{\hbar} \left[ i\gamma_{13}\rho_{13} + \frac{\Omega_p^*}{2}\rho_{23} \right], \quad (2.39)$$

with the detuning of the pump field  $\Delta_p$ , and the decoherence rates  $\gamma_{23}$  and  $\gamma_{13}$ . Assuming a resonant pump field ( $\Delta_p = 0$ ) and neglecting decoherence effects the optical coherence yields

$$\rho_{23} = \frac{i}{\hbar} \sin\left(\frac{\Omega_p}{2}t\right)\rho_{13} \approx \frac{i}{\hbar} \frac{\Omega_p}{2}\rho_{13}t. \quad (2.40)$$

In PrYSO the assumptions above are valid, as long as the duration  $t$  of optical pump field is shorter than the optical decoherence time, i.e.  $\sim 100 \mu\text{s}$ . Also, the Rabi frequency of the pump field should be small such that  $\Omega_p t \ll \pi$ . In this case the optical coherence  $\rho_{23}$  depends linearly on the RF ground state coherence  $\rho_{13}$ . The coherence  $\rho_{23}$  acts as a source of the Stokes field  $E_s$ , which can be understood as a frequency mixing process. The Stokes field  $E_s$  propagates collinear with the readout pump field  $E_p$ . This results in a Raman interference signal

$$I_{\text{RHD}} \propto \frac{1}{2} |E_p + E_s|^2 = \frac{1}{2} \left( \underbrace{|E_p|^2}_a + \underbrace{|E_s|^2}_b + \underbrace{E_p E_s^* + E_s E_p^*}_c \right). \quad (2.41)$$

The terms  $a$  and  $b$  add a constant offset to the signal. The interference term  $c$  oscillates with the beat frequency  $|\omega_p - \omega_s|$ . In the case of a resonant pump field ( $\omega_p = \omega_{12}$ ) the beat note oscillates with the hyperfine transition frequency  $\omega_{13}$ . The magnitude  $R$  of the interference term  $c$  is proportional to the Stokes field  $E_s$ , which depends linearly on the coherence  $\rho_{13}$ . In order to measure the magnitude  $R$  of the beat note,  $I_{\text{RHD}}$  is demodulated with a demodulation frequency  $\omega_D = \omega_{13}$ . Thus, the magnitude  $R$ , linearly proportional to the coherence amplitude  $|\rho_{13}|$ , and a phase  $\phi$  proportional to the coherence phase  $\phi_{13}$  is produced. See [95] for a full description taking into account arbitrary fields and coherences between all levels.

## Chapter 3

### Experimental Setup

In the previous chapters the theoretical background on EIT-based light storage (Chapter 2) in a  $\text{Pr}^{3+}:\text{Y}_2\text{SiO}_5$  crystal (Chapter 1.1) were described. In this chapter a very general experimental setup for conducting light matter interaction experiments in PrYSO is introduced. This setup can be adapted to match the requirements of specific experimental tasks, i.e. EIT-based light storage, coherent two level interactions (optical and RF) and experiments on dynamic decoherence control (DDC). In the following the generation of the required laser radiation, the optical setup, the radio-frequency (RF) magnetic field setup and techniques for signal detection are described.

#### 3.1 Optical Setup

The general experimental setup used in this work is depicted in Figure 3.1. The laser radiation with a wavelength of 605.98 nm is provided by an all solid state laser system based on an optical parametric oscillator (OPO) with an additional intra-cavity sum frequency generation (SFG) [58, 98]. This OPO-SFG cavity unit<sup>1</sup> is pumped by a fiber amplified<sup>2</sup> seed laser system<sup>3</sup> and frequency stabilized by an home built Pound-Drever-Hall [99] stabilization unit. In this configuration the laser system provides tunable visible cw radiation between  $\lambda = 605$  nm and  $\lambda = 616$  nm with an output power of  $P > 1$  W. A frequency jitter of below  $\Delta\nu < 100$  kHz on a time scale of 100 ms was determined by using a commercial linewidth measurement system<sup>4</sup> based on a low finesse Fabry-Perot cavity. The laser radiation is guided from the OPO-SFG system to the optical table with the experimental setup using a single mode optical fiber. The available power after the fiber is approx. 600 mW with a Gaussian spatial profile. In order to prevent unstable operation of the OPO-SFG system due to back reflections from the fiber into the OPO-SFG system, angled ends are used. The polarization is adjusted linearly by a combination of fiber polarization controller, quarter-wave plate and polarizing beam splitter cube (PBSC). The polarization after the single mode fiber is chosen circular, by adjusting the fiber polarization controller. Therefore, internal back reflexions from the fiber end, propagating backwards into the direction of the OPO-SFG system, exhibit in total a change of  $90^\circ$  in linear polarization, and thus

---

<sup>1</sup>Aculight Argos Model 2400 Sf-15, Lockheed Martin

<sup>2</sup>YAR-15K-1064-LP-SF, IPG Photonics

<sup>3</sup>Koheras AdjustiK Y10 PM PztM, NKT Photonics

<sup>4</sup>EagleEye, Sirah



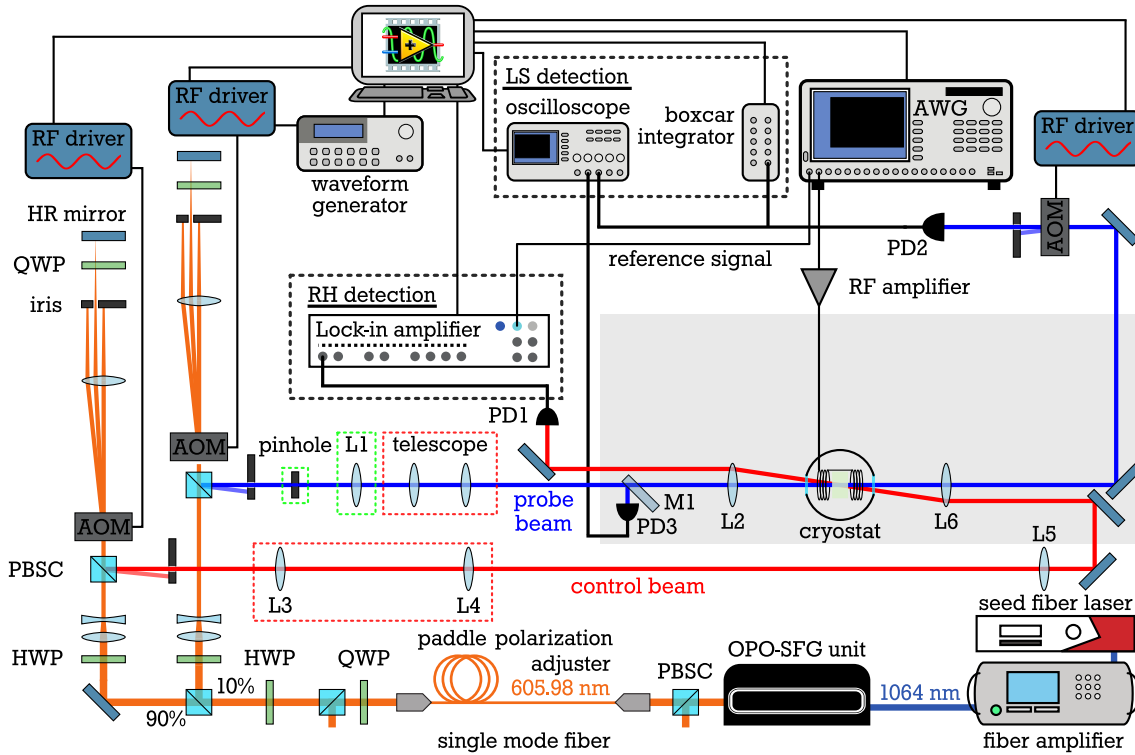


Figure 3.1: Schematic experimental setup used in this work, consisting of the laser source, the optical setup, the PrYSO crystal in the cryostat and the electronic setup. The optical setup is either used with a flat-top spatial probe beam shape (green configuration) and the smaller control beam diameter, or with a Gaussian spatial probe beam shape (red configuration) and a larger control beam diameter.

can be coupled out before entering the laser system using a PBSC. The circular polarization on the experimental table after the single mode fiber is rotated back into linear polarization by the quarter-wave plate. The system can be adjusted, using the fiber polarization controller only, by minimizing the s-polarization output of the PBSC on the experiments optical table. Afterwards the laser radiation is split, by another PBSC into a weak probe beam (10 %) and a strong control beam (90 %). Each beam is guided through a setup of an acousto-optic modulator<sup>5</sup> (AOM) in double-pass configuration [100] to enable frequency shifting and amplitude modulation. The center frequency of the AOMs is 80 MHz, and they feature a maximal frequency modulation bandwidth of  $\pm 25$  MHz. Thus, it is possible to generate pulses with additional relative frequency shifts from the monochromatic, cw laser radiation. The AOMs are controlled using RF-DDS (Direct Digital Synthesis) drivers. The AOM of the probe beam line is driven by a RF-DDS driver<sup>6</sup> with USB frequency control and external analog amplitude modulation driven by a function generator<sup>7</sup>. For the AOM of the control beam line a highly flexible RF-DDS driver<sup>8</sup>, controlled by a 10 MHz digital IO card<sup>9</sup> for direct streaming of most

<sup>5</sup>BRI-TEF-80-50-.606

<sup>6</sup>AODS 20160-1, Crystal Technology

<sup>7</sup>33220A, Agilent Technologies

<sup>8</sup>DDSPA-B8b23b-0, AA opto-electronic

<sup>9</sup>NI PCIe-6535, National Instruments

complex frequency and amplitude waveforms is used [101]. The double-pass configuration of the AOMs prevents beam walkoff due to different AOM frequency shifts and doubles the frequency bandwidth to 100 MHz. The maximum power available at the PrYSO crystal is  $P_c \approx 280$  mW for the control beam and  $P_p \approx 1$  mW for the probe beam. In order to ensure reliable performance of the AOMs in both beam lines the optical power is calibrated with respect to the full range of RF driving frequencies and RF amplitudes. Thus, reproducible experimental conditions for every measurement are guaranteed and any non-linearities of the AOM or RF-DDS drivers are corrected. Depending on the performed experiments the probe beam is used either with a flat-top or Gaussian spatial beam profile. The flat-top beam profile is generated by a  $600 \mu\text{m}$  pinhole and mapped into the crystal using a 4f-configuration telescope<sup>10</sup>, resulting in a diameter of  $d_p \approx 150 \mu\text{m}$ . The Gaussian beam profile is first adjusted by a telescope and then focused by L2 (here  $f_{L2} = 150$  mm) to a FWHM diameter of  $200 \mu\text{m} \times 140 \mu\text{m}$  into the crystal. In front of the cryostat a partially reflective mirror M1 ( $R = 70\%$ ) is placed to detect the input probe beam power on the photo diode PD3<sup>11</sup>. The control beam passes the crystal collimated, with its diameter adjusted by two telescope systems. The first telescope system, with lenses L3 and L4 is removable. The second one is fixed, with L5 ( $f_{L5} = 100$  mm) and L6 ( $f_{L6} = 150$  mm). Thus, it can be chosen between two different Gaussian FWHM diameters of  $775 \mu\text{m} \times 740 \mu\text{m}$  and  $390 \mu\text{m} \times 370 \mu\text{m}$ . The peak Rabi frequencies provided by this setup are:  $\Omega_p \sim 2\pi \cdot (40 - 250)$  kHz for the probe beam and  $\Omega_c \sim 2\pi \cdot (0.1 - 1)$  MHz for the control beam. However, these values strongly depend on the actual beam diameters and the driven hyper-fine transition, see also the transition moments of PrYSO in Table 1.1. The two beam lines are overlapped counter propagating at a small angle of about  $1^\circ$  inside the crystal. Due to the larger control beam diameter compared to the probe beam diameter, the power of the control beam, i.e. its Rabi frequency, can be assumed almost constant over the diameter of the probe beam. After passing the medium the control beam is either blocked, or detected by a photo diode PD1<sup>12</sup>. The probe beam is collimated by lens L6 and guided through an additional gating AOM to protect photo diode PD2<sup>13</sup> from unwanted strong signals, e.g. reflexions of the control beam from mirrors and lenses.

## 3.2 Crystal and Cryostat Setup

The praseodymium doped yttrium-orthosilicate crystal<sup>14</sup> is fixed in a mount and cooled to cryogenic temperatures below 4 K in a continuous flow cryostat<sup>15</sup> to suppress phononic excitations. A vacuum system is attached to the cryostat to evacuate the system to pressures of  $\sim 10^{-6}$  mbar before cool down. The cryostat windows are anti-reflection coated. The crystal has a rather low dopant concen-

<sup>10</sup> $f_{L1} = 400$  mm and  $f_{L2} = 100$  mm

<sup>11</sup>PDA10A-EC, Thorlabs

<sup>12</sup>PDA10A-EC, Thorlabs

<sup>13</sup>2051-FS, New Focus

<sup>14</sup>Scientific Materials

<sup>15</sup>ST-100, Janis



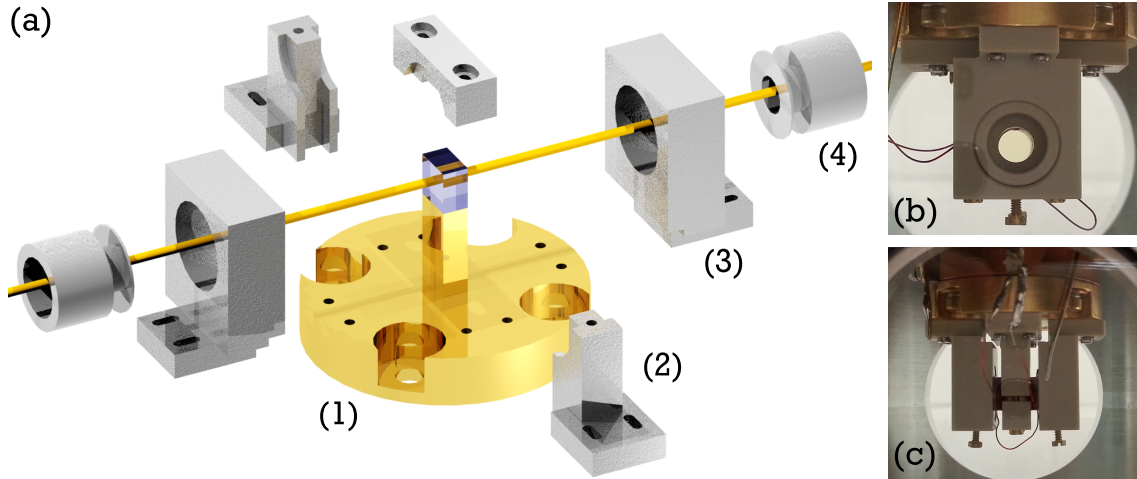


Figure 3.2: (a) Exploded-view drawing of the crystal mount with the copper base plate (1). The mounts to fix the crystal (2) and the RF coils system (3 and 4) are made of PEEK material to reduce eddy currents. Only one side of the crystal is connected to the copper base plate to achieve sufficient thermal contact to the cold finger of the cryostat. (b) View into the direction of the laser beams with the crystal placed in the center. (c) View perpendicular to the laser beam directions, with the RF coils closely attached to the crystal.

tration, i.e. only 0.05 at.% of the yttrium ions are replaced by praseodymium ions. Its dimensions are  $5 \times 5 \times 3$  mm. The optical depth in single pass is  $d \approx 6$ . Also the crystal surfaces are anti-reflection coated. We use different crystal mounts, for simple experiments [60, 102], for experiments involving static magnetic fields [22] and high power RF magnetic fields, described in the following section.

### 3.3 Radio-frequency Magnetic Field System and Mounts

In addition to the laser radiation to couple the optical transitions, radio-frequency (RF) fields are required, in order to directly couple the hyperfine transitions within the ground state of PrYSO. Such a RF magnetic field system enables the application of arbitrary RF pulses, to generate and manipulate atomic coherence and population distributions between the hyperfine levels. For most of the RF pulse experiments realized in this work the hyperfine ground state transition  $|\pm 1/2\rangle \leftrightarrow |\pm 3/2\rangle$  is used. Thus, for a strong coupling in the diabatic regime, of the full inhomogeneous broadening of the transition, RF fields with Rabi frequencies  $\Omega_{\text{RF}} \gg \Gamma_{\text{inhom}} \approx 30$  kHz and of angular frequencies of  $\omega = 2\pi \cdot 10.2 \pm 2$  MHz are required. The RF magnetic fields are produced by RF coils attached close to the crystal inside the cryostat. Two different coil systems have been used in this work. In the first coil system (#1) (see also [58, 60]) each RF coil consists of 7 windings of insulated copper wire with a diameter of  $200 \mu\text{m}$ . The diameter of each coil is  $d = 5$  mm, the length is  $l \approx 2$  mm and the coils are separated by 3.4 mm. Most parts of this system are built from copper. Thus, high frequency fields will induce eddy currents in the copper parts of the mount, which will reduce the effective magnetic field, and thereby limit the maximum Rabi frequency of the

system. Furthermore these strong eddy currents represent an additional thermal energy source, which can become larger than the cooling power of the cryostat, and thus heat up the PrYSO crystal to temperatures  $> 5$  K. In order to generate higher Rabi frequencies, a second coils system (#2) was developed, see Figure 3.2. It consists of 11 windings of insulated copper wire with a diameter of  $200 \mu\text{m}$ . The coil dimensions are slightly larger than of coil system (#1). The coil diameter is  $d = 5.3$  mm, the coil length is  $l = 2.2$  mm and the coils separation is 3.6 mm. Most parts of this system are built from polyether ether ketone (PEEK), to reduce the formation of eddy currents. Both coil systems are driven with RF waves, initially generated by an arbitrary waveform generator<sup>16</sup>. Depending on the experiment, this AWG produces either a continuous single frequency sinusoidal signal or complex pulse sequences with full control over frequency, amplitude and phase with a sampling rate of 1.2 GS/s. The continuous sinusoidal signal is gated by an RF switch<sup>17</sup> to produce RF pulses of any desired duration. The RF switch is controlled with an TTL-I/O card<sup>18</sup>. The complex pulse sequences bypass the RF switch. The RF signals are then amplified by an 10W-RF-amplifier<sup>19</sup> or 30W-RF-amplifier<sup>20</sup> and afterwards sent via an impedance matching circuit to the coils in the cryostat.

An impedance matching circuit is necessary to match the frequency dependent complex impedance of the coil system  $Z_{\text{RF}} = R + i(\omega L - \frac{1}{\omega C})$  to the impedance of the RF amplifier  $Z_{\text{amp}} \approx 50\Omega$ . Otherwise, large parts of the RF wave would be reflected back from the coils into the RF amplifier and only small magnetic fields would be generated at the coils. Here, the impedance matching circuit consists of two tunable capacitors, one parallel and one in series to the RF coils. The idea is to use a tuning capacitor  $C_T$  in parallel to the RF coils to adjust the resonance frequency of the circuit and a matching capacitor  $C_M$  to adjust the imaginary part of the impedance. The adjustment of the circuit to the desired driving frequency of

$\omega \approx 2\pi \cdot 10.2$  MHz is monitored with a vector network analysis tool<sup>21</sup>. This single frequency impedance matching allows to couple the amplifiers with a return loss of 40 dB to the coils, i.e. more than 99 % of the input RF power is transferred to the coils. More details on single-frequency impedance matching and a more general introduction can be found in [103]. With the coil system #1 and the 10W amplifier the maximum Rabi frequency is  $\Omega_{\text{RF}} \approx 2\pi \cdot 140$  kHz. The coil system #2 with the 30W amplifier produces a maximal Rabi frequency of  $\Omega_{\text{RF}} \approx 2\pi \cdot 340$  kHz.

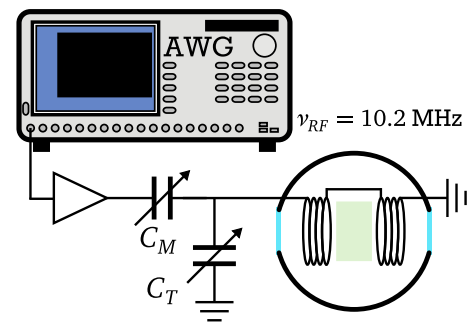


Figure 3.3: Single impedance matching circuit with tunable capacitors  $C_T$  and  $C_M$ . The complex impedance of RF coils is matched to the  $50\Omega$  of the RF amplifier.

<sup>16</sup>AWG 5014, Tektronix

<sup>17</sup>ZYSWA-2-50DR, Minicircuits

<sup>18</sup>NI PCIe-6363, National Instruments

<sup>19</sup>1028-BBM 1C3KAJ, EM Power

<sup>20</sup>LZY-22+, Minicircuits

<sup>21</sup>miniVNA, mini Radio Solutions

### 3.4 Detection of Light Storage Signals

In the case of EIT-based light storage, a input probe pulse, generated by the probe beam line, is stored. A partially reflective mirror M1 ( $R = 70\%$ ) and a photo diode PD3<sup>22</sup> are used to monitor the input pulse energy. In forward readout configuration a retrieved signal pulse leaves the crystal, following the probe beam line, into the direction of the photo diode PD2. This photo diode records the time resolved shape of the retrieved signal pulse, which is then integrated using a boxcar integrator<sup>23</sup>. In parallel input probe pulse and signal pulse can be recorded by an oscilloscope<sup>24</sup>. All signals are acquired and integrated by a computer using a data acquisition card<sup>25</sup> with a LabVIEW software.

### 3.5 Raman Heterodyne Detection

In order to detect a coherence created by an RF magnetic field pulse, we use a Raman heterodyne detection (RHD) scheme which is described in detail in Section 2.4. The control beam is used to read the RF induced coherence by stimulated Raman scattering. Thus the initial control beam with a frequency  $\omega_p$  and a scattered Stokes field with a frequency  $\omega_s = \omega_p - \omega_{13} = \omega_{23}$  interfere and can be detected using photo diode PD1. To measure the coherence amplitude  $|\rho_{13}|$  and phase  $\phi_{13}$ , the signal of the photo diode is demodulated using a lock-in amplifier<sup>26</sup>, with a local oscillator frequency of  $\omega_{13}$ . Thus, a magnitude  $R = \sqrt{X^2 + Y^2} \propto |\rho_{13}|$  and a phase signal  $\theta = \tan^{-1}(Y/X) \propto \phi_{13}$  can be measured. These signals are acquired by the computer with a data acquisition card<sup>27</sup> by a LabVIEW software.

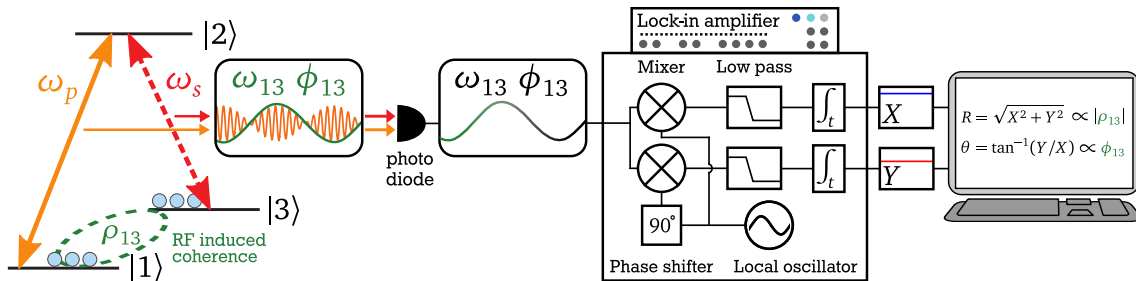


Figure 3.4: Detection of a RF pulse induced coherence by stimulated Raman scattering. The signal of the photo diode is demodulated by a lock-in amplifier which returns the coherence amplitude  $|\rho_{13}|$  and phase  $\phi_{13}$ . Figure adopted from [58].

<sup>22</sup>PDA10A-EC, Thorlabs

<sup>23</sup>SR250, Stanford Research Systems

<sup>24</sup>TDS2014B, Tektronix or PicoScope 4824, Pico Technology

<sup>25</sup>PCIe-6363, National Instruments

<sup>26</sup>HF2LI, Zurich Instruments

<sup>27</sup>PCIe-6363, National Instruments

## Chapter 4

# Optimization of the EIT Light Storage Efficiency

The efficient storage of light is of major importance for the realization of a future realistic quantum information storage device [5, 7]. In recent years considerable efforts on the research of potentially highly efficient quantum memories have been made. Different combinations of storage media, i.e. REIDS, hot atomic gases, cold atomic clouds, and storage protocols, i.e. atomic frequency combs (AFC), gradient echo memories (GEM) and EIT-based memories, have been investigated in the regime of classical light pulses as well as in the single photon regime. So far, the highest storage efficiency was determined in a hot atomic gas using the GEM protocol by Hosseini *et al.* [10]. A storage efficiency of about 87 % was achieved. Regarding the class of REIDS memories, classical light was stored in a PrYSO crystal using the GEM protocol with an efficiency of 69 % by Hedges *et al.* [9]. In the few and single photon regime an efficiency of about 25 % was achieved using an PrYSO crystal in combination with the AFC protocol [104]. The largest efficiency of an EIT-based light storage protocol was accomplished by Chen *et al.* [89] in a cloud of cold rubidium atoms in a magneto optical trap, reaching an efficiency of 71 % in forward readout configuration and 78 % in backward readout. However, so far, combinations of EIT-based light storage in REIDS mostly focused on the prolongation of the storage time [22, 97, 105]. Thus, the storage efficiencies obtained in these experiments have been rather low, i.e. a few % only.

In the following chapter we combine different techniques to optimize and increase the EIT light storage efficiency in the PrYSO crystal. As described in Chapter 2 the theoretical efficiency limit of the EIT light storage protocol is set by the optical depth  $d$ . Most rare-earth ion-doped solids in quantum optics, like PrYSO, feature rather low dopant concentrations to reduce stress induced linewidth broadening mechanisms, which would result in a faster decoherence (see also Chapter 1). Thus, typically optical depths of such media are  $d < 10$ .

In the following section an optimized preparation of the storage medium for EIT light storage is described. We apply this preparation for EIT-based light storage. Then, we optimize the probe pulse duration and control Rabi frequency to achieve an optimal storage in our PrYSO crystal with a rather low optical depth of about 6. We further describe the experimental realization of a pulse shaping algorithm, as introduced in Section 2.3.3 to optimize the probe pulse shape. Different approaches to increase the optical depth of a storage medium are discussed. We introduce a ring-type optical setup to increase the effective optical depth of our PrYSO crystal. This setup also allows us to choose the effective optical depth. Thus, we perform the optimization of the EIT light storage for different effective optical depth of the PrYSO crystal.

## 4.1 Preparation of a $\Lambda$ -System for EIT Light Storage

We introduced in Chapter 1 the complex spectroscopic structure of rare-earth ion-doped crystals. In particular, we found the inhomogeneous broadening of the optical transition  ${}^3\text{H}_4 \leftrightarrow {}^1\text{D}_2$  in PrYSO of several GHz, to be much larger than the splitting of the hyperfine transitions, see Section 1.2. Therefore a monochromatic laser beam couples all nine possible transitions within different ensembles of the inhomogeneous broadening. However, we also saw that EIT-based light storage requires a defined initial situation of a  $\Lambda$ -system with the population in one of the ground states (see Section 2.3.2). Thus, a preparation of the storage medium is necessary before the EIT-based light storage protocol can be applied. We prepare multiple identical  $\Lambda$ -systems, to maximize the optical depth, with a preparation scheme based on optical pumping [106]. This preparation is a slightly modified version of schemes described in [64, 107]. A preparation due to optical pumping is possible, as in PrYSO the population lifetime of the excited hyperfine states ( $T_1^* = 164 \mu\text{s}$ ) is much smaller than the relaxation time between the ground states ( $T_1 \sim \text{sec}$ ), compare with Chapter 1. Therefore, efficient optical pumping within a few milliseconds can be achieved.

The preparation sequence consisting of three steps is shown in Figure 4.1. The control beam, compare with the experimental setup described in Chapter 3, is used for the preparation. The exact values of the optical pumping Rabi frequencies and durations of the control beam do not affect the quality of the preparation, as long as the transitions are driven strongly and much longer than the population lifetime of the excited state hyperfine levels. Thus, in the following only the relative pumping frequencies of the control beam are given. Before the first preparation step the population is equally distributed within the hyperfine levels of the ground state  ${}^3\text{H}_4$ . First, a broad spectral hole is prepared by slowly scanning the frequency of the control beam within a relative frequency range of 0–16 MHz during a time of  $\sim 6 - 15$  milliseconds. This step is repeated several times to prepare a fully transparent spectral hole within the inhomogeneous optical line, as it is depicted in the absorption spectrum (black line) of Figure 4.1. We call this *spectral pit*. This spectral pit is partially repopulated by applying a repump pulse, outside the spectral pit, at a fixed relative frequency of 29.3 MHz. The frequency is chosen such that the repump pulse couples the populated ground state to the three different excited states of three different ensembles. Thus, the relative frequency difference of the repumped ensembles correspond to the hyperfine splitting of the excited state. The absorption spectrum after the repump pulse is depicted in Figure 4.1 (blue line). Several absorption lines are prepared and the population is redistributed into two of the three hyperfine ground states. Thus, in order to prepare  $\Lambda$ -systems with population in only one ground state, as necessary for EIT, an additional cleaner pulse is applied at a relative frequency of 1.8 MHz. This pulse empties state  ${}^3\text{H}_4|\pm \frac{1}{2}\rangle$  and for ensembles  $\epsilon_2$  and  $\epsilon_3$  the population mainly relaxes into  ${}^3\text{H}_4|\pm \frac{3}{2}\rangle$ . However, ensemble  $\epsilon_1$  features a rather unfavorable combination of relative oscillator strengths, which is why most of the population relaxes into  ${}^3\text{H}_4|\pm \frac{5}{2}\rangle$ . The absorption spectrum after the cleaner pulse is depicted by a red line in Figure 4.1.



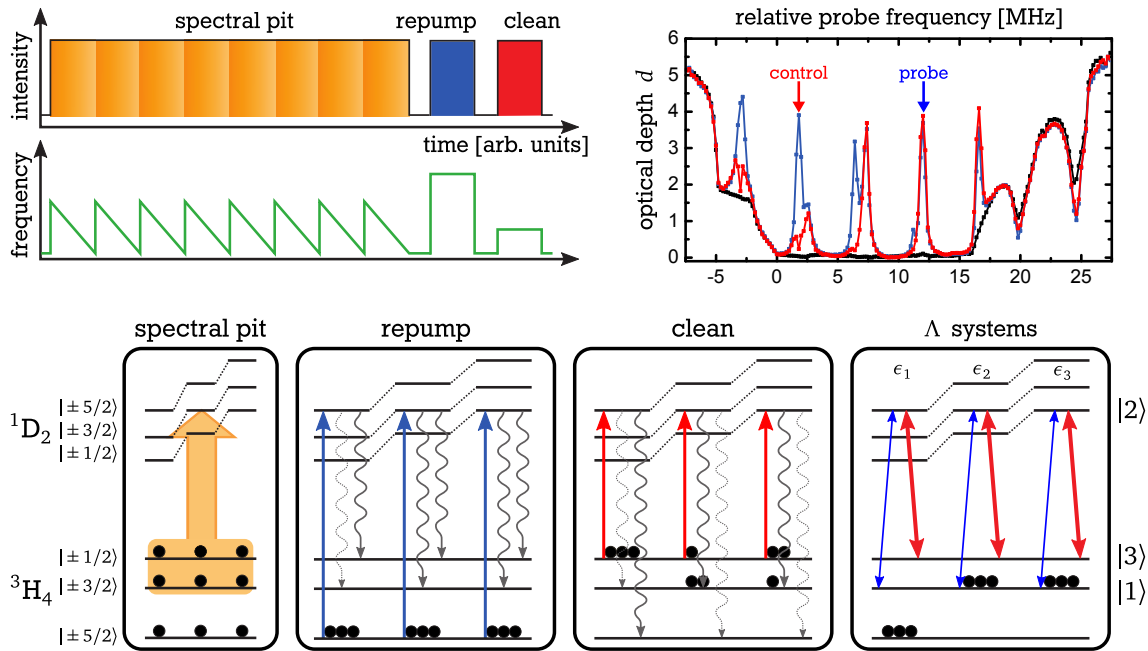


Figure 4.1: Pulse sequence to prepare three isolated  $\Lambda$ -systems within the inhomogeneous broadening of the optical transition of PrYSO. (top left) Optical preparation sequence. (top right) Absorption spectra after each preparation step. (bottom) Effective optical pumping processes for each step of the preparation sequence. The population (black circles) decays approximately with respect to the relative oscillator strength (gray arrows).

Using this preparation scheme, we prepared three isolated  $\Lambda$ -systems, each with a different hyperfine excited state, which can be simultaneously coupled by a monochromatic control pulse on an empty transition  $|3\rangle \leftrightarrow |2\rangle$ , as required for EIT (see Figure 4.1). The probe pulse couples a populated transition in ensembles  $\epsilon_2$  and  $\epsilon_3$ , while in the case of ensemble  $\epsilon_1$  the transition is only weakly populated. Taking into account the relative oscillator strength for each  $\Lambda$ -system, one finds an optical depth for the probe beam of 97 %, compared to the optical depth of the crystal without any preparation. This is a drastic increase compared to previous preparation schemes [107] with only one ensemble, where only 59 % of the optical depth of the crystal was prepared in a single  $\Lambda$ -system.

## 4.2 Experimental Observation of EIT in PrYSO

We prepare the PrYSO crystal as described in the previous Section 4.1. If we apply a strong resonant control pulse on the optical transition  $|3\rangle \leftrightarrow |2\rangle$  the absorption for the probe field vanishes, on resonance with the  $|1\rangle \leftrightarrow |2\rangle$  transition. In order to measure the total EIT feature we simultaneously apply a weak probe pulse ( $P_p \approx 100 \mu\text{W}$ ,  $\tau_p = 20\mu\text{s}$ ), whose frequency is gradually scanned across the two photon resonance of the  $\Lambda$ -systems by a probe detuning  $\Delta_p$ . We detect the transmitted fraction of the probe pulse by using photo diode PD2 (compare with Chapter 3) and calculate the corresponding optical depth  $d$ . Figure 4.2 shows the optical depth  $d$  versus the probe detuning  $\Delta_p$  for different control powers  $P_c$ . If no control pulse ( $P_c = 0 \text{ mW}$ ) is applied, we measure the expected single absorp-

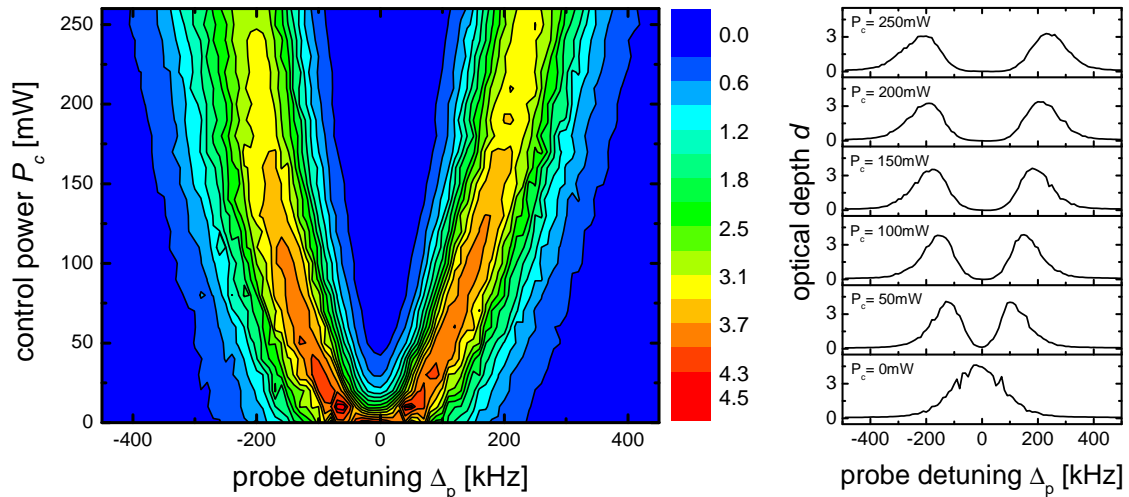


Figure 4.2: (left) Optical depth  $d$ , i.e. absorption spectra, versus the relative probe detuning  $\Delta_p$  and control power  $P_c$ . (right) Cuts at different control powers  $P_c$ . We find a single absorption line if  $P_c = 0$  mW, and EIT for  $P_c > 0$  mW. The EIT window width increases for higher control pulse powers. Full transparency is achieved at control powers  $P_c > 40$  mW.

tion line. With an increase of the control power a splitting occurs. We achieve full transparency at control powers larger 40 mW. At a control power of 250 mW the splitting of the two peaks of the EIT feature is about 450 kHz, which corresponds to a control Rabi frequency of  $\Omega_c \approx 2\pi \cdot 450$  kHz. We find the two photon resonance exactly at zero probe pulse detuning, if  $\nu_p - \nu_c = 10.19$  MHz, i.e. the transition frequency of the ground state hyperfine  $|\pm 3/2\rangle \leftrightarrow |\pm 1/2\rangle$  transition. The slight asymmetry of the EIT spectra, i.e. the asymmetric splitting especially at high control powers, might be due to a small detuning of the control pulse from the transition frequency of the  ${}^3\text{H}_4|\pm 1/2\rangle \leftrightarrow {}^1\text{D}_2|\pm 3/2\rangle$  transitions, i.e.  $\Delta_c \neq 0$  kHz. A comparison with Figure 2.5 shows that already small detunings  $\Delta_c$  lead to an asymmetric EIT feature. We determined in Chapter 2.3.1, the peak splitting  $\Delta_{\text{peak}}$  to be proportional to the control Rabi frequency  $\Omega_c$ , and thus proportional to the square root of the control power  $\sqrt{P_c}$ . The experimentally observed peak splitting is extracted from Figure 4.2 and plotted in Figure 4.3 versus the control power  $P_c$ .

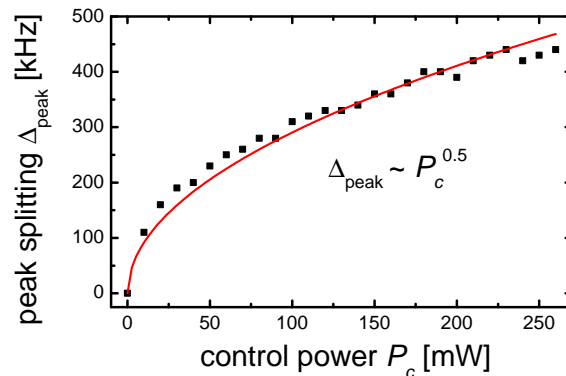


Figure 4.3: Splitting of the EIT absorption line  $\Delta_{\text{peak}}$  versus the control pulse power  $P_c$ . Black squares represent experimental data. Solid red line depicting a square root depending fit to the experimental data.

We find that the experimental data follows the expected square root behavior. We saw that we can achieve EIT in our PrYSO crystal and that we can precisely control the EIT width by the control pulse power. In the following section we will use this control for optimal storage and retrieval of a probe pulse of given duration as an atomic coherent superposition of states in the PrYSO crystal.

### 4.3 Determination of the Light Storage Efficiency

In general, the pulse energies of the probe input pulse  $E_{\text{in}}$  and of the retrieved signal pulse  $E_{\text{out}}$  have to be measured in order to determine the light storage efficiency. We detect the input probe pulse and the signal pulse using standard photo diodes (see also Chapter 3). Thus, the time-integrated photo diode signals are proportional to the pulse energies. The photo diode signals are either integrated using a boxcar integrator or recorded using an oscilloscope and evaluated by a computer. There have been two experimental methods implemented in our optical setup to determine the EIT light storage efficiency. These methods are designed to measure the intrinsic EIT light storage efficiency, neglecting the losses due to the optical setup.

Method #1 uses the photo diodes PD2 and PD3 as well as an oscilloscope to measure the light storage efficiency. PD2 is used to detect the signal pulse, while PD3 detects a fraction of the probe input pulse. Both photo diode signals are acquired by an oscilloscope and integrated by the computer. In order to calculate a precise light storage efficiency, a calibration of the photo diodes, taking into account the transmission of the optical setup, is required. This calibration has to be done before any light storage experiment is conducted. However, any fluctuations and changes in the transmission through the optical setup after the calibration, are not taken into account by this method, and thus will result in a fluctuation of the measured storage efficiency. Therefore, averaging over several identical light storage experiments is necessary to determine a precise average storage efficiency. The fluctuation of the light storage efficiency can give an insight on the stability of the optical setup. With this method the storage efficiency of a single light storage process can not be measured. This method is rather slow and thus usually only used to determine the storage efficiency for constant experimental parameters.

Method #2 uses photo diode PD2 and the boxcar integrator or an oscilloscope. The input probe pulse energy is measured  $\sim 15$  ms prior to the actual light storage experiment, by sending a copy of the probe input pulse through the optical setup and the transparent storage medium directly after the preparation of the spectral pit. Thus, the recorded boxcar signal, or integrated signal from the oscilloscope, is proportional to the input probe pulse energy. A second identical probe input pulse is then used to perform the actual light storage experiment. Afterwards, the signal pulse energy is also measured using either the boxcar integrator or the oscilloscope. As the input pulse energy and signal pulse energy are measured via the same beam path and optical setup, losses are automatically canceled. However, variations in losses and fluctuations in pulse energies between the input probe energy measurement and the actual light storage experiment, i.e. within 15 ms, can not be taken into account by this method. Nevertheless, this method allows an on time determination of the light storage efficiency.

Depending on the experimental requirements, the proper method for determining the light storage efficiency is chosen. Usually method #2 is used if experimental parameters are scanned and the absolute light storage efficiency is not of major importance. In contrast, method #1 is applied whenever precise average light storage efficiencies have to be determined.



## 4.4 Optimization of the Light Storage Efficiency

In Section 2.3.3 it was shown that for efficient EIT light storage the combination of probe pulse duration  $\tau_p$  and control Rabi frequency  $\Omega_c$  has to be chosen carefully. In particular,  $\Omega_c^2 \cdot \tau_p$  has to match Equation 2.34. In this section we introduce a measurement, to adjust the experimental parameters  $\Omega_c$  and  $\tau_p$  in order to fulfill Equation 2.34, and thus to achieve optimal light storage, i.e. maximal light storage efficiency. We use the optical setup as it is described in Chapter 3, with the larger of two possible control beam diameters and a Gaussian spatial probe beam profile. The storage medium is prepared as described in Section 4.1. A probe pulse of rectangular temporal shape and duration  $\tau_p$  is stored. We chose a storage time of  $\Delta T = 2 \mu\text{s}$ , in this way all dephasing and decoherence effects, occurring in PrYSO on time scales  $> 10 \mu\text{s}$ , can be neglected. We thus measure an efficiency  $\eta = \eta_{\text{EIT}}$ , the efficiency of the EIT light storage protocol, as it is defined by Equation 2.29. We determine the storage efficiency by method #2, as it was introduced in the previous section. Since the control power  $P_c$  is proportional to  $\Omega_c^2$ , we can measure the light storage efficiency versus the control power  $P_c$  and the probe pulse duration  $\tau_p$ , to find combinations fulfilling Equation 2.34, thus maximizing the storage efficiency.

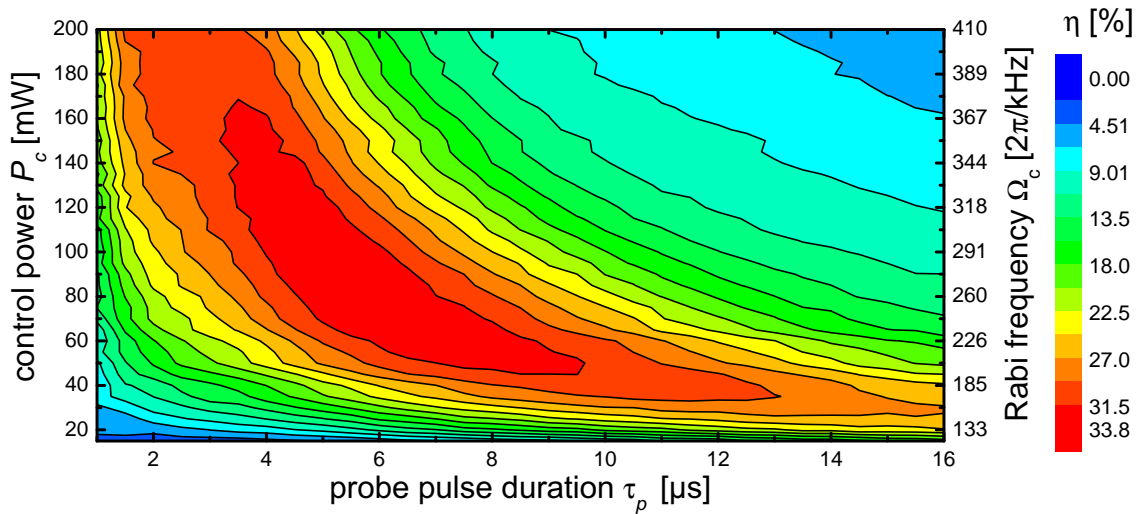


Figure 4.4: Efficiency  $\eta$  versus probe pulse duration  $\tau_p$  and control power  $P_c$ , i.e. the control Rabi frequency  $\Omega_c$ , respectively. The control Rabi frequencies given here are approximate values, extracted from the experimental results on the EIT peak splitting  $\Delta_{\text{peak}}$  of the previous section, see Figure 4.3.

Figure 4.4 depicts the experimentally determined light storage efficiency  $\eta$  versus the probe pulse duration  $\tau_p$  and the control power  $P_c$ , i.e. the control Rabi frequency  $\Omega_c^2$ . A constant storage efficiency is achieved for combinations of  $P_c \tau_p = \text{const.}$ , following hyperbolas as expected from Equation 2.34. We also find maximal storage efficiency following the optimal hyperbola with  $\Omega_c^2 \cdot \tau_p \approx 17 \cdot 10^6 \text{ s}^{-1}$ . The maximal storage efficiency is  $\eta = 33.8 \%$  at a probe pulse duration of  $5.5 \mu\text{s}$  and a control power of  $85 \text{ mW}$ .

The storage efficiency strongly reduces for combinations of  $P_c$  and  $\tau_p$  next to this optimal hyperbola. Combinations of large probe pulse duration and strong control powers lead to an inefficient storage, as large fractions of the probe pulse leak out of the storage medium, due to a insufficient compression of the probe pulse. On the other hand, also very short probe pulse durations result in an inefficient storage, because of a spectral EIT window which is not broad enough to cover the spectral width of the probe pulse, i.e.  $\Gamma_{\text{EIT}} \ll \Gamma_p$ .

Also we find, that the efficiency decreases at the edges of the hyperbola, for control powers larger 160 mW and smaller 40 mW with their corresponding optimal probe pulse durations. For very strong control powers and short probe pulse durations the storage process is no longer sufficiently adiabatic. The system is therefore driven partially via the bright states, this leads to residual absorption during the storage and readout process, and thus reduces the storage efficiency. The effect of weak adiabaticity on the storage process and the storage efficiency is also described theoretically in Gorshkov *et al.* [82]. For small control powers a reduced storage efficiency can be explained by a residual absorption in the center of the EIT window. As described in Section 2.3.1, an inhomogeneous broadening  $\Gamma_{13}$  between the ground states of the  $\Lambda$ -system leads to residual absorption. We achieve full transparency only if  $\Omega_c^2 \gg \Gamma_{13}\Gamma_{12}$ . A comparison with Figure 4.2 confirms this explanation, as we measure full transparency only for control powers larger 40 mW.

Note that the pulse shaping algorithm for optimal spin wave storage, introduced in Section 2.3.3, to optimize the probe pulse shape is not applied here. Nevertheless, we obtain a storage efficiency in the order of 30 % for a large range of combinations of probe pulse durations and control powers.

## 4.5 Concepts to Increase the Optical Depth

The maximal storage efficiency in the previous section was only in the order of 30 %. We have seen in Chapter 2 that the theoretical limit for the efficiency of the EIT light storage protocol is set by the optical depth  $d$ . In previous work different techniques to increase the optical depth were investigated. For example, a higher doped PrYSO crystal, with a dopant concentration of 1%, was investigated. It was expected, that the larger number of praseodymium ions, would lead to an increase of the absorption coefficient  $\alpha$ , and thus to a higher optical depth  $d$ , as  $d = \alpha L$ . However, it was found that the higher dopant concentration leads to an increase of the optical inhomogeneous linewidth by a factor of 40. Moreover, the dephasing and decoherence time had been reduced by a factor of  $\sim 5$  [60]. These spectroscopic changes can be attributed to the different atomic radii of the praseodymium and yttrium ions, which leads to increased stress in the PrYSO crystal matrix for higher dopant concentrations. However, there are rare-earth materials especially designed for high dopant concentrations, with matched atomic radii of the dopant material and the host crystal [61].

Another way to achieve higher optical depth  $d$  could be to increase the length  $L$  of the storage medium. However, in our experimental setup a longer crystal

leads to severe technical problems. It becomes much more difficult to intersect the control beam and probe beam perfectly along the total length of the crystal. Furthermore, it will be almost impossible to achieve the homogeneous static and RF magnetic fields required to obtain long storage times. Therefore, we introduce here a different technique which allows us to increase the effective length, and therefore the effective optical depth of the crystal.

The simplest way to increase the effective length, i.e. the effective optical depth, is to reflect the probe beam after passing through the crystal onto itself. Thereby, the probe pulse propagates through the crystal a second time and the effective optical depth is doubled. In general, with  $N$  the number of passes through the storage medium, we write for the effective length of the medium  $L_{\text{eff}} = NL$ , and for the effective optical depth  $d_N = d_0N$ , with  $d_0$  the optical depth passing the crystal once. In the following, a highly flexible concept for increasing the optical depth of the crystal is described.

#### 4.5.1 Multipass Geometry to Increase the Optical Depth

We discussed in the previous section different ideas to increase the optical depth of a storage medium. Here, we follow the idea of increasing the optical depth by passing the probe pulse several times through our PrYSO crystal. As such a multipass geometry has to be embedded into an already existing optical setup, several constraints and criteria have to be taken into account.

First, techniques to prolong the storage time by RF and static magnetic fields should still be possible. In order to achieve these homogeneous magnetic fields, the storage process has to take place in a rather small interaction region. This interaction region is defined by the control beam. We can minimize this region by guiding the control beam through the crystal only once. Thus, the multipass setup has to be constructed for the probe beam only.

Second, of course, the setup should allow a rather large number  $N$  of probe beam passes through the crystal to enable a high optical depth. In addition, it should be flexible enough, in a way that the number of passes  $N$  can be changed easily. This would allow us to determine the experimentally maximum storage efficiency for different optical depths. The setup further has to match the small aperture and tight geometrical constraints of the crystal and cryostat with its closely attached radio-frequency and optical setup. The maximum acceptance angle of the cryostat setup is  $12^\circ$  with respect to the optical axis. Thus, all beams have to propagate at rather small angles through the optical setup. For optimal storage, the control Rabi frequency should be as constant as possible throughout the probe beam profile. Therefore, the probe beam diameter is chosen much smaller than the control beam diameter. Moreover, the probe beam diameter has to be maintained constant for all passes through the multipass setup.

We have developed and implemented such a multipass setup for the probe beam, which is matched to the small aperture and experimental constraints, and in addition permits systematic measurements for different optical depth by variation of the number of passes  $N$  by simple adjustment of a single optical element.

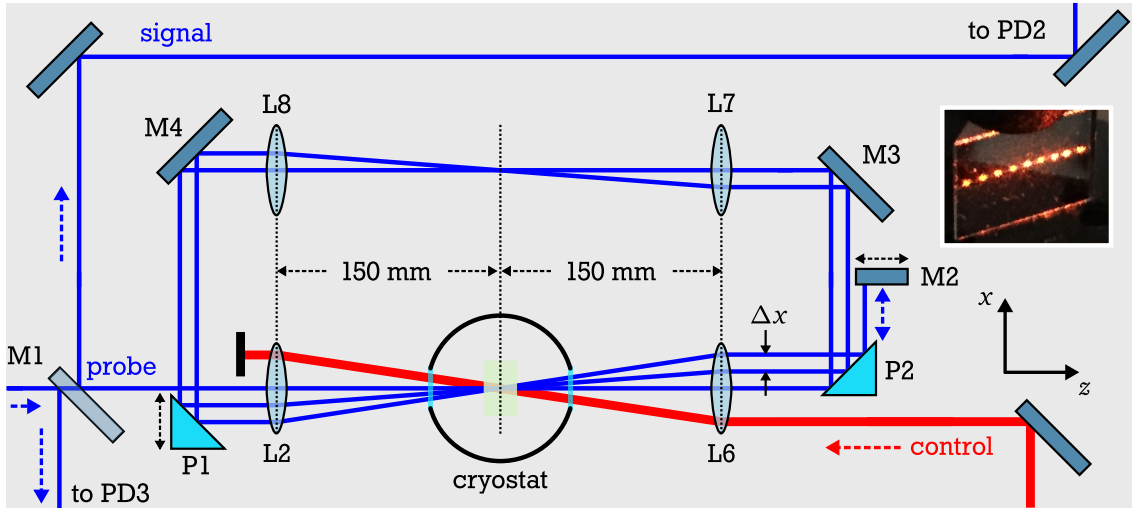


Figure 4.5: Schematic of the multipass setup for a variable number of passes of the probe beam through the PrYSO crystal in a cryostat, with reflective prisms P1, P2, mirrors M2, M3, M4, and two telescope systems in 4f-configurations. This setup is added to the existing optical setup shown in Figure 3.1. Here, the beam path for  $N = 6$  passes is depicted as an example. A lateral shift of prism P1 in  $x$  direction changes the spatial distance  $\Delta x$  between two passes and the total number of round-trips is varied by shifting mirror M2 in  $z$  direction. Inset shows the reflections on prism P2 for  $m = 9$ .

Figure 4.5 shows a schematic of the relevant parts of the multipass setup, depicted for  $N = 6$  passes through the PrYSO crystal. The multipass setup was added to the general optical setup as depicted in Figure 3.1. We used the general optical setup in red configuration, compare with Figure 3.1, with a larger control beam diameter and a Gaussian probe beam profile, to achieve a constant control Rabi frequency throughout the probe beam. Compared to the flat-top profile, the Gaussian probe profile has the advantage that it can be easily mapped by relay imaging, without taking care of a large diffraction pattern, which would be difficult to guide through the compact multipass setup. The setup resembles a ring, made of prisms P1, P2, mirrors M2, M3, M4 and two telescope systems in 4f-configuration. The collimated Gaussian probe beam with a diameter of  $360 \mu\text{m}$  is partially reflected at mirror M1 and detected with the photo diode PD3, the transmitted part is coupled into the ring. The optical path in the ring is chosen such that the probe beam is laterally shifted by a distance  $\Delta x$  after each round-trip. In order to be able to achieve rather small lateral shifts between two consecutive beams, reflective prisms P1 and P2 are used instead of simple mirrors. This setup already permits  $m$  passes, which are limited by the ratio of the prism dimensions and the probe beam diameter.

After  $m$  passes, the probe beam is retro-reflected by mirror M2 and propagates back another  $m$  passes, until it leaves the setup opposite to the initial input direction. The telescope systems in 4f-configuration, consisting of lenses L2, L6, L7 and L8, all with  $f = 150 \text{ mm}$ , serve to focus the beam  $N = 2m$  times into the interaction region and maintain the probe beam profile for each pass by relay imaging with a total length per circulation of 1.2 m. The total number of passes can be var-

ied by simply shifting the position of mirror M2 in  $z$  direction with a translation stage. The distance  $\Delta x$  between two adjacent passes can be adjusted by shifting the prism P1 in  $x$  direction. With a collimated probe beam diameter of  $360 \mu\text{m}$ , we require  $\Delta x \geq 1 \text{ mm}$  in order to be able to separate the beam at mirror M2 without any diffraction. With the prism dimensions of  $10 \times 10 \text{ mm}$  we thus achieve up to  $N = 18$  passes through the crystal. Note that, at pulse durations in the regime of  $10 \mu\text{s}$ , the optical delays (i.e., optical path outside of the crystal) of roughly 4 ns per round-trip have a negligible effect on the storage process. Due to the strong compression the optical path length in the crystal is much larger than the optical path length of the multipass setup. We can thus neglect the small part of the probe pulse outside the crystal during the storage process.

The control beam propagates under a small angle of  $\sim 1^\circ$  with regard to the optical axis and passes only once through the crystal. Therefore, the first half of probe passes (before mirror M2) are stored with an almost counter-propagating control beam, while the second half of probe passes (after M2) are stored with an almost co-propagating control beam. Nevertheless, each temporal slice of the probe beam is retrieved with the control read pulse under the same angle as it was stored before with the control write pulse, due to the phase matching conditions. Thus, in this multipass setup all probe passes are retrieved in the EIT forward readout scheme.

Although all optics of the multipass setup are coated for 606 nm, the overall transmission losses per pass add up to approximately 13%. The optical elements of the multipass setup have to be adjusted such that all probe beam passes intersect with the control beam in the center of the crystal. Because of the rather large total probe beam path length a very precise alignment of the optics is necessary. First, the incident probe beam is aligned with the optical axis of L2 and L6. All subsequent probe passes are then adjusted parallel to this first probe pass. If the distance  $\Delta x$  between the reflections of all probe passes on all optical elements of the multipass are the same, we can be sure that all probe passes are focused by L2 into the same spot inside the crystal. The control beam is then aligned to intersect with this spot. In the following we will perform the optimization of the light storage efficiency in this multipass setup.

## 4.6 EIT Light Storage in a Multipass Setup

We use the multipass setup, introduced in the previous section, to optimize the EIT light storage efficiency for different number of probe passes  $N$  through the crystal. We saw in Section 4.5 that by increasing the number of passes through the crystal, we can achieve higher effective optical depths. Thus, we are able to optimize the EIT light storage efficiency for different optical depths.

In order to optimize the EIT light storage protocol to achieve maximum efficiency, we used in a first step the procedure introduced in Section 4.4. In a second step we used the pulse shaping algorithm for optimal spin wave storage, as it was introduced in Section 2.3.3, to further optimize the storage efficiency.

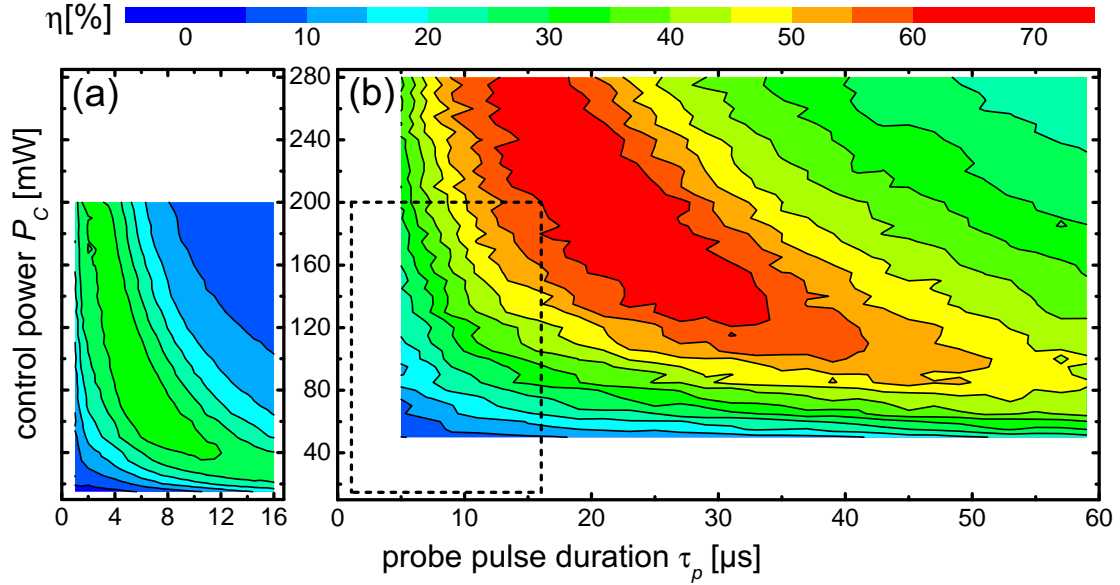


Figure 4.6: EIT light storage efficiency  $\eta$  versus control pulse power  $P_c$  and probe duration  $\tau_p$  of a rectangular pulse. (a) For a single pass ( $N = 1$ ) of the probe beam through the crystal. (b) For the multipass setup with  $N = 10$  passes of the probe beam through the crystal. We note, that the parameter ranges of  $P_c$  and  $\tau_p$  for  $N = 1$  and  $N = 10$  passes are quite different. The dashed square in (b) indicates the parameter range of (a).

In the first optimization step we systematically measured the light storage efficiency  $\eta$  for different combinations of control pulse power  $P_c$  and probe pulse duration  $\tau_p$ . The results are depicted in Figure 4.6 for a single pass ( $N = 1$ ) (a) and with a multipass setup of  $N = 10$  (b) passes through the crystal. Note that the parameter ranges are quite different. The parameter range of the single pass (a) is indicated by a dashed square in the experimental data of the multipass (b) for  $N = 10$ . Both measurements exhibit the region of largest efficiency on a hyperbola, determined by the relation  $P_c \tau_p \propto \Omega_c^2 \tau_p = \text{const.}$ , confirming Equation 2.34. For small control Rabi frequencies (and large probe pulse durations) the efficiency on the hyperbola is reduced. As already noted in Section 4.4 this can be assigned to a residual absorption in the center of the EIT window, due to the inhomogeneous broadening of the hyperfine transition. We find that for  $N = 10$  passes, i.e. a 10 times higher optical depth compared to the single pass, this residual absorption appears for control powers smaller 120 mW. In the case of a single pass we achieved full transparency for control powers larger 40 mW. Thus, in media of higher optical depth stronger control Rabi frequencies are required to suppress residual absorption. The maximal storage efficiency in the single pass yields 33.8 %. As the optical depth increases in the multipass setup with  $N = 10$  passes, Equation 2.34, is fulfilled better and the maximal storage efficiency is higher, reaching 67 %. A comparison of Figure 4.6 (a) and (b) shows that the optimal combination of probe pulse duration  $\tau_p$  and control power  $P_c$  is shifted with an increase of the optical depth, from  $N = 1$ : ( $P_c \approx 80$  mW/ $\tau_p \approx 6$   $\mu$ s) to  $N = 10$ : ( $P_c \approx 180$  mW/ $\tau_p \approx 24$   $\mu$ s). This can also be explained using Equation 2.34. With larger optical depths, longer probe pulses can be compressed in the crystal. However, at the same time the EIT



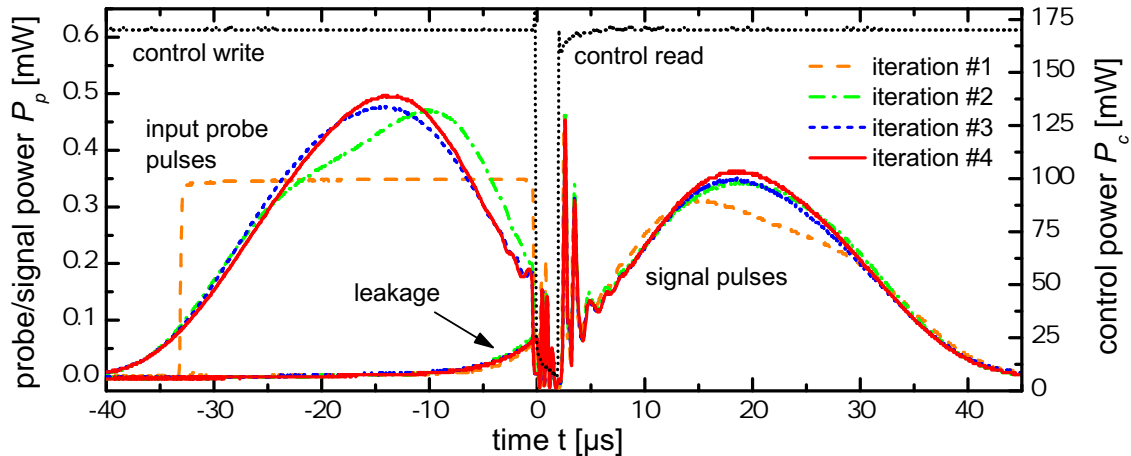


Figure 4.7: Probe and signal pulse shapes after each iteration of the pulse shaping algorithm for  $N = 14$  passes through the multipass setup. A rectangular control pulse shape was used with a control power of  $P_c = 170$  mW. The algorithm started with a rectangular probe pulse shape with a duration of  $\tau_p = 33$   $\mu$ s.

bandwidth is reduced. Therefore larger control Rabi frequencies, i.e. control powers, are required for compensation. Thus, with an increase of the optical depth the optimal combination of  $P_c \tau_c$  shifts towards larger values.

In the second step we varied the probe pulse shape, i.e. its temporal intensity profile, to optimize the spin wave  $S(z)$  for maximal light storage efficiency. We therefore applied the iterative pulse shaping algorithm developed and first implemented by Novikova *et al.* [87, 88] (see also Section 2.3.3). We conducted this iterative algorithm for a multipass setup with  $N = 14$ , starting with a rectangular probe pulse shape with duration of  $\tau_p = 33$   $\mu$ s, a probe power of  $P_p = 350$   $\mu$ W and a control power of  $P_c = 170$  mW, i.e. the optimal combination of  $P_c \tau_p$  for  $N = 14$ . The storage time was set to 2  $\mu$ s. During the pulse shaping algorithm the light storage efficiency is measured using method #1. In order to precisely determine the efficiency, each iteration is averaged about 50 times. The probe and signal pulse shapes are averaged 128 times and recorded with the oscilloscope.

Figure 4.7 shows the probe and signal pulse shapes after each iteration. The recorded signal pulse shape of the first iteration is time reversed and normalized with respect to the input probe energy. In addition, a frequency filtering is applied to suppress the fast oscillations in the beginning of the signal pulse. This new pulse is then used as the probe pulse of the second iteration. We note that these fast oscillations in the signal pulse could be due to residual diabatic couplings, generated by the fast switching (100 ns) of the control read pulse. We found that the oscillations are considerably suppressed if the control read pulse is switched on more slowly. Further investigations showed that the oscillation period scales with the inverse of the control read Rabi frequency  $\Omega_c$ . It is thus very likely that the control read pulse diabatically couples to a partially populated transition of the hyperfine levels of PrYSO driving Rabi oscillations, which are then mapped onto the signal pulse shape. After four iterations the algorithm converges to an optimal solution, with almost identical shapes of the probe and signal pulses. The

optimized probe pulse resembles a Gaussian-like shape, which is able to create the optimal spin wave during the storage process. The efficiency increases by 6 % from  $\eta_1 = (70.4 \pm 3.3) \%$  in the first iteration to  $\eta_4 = (76.3 \pm 3.5) \%$  after the fourth iteration.

#### 4.6.1 Maximum Light Storage Efficiency for Variable Optical Depths

In the previous section the optimization of the light storage efficiency in the multipass setup was described for a fixed number of probe passes  $N$ . Here, we repeat this optimization procedure for different number of passes  $N$  through the crystal. If we assume perfect overlap of all probe passes with the control beam, the optical depth  $d$  scales linearly with the number of passes  $N$ , i.e.  $d_N = d_0 N$ , with  $d_0$  the optical depth of the crystal in a single pass configuration. We can thus optimize the light storage efficiency for different optical depths.

Figure 4.8 shows the maximal achieved EIT light storage protocol efficiency  $\eta_{\text{EIT}}$  versus the number of passes  $N$ , i.e. the optical depth  $d_N$ , assuming the optical depth of a single pass to be  $d_0 = 6$ . We find that, up to  $N = 10$  passes, the maximal efficiency increases with increasing optical depth  $d_N$ . Our experimental data fits the theoretical limit of the storage efficiency for forward readout [82] very well. This indicates that our optimization procedure determined the almost optimal spin wave for the storage/retrieval process at given optical depth  $d$ . However, for passes  $N > 10$ , the efficiency does not increase any more. We assign this mainly to technical problems at larger numbers of passes. For  $N > 10$ , the probe beam profile deteriorates due to more than 20 relay imaging processes and passing through 14 optical interfaces with a total beam path length of more than 12 m. In addition, small vibrations lead to problems in the overlap of the control beam with the probe beam passes and propagation of the probe beam through the multipass setup. Also, the total transmission  $T_{\text{setup}}$  through the multipass setup reduces with an increasing number of passes  $N$ , due to losses at all optical components. This makes it rather difficult to detect the retrieved signal pulse for large numbers  $N$ .

We measured the total transmission  $T_{\text{setup}}$  for each number of passes  $N$  after aligning the probe passes and the control beam for optimal storage. The transmission reduces almost exponentially. However for  $N > 10$  it stays constant. This might be due to the fact that we are optimizing the beam alignment for a maximal EIT light storage protocol efficiency  $\eta_{\text{EIT}}$  and not for a optimal transmission through the multipass setup. With the transmission  $T_{\text{setup}}$  and the protocol efficiency  $\eta_{\text{EIT}}$  we can calculate an efficiency for the total setup  $\eta_{\text{setup}} = T_{\text{setup}} \eta_{\text{EIT}}$ , see also Figure 4.8. We find the largest setup efficiency  $\eta_{\text{setup}} = 25.2 \%$  for  $N = 2$ , i.e. in double pass configuration. We note that this results from the rather high transmission losses per pass of approximately 13 %. It was found that these high losses are mainly due to high reflections, i.e. of several %, of the PrYSO crystal surfaces at low temperatures. Optimized anti-reflection coatings could be used to further increase the setup efficiency.

With the multipass setup, we could increase the optical depth of our storage medium by a factor of 16 from the single pass  $d_1 = 6$  to  $d_{16} = 96$  for  $N = 16$  passes through the crystal. For  $N = 14$  passes, we achieved a maximal light storage



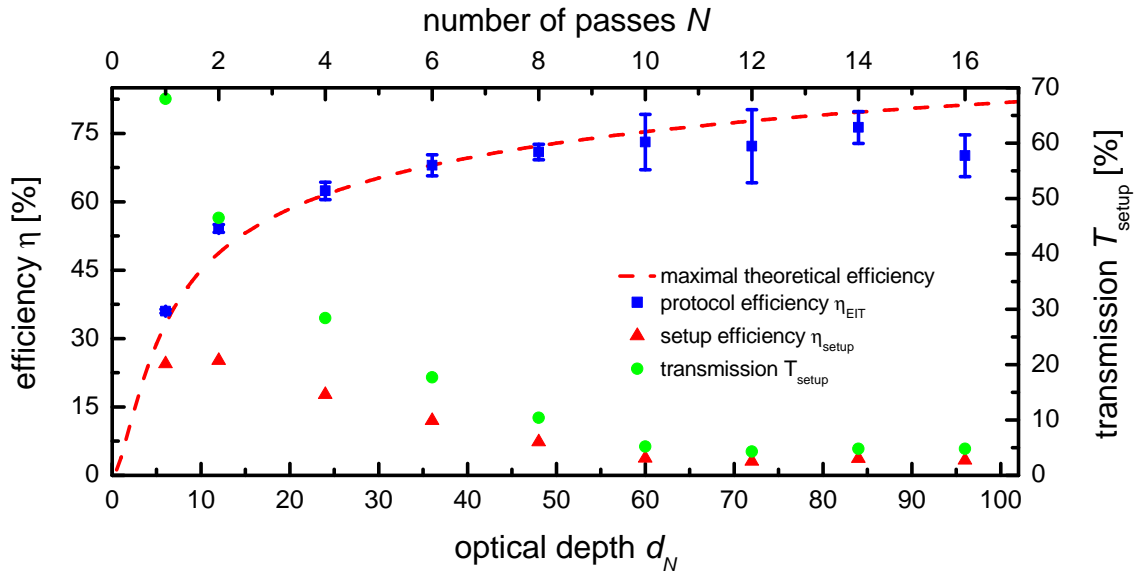


Figure 4.8: Maximal efficiency versus the number of probe passes  $N$  through the storage medium, i.e. the optical depth  $d_N$ . Depicted is the experimentally determined protocol efficiency  $\eta_{\text{EIT}}$ , the corresponding theoretical limit for forward readout by Gorshkov *et al.* [82] versus the optical depth  $d$ , the measured transmission through the multipass setup  $T_{\text{setup}}$  and the calculated setup efficiency  $\eta_{\text{setup}}$ .

efficiency  $\eta_{\text{EIT}}$  of  $(76.3 \pm 3.5)$  % in forward retrieval configuration. This is about 5 % higher than the best result for light storage in EIT forward configuration obtained in a cold atomic gas [89] and by far the largest ever obtained EIT light storage efficiency in a REIDS memory, setting a new benchmark for solid state quantum memories.

We note that in principle a backward readout configuration could yield even higher storage efficiencies, i.e. up to 90 % for an optical depth of 100. We saw in Section 2.3.3 that perfectly fulfilling the phase matching condition can become rather difficult in our PrYSO crystal with its non degenerate hyperfine states and a optical setup with small angles between probe and control beams. However, combining our multipass setup with the backward readout configuration is almost impossible. In the case of perfect phase matching for backward readout the signal pulse would leave the storage medium in a different direction compared to the input probe pulse, see also Figure 2.11 (general scheme). Thus, the generated signal pulse would not be able to propagate properly through the multipass setup.

Figure 2.11 (backward readout) depicts another possible, however non-perfect backward readout configuration. Here, the control read pulse is applied counter-propagating to the input probe pulse. For a multipass setup, as it is described here, this phase matching scheme can be fulfilled by coupling the control read pulse into the probe multipass setup. Note that this concept for backward readout is only possible in a mirrored multipass, in our case due to M2, compare with Figure 4.5. In this way the first half of the probe passes are stored with a propagation approximately in  $z$  direction, while the second half of the probe passes is stored propagating in the  $-z$  direction. Thus we find, with a control read pulse applied

in the direction of the input probe pulse through the multipass setup, for all individual probe passes stored, a counter-propagating configuration, i.e. a backward readout scheme. From the phase matching condition we find, that the generated signal pulse leaves the storage medium counter-propagating to the control write pulse, without a propagation through the multipass setup. However, the individual parts of the signal pulse are read out almost simultaneously, as the control read pulse propagates through the multipass with the vacuum speed of light. We thus can measure a signal pulse which is compressed compared to the stored probe pulse. However, as the individual parts of the stored probe pulse feature different relative phases with respect to each other, the individual parts of the signal pulse do not necessarily interfere constructively, which limits the readout efficiency.

## 4.7 Conclusion

We presented systematic measurements of the EIT light storage efficiency in a PrYSO crystal. In particular, we optimized the storage efficiency by systematic variations of the control power, i.e. the control Rabi frequency and the probe pulse duration. We further optimized the probe pulse shape using an iterative algorithm to prepare an optimal spin wave in the PrYSO crystal during storage. Due to this optimization we achieved a protocol efficiency  $\eta_{\text{EIT}}$  of about 36 %, which is close to the maximal efficiency predicted from theory for the given optical depth  $d$  of 6 of our PrYSO crystal. We discussed different ideas to increase the optical depth of the storage medium. We followed the concept of a ring-like multipass setup for the probe pulse, which permits simple variation of the number of passes of the probe pulse through the crystal. We could achieve up to 16 passes, which lead to an increase of the effective optical depth  $d_N$  from 6 to 96. We performed systematic optimizations of the EIT light storage efficiency for different number of passes  $N$ , i.e. different optical depths, through the crystal. At  $N = 14$  we achieved a storage efficiency in forward readout of  $\eta_{\text{EIT}} = (76.3 \pm 3.5) \%$ . This is about 5 % higher than the previously highest EIT storage efficiency in forward readout conducted in cold atoms [89] and by far the highest EIT storage efficiency ever obtained in a solid state medium [23].

## Chapter 5

# Rephasing of Atomic Coherences by Composite/Adiabatic Techniques

In Chapter 4 we discussed the storage of optical information as coherent atomic superpositions driven by EIT-based light storage. The efficiency of the storage protocol was optimized, and storage efficiencies of up to 76 % were achieved. However, the storage durations in these experiments was rather short, i.e. only  $2 \mu\text{s}$ , to minimize storage medium related reductions of the efficiency.

In inhomogeneously broadened media, such as PrYSO, collective atomic coherences usually suffer from losses due to dephasing and decoherence effects, see Chapter 1. The inhomogeneous broadening leads to a different time evolution of individual coherence phases, resulting in a destructive interference upon readout, and thus to reduced readout signals already after a few  $\mu\text{s}$ . We call this effect dephasing. As long as the coherence phase evolution is deterministic, i.e. no random phase changes occur during the time evolution, dephasing is a fully reversible effect. The phase evolution can be inverted by the application of a  $\pi$ -pulse. This leads to a rephasing of individual coherences. This rephasing technique by a single  $\pi$ -pulse is well known as Hahn spin echo [108]. However, we already saw in Section 2.1.1, that the inversion efficiency of a  $\pi$ -pulse critically depends on a correct choice of the effective pulse area, which makes it inefficient in inhomogeneous systems with Rabi frequency and detuning variations, and sensitive to errors and fluctuations in experimental parameters.

In this Chapter we will present composite and adiabatic techniques which feature an enhanced robustness with respect to system inhomogeneities and fluctuations in experimental parameters. In NMR, composite pulses (CP) are used for decades as a well established technique for compensation of different type of pulse errors and system inhomogeneities [72, 74, 109]. Since recently CP became of interest to the field of quantum information processing and quantum optics [31, 110–115] for precise and robust qubit rotations. However, most CP are derived to compensate one, at most two specific types of errors at a time, while most systems and setups suffer from a collection of different type of errors. Here we will present universal composite pulses (UCP), which simultaneously compensate any type of systematic error. We apply these UCP for rephasing of atomic coherences prepared by the EIT-LS protocol.

Beyond CP techniques, also adiabatic passage (AP) techniques for robust population manipulation and rephasing of coherent superpositions are frequently used in NMR [116–118]. Such AP techniques recently became of interest to the quantum optics community. A very basic AP technique known as rapid adiabatic pas-

sage (RAP) has been investigated for total population inversion [119, 120] and for rephasing of atomic coherences [121–124]. However, in most cases AP techniques require a very long interaction time and strong couplings to fulfill the adiabaticity criteria and to achieve a satisfying, mostly still incomplete population inversion, thus a ultra-high fidelity cannot easily be achieved. Recently, a composite RAP technique has been proposed, composite adiabatic passage (CAP) [25], which overcomes the problems arising from weakly fulfilled adiabaticity. We present an experimental realization of CAP, applied for rephasing of atomic coherences prepared by EIT-LS in PrYSO. We compare RAP and CAP in a situation of weak adiabaticity. We further demonstrate the advanced robustness of CAP with respect to variations of experimental parameters.

Another approach to overcome the long interaction times of AP techniques, while keeping the adiabaticity criteria sufficiently fulfilled, is based on shortcuts to adiabaticity [125, 126]. This technique still drives a system in an adiabatic way, while minimizing the adiabatic path length to the desired state. This enables operation, e.g. with shorter interaction times. One version of shortcuts to adiabaticity are single-shot shaped pulses (SSSP) [26, 127]. We show a first experimental demonstration of SSSP for rephasing of RF-induced coherences in PrYSO and analyze their performance with respect to variations of experimental parameters.

## 5.1 Introduction to Rephasing of Atomic Coherences

This section gives a general introduction on dephasing and rephasing of atomic coherences in an inhomogeneously broadened medium, and shows a comparison of the properties of RF-induced and EIT-LS coherences stored in PrYSO. First the preparation of RF-prepared atomic coherences is described. Afterwards the dephasing behavior of RF and EIT-LS coherences are investigated. Diabatic rephasing experiments are discussed, and pulse phase dependencies are examined.

### 5.1.1 Generation and Detection of an RF-induced Coherence

In Chapter 4 we discussed the storage of atomic coherences using the EIT-LS protocol. Alternatively to the preparation of atomic coherences by two optical pulses, it is also possible to drive a hyperfine coherence in PrYSO directly by a single RF-pulse resonant to the hyperfine transition. This is experimentally easier to implement and allows further investigations on the coherence properties in PrYSO and the performance of RF rephasing pulses. In the following we discuss the generation of RF-induced coherences in PrYSO. In order to generate RF-induced coherences we apply an RF- $\pi/2$ -pulse, resonant between two hyperfine states of the ground state  $^3\text{H}_4$  of PrYSO, preparing a maximal coherent superposition. Before the generation of such a coherence the storage medium has to be prepared by optical pumping, as described in Section 4.1. We prepare a spectral pit using the control beam path. Here the smaller of two control beam diameters is used, compare with Chapter 3. The frequency is chirped across a relative frequency range of 0 – 17.9 MHz during 20 ms with a constant power of 1 mW for six times. Af-

terwards an RF- $\pi/2$ -pulse with a angular frequency of  $\omega = 2\pi \cdot 10.2$  MHz, almost resonant to the transition between the ground state  $^3\text{H}_4$  hyperfine levels  $|\pm 1/2\rangle$  and  $|\pm 3/2\rangle$ , is applied. An appropriate choice of Rabi frequency and pulse duration is made to achieve an approximate  $\pi/2$ -pulse. Note that a perfect RF- $\pi/2$ -pulse can not be achieved for all ensembles of the inhomogeneously broadened hyperfine transition due to pulse area errors caused by static detunings  $\Delta_\epsilon$  of the ensembles. This pulse creates a RF-induced coherence on the inhomogeneously broadened hyperfine transition. In principle the RF- $\pi/2$ -pulse acts on all ensembles of the inhomogeneous broadening of the optical transition. In order to detect the RF coherence after a storage time  $\Delta T$  we use the Raman heterodyne detection scheme as introduced in Sections 2.4, and 3.5. The optical detection pulse of a constant relative frequency of 3.2 MHz and a power of 6.6 mW selects a part the optical inhomogeneous line, still coupling all nine possible transitions within different ensembles of the inhomogeneous broadening, compare with Section 4.1. However, due to the demodulation of the lock-in amplifier, with a demodulation frequency of  $\sim 10.2$  MHz, a signal proportional only to the coherence between states  $|\pm 1/2\rangle$  and  $|\pm 3/2\rangle$  is detected. Possible signals from other transitions are filtered by the lock-in amplifier.

### 5.1.2 Atomic Coherences in Inhomogeneous Broadened Transitions

As introduced in Chapter 2, coherences in an inhomogeneous broadened transition exhibit different phase evolutions in time, see Equation 2.10. This leads to a reduction of the collective coherence signal due to destructive interference of the individual coherences, called dephasing. We measured the reduction of the retrieved signal depending on the total storage time  $\Delta T$  for a coherence created by an RF- $\pi/2$ -pulse, and by the EIT-LS protocol.

The RF coherences were created by RF pulses with adjusted pulse areas to optimally match the condition  $\Omega\tau = \pi/2$ , for Rabi frequencies larger than the inhomogeneous broadening, to cover the full bandwidth of the transition. The storage medium was prepared and the RF coherences detected, as described in Section 5.1.1. In order to store a EIT-LS coherence the PrYSO storage medium was prepared by optical pumping in a three-state  $\Lambda$ -system, as shown in Section 4.1. However, here only a single  $\Lambda$ -system was prepared by choosing a slightly different repump frequency (24.7 MHz). Afterwards, the EIT-LS protocol was applied, generating a coherence between the hyperfine levels  $|\pm 1/2\rangle$  and  $|\pm 3/2\rangle$  of the ground state  $^3\text{H}_4$  of PrYSO.

Figure 5.1 depicts the retrieved, integrated signal  $S$  versus the total storage time  $\Delta T$ , for a coherence prepared by a weak RF- $\pi/2$ -pulse (black solid squares:  $\Omega = 2\pi \cdot 50$  kHz), a strong RF- $\pi/2$ -pulse (black open squares:  $\Omega = 2\pi \cdot 250$  kHz), and for a coherence created by the EIT-LS protocol (red solid dots). In all cases the integrated signal  $S$  decays with increasing total storage time  $\Delta T$  due to dephasing of the collective coherence. Both RF-prepared coherences show a identical decay behavior. We thus can be sure that already the weak  $\pi/2$ -pulse, with a Rabi frequency of  $\Omega = 2\pi \cdot 50$  kHz, is able to cover most of the inhomogeneous broadening of the transition. Comparing RF and EIT-based coherences, we find that the EIT-

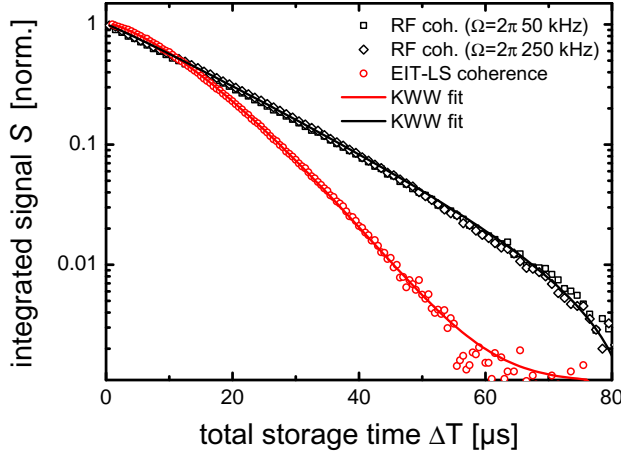


Figure 5.1: Retrieved, integrated signal  $S$  versus total storage time  $\Delta T$  for coherences created by a weak RF- $\pi/2$ -pulse (black solid squares:  $\tau = 5 \mu\text{s}$ ;  $\Omega = 2\pi \cdot 50 \text{ kHz}$ ), a strong RF- $\pi/2$ -pulse (black open squares:  $\tau = 1 \mu\text{s}$ ;  $\Omega = 2\pi \cdot 250 \text{ kHz}$ ) and by the EIT-LS protocol (red solid dots). Solid lines represent best fit results by Kohlrausch-William-Watts (KWW) functions.

LS coherence shows a similar behavior for short total storage times. However, at storage times larger  $\Delta T = 20 \mu\text{s}$  the EIT-LS coherence decays faster than the RF coherence. A stretched exponential function, called Kohlrausch-William-Watts (KWW) function, [128, 129] of the form

$$S(t) = S_0 \cdot e^{-(t/T_{deph})^\beta} \quad (5.1)$$

is fitted to the experimental data. Here  $\beta$  is a stretching exponent. With  $\beta = 1$ , we get the usual exponential function, for  $0 < \beta < 1$  the exponential function is stretched, while for  $\beta > 1$  the exponential function is compressed.

In the case of RF coherences we find the expected single exponential decay with  $\beta = 1.03 \pm 0.004$  and  $T_{deph} = (16.9 \pm 0.05) \mu\text{s}$ . From the dephasing time we calculate the inhomogeneous broadening to  $\Gamma_{inhom} \approx 18 \text{ kHz}$  (FWHM), in the absence of spectral diffusion. The signal from the EIT-LS coherence dephases faster in a compressed exponential form, with  $T_{deph} = (15 \pm 0.02) \mu\text{s}$  and  $\beta = 1.4 \pm 0.004$ . This faster non-exponential decay might be attributed to spectral diffusion in the optical transition, i.e. frequency shifts of the excited state hyperfine levels in PrYSO due to magnetic dipole-dipole interactions during the storage time [130], see also Section 1.3 and Section 2.3.4. Thus, a complete readout of the coherence by a control read pulse is no longer possible, as some of the ensembles in which a coherence had been stored can no longer be addressed by the readout pulse. We note that this effect does not play a role in the case of an RF coherence, as here coherences are usually created in a broad frequency range inside the inhomogeneous optical transition. Spectral diffusion in the optical transition occurs, like in the EIT-LS coherence case, however it does not affect the retrieved signal from the RF coherence. We conclude, that the two techniques preparing atomic coherent superpositions result in a different dephasing dependence. In the future this might be useful to get a broader insight into the dynamics of the PrYSO crystal.

### 5.1.3 Diabatic Rephasing of Atomic Coherences

The most common way to deal with the effect of a reduction of the collective macroscopic coherence signal due to dephasing is the application of resonant rectangular diabatic rephasing pulses. In the simplest case, this can be achieved by



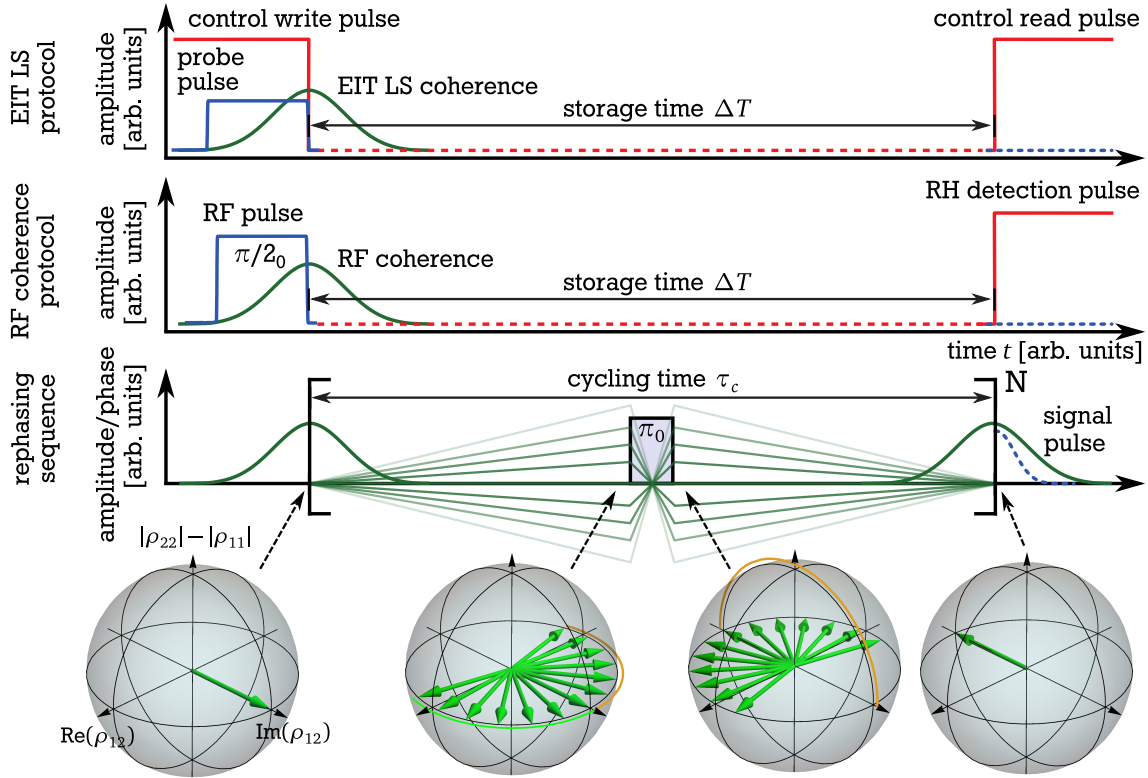


Figure 5.2: Pulse sequences for the preparation of atomic coherences by the EIT-LS protocol or by an RF- $\pi/2$ -pulse in an inhomogeneous broadened transition. Here the dephasing and rephasing process by a single  $\pi$ -pulse during a cycle time  $\tau_c$  is depicted. In general this process can be repeated, leading to a total storage time given by  $\Delta T = N\tau_c$ . The Bloch representation shows the evolution of a collective coherence prepared by an RF- $\pi/2_0$ -pulse, which is rephased by an RF- $\pi_0$ -pulse. We will see that this representation only holds true for RF-induced coherences.

a single rectangular pulse with a pulse area  $\pi$ , applied symmetric during a storage time  $\Delta T$ , i.e. the so called Hahn spin echo (HSE) sequence [108] known from NMR. Figure 5.2 depicts the general timing sequence of the dephasing and rephasing process. The initial coherence can either be prepared by the EIT-based light storage protocol (top row), or by an RF- $\pi/2$ -pulse (center row). After the preparation the collective macroscopic coherence starts to dephase, because of different phase factors  $\exp(i\Delta_\epsilon t)$  of the individual coherences  $\rho_{12}^\epsilon$ , compare with Equation 2.10. These individual phase evolutions are depicted in Figure 5.2 (bottom row) and on the Bloch sphere. The Bloch vectors correspond to a coherence preparation with an RF- $\pi/2_0$ -pulse, i.e. with a driving phase  $\phi = 0^\circ$ , driving the Bloch vectors into the  $\text{Im}(\rho_{12})$ -axis of the Bloch sphere, i.e. the phase of the coherence  $\gamma = \phi + 90^\circ$ . Note that in contrast, to the RF-prepared coherence, the collective coherence prepared by the EIT-LS protocol is not a maximal coherent superposition state, i.e.  $\rho_{11} = \rho_{22} = 1/2$ , but rather  $\rho_{11} \gg \rho_{22}$ , and we will see that a phase  $\gamma$  of the coherence after the preparation can not easily be defined.

If  $\Delta T \gg T_{deph}$  no collective macroscopic coherence can be detected, because of complete destructive interference between the individual coherences. During the

dephasing, the Bloch vectors, each representing a individual coherence  $\rho_{12}^e$ , fan out on the Bloch sphere, due to their different transition frequencies with respect to the rotating frame of the Bloch sphere. After a time of free evolution, a  $\pi_0$ -pulse is applied, centered at  $\tau_c/2$ , rotating the Bloch vectors around their individual torque vectors (not depicted here), pointing approximately into the direction of the  $\text{Re}(\rho_{12})$ -axis. Note that for weak Rabi frequencies or far detuned coherences the torque vector can possess a non negligible component in the population axis of the Bloch sphere, which lead to a non perfect  $\pi$ -rotation, compare with Section 2.1.1. However, Figure 5.2 depicts the case of a strong driving. Due to the  $\pi_0$ -pulse the Bloch vectors are rotated by  $180^\circ$  around their torque vector axis. After the pulse, the free evolution continues and the coherences begin to rephase. After a cycling time  $\tau_c$ , all Bloch vectors point into the  $-\text{Im}(\rho_{12})$ -axis, sharing the same instantaneous phase, and hence can interfere constructively, with a total phase shift of  $180^\circ$  compared to the initial coherence. Note, that the total phase shift of the rephased coherence can be controlled by the phase  $\phi$  of the rephasing pulse. For example a  $\pi_{90}$ -pulse would invert the Bloch vectors with a rotation around the  $\text{Im}(\rho_{12})$ -axis. Thus, the collective coherence would not experience a phase shift compared to the initial coherence. In Figure 5.2 the rephasing process due to a single  $\pi$ -pulse is shown. In general a number of rephasing cycles  $N$  with cycling times  $\tau_c$ , can be applied during the storage time  $\Delta T$ , with  $\Delta T = N\tau_c$ . We find for  $N = 1$  the Hahn spin echo (HSE) [108]. Pulse trains with  $N \geq 2$  rephasing cycles are also known as Carr-Purcell or Carr-Purcell-Meiboom-Gill (CPMG) sequences [131,132]. In general the CPMG sequence is applied with a phase shift of  $90^\circ$  compared to the initial  $\pi/2$ -pulse. After the rephasing sequence, i.e. after a storage time  $\Delta T \equiv N\tau_c$ , the collective coherence is detected either by a control read pulse to generate a signal pulse from the EIT-LS coherence, or by a RH detection pulse to measure the RF-prepared coherence.

#### 5.1.4 Rephasing Efficiency of Imperfect $\pi$ -Pulses

The best choice for rephasing are obviously perfect  $\pi$ -pulses without any pulse errors. However, in reality the rephasing process suffers from errors of the applied pulses. These pulse errors become especially apparent if the rephasing efficiency is investigated with respect to the phase  $\gamma$  of the prepared coherence, i.e. the phase  $\phi$  of the initial  $\pi/2$ -pulse with  $\gamma = \phi + 90^\circ$  and the phases  $\phi$  of the applied rephasing pulses. Thus, we measured the dependence of the rephasing efficiency, i.e. the retrieved integrated signal, versus the phase  $\phi$  of the initial  $\pi/2$ -pulse and the rephasing pulses. We performed measurements for RF coherences (see Section 5.1.1 for details on the preparation) and EIT-LS coherences (prepared as described in Section 5.1.2). Figure 5.3 (top row) depicts the experimental results for RF coherences (left) and EIT-LS coherences (right). Both graphs show the retrieved integrated signal after a total storage time of  $600 \mu\text{s}$  versus a pulse phase  $\phi$ . The varied pulse phases  $\phi$  and the applied rephasing sequences are indicated in the figure labels. The rephasing sequences are applied such that  $N\tau_c = 600 \mu\text{s} = \text{const}$ . The  $\pi$ -pulse duration is  $\tau = 3.2 \mu\text{s}$ , corresponding to a Rabi frequency of  $\Omega = 2\pi \cdot 156 \text{ kHz}$ .



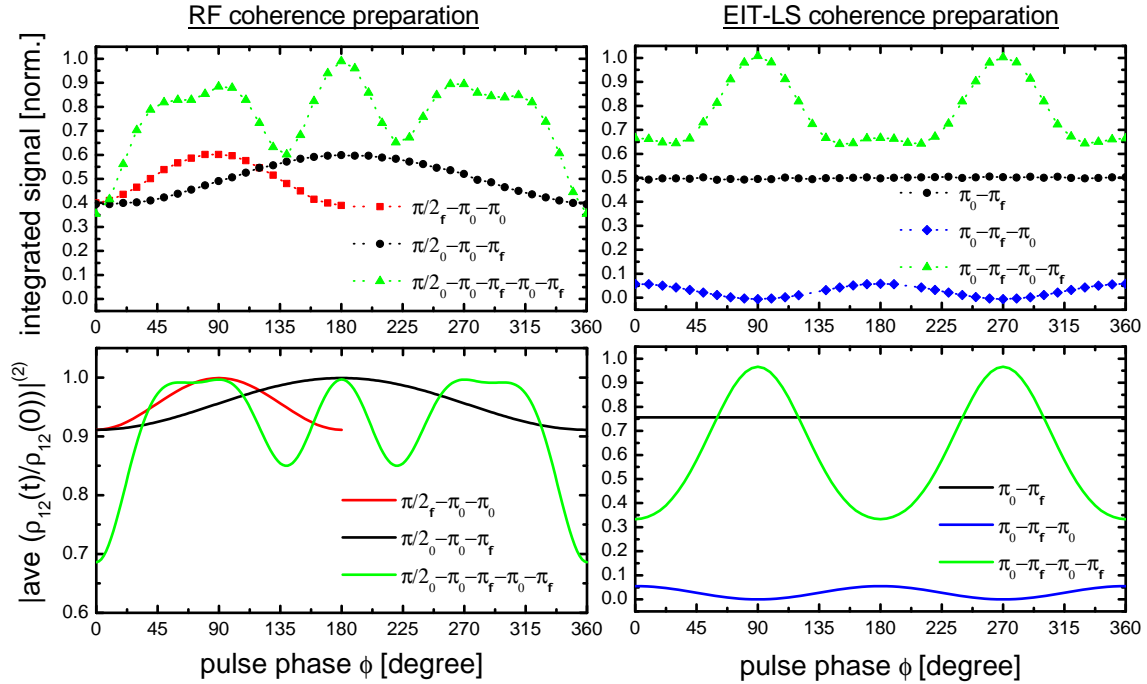


Figure 5.3: Experimental data (top row) of the retrieved integrated signal versus the pulse phase  $\phi$  for a RF coherence (left) and a EIT-LS coherence (right) for different rephasing sequences (see labels in graph). (bottom row) Corresponding simulations modeling the phase behavior of the rephasing experiments. (left) A collective initial coherence  $\rho_{12}(0)$  with a defined initial phase  $\gamma$  is assumed. (right) The collective initial coherence features a equal distribution of phases, i.e.  $\gamma \in \{0 : 2\pi\}$ .

In a first measurements we changed the phase of the initial RF- $\pi/2$ -pulse (red solid squares) preparing an RF coherence which is rephased by a  $\pi_0 - \pi_0$  sequence, see Figure 5.3 (top left). We find the largest signal for  $\phi = 90^\circ$ , i.e.  $\gamma = 180^\circ$ , which corresponds to the application of the rephasing pulses along the axis of the prepared coherence, i.e. the CPMG sequence [132]. In this configuration we retrieve the largest signal because the pulse area errors of the first rephasing pulse can be compensated by the second rephasing pulse [132]. On the other hand for  $\phi = 0^\circ$  and  $\phi = 180^\circ$  the pulse area errors of the two rephasing pulses add up, compare with the Bloch spheres in Figure 5.2. The same holds true for the  $\pi/2_0 - \pi_0 - \pi_\phi$  sequence (black solid dots). Pulse errors are compensated if the second rephasing pulse is  $\pi_{180}$ , i.e. when the rotation direction of the Bloch vectors is reversed by the second rephasing pulse. In the case of four rephasing pulses applied (green solid triangles) we find a more complex dependence of the rephasing efficiency with respect to the phase  $\phi$ . Still the largest signal is detected if  $\phi = 180^\circ$ . We conclude that in the case of imperfect pulses applied for rephasing of RF coherences in a inhomogeneously broadened transition it is favorable to apply phase shifted rephasing pulses. In this way for some specific phases the pulse errors can cancel themselves.

In a second experiment, we repeated these phase investigations for a coherence prepared by the EIT-LS protocol, see Figure 5.3 (top right). A quite different phase dependent rephasing efficiency, compared with the case of a RF-prepared

coherence, was determined. We found no phase dependent rephasing efficiency for a two pulse rephasing sequence (black solid dots). In case of the four pulse rephasing sequence we found largest signal for  $\phi = 90^\circ$  and  $\phi = 180^\circ$ . For a three pulse rephasing (solid blue diamonds) almost no signal could be detected and also for a single pulse rephasing sequence (HSE) (not depicted here) no signal could be retrieved, although in both cases the individual coherences should be in phase after the rephasing sequences. We can explain this behavior by the special properties a coherence prepared by the EIT-LS protocol. During the adiabatic storage only a rather weak coherence is prepared. Thus, most of the population is still in state  $|1\rangle$  after the EIT-LS protocol, As expected a odd number of rephasing pulses will result in a inverted population distribution, compared to the initial situation. Thus, the optical control read pulse is applied on a populated transition leading to improper EIT conditions and a inefficient readout of the coherence (compare with Section 2.3). In the spin wave picture a odd number of rephasing pulses lead to a inversion of the spin wave phase, i.e. an inversion of the wave vector  $\vec{\kappa}$  of the spin wave, compare with the phase matching in Section 2.3.3. Hence, the phase matching condition can not be fulfilled in the standard forward readout configuration. We thus find that a rephasing of EIT-LS coherences is only possible if a even number of rephasing pulses are applied.

In order to investigate the different phase behavior of EIT-LS and RF coherence we performed extensive simulations of the rephasing process. We assumed a perfect collective initial coherence created by a  $\pi/2_\phi$ -pulse, i.e.  $\rho_{12}(0) = \sum_\epsilon \rho_{12} \exp(-i(\Delta_\epsilon t + \gamma))$  with  $\gamma = \phi + 90^\circ$ . We let the collective coherence completely dephase before the rephasing process. We thus calculate the rephased collective coherence at the rephasing time  $t_f$  by  $\rho_{12}(t_f) = \hat{U} \rho_{12}(0) \hat{U}^\dagger$  with the propagator  $\hat{U}(\epsilon, \phi)$ , depending on the individual coherence parameter  $\epsilon$  and the phase  $\phi$  of the rephasing pulse. Here  $\hat{U}(\epsilon, \phi)$  describes the dephasing, the application of the rephasing pulse and the rephasing process. We average over a constant distribution of detunings with a range of  $\Delta_\epsilon = -0.26\Omega \dots 0.26\Omega$ , with a Rabi frequency  $\Omega = 2\pi \cdot 156$  kHz. Thus, we can calculate the average coherence  $\overline{\rho_{12}(t_f)}$  depending on the phase  $\phi$  of the pulses. The results are depicted in Figure 5.3 (bottom left). Although this simulation strongly simplifies the actual experiment conducted, we find a remarkably good agreement of the overall phase dependence with the experimental data for rephasing of an RF coherence.

We also tried to model the experimental results obtained with a EIT-LS coherence. We found the experimental data to be modeled best, if we assume a initial collective coherence featuring a equal distribution of all possible initial phases  $\gamma$ , i.e.  $\rho_{12}(0) = \sum_{\gamma=0}^{2\pi} \sum_\epsilon \rho_{12} \exp(-i(\Delta_\epsilon t + \gamma))$ , and calculate  $\overline{\rho_{12}(t_f)^2}$ . The results are depicted in Figure 5.3 (bottom right), modeling the experimental data (top right) in a proper way. This way of modeling confirms the statements of Section 2.3.3, in which we found that the generated spin wave  $S(z)$  exhibits a position  $z$  dependent phase factor  $\exp(-i\kappa z)$ , if the probe and control field have different frequencies or are applied with a slight angle between them. Thus, the initial collective coherence phase  $\gamma$  depends on the position  $z$  inside the PrYSO crystal. These properties of EIT-LS coherences will be of relevance when dynamic decoherence control (DDC) techniques are applied to preserve atomic coherences, see Chapter 6.

## 5.2 Universal Composite Pulses

The development of high fidelity state manipulations is an important challenge towards reliable quantum information processing [31, 110–115]. However, even most simple state manipulations, like a high fidelity total population transfer, can be rather difficult to achieve under real experimental conditions including inhomogeneities. Most techniques provide either high population transfer efficiency, i.e. inversion efficiency, or robustness against variations of experimental parameters. We saw in Chapter 2, that diabatic resonant techniques can provide perfect inversion efficiency in an ideal two-state system. However, these techniques are very sensitive to variations in pulse parameters and usually suffer due to experimental inhomogeneities, compare with Section 5.1.4. On the other hand, adiabatic techniques [119, 122, 123], can be robust with respect to inhomogeneities and systematic pulse errors, but in most cases a very long interaction time and strong interactions are needed to fulfill the adiabaticity criteria in order to achieve a satisfying, mostly still incomplete transfer efficiency.

The technique of composite pulses (CP) is unique in combining the advantages of diabatic resonant techniques, i.e. high fidelity, and adiabatic techniques, i.e. robustness to inhomogeneities and pulse errors. However, the existing CP compensate one, at most two types of errors at a time and are usually designed for rectangular temporal pulse shapes. In the following section we describe an advanced technique based on CP for complete state inversion, which compensates systematic deviations in any experimental parameter, works for any system environment and with any temporal pulse shape. The only assumptions made are those of a two-state system, coherent evolution and identical pulse areas and shapes of the individual pulse elements of these universal composite pulses (UCP) [24].

The section is structured as follows: First, we derive the UCP by using a novel theoretical approach. Second, we apply them for rephasing of atomic coherences created by the EIT-based light storage protocol. Then we demonstrate the efficiency and universality of these universal composite pulses and show their robustness with respect to variations of pulse area, static detuning, pulse shape and additional chirps. In all cases we compare the performance of UCP with standard diabatic  $\pi$ -pulses.

### 5.2.1 Theory of Universal Composite Pulses

We assume a coherently driven two-state system as introduced in Section 2.1. However, we write the RWA Hamilton operator in interaction representation,

$$\hat{H}_{\text{RWA}}(t) = \frac{\hbar}{2} \begin{pmatrix} 0 & \Omega(t)e^{-i\delta(t)} \\ \Omega^*(t)e^{-i\delta(t)} & 0 \end{pmatrix} \quad (5.2)$$

where the time dependent detuning  $\Delta(t)$  is expressed through the phase  $\delta(t) = \int_0^t \Delta(t')dt'$ . We further assume the interaction to be much shorter than relaxation and decoherence processes in the system. The time evolution of the system is described by the propagator  $\hat{U}$ . It connects the probability amplitudes

$c(t)$  at initial and final time of the interaction,  $t_i$  and  $t_f$ . Thus, we can write:  $c(t_f) = \hat{U}(t_f, t_i)c(t_i)$ . The general propagator  $\hat{U}$  is parametrized with three real Stückelberg variables  $q(0 \leq q \leq 1)$ ,  $\alpha$ , and  $\beta$ ,

$$\hat{U} = \begin{pmatrix} qe^{i\alpha} & pe^{i\beta} \\ -pe^{-i\beta} & qe^{-i\alpha} \end{pmatrix}. \quad (5.3)$$

Here,  $p = \sqrt{1 - q^2}$ , where  $p^2$  is the single pulse transition probability from state  $|1\rangle$  to  $|2\rangle$ , and the probability for no transition is  $q^2$ . We construct the propagator of a composite pulse sequence of  $n$  pulses as

$$\hat{U}^{(n)} = \hat{U}(\phi_n) \dots \hat{U}(\phi_2) \hat{U}(\phi_1), \quad (5.4)$$

where the phases  $\phi_k$  describe constant phase shifts of the Rabi frequency,  $\Omega(t) \rightarrow \Omega(t)e^{i\phi_k}$ . This phase shift is imprinted in the propagator  $\hat{U}(\phi)$  by taking  $\beta \rightarrow \beta + \phi$ . The only assumption is that the constituent pulses of the composite pulse sequence are identical, and the only control parameters are their relative phases  $\phi_k$ . All other properties of the driving pulses are unknown, which means that the constituent pulses can have any arbitrary time dependence of their pulse parameters, such as Rabi frequency, detuning from the resonance and duration. Thus, the design of the UCP aims at universal robustness with respect to deviations in any pulse parameter, with the goal to transfer all population from state  $|1\rangle$  to state  $|2\rangle$  [24]. A total transfer is achieved if the transition probability is maximized, i.e. if  $P^{(n)} \equiv |\hat{U}_{21}^{(n)}|^2 = 1$ , for any values of  $q$ ,  $\alpha$ ,  $\beta$ . This is the case if  $Q^{(n)} \equiv |\hat{U}_{11}^{(n)}|^2$  is minimized, i.e.  $Q^{(n)} = 0$ . The propagator element  $\hat{U}_{11}^{(n)}$  is calculated to determine the phases  $\phi_k$  of a UCP sequence of  $n$  pulses.  $\hat{U}_{11}^{(n)} = \sum_{j=1}^n a_{nj}q^j$ , where  $a_{nj}$  only depends on  $\alpha$  and  $\phi_k$ . The phases  $\phi_k$  are then chosen such that  $a_{nj}$  is nullified for any  $\alpha$  up to a highest possible order. In the case of symmetric UCP, i.e.  $\phi_{n+1-k} = \phi_k$  with  $k = 1, 2, \dots, (n-1)/2$ ,  $a_{nj}$  automatically nullifies for even  $j$ . For a UCP sequence of  $n = 5$  pulses with phases  $(0, \phi_2, \phi_3, \phi_2, 0)$  the propagator is given by

$$\hat{U}_{11}^{(5)} = [(1 + 2 \cos(2\phi_2 - \phi_3))e^{i\alpha} + 2 \cos(\phi_2 - \phi_3)e^{-i\alpha}]q + O(q^3). \quad (5.5)$$

Here the first term vanishes for two different sets of phases:  $(\phi_2 = 5\pi/6, \phi_3 = \pi/3)$  and  $(\phi_2 = 11\pi/6, \phi_3 = \pi/3)$ . This leads to a maximal transition probability of  $P^{(5)} = 1 - |\hat{U}_{11}^{(5)}|^2 = 1 - O(q^6)$ . In Table 5.1, we show the phases of UCP sequences with up to  $n = 9$  pulses. Even though UCP were originally designed for a total population transfer in a single two-state system, they can in principle be used for the inversion of any initial quantum state. In the following we apply UCP for rephasing of atomic coherences in PrYSO.

## 5.2.2 Experimental Results on Universal Composite Pulses

We experimentally investigate the performance of universal composite pulse (UCP) sequences by rephasing of atomic coherences created with the EIT-based

Table 5.1: Phases of UCP with up to  $n = 9$  pulses in the sequence. The phases of higher order UCP can be found in [24]. UCP labeled with “a” perform slightly better against variations in the pulse area, in contrast UCP labeled with “b” perform slightly better against variations in static detuning.

UCP sequence	Phases $\phi$
U3	$(0, 1, 0)\pi/2$
U5a	$(0, 5, 2, 5, 0)\pi/6$
U5b	$(0, 11, 2, 11, 0)\pi/6$
U7a	$(0, 11, 10, 17, 10, 11, 0)\pi/12$
U7b	$(0, 23, 10, 5, 10, 23, 0)\pi/12$
U9a	$(0, 0.635, 1.35, 0.553, 0.297, 0.553, 1.35, 0.635, 0)\pi$
U9b	$(0, 1.635, 1.35, 1.553, 0.297, 1.553, 1.35, 1.635, 0)\pi$

light storage protocol. The experimental setup is used with the flat-top probe beam profile and with the coil system #1, as described in Chapter 3. The PrYSO storage medium is prepared by optical pumping in a three-state  $\Lambda$ -system, as shown in Section 4.1. However, here the repump frequency is chosen slightly different, to be 24.7 MHz. In this way only a single ensemble of the inhomogeneous broadening of PrYSO is prepared for EIT. Next, we apply the EIT-LS protocol, and a atomic coherent superposition is generated between state  $|1\rangle$  and state  $|3\rangle$ , i.e. between the ground state hyperfine levels  $|\pm 1/2\rangle$  and  $|\pm 3/2\rangle$  of PrYSO. This collective coherence suffers from dephasing due to the inhomogeneous broadening of the hyperfine transition, compare with Section 5.1.2. Thus, rephasing by radio frequency pulses is needed to retrieve a signal pulse after storage times  $\Delta T$  larger than the dephasing time  $T_{deph}$ . Here, we set the total storage  $\Delta T = 600 \mu s$ . During this storage time two RF rephasing cycles are necessary to rephase a coherence generated by the EIT-LS protocol, see Section 5.1. We apply them in a symmetric configuration, centered at  $150 \mu s$ , and  $450 \mu s$ , as defined for CPMG [132]. In order to investigate the performance of UCP, and to compare with other diabatic rephasing techniques, we keep all parameters of the optical EIT-LS protocol fixed and vary only the RF rephasing sequences. Hence, the retrieved light storage signal pulse is a direct measure for the efficiency  $\eta_{reph}$  of the applied rephasing sequence.

Figure 5.4 depicts the rephasing efficiency  $\eta_{reph}$  versus the single pulse duration  $\tau$  and the static detuning  $\Delta$  for different diabatic rephasing sequences of a rectangular pulse shape. Note, that the total duration of the rephasing sequence is given by the number of constituent pulses  $n$  of the applied sequence times the single pulse duration  $\tau$ , and  $\Delta$  is the static detuning from the hyperfine transition  $|\pm 1/2\rangle$  and  $|\pm 3/2\rangle$  with its (angular) transition frequency of  $\omega = 2\pi \cdot 10.2$  MHz. The Rabi frequency is fixed for all constituent pulses at  $\Omega \approx 2\pi \cdot 156$  kHz. The experimentally determined rephasing efficiency (top row), and corresponding simulations (bottom row) are shown for a single rectangular diabatic pulse, i.e. a  $\pi$ -pulse if the appropriate single pulse duration  $\tau$  is chosen, a low order area compensat-



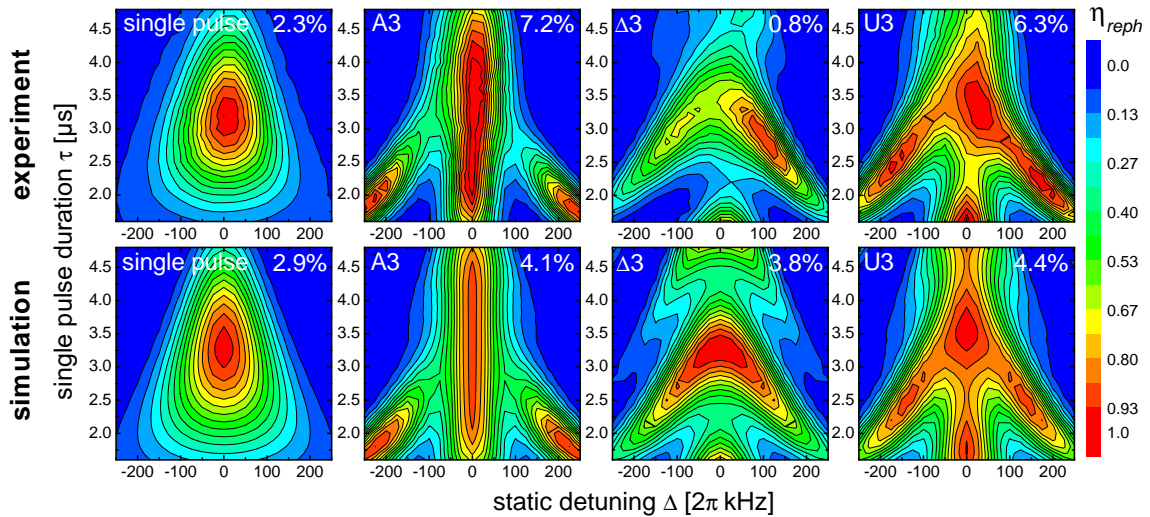


Figure 5.4: Rephasing efficiency of a EIT-LS coherence versus the single pulse duration  $\tau$ , and the static detuning  $\Delta$ . (top row) Experimental data for a single diabatic pulse, a low order area compensating pulse A3 with phases  $(0, 2\pi/3, 0)$ , a low order static detuning compensating pulse  $\Delta 3$  with phases  $(0, \pi/3, 0)$  and the UCP U3  $(0, \pi/2, 0)$ . All pulses are of rectangular temporal shape. The Rabi frequency is fixed for all pulses at  $\Omega \approx 2\pi \cdot 156$  kHz, thus a  $\pi$ -pulse is achieved at a single pulse duration of  $\tau = 3.2$   $\mu$ s. (bottom row) Corresponding simulations depict the transition probability  $|U_{21}^{(n)}|^4$ , i.e. the rephasing efficiency after two rephasing cycles. For a better comparison we calculated the area of high efficiency, i.e.  $\eta_{reph} > 0.9$ , see labels in figure.

ing pulse A3 with phases  $(0, 2\pi/3, 0)$ , a low order static detuning compensating pulse  $\Delta 3$  with phases  $(0, \pi/3, 0)$  and the lowest order UCP U3. The rephasing efficiency  $\eta_{reph}$  is normalized with respect to the maximal achieved efficiency by a single pulse, i.e. a  $\pi$ -pulse. For the single pulse, we find that a high rephasing efficiency is only achieved in a tiny area at almost resonant coupling, and for single pulse durations  $\tau$ , such that  $\Omega\tau \approx \pi$ . A maximal rephasing efficiency is reached at  $\tau = 3.2$   $\mu$ s. For the pulse area compensating pulse A3, we find the expected high and almost constant rephasing efficiency for a broad variety of single pulse durations  $\tau$ , i.e. from 2–4.2  $\mu$ s, a variation of more than  $\pm 30$  % from the optimal value of 3.2  $\mu$ s. However, the robustness against variations in the static detuning is rather small. For the CP  $\Delta 3$ , originally designed to compensate variations in the static detuning, experimental data shows a profile of high rephasing efficiency for a large variation static detunings  $\Delta$ . However, the maximal rephasing efficiency is about 10 % lower compared to the  $\pi$ -pulse rephasing. In addition the profile seems to be slightly asymmetric with higher rephasing efficiencies at positive static detunings  $\Delta$ . We assign the overall lower rephasing efficiency to the experimental coil system #1 which features a intrinsic RF field inhomogeneity of approximately 10 %. Thus, also the Rabi frequency of the applied pulses is inhomogeneous. As the CP  $\Delta 3$ , is not designed to compensate such a inhomogeneity the maximal rephasing efficiency is reduced. The slight asymmetry and the shift towards positive static detunings, could be due to additional Stark shifts from other hyperfine levels. Preliminary investigations have shown that a shift of the

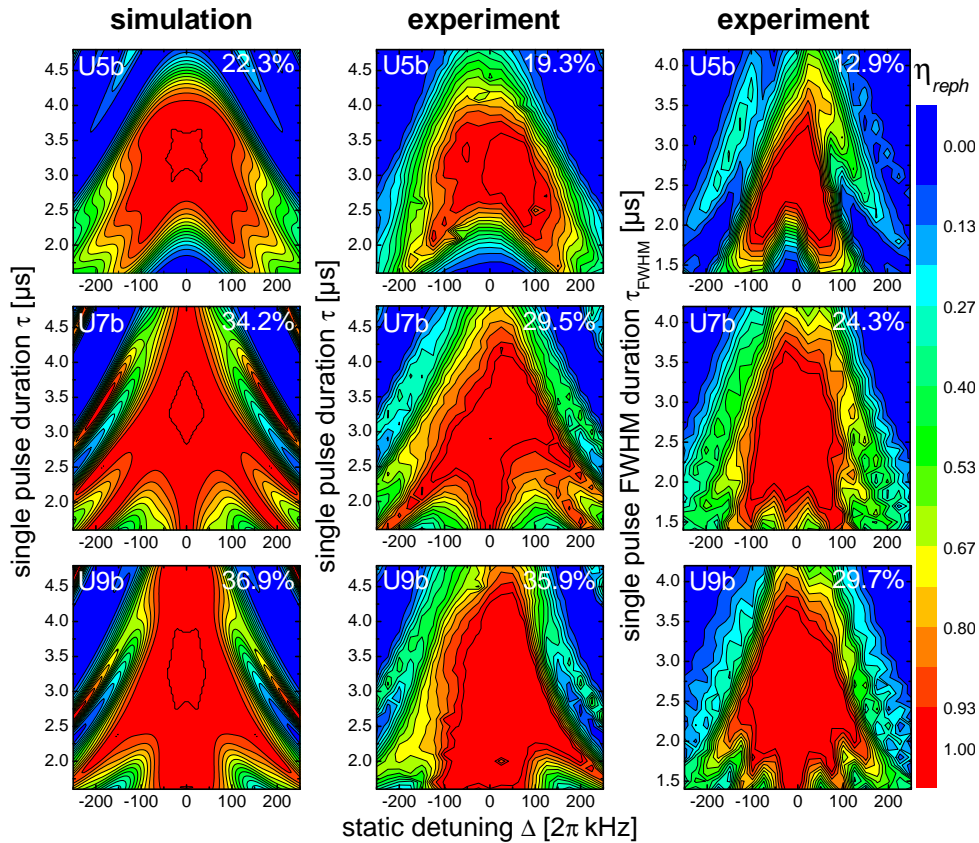


Figure 5.5: Experimentally determined rephasing efficiency  $\eta_{reph}$  of an EIT-LS coherence versus the single pulse duration, and the static detuning  $\Delta$  for high order UCP. (center column) UCP applied with a rectangular temporal pulse shape. (right column) UCP applied with a Gaussian temporal pulse shape. The depicted UCP are U5b (top row), U7b (center row), and U9b (bottom row). The Rabi frequency is fixed for all pulses at  $\Omega \approx 2\pi \cdot 156$  kHz. Hence, for a rectangular pulse shape the optimal duration for a  $\pi$ -pulse is  $\tau \approx 3.2$   $\mu\text{s}$ , and for a Gaussian pulse shape, it is 2.8  $\mu\text{s}$  (FWHM). (left column) Corresponding numerical simulations with a rectangular pulse shape were performed.

rephasing profile towards positive static detunings  $\Delta$  depends slightly on the Rabi frequencies of the applied pulses. For the UCP U3 sequence we find robustness with respect to single pulse duration  $\tau$  and static detuning  $\Delta$  for a large variation of experimental parameters. For a better comparison of the rephasing sequences we calculated the area of high efficiency, i.e.  $\eta_{reph} > 0.9$ , see labels in Figure 5.4. For all experimental data, corresponding numerical simulations were performed. We simulated the transition probability  $|U_{21}^{(n)}|^4$ , i.e. the rephasing efficiency after two rephasing cycles, for a single two-state system. Even though this assumption is a strong simplification of the actual experimental process, the simulation results, shown in Figure 5.4 (bottom row), agree very well with the experimental data. Hence, we have seen that UCP can be simultaneously robust with respect to multiple experimental parameters.

We further investigated higher order universal composite pulses and their robustness with respect to changes in the temporal pulse shape. The experimental results are shown in Figure 5.5. The rephasing profiles for rectangular pulse



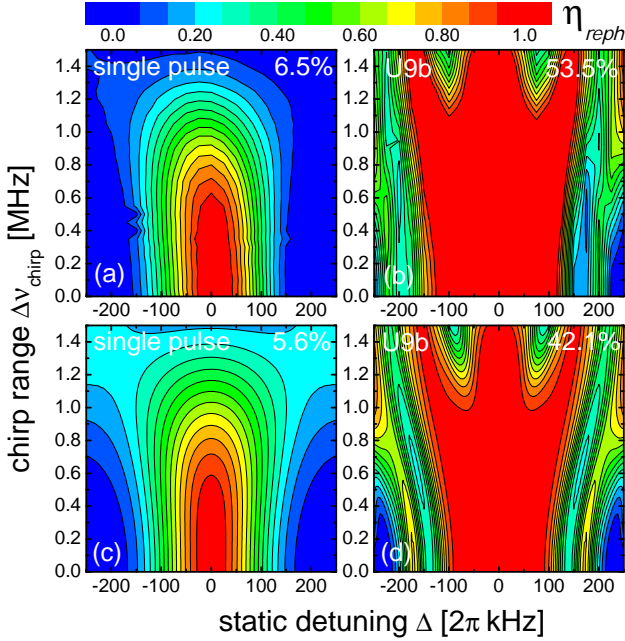


Figure 5.6: Rephasing efficiency of an EIT-LS coherence versus the total chirp range  $\Delta\nu_{\text{chirp}}$ , and the static detuning  $\Delta$ . (top row) Experimental data for a  $\pi$ -pulse (a), and a UCP U9b (b). The frequency chirp is applied linear, symmetric around the resonance of the transition on each constituent pulse of the rephasing sequence. All pulses are of rectangular temporal shape. The Rabi frequency is fixed at  $\Omega \approx 2\pi \cdot 156$  kHz, and the single pulse duration is fixed at  $\tau = 3.2 \mu\text{s}$ . (bottom row) Corresponding numerical simulations depict the transition probability  $|U_{21}^{(n)}|^4$ , i.e. the rephasing efficiency after two rephasing cycles.

shapes are depicted in Figure 5.5 (center column) for U5b, U7b, and U9b. We find that with higher order UCP the robustness with respect to variations in single pulse duration  $\tau$  and static detuning  $\Delta$  increases. Additionally we achieve higher maximal rephasing efficiencies with all UCP. In the case of U9b the maximal rephasing efficiency is up to 25 % higher than with optimal conditions for the  $\pi$ -pulse rephasing. In Figure 5.5 (right column) the experimental rephasing efficiency for UCP of Gaussian temporal pulse shapes are shown. We replaced each constituent pulse of the UCP sequence of rectangular shape by a Gaussian pulse shape truncated at  $3\tau_{\text{FWHM}}$ . We scanned the single pulse FWHM duration  $\tau_{\text{FWHM}}$ , while adjusting the truncation accordingly. We found the maximal rephasing efficiency at FWHM durations of about  $2.8 \mu\text{s}$ . From the relation between the pulse area of a rectangular pulse ( $\Omega\tau$ ) and a Gaussian pulse ( $\Omega\tau_{\text{FWHM}}\sqrt{2\pi}/2.355$ ) one would expect slightly larger optimal FWHM durations of about  $3 \mu\text{s}$ .

Nevertheless, we find a similar behavior for the experimental rephasing efficiency for UCP of Gaussian shapes, and for rectangular pulse shapes. The UCP with a Gaussian pulse shape feature a slightly lower robustness with respect to the static detuning, i.e. the rephasing profiles seem to be compressed on the static detuning axis. This could be due to the lower bandwidth of the Gaussian pulses. The robustness with respect to the pulse durations are comparable. Numerical simulations with a rectangular pulse shape were performed for high order UCP. The results are shown in Figure 5.5 (left column). The experimental data agrees quite well with the simulations, and confirms the superior robustness of UCP in comparison to a  $\pi$ -pulse. The area of high rephasing efficiency increased from about 2.5 % for a single pulse, up to 35.9 % for the UCP U9b, compare with labels in Figures 5.4, and 5.5.

In addition, we investigated the robustness of UCP with respect to residual frequency chirps, as these may occur in the generation of ultra short laser pulses [133]. Figure 5.6 shows the comparison of the efficiency  $\eta_{\text{reph}}$ , of a rephasing

by  $\pi$ -pulses and a rephasing by UCP U9b, versus the static detuning  $\Delta$ , and an additional artificial frequency chirp with a total chirp range  $\Delta\nu_{\text{chirp}}$ . This chirp is applied linear, and symmetric across the resonance of the transition, on each constituent pulse. For the  $\pi$ -pulse rephasing, see Figure 5.6 (a), we find that the rephasing efficiency quickly drops with static detunings larger than  $\pm 2\pi \cdot 50$  kHz and total chirp ranges larger than 700 kHz. Hence, the  $\pi$ -pulses show only a weak robustness with respect to additional frequency chirps. In contrast, the UCP U9b, depicted in Figure 5.6 (b), shows a remarkable robustness with respect to variations in both parameters. We find that the UCP can easily compensate errors due to additional frequency chirps. The corresponding simulations agree very well with the experimental data, and confirm the robustness of UCP sequences.

### 5.3 Composite Adiabatic Passage

Adiabatic passage (AP) processes have been investigated and used in NMR [117] and in coherent optical excitation in the field of quantum optics [119] for many years. Some of the most popular and well-known adiabatic processes in quantum optics are rapid adiabatic passage (RAP) [120, 134], and stimulated Raman adiabatic passage (STIRAP) [135, 136] for population transfer in a two-, respectively three-state quantum system. These processes exhibit a high robustness against fluctuations, and/or variations of driving field and quantum system parameters. However, in practice, experimental restrictions often do not allow to satisfy the adiabaticity conditions sufficiently, which leads to a reduced robustness and inefficient, i.e. incomplete population transfer.

In this section we present a concept proposed by Torosov *et al.* [25] to optimize the efficiency and operation bandwidth of RAP. This concept combines the techniques of diabatic composite pulses with the RAP processes into a composite version, i.e. composite adiabatic passage (CAP). We implement CAP pulses experimentally and apply them to rephase atomic coherences prepared by the EIT-LS protocol in PrYSO. We investigate their performance and compare the results with RAP. The section is structured as follows: First, we give an introduction to AP processes and RAP for rephasing of coherences in an inhomogeneously broadened transition. Second, we give the theoretical derivation of composite adiabatic passage. Third, we show an experimental implementation of CAP for rephasing of EIT-LS coherences in PrYSO.

#### 5.3.1 Adiabatic Passage Processes

In Section 2.1 we described the diabatic coherent interactions in a two-state system in the bare state basis of the system. Following the arguments from Section 2.2 we diagonalize the RWA Hamiltonian of Equation 2.5, and find the new set of adiabatic eigenstates:

$$\begin{aligned} |\psi_+\rangle &= \sin\theta|1\rangle + \cos\theta|2\rangle, \\ |\psi_-\rangle &= -\cos\theta|1\rangle + \sin\theta|2\rangle, \end{aligned} \tag{5.6}$$

with the mixing angle  $\theta$  defined as

$$\tan \theta = \frac{\Delta}{\Omega} + \sqrt{1 + \frac{\Delta^2}{\Omega^2}}. \quad (5.7)$$

The energies of the adiabatic states are given by the eigenvalues of the RWA Hamiltonian of Equation 2.5, yielding  $\epsilon_{\pm} = \pm \frac{\hbar}{2} \sqrt{\Omega^2 + \Delta^2}$ . In general, the driving Rabi frequency  $\Omega(t)$  and the static detuning  $\Delta(t)$  can be time dependent. This leads to a coupling of between the adiabatic eigenstates. The Hamiltonian in the adiabatic basis thus reads

$$\hat{H}_{AB} = \begin{pmatrix} \epsilon_+(t) & -i\hbar\dot{\theta}(t) \\ i\hbar\dot{\theta}(t) & \epsilon_-(t) \end{pmatrix}. \quad (5.8)$$

The time evolution is termed adiabatic, i.e. there is negligible coupling between the eigenstates, when the separation between the adiabatic eigenvalues  $\epsilon_{\pm}$  is much larger than the time derivative of the mixing angle  $\theta(t)$ :

$$|\epsilon_+(t) - \epsilon_-(t)| \gg |\dot{\theta}(t)|. \quad (5.9)$$

If Equation 5.9 is fulfilled the system will stay in its initially prepared adiabatic eigenstate. Only slow changes of  $\theta(t)$  are allowed to drive the system in the adiabatic basis. Condition 5.9 can be re-written in terms of  $\Omega$  and  $\Delta$  to

$$\frac{1}{2} |\dot{\Omega}\Delta - \Omega\dot{\Delta}| \ll (\Omega^2 + \Delta^2)^{3/2}. \quad (5.10)$$

Hence, adiabatic evolution is achieved if  $\Omega$  and  $\Delta$  are changing slowly in time, compared to the effective coupling, i.e. the effective Rabi frequency  $\Omega_{\text{eff}}$ . This requires in general smooth pulses, with a long interaction times, large Rabi frequencies and large detunings.

A special type of an adiabatic passage process in a two-state system is rapid adiabatic passage (RAP), where the system interacts with a driving pulse with constant linear change of the detuning  $\Delta(t)$ , which is symmetric around the resonance frequency of the two-state system. Initially, this most simple adiabatic passage process was designed for efficient population transfer [119, 120]. Recently, this technique was also used for rephasing of atomic coherences [121, 122, 124]. Provided that the adiabaticity criteria are maintained, RAP efficiently inverts the population distribution, irrespective of the exact values of pulse and system parameters. In particular, RAP permits a population inversion in strongly inhomogeneous broadened media, if the maximal detuning of the RAP pulse, i.e. the total chirp range, exceeds the inhomogeneous broadening [122, 123].

The interaction of a RAP pulse with a single two-state system is depicted in Figure 5.7 for a Gaussian (top row) and for a rectangular (bottom row) temporal shape of the Rabi frequency. In both cases  $\pm\Delta_{\text{max}} = \pm\pi\Omega_{\text{max}}$ , the duration is  $\tau_{\text{FWHM}} = 26\Omega_{\text{max}}$ , and  $\tau = 20\pi\Omega_{\text{max}}$  respectively. The system is initially prepared in state  $|1\rangle$ , a RAP pulse is applied and the population is transferred into state  $|2\rangle$ . We find that the Gaussian RAP pulse is capable to fully transfer the population,

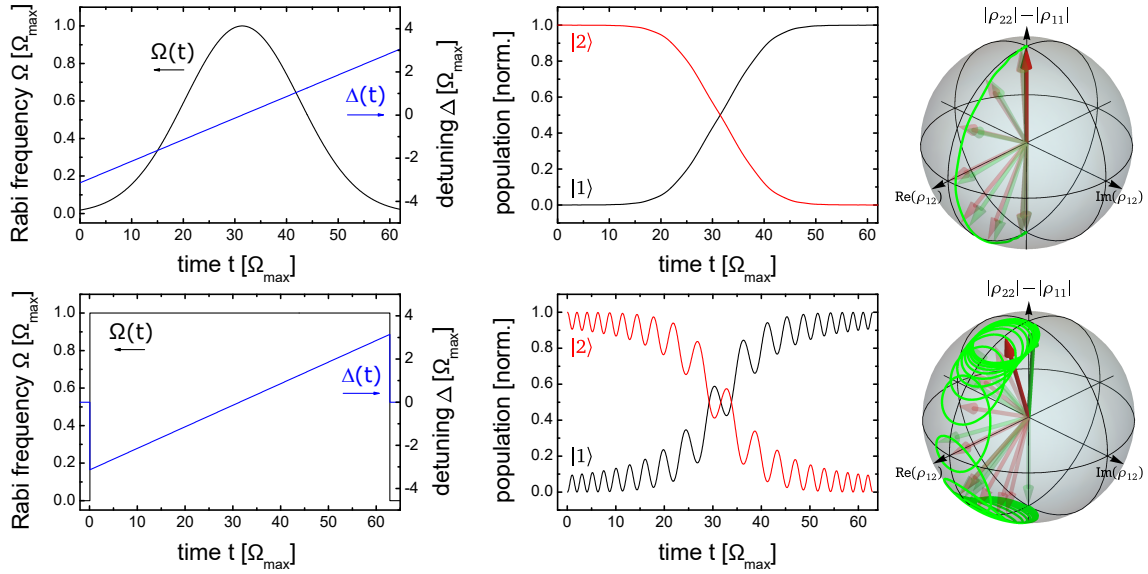


Figure 5.7: Two-state system driven by a RAP pulse of Gaussian (top row) and rectangular (bottom row) temporal shape of the Rabi frequency. (left column) Rabi frequency and detunings of the applied pulses. (center column) Population dynamics during the interaction. (right column) Corresponding path of the Bloch vector on the Bloch sphere.

while the rectangular RAP pulse shows some residual diabatic oscillations due to imperfect adiabaticity, see Figure 5.7 (center column). Figure 5.7 (right column) depicts the RAP process on the Bloch sphere. The Bloch vector is initially pointing along the (-z)-axis. In the beginning of the interaction the RAP pulse is strongly negative detuned from the two-state system resonance, and the Rabi frequency is rather small. Thus, the torque vector also points along the (-z)-axis, see also Equation 2.14. During the RAP pulse, as the detuning  $\Delta$  reduces, and the Rabi frequency  $\Omega$  larger, the torque vector starts slowly moving into the positive direction of the z-axis. If the motion of torque vector is slow, compared to the coupling between torque and Bloch vector, the Bloch vector follows the path of the torque vector. This is also known as *adiabatic following*. At the end of the interaction the RAP pulse is strongly positive detuned. If the adiabaticity condition is fulfilled during the entire interaction, torque and Bloch vector are pointing into the z-axis, with the system completely driven into state  $|2\rangle$ .

In the following we will describe the rephasing of a collective coherent superposition using RAP [121]. Figure 5.8 depicts this rephasing process in an inhomogeneously broadened transition on Bloch sphere. We assume that the system is initially prepared in a maximum coherent superposition. The free evolution time before the rephasing RAP pulse is large compared to the dephasing time, thus the individual coherences are completely dephased in the x-y plane of the Bloch sphere. At the beginning of the RAP pulse the torque vector is pointing into the (-z)-axis. Thus, the Bloch vectors of the individual coherences will start rotating around the z-axis in the x-y-plane (in addition to their rotation due to their detuning from the resonance, i.e. the reference frame of the Bloch sphere) in the beginning of the RAP pulse, i.e. when it is far detuned from the center of the inho-

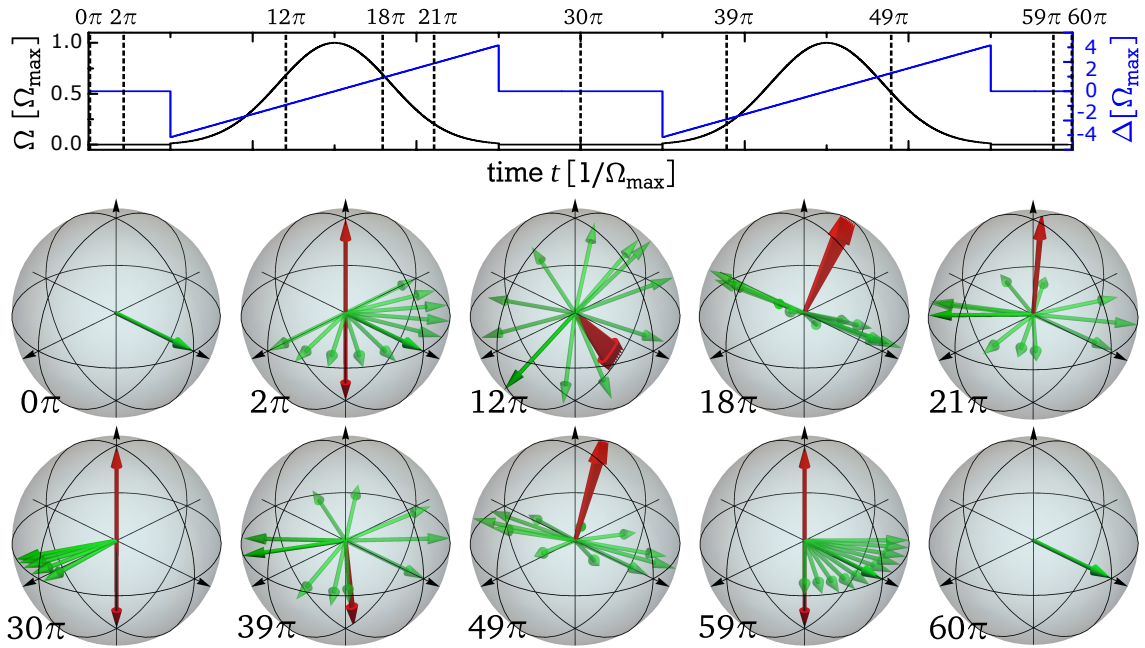


Figure 5.8: Rephasing of a collective coherence prepared in an inhomogeneously broadened transition using a RAP pulse. After the first RAP rephasing cycle the collective coherence is not rephased. RAP imprints an additional phase shift, different for each ensemble of the inhomogeneous line. A second RAP rephasing cycles compensates this phase shift.

mogeneous line. The rotation speed depends on the effective Rabi frequency, i.e. the detuning of the individual coherences. Note that in principle each individual coherence features its own torque vector with a individual detuning  $\Delta$  depending on the position in the inhomogeneous line. However, if we assume a initially large detuning of the RAP pulse, compared to the inhomogeneous linewidth, the torque vectors are almost identical. In a fully adiabatic limit the torque vector of the RAP pulse moves slowly into the positive z-axis, with the dephased Bloch vectors distributed on a disc perpendicular to the torque vector following the motion of the torque vector. After the RAP pulse the system is inverted, and the Bloch vectors are again in the x-y-plane. The phase evolution of the individual coherences continues. However, the RAP pulse imprinted an additional, for each ensemble of the inhomogeneous line different, phase on the individual coherences. Thus, after a free evolution we find that the Bloch vectors do not point in a same direction and thus only a imperfect rephasing is achieved, see with Figure 5.8 at  $t = 30\pi$ . Note that the dephasing, i.e. the individual phase accumulated during free evolution has been reversed, but the RAP pulse added an additional phase shift, which depends upon the individual detunings of the ensembles. These additional phase shifts also strongly depend on the pulse area  $A$ , and pulse duration  $\tau$  of the RAP pulse [124]. The easiest way to compensate for these phase shifts is to apply a second *identical* RAP rephasing process. The second RAP pulse imprints a phase shift of opposite sign on the individual coherences and hence compensates for all additional phase shifts accumulated during the first RAP pulse. We thus find the individual coherences fully in phase after the second RAP rephasing process, see Figure 5.8 at  $t = 60\pi$ . Hence, RAP can be applied not only for efficient population



transfer, but also for robust rephasing of atomic coherences in strongly inhomogeneous broadened systems.

We saw that RAP pulses should feature large detunings, compared to the Rabi frequency, at start and end of the interaction, i.e.  $2\pi\Delta\nu/\Omega \gg 1$ . In addition, the Rabi frequency and the detuning have to change slowly to fulfill the adiabaticity condition of Equation 5.10. If we assume a resonant pulse, Equation 5.10 reduces to  $1 \ll \Omega^2/R$ , with the chirp rate  $R = 2\pi d[\Delta(t)]/dt$ , or in the case of a linear symmetric chirp,  $R = \Delta\nu/\tau$ , with the pulse duration  $\tau$ . As long as these conditions are fulfilled RAP pulses are rather robust against fluctuations, and variations of the driving pulse parameters, and inhomogeneities of the two-state system. However, in order to achieve high fidelities rather long interaction times are required. Usually the experimental parameters, i.e. the Rabi frequencies  $\Omega$ , chirp ranges  $\Delta\nu$ , and pulse durations  $\tau$ , are limited. Thus, in many cases it is not possible to perfectly satisfy the adiabaticity conditions. RAP suffers under weakly fulfilled adiabaticity conditions, and residual diabatic couplings limit the efficiency of RAP, i.e. the population transfer and rephasing efficiency become non-perfect. In order to reduce the effects of residual diabatic couplings and to improve RAP under weakly fulfilled adiabaticity conditions Torosov *et al.* [25] proposed the idea of composite adiabatic passage (CAP), a combination of RAP and composite pulse sequences. In the following section we summarize the theoretical idea of CAP, and show the first experimental realization of CAP under weakly fulfilled adiabaticity conditions for rephasing of atomic coherences in PrYSO.

### 5.3.2 Theory on Composite Adiabatic Passage

The derivation of composite adiabatic passage (CAP) [25, 137] follows in large parts the arguments of the theoretical derivation of universal composite pulses, as described Section 5.2.1. However, in contrast to universal composite pulses, where the only assumption on the pulses was, that all pulses of a sequence are identical, we assume here a model in which the Rabi frequency  $\Omega(t)$  is an even function of time, i.e.  $\Omega(t) = \Omega(-t)$  and the detuning  $\Delta(t)$  is odd, i.e.  $\Delta(t) = -\Delta(-t)$ . The propagator of a driving field  $\Omega(t) \rightarrow \Omega(t)e^{i\phi}$  with constant phase  $\phi$  is defined by

$$\hat{U} = \begin{pmatrix} a & be^{i\phi} \\ -b^*e^{-i\phi} & a^* \end{pmatrix}. \quad (5.11)$$

with the Cayley-Klein parameters  $a$  and  $b$ . The transition probability is  $p = |b|^2 = 1 - |a|^2$ . Thus, a composite sequence of  $n$  identical pulses, each with is constructed by a total propagator  $\hat{U}^{(n)}$  as defined by Equation 5.4. Due to the assumptions on the driving pulses the Cayley-Klein parameter  $a$  is real [138]. As an example, for a CAP 3 sequence, with phases  $(0, \phi, 0)$ , the transition probability reads  $P^{(3)} = 1 - |U_{11}^{(3)}|^2$ , with  $U_{11}^{(3)} = a^3 - a|b|^2(1 + 2\cos\phi)$ . With  $\phi = 2\pi/3$  the second term vanishes, giving  $U_{11}^{(3)} = a^3$ . Thus,  $U_{11}^{(3)}$  and its first derivatives vanish for  $a = 0$ . For a single pulse we only find  $U_{11}^{(1)} = a$ , thus the composite pulse features an enhanced robustness, compared to the single pulses, with respect to variations around  $a = 0$ .

Table 5.2: Theoretically calculated phases  $\phi$  [25] for CAP sequences.

$n$ th CAP sequence	Phases $\phi$
CAP 3	(0, 2, 0) $\pi/3$
CAP 5	(0, 4, 2, 4, 0) $\pi/5$
CAP 7	(0, 6, 4, 8, 4, 6, 0) $\pi/7$
CAP 9	(0, 8, 6, 12, 8, 12, 6, 8, 0) $\pi/9$

For a CAP 5 sequence with phases  $(0, \phi_2, \phi_3, \phi_2, 0)$ , we find

$$U_{11}^{(5)} = a^5 - 2a^3|b|^2 [1 + 2 \cos \phi_2 + \cos(\phi_2 - \phi_3) + \cos \phi_2] + a|b|^4 [1 + 2 \cos(\phi_2 - \phi_3) + 2 \cos(2\phi_2 - \phi_3)]. \quad (5.12)$$

Choosing phases  $\phi_2 = 4\pi/5$ , and  $\phi_3 = 2\pi/5$ , nullifies all terms except the first, thus  $U_{11}^{(5)} = a^5$ . This derivation generalizes for an arbitrary number  $n$  of pulses. An analytic formula describes the phases of the CAP sequence of an arbitrary number  $n$  of pulses, which optimizes RAP against variations in the pulse area and the chirp rate [25],

$$\phi_k^{(n)} = \left( n + 1 - 2 \left\lfloor \frac{k+1}{2} \right\rfloor \right) \left\lfloor \frac{k}{2} \right\rfloor \frac{\pi}{n} \quad (5.13)$$

where  $k = 1, 2, \dots, n$ , and  $\phi_k^{(n)}$  is the phase of the  $k$ th pulse of the sequence. Table 5.2 depicts the theoretical phases for CAP up to  $n = 9$  pulses per CAP sequence.

### 5.3.3 Experimental Results on Composite Adiabatic Passage

We apply the composite adiabatic passage (CAP) sequences, derived in the previous section, for rephasing of atomic coherences prepared by the EIT-LS protocol, see Section 2.3 and Chapter 4. We investigate the performance and robustness of CAP with respect to variations in experimental parameters, and compare with RAP in the case of weak adiabaticity. We use the experimental setup as described in Chapter 3, with the RF coil system #1, providing a maximal Rabi frequency of  $\Omega = 2\pi \cdot 145$  kHz. We use the flat-top probe beam profile, and the smaller of two control beam diameters. Note that for these experiments the OPO-SFG laser system was not yet available. Instead a frequency stabilized dye laser system (Matisse DX, Sirah) provided radiation at 605.98 nm with a frequency jitter of about 100 kHz on a time scale of 100 ms.

Figure 5.9 depicts the schematic pulse sequence for EIT-LS, involving two rephasing cycles. The storage time is chosen to be  $\Delta T = 600 \mu\text{s}$ , i.e. larger than the dephasing time of the hyperfine states of the ground state  $^3\text{H}_4$  of PrYSO. During the storage time the collective coherence, prepared by the EIT-LS protocol, is rephased twice with RF pulses. These RF pulses directly couple the hyperfine transition  $|\pm 3/2\rangle \leftrightarrow |\pm 1/2\rangle$ , in which the collective coherence is prepared. They are applied symmetric around  $\Delta T/4$  and  $3\Delta T/4$  of the total storage time  $\Delta T$ . Figure 5.9 shows as an example a CAP 5 sequence. Each pulse element of the CAP



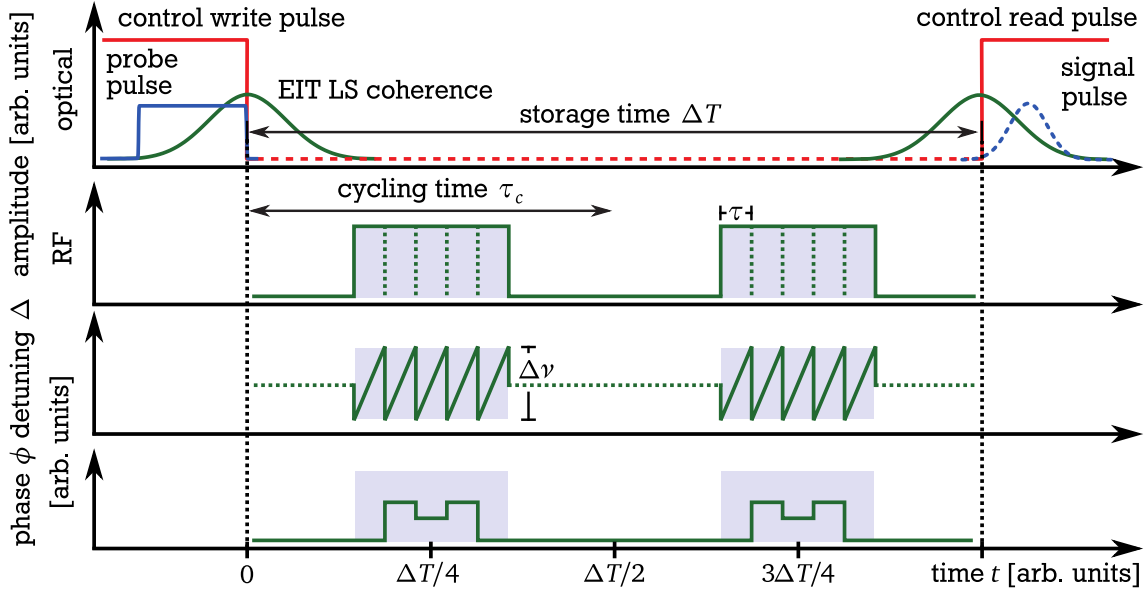


Figure 5.9: Schematic pulse sequence for EIT-LS, involving two rephasing cycles during the storage time  $\Delta T$ . As an example, the scheme shows a CAP rephasing sequence with  $n = 5$  pulse elements. Each element features a linear chirp with a total chirp range  $\Delta \nu$  symmetric around the hyperfine transition  $|\pm 3/2\rangle \leftrightarrow |\pm 1/2\rangle$  of PrYSO, and a static phase  $\phi$ . The rephasing pulses are applied symmetric around  $\Delta T/4$  and  $3\Delta T/4$ .

sequence features a static phase  $\phi$ , and a linear chirp with a chirp range  $\Delta \nu$ . The chirp is applied symmetric around the resonance frequency of the hyperfine transition. The pulse elements feature a rectangular temporal shape and are applied right after each other. Other CAP sequences and RAP pulses are applied in the same way.

We measure the pulse energy of the retrieved signal pulse after the EIT readout, and calculate the light storage efficiency  $\eta_{\text{EXP}}$ , which includes the efficiency of the EIT-LS protocol, decoherence during the storage time  $\Delta T$ , and the efficiency of the rephasing techniques applied, compare with Section 2.3.3. In order to compare the rephasing performance of CAP and RAP, we maintain all experimental parameters of the optical preparation, the EIT storage and readout process fixed, while we vary the parameters of the rephasing sequences. In this way the light storage efficiency  $\eta_{\text{EXP}}$  depends only on the rephasing efficiency of the RAP and CAP sequences and serves as a measure to compare the performance of CAP and RAP. Note that in the following experimental results the absolute measured light storage efficiencies are rather low, because the parameters of the EIT-LS protocol had not been adjusted for optimal storage. However, this does not affect the comparison of RAP and CAP, because here only the relative difference in the light storage efficiency matters.

We investigate the performance of CAP and RAP in realistic situations of weakly fulfilled adiabaticity conditions. In a first experiment we measure the light storage efficiency versus the duration of the driving RF pulses, at a constant maximal Rabi frequency of  $\Omega = 2\pi \cdot 145$  kHz. The RF pulses are applied with a rectangular temporal shape to be able to clearly separate the single pulse elements of

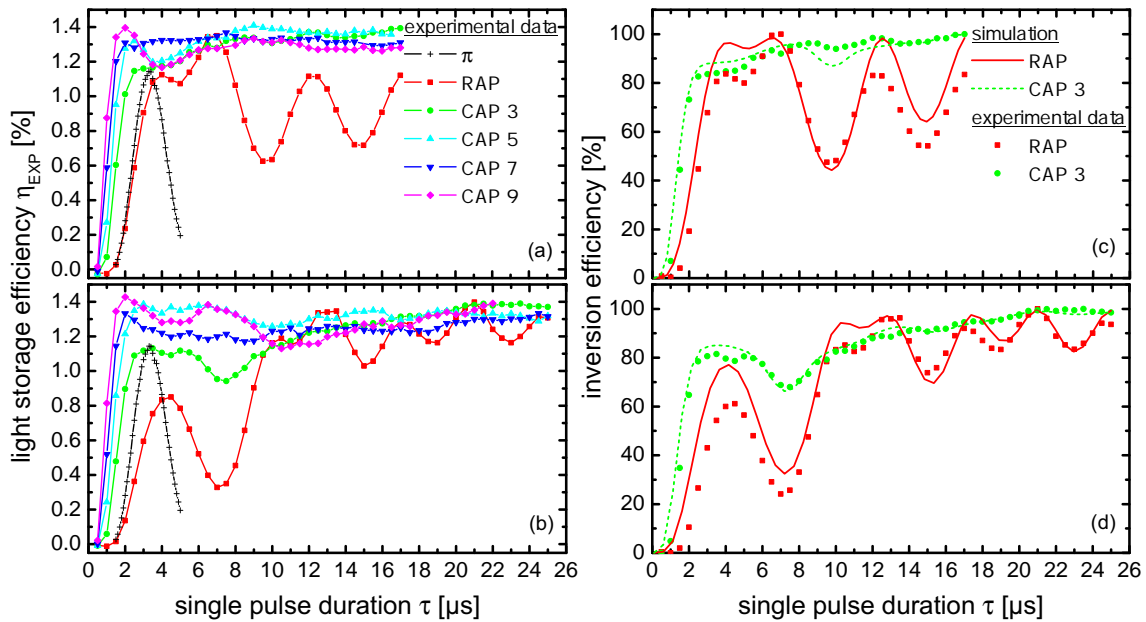


Figure 5.10: Light storage efficiency  $\eta_{\text{EXP}}$  after the rephasing by diabatic resonant pulses, RAP, and CAP versus the single pulse duration  $\tau$ . The Rabi frequency was fixed at  $\Omega = 2\pi \cdot 145$  kHz. Experimental data conducted with a fixed total chirp range of  $\Delta\nu = 600$  kHz (a) and  $\Delta\nu = 900$  kHz (b) for RAP and CAP. (c,d) Simulations and corresponding experimental data for RAP and CAP 3, depicting the calculated inversion efficiency, proportional to  $\eta_{\text{EXP}}$ .

the CAP sequences. In general, a rectangular temporal shape is not optimal for adiabatic processes, compare with Section 5.3.1. We perform the measurement for two different chirp ranges  $\Delta\nu$ . In both cases the adiabaticity conditions are fairly fulfilled. Figure 5.10 (a) shows the experimentally determined light storage efficiency  $\eta_{\text{EXP}}$  versus the single pulse duration  $\tau$  for diabatic resonant pulses ( $\pi$ -pulses), RAP pulses and different orders of CAP sequences, with a total chirp range of  $\Delta\nu = 600$  kHz. The single pulse duration  $\tau$  defines the duration of a single pulse in the CAP sequence. Hence, the total pulse duration of a CAP sequences is  $\tau_{\text{tot}} = n \cdot \tau$ . Thus, RAP can be understood as a CAP sequence of order  $n = 1$ , with the total pulse duration equal the single pulse duration. The CAP sequences are applied with the theoretical phases as calculated in [25] and listed in Table 5.2.

The performance of the adiabatic process is mainly determined by the adiabaticity of the driving pulses. A fair comparison thus requires the same adiabaticity of the RAP pulses and CAP sequences applied for the rephasing process. We compare RAP and CAP for the same single pulse durations. This leads to identical values of adiabaticity for the single pulses of the CAP sequences and the RAP pulse, i.e. the same interaction time, and chirp rate. One could argue that this comparison privileges the CAP sequence, because they feature in total a  $n$  times larger interaction duration, compared to the single RAP pulse. However, note that as we consider an imperfect RAP pulse, a sequence of  $n$  identical RAP pulses would perform even worse. It is thus fair to compare a CAP sequence of  $n$  single pulses each of duration  $\tau$ , with a single RAP pulse of duration  $\tau$ .

As Figure 5.10 (a) shows, the largest rephasing efficiency with a diabatic resonant pulse (black crosses) is achieved at a single pulse duration of about  $3.4 \mu\text{s}$ ,

which corresponds to a  $\pi$ -pulse with  $\Omega = 2\pi \cdot 145$  kHz. Here, the light storage efficiency is approximately 1.15 %. As expected from a diabatic resonant coupling the rephasing efficiency strongly decreases already for small variations in the single pulse duration  $\tau$ . The robustness improves for rephasing by RAP (solid red square). High rephasing efficiency is achieved for single pulse durations between  $4 \mu\text{s}$  and  $8 \mu\text{s}$ . Compared to the  $\pi$ -pulse rephasing the maximal efficiency increased by 13 %. However, we also find that rephasing by RAP still features some pronounced variations of the efficiency with respect to the single pulse duration. This can be assigned to the fact that the adiabaticity conditions are only fairly fulfilled. For the first adiabaticity condition (as introduced in Section 5.3.1), we find with a chirp range of  $\Delta\nu = 600$  kHz and a Rabi frequency of  $\Omega = 2\pi \cdot 145$  kHz, that  $1 \ll 2\pi\Delta\nu/\Omega = 4.14$ . Thus, the first adiabaticity condition is only fairly fulfilled. Moreover the second adiabaticity condition, ( $\Omega^2/R \gg 1$ ) varies, as the chirp rate  $R$  depends on the single pulse duration  $\tau$ . For the single pulse durations depicted in Figure 5.10 (a), we find  $\Omega^2/R = 0.11 - 3.74$ . Hence, also the second adiabaticity condition is not well fulfilled, especially for small single pulse durations  $\tau$ . Residual diabatic couplings render the efficiency of the RAP process dependent on the actual single pulse duration. This explains the variations of the efficiency with respect to the single pulse duration.

In a next step we exchange the single RAP pulses by CAP sequences with  $n$  single pulses. All pulses feature the same Rabi frequency  $\Omega$  and chirp range  $\Delta\nu$ , however they differ in their relative phases  $\phi$ . We find that all CAP sequences clearly outperform the RAP pulses, see Figure 5.10 (a). The CAP sequences feature high rephasing efficiencies over a large range of single pulse durations. The pronounced variations of the rephasing efficiency, observed using RAP, completely vanish in the case of rephasing by CAP sequences. Thus, the appropriately chosen phases of the CAP sequences reduce the effect of the residual diabatic couplings due to weakly fulfilled adiabaticity conditions. Already the CAP 3 sequence is able to compensate the residual diabatic couplings. We find with increasing  $n$ , that high rephasing efficiencies are achieved earlier, i.e. already for shorter single pulse durations. However, the maximal rephasing efficiency does not significantly increase for higher orders of CAP sequences. Thus, we have seen that CAP sequences can enhance the performance of adiabatic processes in situations of fairly fulfilled adiabaticity conditions.

We repeated the measurements for a larger chirp range of  $\Delta\nu = 900$  kHz, while maintaining the Rabi frequency at  $\Omega = 2\pi \cdot 145$  kHz. This yields a better adiabaticity, as the first adiabaticity condition now reads  $2\pi\Delta\nu/\Omega = 6.21$  and should lead to reduced residual diabatic couplings. Figure 5.10 (b) depicts the experimental results. RAP still features strong variations in the rephasing efficiency, especially for short pulse durations. This becomes clear if one checks the second adiabaticity condition.  $\Omega^2/R$  varies between 0.07 and 3.67 for single pulse durations between  $0.5 \mu\text{s}$  and  $25 \mu\text{s}$ . Thus, for short pulse durations the second adiabaticity condition is even fulfilled worse, compared to the case of  $\Delta\nu = 600$  kHz. However, at longer single pulse durations both adiabaticity conditions are fulfilled better than for the  $\Delta\nu = 600$  kHz case and we find reduced oscillations of the RAP rephasing efficiency. The improved adiabaticity of RAP does not affect significantly the

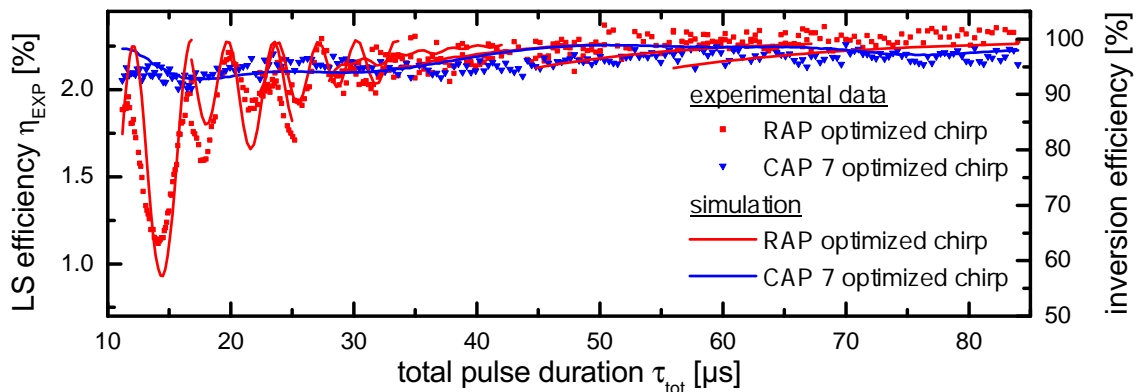


Figure 5.11: Light storage efficiency  $\eta_{\text{EXP}}$  versus the total pulse duration  $\tau_{\text{tot}}$  of the RAP and CAP 7 sequences. The single pulse duration is given by  $\tau = n/\tau_{\text{tot}}$ . All pulses feature a rectangular temporal intensity shape with a fixed Rabi frequency of  $\Omega = 2\pi \cdot 145$  kHz. The experimental data on RAP consists of several measurements each with optimized chirp ranges, from  $\Delta\nu = 0.6$  MHz for short total pulse durations up to  $\Delta\nu = 3.2$  MHz for the longest total pulse durations. In the case of CAP the chirp range was fixed at  $\Delta\nu = 0.5$  MHz for all total pulse durations. Corresponding numerical simulations are shown.

maximal rephasing efficiency. Again all CAP sequences outperform RAP in terms of robustness with regard to variations in single pulse duration. However, we find that low order CAP sequences can not fully compensate the lack of adiabaticity at short single pulse durations, especially the CAP 3 sequence still seems to follow the RAP behavior for short pulse durations in a range of  $2 - 10 \mu\text{s}$ . Nevertheless, the rephasing efficiency and robustness at short pulse durations improve for higher order CAP sequences. We thus find that higher order CAP sequences can compensate a larger lack of adiabaticity.

In order to validate our experimental data, we performed numerical simulations of rephasing in an inhomogeneously broadened two-state system. In particular, we investigated the population inversion dynamics of the system driven by RAP and CAP, which is proportional to the rephasing efficiency in the case of an EIT prepared coherence rephased by two rephasing processes. Figures 5.10 (c) and 5.10 (d) depict the inversion efficiency versus the single pulse duration  $\tau$  for  $\Delta\nu = 600$  kHz and 900 kHz, respectively. Simulations (solid and dotted lines) and corresponding experimental data (solid symbols) for RAP and the CAP 3 sequence, as an example, are shown. We find the simulations fit the experimental data very well. All main features, especially the strong variations in the rephasing efficiency in the case of RAP, could be confirmed by this simplified modeling of the experiment.

So far we compared RAP pulses and CAP sequences under equal adiabaticity conditions. This required identical Rabi frequencies, chirp rates, and single pulse durations of the applied pulses. Therefore CAP sequences always exhibited a  $n$  times larger total pulse duration with  $\tau_{\text{tot}} = n\tau$ , compared to RAP pulses. We show in the following a comparison of RAP and CAP from a more practical point of view, with experimentally limited total interaction duration and limited Rabi frequency. We thus compare the performance of RAP and CAP at same total pulse

durations  $\tau_{\text{tot}}$ . In addition, we optimize the total chirp ranges  $\Delta\nu$ , in order to achieve optimal chirp rates  $R$  for the given total pulse duration. This optimization is done independently for RAP and CAP. Hence, RAP and CAP might differently fulfill the adiabaticity conditions.

Figure 5.11 shows the experimentally determined light storage efficiency  $\eta_{\text{EXP}}$  versus the total pulse duration  $\tau_{\text{tot}}$  after rephasing by RAP pulses and the CAP 7 sequence. We separated the full range of total pulse durations  $\tau_{\text{tot}} = 11\text{--}84\ \mu\text{s}$  into 7 intervals. In the center of each interval we optimized the chirp range  $\Delta\nu$  of the RAP pulses to provide maximal efficiency. With this optimized chirp range we then measured the light storage efficiency for the total interval. This procedure was repeated for all 7 intervals. The optimal chirp range varied from  $\Delta\nu = 0.6\ \text{MHz}$  for short total pulse durations up to  $\Delta\nu = 3.2\ \text{MHz}$  for long total pulse durations, keeping the adiabaticity condition  $\Omega^2/R$  in the order of 3.2, depending on the actual total pulse duration. We optimized the CAP 7 sequence in the same way. However, for CAP we found that the optimal chirp range is almost independent from the total pulse duration  $\tau_{\text{tot}}$ . We found the optimal value to be  $\Delta\nu = 500\ \text{kHz}$  over the full range of total pulse durations. This confirms that CAP is far less sensitive to variations of the adiabaticity, for example due to changes in the total pulse duration. Note that the CAP 7 sequence with  $\Delta\nu = 500\ \text{kHz}$  exhibits a chirp rate  $R$  which is larger than the chirp rates of the RAP pulses for almost the full range of total pulse durations. Thus, the RAP pulses fulfill the adiabaticity condition  $\Omega^2/R$  better, which makes this comparison very conservative.

The experimental data in Figure 5.11 confirm the enhanced robustness of CAP with regard to variations in the total pulse duration. Especially for short total pulse durations we find that RAP still suffers very much from the low adiabaticity. Although both adiabaticity conditions yield values in the order of 3–4, RAP shows pronounced variations of the rephasing efficiency with changes in the total pulse duration. In contrast CAP exhibits already at short total pulse durations a high and stable rephasing efficiency. The variations in the rephasing efficiency by RAP are about a factor of 6 larger, compared to CAP. At long total pulse durations RAP and CAP essentially yield the same rephasing efficiencies. The adiabaticity conditions of the RAP pulses are here well enough fulfilled, thus CAP can not further improve the rephasing process. We performed numerical simulations, as described before, in order to confirm our experimental data. Figure 5.11 shows the results (solid lines) for the corresponding experimental data. The simulation confirms the behavior of RAP and CAP quite well. We find a strong robustness of CAP over the full range of total pulse durations. The simulation also confirms the experimental results from RAP, with strong variations in the rephasing efficiency at short pulse durations, which vanish towards long pulse durations. These results prove the superior robustness of CAP compared to RAP in situations of fairly fulfilled adiabaticity conditions for equal total pulse durations  $\tau_{\text{tot}}$ , i.e. equal total interaction times.

So far, we only discussed the stability of the applied rephasing pulses with regard to variations in the pulse duration for a fixed Rabi frequency. However, there might be also variations or fluctuations of the transition frequency of the two-state system, as it is the case in inhomogeneously broadened media (also



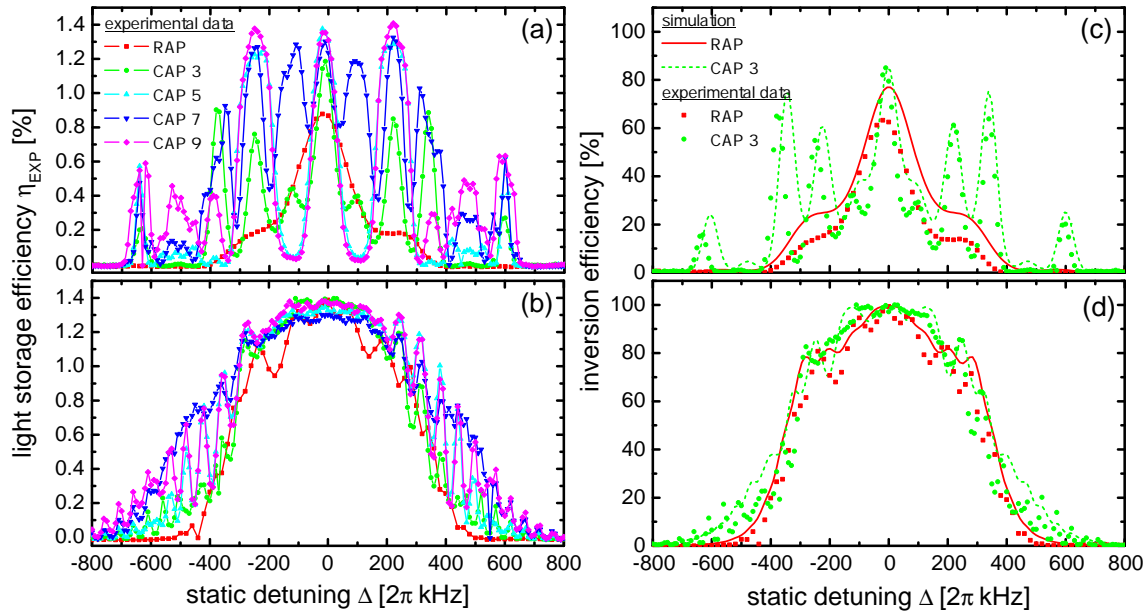


Figure 5.12: Light storage efficiency  $\eta_{\text{EXP}}$  after rephasing by RAP, and CAP versus the static detuning  $\Delta$  at  $\tau = 4 \mu\text{s}$  (a) and  $\tau = 21 \mu\text{s}$  (b). The Rabi frequency is  $\Omega = 2\pi \cdot 145 \text{ kHz}$ , and the chirp range is fixed at  $\Delta\nu = 900 \text{ kHz}$ . All rephasing pulses exhibit a rectangular temporal shape of intensity. (c,d) Simulations of the inversion efficiency and corresponding experimental data for RAP and CAP 3 at  $\tau = 4 \mu\text{s}$  (c) and  $\tau = 21 \mu\text{s}$  (d).

in PrYSO), or even in the carrier frequency of the driving pulses. Both type of variations lead to an additional static detuning  $\Delta$  of the driving pulse from the two-state resonance. In order to cope with this, the spectral bandwidth of the rephasing process has to be larger than the bandwidth of the frequency variations.

In general, adiabatic processes, like RAP, will offer robust operation with regard to variations in the static detuning  $\Delta$ , especially compared to diabatic  $\pi$ -pulses. However, CAP was initially not meant to compensate for additional static detunings, as the derivation of CAP assumed a symmetric linear chirp around the resonance of a two-state system. Thus, it is of interest to understand if the gain in robustness with regard to the pulse duration (pulse area), leads to a reduced robustness with regard to a static detuning  $\Delta$ . compared to RAP. We therefore add an additional static detuning  $\Delta$  to the driving RAP and CAP rephasing pulses. This leads to an asymmetry of the linear chirp  $\Delta(t)$  around the resonance frequency of the  $|\pm 3/2\rangle \leftrightarrow |\pm 1/2\rangle$  transition in PrYSO in which the EIT-LS coherence is prepared.

Figure 5.12 (a-d) shows the experimental results and corresponding simulations for RAP pulses and CAP sequences. Depicted is the light storage efficiency  $\eta_{\text{EXP}}$ , and the inversion efficiency versus the static detuning  $\Delta$ . For all measurements the Rabi frequency was fixed at  $\Omega = 2\pi \cdot 145 \text{ kHz}$ , and the pulses featured a rectangular temporal shape of intensity. The chirp range was  $\Delta\nu = 900 \text{ kHz}$ . We performed measurements under fairly fulfilled adiabaticity conditions, i.e. at short single pulse durations, and under slightly better fulfilled adiabaticity at long single pulse duration. Figure 5.12 (a) shows the experimental results for a single pulse duration of  $\tau = 4 \mu\text{s}$ , when RAP reaches a first maximum in rephasing effi-

ciency, compare with Figure 5.10 (b). However, RAP does not work very well at this pulse duration, as the second adiabaticity condition only yields  $\Omega^2/R = 0.6$ . As expected, the rephasing efficiency exhibits a maximum at  $\Delta \approx 0$  kHz, when the chirp is applied symmetric around the resonance frequency of the transition. Note that the small shift towards negative static detunings is due to the fact that here the resonance of the relevant hyperfine transition in PrYSO was assumed to be at 10.2 MHz, while it is actually found at 10.191 MHz. The efficiency quickly reduces with increasing static detuning  $\Delta$  and drops to zero at about  $\Delta = \pm 2\pi \cdot 400$  kHz. Here the chirp is applied very asymmetric around the resonance. Thus, the total chirp range of  $\Delta\nu = 900$  kHz is not sufficient to fully cover the inhomogeneous broadening of the hyperfine transition of PrYSO in which the coherence is prepared. The single pulse duration of  $\tau = 4 \mu\text{s}$  is of the order of the  $\pi$ -pulse duration, which is about  $3.4 \mu\text{s}$ . Thus, the RAP couples the transition almost fully diabatic. This explains the strong reduction of the rephasing efficiency between  $\Delta = 0$  kHz and  $\Delta = 2\pi \cdot 150$  kHz, which approximately corresponds to the bandwidth of the RAP pulse, as  $\Omega = 2\pi \cdot 145$  kHz. Figure 5.12 (a) also shows the experimental results for CAP sequences. All CAP sequences feature a quite complicated, periodic variation of the rephasing efficiency with respect to the static detuning  $\Delta$ . As expected at  $\Delta \approx 0$  kHz all CAP sequences clearly achieve higher rephasing efficiencies in comparison to the RAP pulses. However, already for rather small static detunings the efficiency strongly reduces, even faster than it is the case for RAP. All CAP sequences show prominent sidebands for static detuning up to about  $\Delta = \pm 2\pi \cdot 600$  kHz. Hence, we find that CAP does not provide an enhanced robustness with respect to static detunings at the short single pulse duration of  $\tau = 4 \mu\text{s}$ .

We repeated the experiment at a longer single pulse duration of  $\tau = 21 \mu\text{s}$ , while keeping the Rabi frequency and chirp range as before. Now we find the second adiabaticity condition to be  $\Omega^2/R = 3.1$ . Thus, RAP and CAP will suffer less from residual diabatic couplings. We see in Figure 5.12 (b) that RAP and CAP yield high and comparable rephasing efficiencies for  $\Delta = 0$  kHz. The spectral bandwidth of the RAP pulses increases to roughly  $\pm 2\pi \cdot 300$  kHz (FWHM). It is now limited by the bandwidth of the adiabatic process, due to the chirp range  $\Delta\nu$ , and no longer by the bandwidth given by the Rabi frequency. For the CAP sequences we see that the complicated structure found in Figure 5.12 (a) for single pulse durations of  $\tau = 4 \mu\text{s}$  completely vanished for  $\tau = 21 \mu\text{s}$  in the range of static detunings between  $\Delta = \pm 2\pi \cdot 200$  kHz. All CAP sequences feature a stable and almost constant rephasing efficiency, and perform slightly better than RAP. Moreover, higher order CAP sequences exhibit a larger operation bandwidth with respect to the static detuning. However, the CAP 5 and CAP 9 sequences still show some oscillations of the rephasing efficiency, especially for static detuning larger  $\pm 2\pi \cdot 250$  kHz. The CAP 7 sequence features the largest bandwidth of about  $2\pi \cdot 1000$  kHz (FWHM). Thus, CAP provides an improved spectral bandwidth and robustness compared to RAP, with regard to variations in the static detuning, though it was not originally derived for this application. We note, that if we would apply CAP with the phases of the universal composite pulses, introduced in Section 5.2, one might obtain an even more robust behavior with respect to the static detuning. We again performed numerical simulations of an inhomogeneously broadened two-state sys-



tem. Figure 5.12 shows the results for a single pulse duration of  $\tau = 4 \mu\text{s}$  (c) and  $\tau = 21 \mu\text{s}$  (d). Simulations for RAP (solid red line), CAP 3 (dashed green line), and corresponding experimental data are depicted. The simulations clearly confirm our experimental results.

### 5.3.4 Conclusion

In the previous section we demonstrated an experimental implementation of composite adiabatic passage (CAP). CAP was originally proposed as an extension of RAP, i.e. to improve RAP in situations of fairly fulfilled adiabaticity, for an efficient and robust inversion of the population distribution in a two-state system [25]. CAP is a composite version of RAP, consisting of a sequence of RAP pulses with appropriate chosen relative phases. The ability to precisely control these relative phases, i.e. within a few degrees, is essential for CAP. It is only these phases which makes the adiabatic passage driven by a CAP sequence robust in situations of otherwise fairly fulfilled adiabaticity conditions. Thus CAP can only be applied to enhance RAP if a relative phase control is possible. We used CAP for rephasing of atomic coherences, prepared by EIT-LS in PrYSO, driven by RF radiation pulses. We compared the rephasing performance of CAP and RAP at different degrees of adiabaticity. In particular, we systematically investigated the variation of the rephasing efficiency with respect to changes in the pulse duration and static detuning. We found that if the adiabaticity conditions are only fairly fulfilled, CAP is capable to strongly reduce the residual diabatic couplings visible for RAP pulses, leading to a high rephasing efficiency, irrespective of the exact choice of the experimental parameters, i.e. pulse duration and static detuning. These characteristics of CAP can be of interest, whenever an efficient and robust state manipulation is required, and full adiabaticity can not be provided due to experimental restrictions.

## 5.4 Single-Shot Shaped Pulses

We saw in Section 2.1 that diabatic interactions can feature in general a high fidelity, i.e. rephasing or inversion efficiency, if the pulse parameters are chosen very carefully, i.e. appropriately, within a small parameter range. Unfortunately, any variations from the optimal pulse parameters will substantially reduce the fidelity. Thus, diabatic interactions exhibit a low robustness with regard to variations or fluctuation of experimental parameters. We saw in Section 5.2 that composite pulses, in particular UCP, can be used to enhance the robustness of a diabatic interaction for any type of experimental fluctuations. However, larger total pulse areas and a precise phase control are necessary to achieve this stability. In the previous section we applied the idea of composite pulses on adiabatic passage processes to compensate for the lack of adiabaticity. In general, adiabatic processes feature a great robustness as long as the adiabaticity conditions are fulfilled well. However, often experimental limitations, especially in the long interaction times, required by the adiabatic processes, inhibit a sufficient fulfillment of the adiabaticity conditions. Recently techniques based on parallel adiabatic passage [139, 140], and shortcuts to adiabaticity [125, 126], were developed to optimize the speed of the

adiabatic process, in order to overcome these limitations. The latter also includes single-shot shaped pulses (SSSP). These types of pulses can be derived by analytic control techniques for simple tasks like population inversion [26, 127], and can be combined with numerical optimal control techniques [141, 142] to reach more complex target states. They yield solutions of pulses with complex time dependent Rabi frequencies and detunings, which are able to drive a system from its initial state to a desired final state in a fast and robust way. We demonstrate here the first experimental application of single-shot shaped pulses. We experimentally demonstrate the applicability, efficiency and robustness of SSSP to rephase of atomic coherences prepared by in PrYSO. Next we give a short introduction on the derivation of single-shot shaped pulses, which is followed by a description of our experimental results.

### 5.4.1 Derivation of Single-Shot Shaped Pulses

We provide here a short derivation of SSSP, and would like to refer the interested reader to [126] for a general introduction on shortcuts to adiabaticity, and to [26, 127] for a comprehensive review on single-shot shaped pulses. In the following, we will only describe the general idea of the derivation of SSSP and present one specific solution. The derivation given here combines the advantages of analytical and numerical optimal control approaches, i.e. smooth and not too complex general solutions, which still provide high fidelity. It is based on the idea to achieve robust pulses in an perturbative expansion of the excitation profile [26]. In a first step, a specific analytic parametrization of the pulse based on continuous trigonometric functions is derived. This is the key difference to known methods which usually make use stepwise functions, as it is for example the phases of composite pulses. The parametrization typically leads to a set of about ten parameters determined by analytical procedure and further optimized by an numerical optimal control procedure, based on the Gradient Ascent Pulse Engineering (GRAPE) algorithm [143, 144]. We consider a two-state system, driven by a coherent field. The Hamiltonian of the system in rotating-wave approximation reads

$$\hat{H}_{\alpha,\delta} \equiv \hat{H}_0 + \hat{V} = \frac{\hbar}{2} \begin{bmatrix} 0 & \Omega_c \\ \Omega_c^* & 0 \end{bmatrix} + \frac{\hbar}{2} \begin{bmatrix} -\delta & \alpha\Omega_c \\ \alpha\Omega_c^* & \delta \end{bmatrix} \quad (5.14)$$

where  $\Omega_c(t) = \Omega(t)e^{-i\eta(t)} = \Omega_x(t) - i\Omega_y(t)$  is the time-dependent complex Rabi frequency with a real and positive amplitude  $\Omega(t)$  and the phase  $\eta(t) = \int_0^t \Delta(t')dt'$ . We define the time dependent (controlled) detuning  $\Delta(t) = \omega_{12} - \omega(t)$  in contrast to Section 2.1. We also assume an additional unknown detuning  $\delta$ , which could be due to an inhomogeneous broadening, or a detuned driving field. Also we describe possible variations of the Rabi frequency by a scaling factor  $\alpha$ . The idea is to determine the shape of the complex Rabi frequency  $\Omega_c(t)$  of the pulse such that it is robust with regard to variations of the parameters  $\delta$  and  $\alpha$ . We parametrize a general solution  $|\Psi_0\rangle$  of the TDSE  $i\hbar \frac{\partial}{\partial t} |\Psi_0\rangle = \hat{H}_0 |\Psi_0\rangle$ , by a mixing angle  $\theta$ , a relative phase  $\chi$  and a global phase  $\gamma$  in the form:

$$|\Psi_0\rangle = \begin{bmatrix} e^{i\chi/2} \cos(\theta/2) \\ e^{-i\chi/2} \sin(\theta/2) \end{bmatrix} e^{-i\gamma/2}. \quad (5.15)$$

Inserting Equation 5.15 into the TDSE we find,

$$\begin{aligned}\dot{\theta} &= \Omega_x \sin \chi + \Omega_y \cos \chi, \\ \dot{\chi} &= \dot{\gamma} \cos \theta, \\ \dot{\gamma} &= \frac{1}{\sin \theta} (\Omega_x \cos \chi - \Omega_y \sin \chi).\end{aligned}\quad (5.16)$$

From this set of non-linear differential equations one can calculate the components of the Rabi frequency:

$$\Omega_x = \dot{\theta} \sin \chi + \dot{\gamma} \sin \theta \cos \chi, \quad \Omega_y = \dot{\theta} \cos \chi - \dot{\gamma} \sin \theta \sin \chi \quad (5.17)$$

A NOT-type gate operation can be described by the propagator

$$\hat{U}_0 = \begin{bmatrix} 0 & -e^{-i\kappa} \\ e^{i\kappa} & 0 \end{bmatrix} \quad (5.18)$$

with a target phase  $\kappa$ , which can be freely chosen, driving the system from an initial time  $t_i = 0$  to a final time  $t_f = T$ , with the final state given by  $|\Psi_0(T)\rangle = \hat{U}_0|\Psi_0(0)\rangle$ . For the traceless Hamiltonian  $\hat{H}_{\alpha,\delta}$  the elements of a general propagator  $\hat{U}$  take the form  $U_{11} = U_{22}^* = a$ , and  $U_{21} = -U_{12}^* = b$ , with complex numbers  $a$  and  $b$ . We thus can reduce the problem to driving the system from an initial state  $|\Psi_0(0)\rangle = |1\rangle$  to the final state  $|\Psi_0(T)\rangle = e^{i\kappa}|2\rangle$ , which means fixing the boundary conditions to:  $\theta_i = 0$ ,  $\gamma_i = \chi_i$ , and  $\gamma_f = -2\kappa - \chi_f$ . The transfer profile  $\langle\Psi_0(T)|\Psi_{\alpha,\delta}(T)\rangle$ , where  $|\Psi_{\alpha,\delta}(T)\rangle = \hat{U}|\Psi_0(0)\rangle$  is the solution of the TDSE for  $\hat{H}_{\alpha,\delta}$ , is expanded in a power series of  $\alpha$  and  $\delta$ . The robust SSSP trajectory is derived, with the restrictions of low total pulse area, and pulse amplitudes, with regard to variations in  $\alpha$  and  $\delta$ . To do so,  $\gamma(\theta)$ , and  $\theta(t)$  are expressed as a function by sine Fourier series:

$$\gamma(t) \equiv \tilde{\gamma}(\theta) = \chi_i + 2\theta + \sum_{n=1}^N C_n \sin(2n\theta), \quad \theta(t) = \frac{\pi}{T}t + \sum_{m=1}^M \theta_m \sin\left(2m\frac{\pi}{T}t\right) \quad (5.19)$$

The coefficients  $C_n$  and  $\theta_m$  are then determined via the perturbation expansion. However, it is rather difficult to identify higher order coefficients. Thus, the analytic perturbation expansion is only used up to the second order coefficients. In a second step, the higher order coefficients are determined by the numerical GRAPE algorithm, maximizing the fidelity  $J$  for a defined range of variations of  $\alpha$  and  $\delta$ , with  $J$  defined as,

$$J = \frac{1}{2} \mathbf{R}[\text{Tr}(U_0^\dagger U)] = \mathbf{R}(\langle\Psi_0(T)|\Psi_{\alpha,\delta}(T)\rangle). \quad (5.20)$$

Table 5.3 shows the resulting coefficients  $C_n$  and  $\theta_m$ , derived by the numerical optimization. The pulse was optimized for variations  $\alpha = [-0.5\dots 0.5]$ , and  $\delta = [-0.375\Omega_{\max}\dots 0.375\Omega_{\max}]$ . Here  $\Omega_{\max}$  is the peak Rabi frequency of the optimized pulse. Figure 5.13 (right) depicts the fidelity  $J$  of a single two-state system driven by the single-shot shaped pulse, defined by the coefficients in Table 5.3.

Table 5.3: Resulting coefficients  $C_n$  and  $\theta_m$  from the numerical optimization, defining the single-shot shaped pulse, optimized for variations  $\alpha = [-0.5\dots 0.5]$ , and  $\delta = [-0.375\Omega_{\max}\dots 0.375\Omega_{\max}]$ , with  $\Omega_{\max}$  the peak Rabi frequency of the pulse.

$C_1$	$C_2$	$C_3$	$C_4$	$C_5$	pulse area [in units of $\pi$ ]
2.3347	-1.9450	0.3944	-0.1139	-0.3723	5.06
$\theta_1$	$\theta_2$	$\theta_3$	$\theta_4$	$\theta_5$	fidelity $\bar{J}$
-0.0990	-0.1176	-0.0394	-0.0119	0	0.95

The black dotted box indicates the optimization range in variations of  $\alpha$  and  $\delta$ . The pulse features a high robustness with regard to variations of up to 50 % from the optimal Rabi frequency, and also with regard to variations in the unknown detuning  $\delta$ . The corresponding time-dependent Rabi frequency and detuning  $\Delta$  of the pulse are shown in Figure 5.13 (left). The pulse has a rather smooth symmetric shape in the Rabi frequency. From the time-dependent detuning  $\Delta$  one finds that the pulse can be divided into three parts, separated by two steep large detunings. These features can be interpreted as rapid phase changes, comparable to the phase changes of composite pulses. In the first part the pulse is positively detuned, driving the system off resonance, i.e. adding an additional phase factor to the system. The second part features a almost linear change in the detuning,

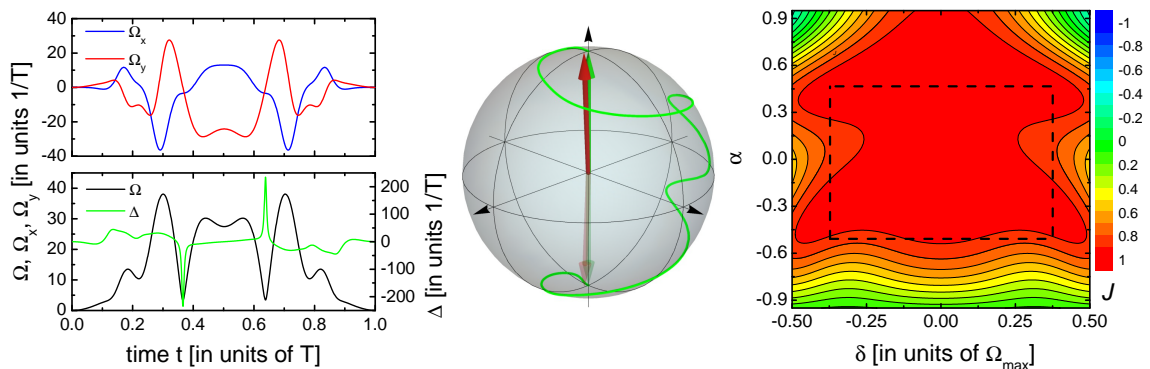


Figure 5.13: (left) Time-dependent shape of the SSSP, i.e. complex Rabi frequency  $\Omega_x$ ,  $\Omega_y$ , real Rabi frequency  $\Omega$  and detuning  $\Delta$  in units of the pulse duration  $T$ . (center) Bloch sphere picture of an SSSP driving a population inversion. (right) Fidelity  $J$  of the single-shot shaped pulse, as defined by coefficients of Table 5.3 with respect to variations in  $\alpha$  and  $\delta$ . Black dotted box indicates the optimization range.

crossing the resonance of the system, comparable to RAP. The third part is negatively detuned otherwise identical to the first part, compensating the phase factor of the first part. Figure 5.13 (center) depicts the SSSP driving a population inversion on the Bloch sphere. For an experimental implementation of SSSP, the rather complex shaped Rabi frequency and detuning have to be controlled with a high precision. In contrast to CP, CAP, or RAP, with their constant relative phases as only control parameters, SSSP requires a much more delicate control over experimental parameters.

### 5.4.2 Experimental Results on Single-Shot Shaped Pulses

We investigate the performance of the SSSP derived in the previous section. We apply the pulses for rephasing of a coherence, prepared by an RF- $\pi/2_0$ -pulse in the hyperfine transition  $|\pm 3/2\rangle \leftrightarrow |\pm 1/2\rangle$  in PrYSO, compare with Section 5.1.1. In the following measurements the coil system #2, described in Section 3.3, is used. The rephasing pulse sequence is comparable to the schematic depicted in Figure 5.2, i.e. the standard Hahn spin echo sequence. The storage time  $\Delta T$  is  $300 \mu\text{s}$ , larger than the dephasing time  $T_{deph}$ . In contrast to Figure 5.2 where the RHD pulse for detection is applied after the total storage time  $\Delta T$ , with the rephasing pulse applied symmetric during the storage, we apply here the detection pulse about  $75 \mu\text{s}$  earlier, i.e. before the coherence are fully rephased. Note that full rephasing is achieved after  $300 \mu\text{s}$ , as the SSSP pulse is applied  $150 \mu\text{s}$  after the coherence preparation.

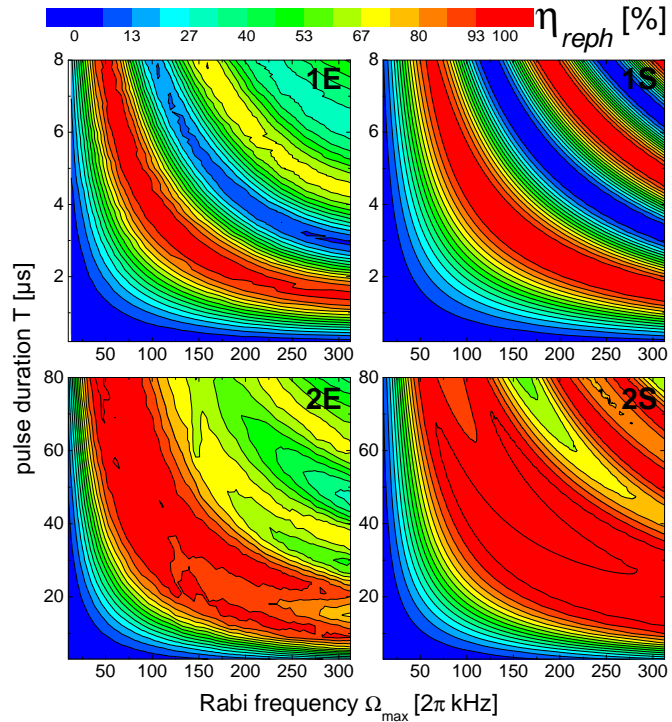
We first investigate the rephasing capability, i.e. rephasing efficiency  $\eta_{reph}$  normalized to the maximal rephasing efficiency of the  $\pi$ -pulse, of the SSSP with respect to variations in the pulse duration  $T$  and the peak Rabi frequency  $\Omega_{\max}$ . We compare the results with the standard Hahn spin echo by a diabatic pulse of rectangular temporal shape. Figure 5.14 (1E) show the rephasing efficiency by standard diabatic pulses. We find regions of high rephasing efficiency for pulse areas of  $\pi$ ,  $3\pi$ , and  $5\pi$  following the expected hyperbola, as the pulse area  $A = \Omega_{\max} T$ . However, high rephasing efficiency is only achieved for precisely defined combinations of peak Rabi frequency  $\Omega_{\max}$  and pulse duration  $T$ , i.e. a low robustness with respect to variations of these experimental parameters. We also find that the maximal rephasing efficiency decreases from the  $\pi$ -pulse towards the  $5\pi$ -pulse, due to averaging effects by the inhomogeneous broadening of the hyperfine transition, and inhomogeneities of the applied RF field, i.e. variations in the applied peak Rabi frequency  $\Omega_{\max}$ .

Figure 5.14 (2E) depicts the rephasing efficiency  $\eta_{reph}$  for the single-shot shaped pulse. We find a broad region of almost constant and high rephasing efficiency. As expected from theory, the highest rephasing efficiencies are achieved for  $\Omega_{\max} T = \text{const.}$  following a hyperbolic behavior. The maximal rephasing efficiencies achieved by  $\pi$ -pulses and single-shot shaped pulses are comparable. However, the rephasing efficiency of SSSPs depends much less upon small variations in the experimental parameters. Note the quite different scales of the pulse durations  $T$ . For diabatic rephasing the pulse duration  $T$  is changed between  $0.2 \mu\text{s}$  and  $8 \mu\text{s}$ , while for the SSSP the pulse durations are a factor of 10 larger. Thus, the SSSP features much better robustness compared to the rephasing by  $\pi$ -pulses.

In order to compare our experimental results on SSSP with the theory, originally derived for a single two-state system, we expanded the numerical simulation, taking into account the inhomogeneous broadening of the hyperfine transition in PrYSO, and inhomogeneities of the RF coil system. The simulations for the corresponding experimental data are shown in Figure 5.14 (1S) and (2S). Experimental data and simulations show a good agreement for the diabatic rephasing. However, the reduced rephasing efficiency for  $3\pi$ , and  $5\pi$ -pulses could not be reproduced by the simulation. Also in the case of the SSSP the simulation shows the over-



Figure 5.14: Rephasing efficiency  $\eta_{reph}$  versus the pulse duration  $T$  and peak Rabi frequency  $\Omega_{max}$  for a diabatic ( $\pi$ )-pulse (1) and the single-shot shaped pulse (2). Experimental data (E) on the left column, and corresponding simulations (S) on the right column. The depicted rephasing efficiency is normalized with respect to the rephasing efficiency achieved with a  $\pi$ -pulse.



all hyperbolic behavior of the experimental data, though smaller structures could not be reproduced. This could be due to the limited frequency bandwidth of the impedance matching used to match the RF coils to the amplifier, which might modify the actual SSSP pulse applied at the coil system.

Second, we investigate the rephasing efficiency  $\eta_{reph}$  versus the pulse duration  $T$  and the static detuning  $\delta$ . For this measurement we kept the Rabi frequency fixed at  $\Omega_{max} = 2\pi \cdot 125$  kHz. Figure 5.15 (3E) show the result for rephasing with the diabatic pulse. We find the highest rephasing efficiency around  $\delta \approx 0$  kHz, and a pulse duration of  $T = 4 \mu\text{s}$ , which fits to  $\Omega_{max} = 2\pi \cdot 125$  kHz for a  $\pi$ -pulse. The efficiency is very sensitive to small deviations from the optimal pulse parameters. The experimental results for the SSSP is depicted in Figure 5.15 (4E). The highest rephasing efficiency is achieved at  $\delta = 0$  kHz and a pulse duration of  $T \approx 30 \mu\text{s}$ . The SSSP features a better robustness with respect to the pulse duration  $T$ , and a comparable robustness with respect to the static detuning  $\delta$ , in comparison to the diabatic rephasing.

Note we found that for static detunings  $\delta \neq 0$  kHz the detected RHD signal is slightly shifted in time. We address this to the effective change of the time dependent detuning of the pulse relative to the transition frequency of the system. Due to the quite linear chirp in the center of the SSSP, a static detuning  $\delta \neq 0$  kHz shifts the position in time when the SSSP crosses the transition of the system, which effectively changes the time the system is rephased. In order to detect the full RHD signal the optical readout pulse is thus applied earlier compared to the expected rephasing of the coherence. Note that this is not necessary if  $N = 2$  rephasing cycles are applied. In this case the time shift introduced by the first off resonant SSSP rephasing cycle is compensated by the second rephasing cycle. We performed numerical simulations including the inhomogeneous broadening of the hyperfine



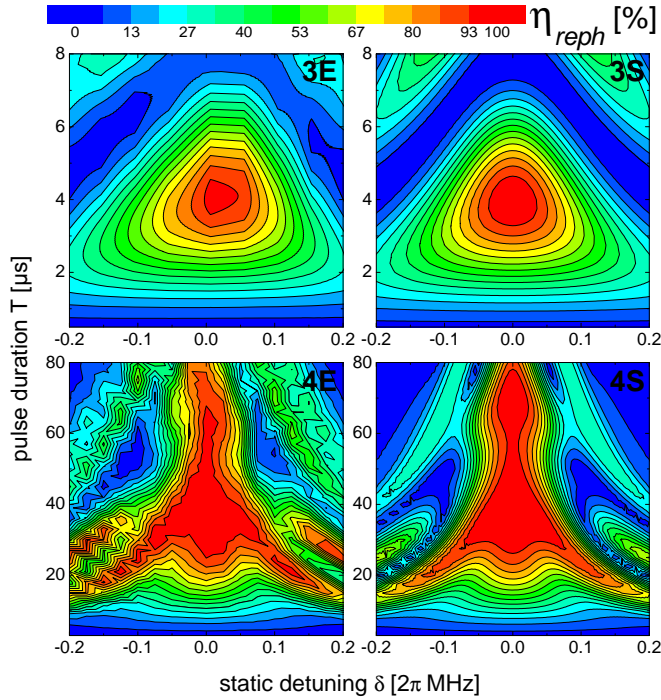


Figure 5.15: Rephasing efficiency  $\eta_{reph}$  versus the pulse duration  $T$  and the static detuning  $\delta$  for a diabatic ( $\pi$ ) pulse (3) and the single-shot shaped pulse (4). The peak Rabi frequency is fixed at  $\Omega_{max} = 2\pi \cdot 125$  kHz. Experimental data (E) on the left column, and corresponding simulations (S) on the right column. The depicted rephasing efficiency is normalized with respect to the rephasing efficiency achieved with a  $\pi$ -pulse.

transition in PrYSO, and inhomogeneities of the RF coil system. Figure 5.15 (3S) and (4S) depict the simulation results for the corresponding experimental data (3E) and (4E). Experimental data and simulations show a very good agreement for the diabatic pulse, as well as for the SSSP pulse. Also, even the small structures of the SSSP experimental data could be reproduced by the simulation.

### 5.4.3 Conclusion

We performed the first experimental demonstration of single-shot shaped pulses, designed to achieve a robust and high-fidelity NOT-quantum-gate operation. These pulses emerge from the ideas of shortcuts to adiabaticity, searching for robust and shorter pathways compared to usual adiabatic passage processes. The derivation combines the advantages from an analytic parametrization with a numerical optimization procedure, which allows a strong reduction of the parameters to be optimized. Here one possible solution with a smooth time dependent Rabi frequency  $\Omega$  and detuning  $\Delta$ , and an optimal pulse area of only  $5.06\pi$  was presented. We applied this SSSP for rephasing of atomic coherences directly prepared by an RF- $\pi/2$ -pulse in the inhomogeneously broadened hyperfine transition of PrYSO. We demonstrated the capability of SSSP to efficiently rephase the prepared atomic coherences. We investigated the robustness of SSSP with regard to variations of the pulse duration  $T$ , the peak Rabi frequency  $\Omega_{max}$ , and the static detuning  $\delta$  and compared the experimental results with diabatic rephasing by a single  $\pi$ -pulses. We found an enhanced robustness especially with regard to variations in pulse duration  $T$  and peak Rabi frequency  $\Omega_{max}$ . Thus, single-shot shaped pulses can be an alternative technique whenever strong fluctuations or variations of experimental parameters, or experimental restrictions on adiabaticity, prevent the usage of diabatic and adiabatic techniques.

## Chapter 6

# Composite Pulses for Dynamic Decoherence Control

So far, we showed advanced composite techniques for rephasing of atomic coherences in an inhomogeneous broadened media, where they feature a high robustness with respect to variations in the experimental parameters, e.g. compared to diabatic  $\pi$ -pulse. As long as the phase evolution of the individual coherences prepared in the inhomogeneous line is reversible, i.e. pure dephasing, these sequences can efficiently rephase the system. However, in many systems the interaction with the environment introduce additional stochastic changes in the phase evolution, compare with Chapter 1 and Section 2.3.4, which lead to irreversible decoherence. One promising technique to avoid decoherence phenomena is dynamic decoherence control (DDC). This technique focuses on the reduction of decoherence by minimizing the interaction of the system with the noisy environment. Effectively the system is decoupled from the environment.

In this chapter we investigate the performance of UCP for DDC, and compare with familiar dynamical decoupling (DD) sequences, e.g. CPMG [131, 132], Knill DD (KDD) [145], UDD [146] and KDD in XY4 [93, 147] sequences. We compare the performance of these DD sequences in the case of directly prepared coherences, by RF- $\pi/2$ -pulses, and coherences generated by the EIT-LS protocol. In addition we experimentally demonstrate recently derived universal robust (UR) sequence for DDC. For simplicity we investigate here only CP (not RAP and SSSP) for DDC. We already saw that CPs perform quite well for rephasing, and are much easier to implement experimentally than RAP and SSSP. Our aim is to determine the DD sequence which yields the best performance for EIT-LS, i.e. with regard to the efficiency. In addition this DD sequence has to work independent of the coherence phase, i.e. with the same fidelity for any arbitrary coherence phase, as the phase information is of high relevance for future applications of EIT light storage.

## 6.1 Implementation of Dynamical Decoupling Sequences

We use dynamical decoupling (DD) sequences in order to reduce decoherence due to system-environment interactions. These DD sequences usually are applied in a series during the total storage time  $\Delta T$ . In order to achieve a fair comparison between different DD sequences, we define three types, with different definitions of a decoupling cycle, see Figure 6.1. For the well known CPMG sequence the

decoupling cycle consists of a single  $\pi_0$ -pulse applied centered during the cycling time  $\tau_c$ . The total storage time is thus given by  $\Delta T = N\tau_c$ , with  $N$  the number of decoupling cycles applied. In order to compare this CPMG DD sequence with other DD sequences based on composite pulses, such as UCP or KDD, we first define time separated DD sequences where the pulses of a CP sequence are applied time separated, each centered during the cycling time  $\tau_c$ . The duration of a full decoupling cycle is thus given by the order  $n$  of the CP sequence times the cycling time  $\tau_c$ , and the total storage time by  $\Delta T = Nn\tau_c$ . This definition allows a fair comparison of CPMG DD sequences and CP DD sequences, as the only difference are the phases imprinted on the pulses of the CP sequence. Second, we define non-time separated sequences, where the full composite pulse is applied without a time separation during the DD cycle with a cycling time  $\tau_c$ , i.e. the usual way CP are applied. Here, the single pulse of the CPMG DD sequence is just replaced by a full CP sequence. Thus the total storage time es given again given by  $\Delta T = N\tau_c$ . As an example, Figure 6.1 depicts time separated and non-time separated DD sequences for a CP sequence consisting of  $n = 3$  pulses. Dynamic decoherence

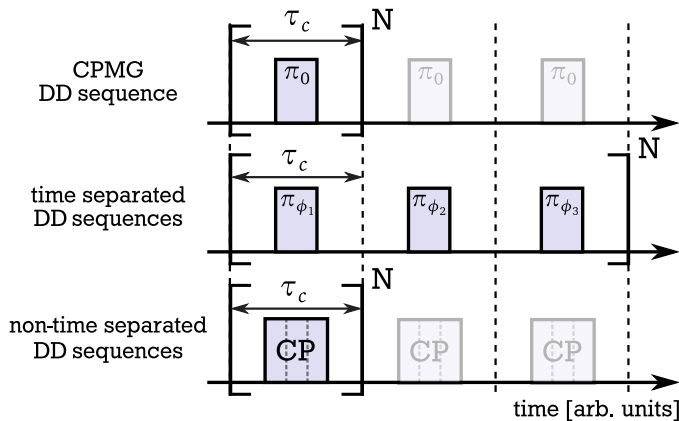


Figure 6.1: Schematic of different decoupling cycles for CPMG DD sequences, time separated DD sequences, and non-time separated DD sequences, here as an example for a CP sequence consisting of  $n = 3$  pulses.

control becomes most effective if the cycling time  $\tau_c$  is much shorter than the correlation time  $\tau_{\text{corr}}$  of the system, i.e. the time scale of system-environment interactions. However, usually one cannot specify a specific time scale of these interactions, but a distribution of time scales on which these interactions occur. Thus, the effectivity of the DD sequences depend strongly on the cycling time  $\tau_c$  with which the pulses can be applied.

## 6.2 DDC for Coherences prepared by RF-Pulses

In the following section we present experimental results on DDC of atomic coherences, which are prepared by RF- $\pi/2$ -pulses in PrYSO. The storage medium is prepared as described in Section 5.1.1. We create a collective coherence by a resonant RF- $\pi/2$ -pulse with a frequency of  $\omega = 2\pi \cdot 10.2$  MHz, a duration of  $\tau = 5 \mu\text{s}$ , and a Rabi frequency of  $\Omega \approx 2\pi \cdot 50$  kHz, covering the inhomogeneous linewidth of the hyperfine transition in PrYSO. Since thermal heating effects arise when we apply many RF decoupling pulses, we use here the RF coil system #2 (compare

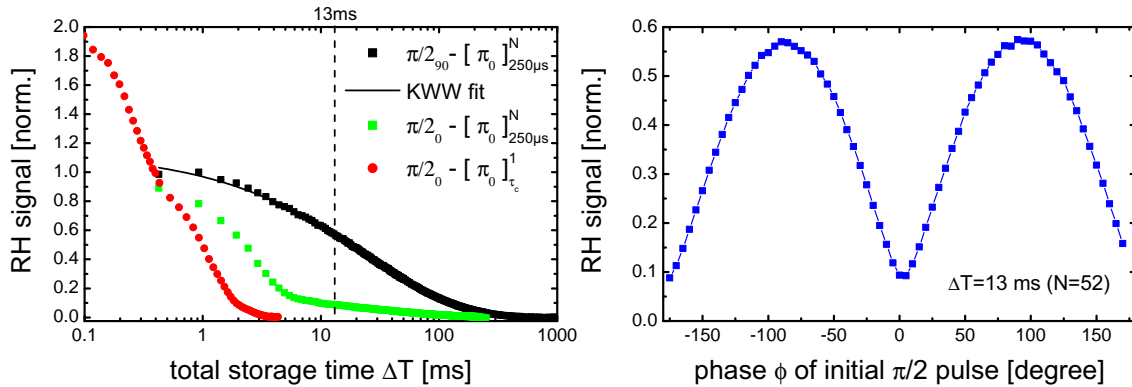


Figure 6.2: (left) Experimental results on CPMG DD. Depicted is the normalized, integrated RH signal versus the total storage time  $\Delta T$  of an initial coherence prepared by an RF- $\pi/2_{90}$ -pulse (black squares) with a fit of an KWW function (black line), and by an RF- $\pi/2_0$ -pulse (green squares). As a reference the coherence lifetime was also determined by a simple HSE experiment (red dots). (right) Integrated RH signal versus the phase  $\phi$  of the initial RF- $\pi/2$ -pulse at a fixed total storage time of  $\Delta T = 13$  ms, i.e.  $N = 52$  decoupling cycles.

with Chapter 3) to minimize eddy currents and apply weaker RF pulses in comparison to Chapter 5 in order to minimize thermal heating effects. The experimental parameters of the decoupling pulses, i.e.  $\pi$ -pulses, are fixed to a pulse duration of  $\tau = 10 \mu\text{s}$  and a Rabi frequency of  $\Omega \approx 2\pi \cdot 50$  kHz. The remaining free experimental parameters are the phases of the decoupling pulses, the type of decoupling cycle, the number of decoupling cycles  $N$  and the cycling time  $\tau_c$ . We detect the collective coherence after a storage time  $\Delta T$  by RH detection, see Section 5.1.1.

In a first measurement we investigate the performance of the CPMG DD sequence [132], consisting of a simple train of  $\pi_0$ -pulses. We fix the cycling time to  $\tau_c = 250 \mu\text{s}$ , and change the total storage time  $\Delta T$  by varying the number of decoupling cycles  $N$ , with  $\Delta T = N\tau_c$ . Figure 6.2 (left) depicts the normalized integrated RH signal versus the total storage time  $\Delta T$  for two different phases  $\phi$  of the initial RF- $\pi/2_\phi$ -pulse. Note that the phase  $\gamma$  of the initially prepared collective coherence is given by  $\gamma = \phi + 90^\circ$ . The coherence decay by a Hahn spin echo is also depicted (red dots) for comparison, leading to a coherence lifetime of about  $580 \mu\text{s}$  confirming previous results [27]. The slight oscillation on the HSE decay might be attributed to a not fully suppressed dark state beating [148].

We find a large increase of the coherence lifetime for the DD sequences compared to the simple HSE. We thus could effectively decouple the system from the environment. However, the coherence lifetime strongly depends on the phase  $\gamma$  of the initially prepared coherence [93, 132]. If the coherence is prepared by a  $\pi/2_{90}$ -pulse (black squares) we observe a single, however stretched exponential decay of the retrieved RH signal. A fitting of Equation 5.1 yields a stretching factor of  $\beta = 0.56$  and an effective coherence lifetime  $T_2 = 25.4$  ms (black line), an increase by a factor of about 50, compared to the coherence lifetime determined by the HSE. If the coherence is prepared by a  $\pi/2_0$ -pulse (green squares), i.e. the coherence features a phase  $\gamma = 90^\circ$  with respect to the decoupling  $\pi_0$ -pulses, we observe a signal decay on a fast and a slow time scale. The fast decay can be attributed to pulse area errors of the decoupling pulses, which in this configuration add up,

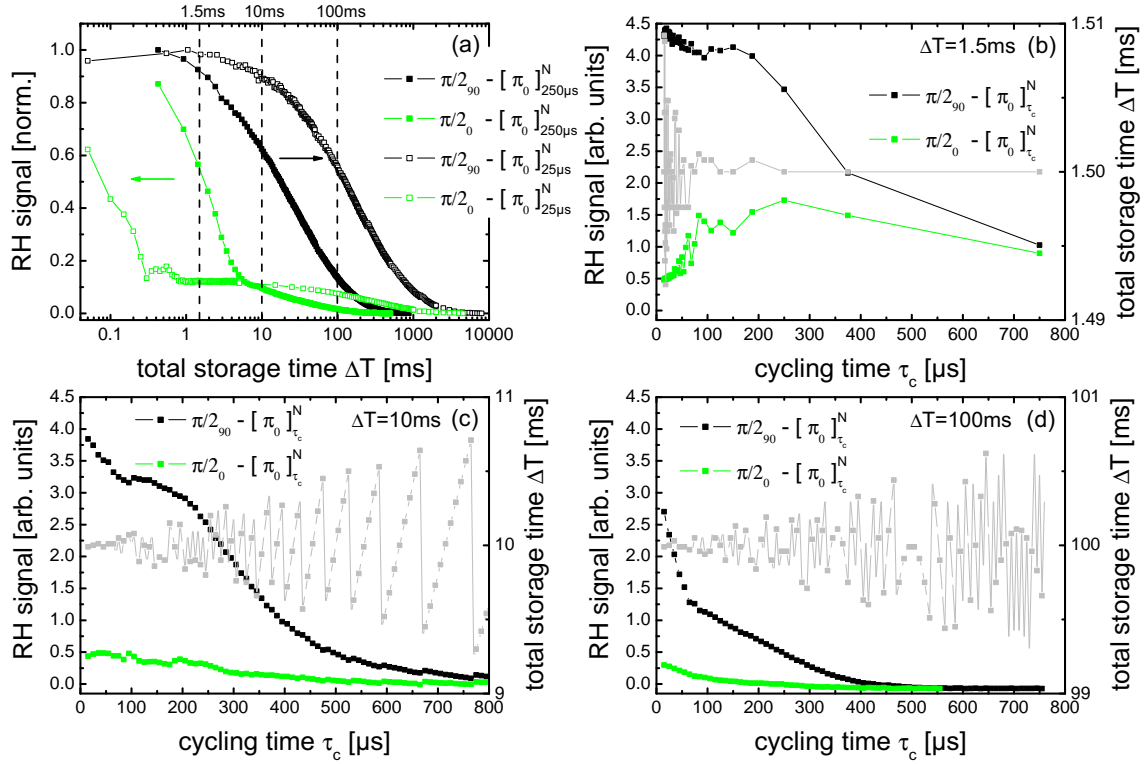


Figure 6.3: (a) Normalized, integrated RH signal versus the total storage time  $\Delta T$  for cycling times  $\tau_c$  of 250  $\mu s$  (solid squares) and 25  $\mu s$  (open squares) prepared by a  $\pi/2_0$ -pulse (green symbols) and a  $\pi/2_{90}$ -pulse (black symbols). (b)-(d) Integrated RH signal versus the cycling time  $\tau_c$  for fixed total storage times  $\Delta T$  of approximately 1.5 ms (b), 10 ms (c), and 100 ms (d). Gray symbol/lines depict the actual total storage time  $\Delta T$ .

and thus lead to a fast reduction of the retrieved signal [132]. Due to these pulse errors, after a few decoupling cycles the phase information of the initial coherence is lost, and the decoupling pulses have mapped a small fraction of the initial coherence onto the axis of rotation of the decoupling pulses, defined by their phase  $\phi$ . Thus, the second decay features the same decay time as the coherence prepared by the  $\pi/2_{90}$ -pulse (black squares), just with a reduced signal. We measured the dependence of the retrieved signal with respect to the phase  $\phi$  of the  $\pi/2$ -pulse, i.e. with respect to the phase  $\gamma$  of the initial coherence at a fixed storage time of 13 ms, i.e. for  $N = 52$  decoupling cycles, see Figure 6.2 (right). We find that the retrieved signal strongly depends on the phase of the initial coherence. We can conclude that the CPMG sequence is not capable to preserve any arbitrary initial state with equal fidelity [93]. CPMG DD works efficiently for one specific initial state only. Moreover, all other initial states are strongly modified due to pulse errors, and finally mapped onto the rotation axis of the decoupling pulses, compare also with Figure 6.7. Thus, the CPMG DD sequence is not suitable to protect an arbitrary quantum state from unwanted interactions with the environment in the presence of pulse errors.

So far we performed CPMG DD with a fixed cycling time  $\tau_c$  of 250  $\mu s$ . This cycling time was already short enough to increase the effective coherence time of the system, i.e. to partially decouple the system from the environment. However,



the degree of decoupling strongly depends on the applied cycling time. In the following, we investigate the effect of the cycling time  $\tau_c$  on the coherence lifetime. Figure 6.3 (a) shows the experimental results for CPMG DD sequences with cycling times  $\tau_c$  of 250  $\mu\text{s}$  (solid squares) and 25  $\mu\text{s}$  (open squares), for an initial  $\pi/2_0$ -pulse (green) and a  $\pi/2_{90}$ -pulse (black). The coherence prepared, by the  $\pi/2_{90}$ -pulse, i.e. onto the axis of rotation of the decoupling pulses, shows a strong increase of the coherence lifetime by a factor of more than 8 towards  $T_2 = 209$  ms, compared to  $\tau_c = 250$   $\mu\text{s}$ , with a similar stretching factor of  $\beta = 0.61$ . For the coherence prepared, by the  $\pi/2_0$ -pulse, i.e. perpendicular to the axis rotation of the decoupling pulses, we find for  $\tau_c = 25$   $\mu\text{s}$  the fast decay to be shifted towards shorter total storage times  $\Delta T$ . For both cycling times the initial coherence is lost after about  $N = 15$  decoupling cycles, i.e. after a total storage time of  $\Delta T = 15\tau_c$ , with a small fraction of the initial coherence mapped onto the axis of rotation of the decoupling pulses. This result confirms the origin of the fast decay, arising from pulse area errors.

In order to further investigate the dependence of the coherence lifetime on the cycling time, we measure the retrieved RH signal versus the cycling time  $\tau_c$  for fixed total storage times  $\Delta T$ , see Figure 6.3 (b-d). Hence, we choose combinations of decoupling cycles  $N$  and cycling times  $\tau_c$  such that  $\Delta T = \text{const}$ . Due to experimental limitations it is not possible to use any desired combination of  $\tau_c$ , and  $N$ , thus the total storage time still varies in the order of a few %. Figure 6.3 (b-d) shows the experimental results for approximate total storage times  $\Delta T$  of 1.5 ms (b), 10 ms (c), and 100 ms (d). For each  $\Delta T$  we vary the cycling time  $\tau_c$  between 15  $\mu\text{s}$  and about 800  $\mu\text{s}$ . We find for the coherence prepared by a  $\pi/2_{90}$ -pulse, it is the best to use as small cycling times as possible, for any  $\Delta T$ , see Figure 6.3 (b-d) (black solid squares). Because pulse area errors do not affect a coherence on the axis of rotation of the decoupling pulses, best decoupling, i.e. reduced decoherence, is achieved for extra short  $\tau_c$ . We also investigated a version of continuous decoupling, i.e. applying a weak, continuous RF field during the whole storage time  $\Delta T$  (not shown here). We found this leads to cooling problems of the PrYSO crystal, due to thermal energy input induced by eddy currents in the crystal mount, which results in a reduction of the coherence lifetime. In Figure 6.3 (d), i.e. at  $\Delta T = 100$  ms, we find for both phases  $\phi$  of the initial  $\pi/2$ -pulse an identical dependence with respect to changes in the cycling time  $\tau_c$ , except from the strong difference in the absolute signal. This confirms the assumption that for an  $\pi/2_0$ -pulse and  $N > 15$  decoupling cycles the coherence is mapped onto the axis of rotation of the decoupling pulses, i.e. coherence at  $\Delta T = 100$  ms feature the same phase  $\gamma$ . In Figure 6.3 (b), i.e. at  $\Delta T = 1.5$  ms, we find a quite different behavior. Up to about  $\tau_c = 250$   $\mu\text{s}$  the retrieved RH signal increases. We attribute the signal reduction at very short cycling times to the pulse area errors of the decoupling sequence, and the reduction towards long cycling times to an insufficient decoupling, and thus to decoherence. For  $\Delta T = 1.5$  s we find the best compromise between both effects, i.e. a efficient decoupling of the system without a reduction due to pulse area errors, at a cycling time of  $\tau_c = 250$   $\mu\text{s}$ . Note that the optimal cycling time strongly depends on the actual total storage time  $\Delta T$ .



In the following, we use UCP [24], see also Section 5.2, for dynamical decoupling. We apply UCP as non-time separated sequences, compare with Figure 6.1. We keep the cycling time fixed at  $\tau_c = 250 \mu\text{s}$ . Figure 6.4 depicts the experimental results for UCP DD. The RH signal is normalized with respect to the maximal signal retrieved by CPMG DD. In a first step we measured the dependence of the RH signal with respect to the phase  $\phi$  of the initial  $\pi/2_\phi$ -pulse at a fixed total storage time of  $\Delta T = 13 \text{ ms}$ . The results are shown in Figure 6.4 (f). At this storage time the decoupling efficiency of the UCPs depends on the phase  $\phi$ , i.e. the initial phase  $\gamma$  of the coherence, comparable to the situation of CPMG DD, depicted in Figure 6.2 (right).

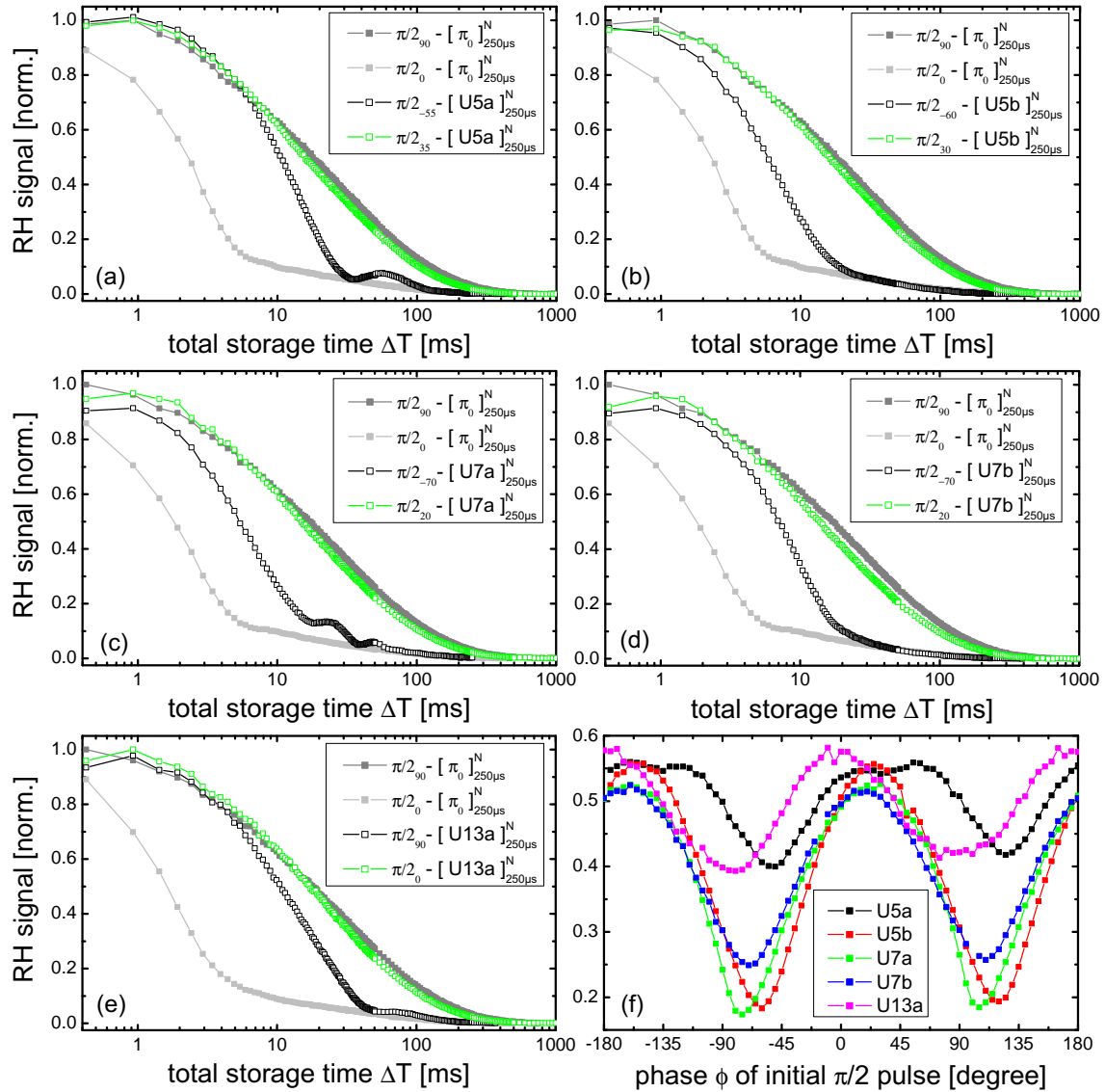


Figure 6.4: Integrated RH signal versus the total storage time  $\Delta T$  for UCP decoupling sequences U5a (a), U5b (b), U7a (c), U7b (d), and U13a (e), for fixed cycling time of  $\tau_c = 250 \mu\text{s}$ . (f) RH signal versus the phase  $\phi$  of the initial  $\pi/2$ -pulse for UCP sequences at a fixed total storage time of  $\Delta T = 13 \text{ ms}$ . The resulting best and worst phases from (f), were used as the phases  $\phi$  of the initial  $\pi/2_\phi$ -pulse for the measurements (a)-(e).



identical to UCP U5b except a global phase shift of  $30^\circ$ . First, we measure the integrated RH signal versus the phase  $\phi$  of the initial  $\pi/2_\phi$ -pulse for a single DD cycle ( $N = 1$ ) (black squares), and  $N = 26$ , corresponding to total storage times of  $\Delta T = 1.25$  ms and 32.5 ms, see Figure 6.5 (right column). We find only a small dependence of the RH signal with respect variations of the phase  $\phi$ . Second, we choose the phases  $\phi$  at which the maximal and minimal RH signal is detected and measure the integrated RH signal with respect to the total storage time  $\Delta T$ , see Figure 6.5 (left column). KDD and UCP U5a show for both phases (black/green open squares) a similar decay with respect to the total storage time  $\Delta T$ . This is reasonable, as U5a and KDD feature very similar phases as control parameters, i.e. the only difference is a  $180^\circ$  phase shift on the second/fourth pulse of the sequence. Thus, UCP DD sequences in a time separated version might be capable to preserve arbitrary coherences with equal fidelity. For KDD a fit of a stretched exponential function yields a effective coherence time of  $T_2 = 11.3$  ms ( $\beta = 0.64$ ). The results for CPMG DD sequences are depicted for comparison. We find the coherence lifetime for these time separated DD sequences to be about a factor of 2 smaller, compared to the best result obtained by the CPMG DD. However, time separated DD sequences are capable to preserve coherences of any phase  $\gamma$ , with a equal fidelity, i.e. they feature an equal phase sensitivity.

In the following, we introduce a new type of time separated DD sequence, bases on composite pulses, i.e universal robust (UR) sequences. These UR sequences have been especially derived to preserve an arbitrary quantum state of a two-state system. Additionally, the UR sequences are designed to be robust with respect to pulse errors. The derivation of the UR sequences is similar to the derivation of the UCP, as described in Section 5.2.1. However, while UCP had been derived to achieve an optimized transition probability, UR sequence are optimized with respect to the fidelity. Moreover, in contrast to UCP, the UR sequences consist of a sequence of a even number  $n$  of time separated pulses with a time of free evolution between the pulses. No additional assumption on the pulses are made. The only control parameter is the relative phase shift  $\phi$  between the pulses. Table 6.1 depicts the phases  $\phi$  for low order symmetric UR sequences, calculated by an analytic formula. A more detailed description of the derivation of UR sequence, and systematic investigation on their robustness with respect to pulse errors can be found in [149].

 Table 6.1: Phases  $\phi$  of symmetric UR DD sequences with  $n$  time separated pulses.

UR sequence	Phases $\phi$
UR4	$(0, 1, 1, 0)\pi$
UR6	$(0, 2, 0, 0, 2, 0)\pi/3$
UR8	$(0, 1, 3, 2, 2, 3, 1, 0)\pi/2$
UR10	$(0, 4, 2, 4, 0, 0, 4, 2, 4, 0)\pi/5$
UR12	$(0, 1, 3, 0, 4, 3, 3, 4, 0, 3, 1, 0)\pi/3$
UR16	$(0, 1, 3, 6, 2, 7, 5, 4, 4, 5, 7, 2, 6, 3, 1, 0)\pi/4$

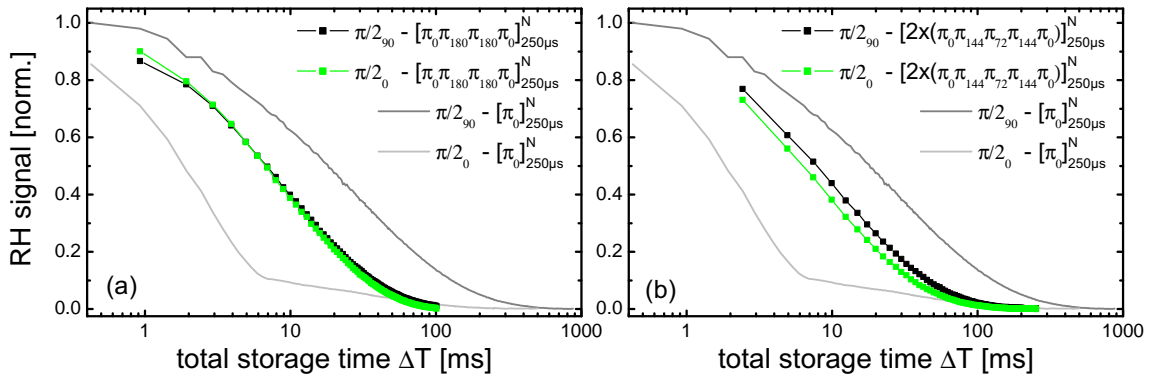


Figure 6.6: Normalized integrated RH signal versus the total storage time  $\Delta T$  for UR4 DD (a), and UR10 DD (d) with a fixed cycling time  $\tau_c$  of  $250 \mu s$ . The coherence was prepared with an  $\pi/2_{90}$ -pulse (black squares/lines), and an  $\pi/2_{0}$ -pulse (green symbols/lines).

Figure 6.6 depicts the experimental results for UR4 (a), and UR10 (b) for a fixed cycling time  $\tau_c$  of  $250 \mu s$ . Note that in these measurements the phases  $\phi$  of the initial  $\pi/2$ -pulses are  $90^\circ$  (black symbols/lines) and  $0^\circ$  (green symbols/lines). The UR DD sequences feature a strong robustness with regard to variations of the phase  $\gamma$  of the coherence, and yield coherence lifetimes comparable to UCP U5a and KDD. However, even high order UR sequences, e.g. UR10 see Figure 6.6 (b), could not substantially increase the coherence lifetime. Thus, further investigations on higher order UR sequences are necessary.

In order to confirm the phase, and state sensitivity of the DD sequences in the presence of pulse errors we performed Bloch simulations, see Figure 6.7. We assumed initial Bloch vectors uniformly distributed on the Bloch sphere, representing any possible initial state, and included an additional inhomogeneous broadening of  $\Gamma = -0.33\Omega \dots 0.33\Omega$ . For each initial Bloch vector we calculated the final Bloch vector, averaged over the inhomogeneous broadening. We applied DD sequences consisting of 240 pulses. Figure 6.7 depicts the final Bloch vectors, i.e. its directions (green dots), on the Bloch sphere for different DD sequences. In addition, the torque vector of the first pulse of the DD sequences is indicated by the red

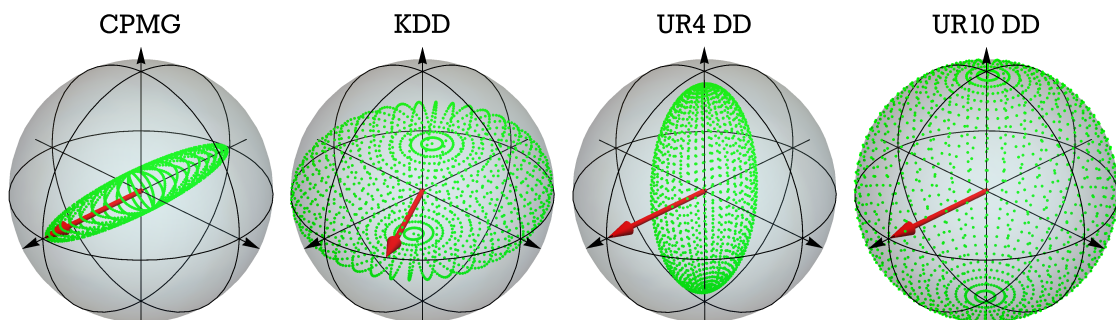


Figure 6.7: Bloch spheres depicting the final Bloch vectors, i.e. its directions (green dots) after 240 pulses for CPMG, KDD, UR4 DD and UR10 DD including an inhomogeneous broadening. The initial Bloch vectors had been distributed uniformly on the Bloch sphere. The torque vector of the first pulse of the DD sequences is indicated by the red arrow.

arrow. We find the final Bloch vectors in the case of CPMG DD strongly confined along the axis of the torque vector, i.e. the axis of rotation of the applied pulses, confirming the projecting behavior of CPMG. Compared to CPMG, KDD shows a reduced state sensitivity without a preferred axis. However, the initial states are still strongly modified by the DD sequence. In contrast UR10 DD is capable to preserve the initial states almost perfectly.

To conclude, we find all measurements for time separated DD sequences to feature coherence lifetimes about a factor of 2 shorter than the best result we achieved with the CPMG DD. However, CPMG DD is not capable to preserve a full quantum state. In contrast, time separated DD sequences are favorable whenever a unknown coherence has to be preserved, or when the phase  $\gamma$  of the coherence is not well defined, as it the case for EIT-LS coherences, compare with Section 5.1.4. We will thus investigate in the following section time separated sequences for dynamical decoupling of coherences prepared by the EIT-LS protocol.

### 6.3 DDC for EIT-LS Coherences

In this section we present experimental results on DDC for coherences prepared by the EIT-LS protocol. We apply the EIT-based light storage protocol in a single probe pass configuration, for details see Chapters 2.3 and 4. We keep the optical sequence fixed, and only vary the total storage time  $\Delta T$ , while applying different DD sequences. We saw in Section 5.1.4, that coherences, i.e. the spin wave  $S(z)$ , prepared using the EIT-LS protocol feature a position dependent phase factor  $\exp(-i\kappa z)$  along the propagation direction of the optical pulses. In our experimental setup this phase factor becomes large enough, so that the collective coherence, i.e.  $S(z)$ , can have a phase that varies between 0 and  $2\pi$  along the propagation axis  $z$ . Considering these coherence properties, we apply in the following only time separated DD sequences which do not feature a significant dependence regarding the phase  $\gamma$  of the coherences. The RF- $\pi$ -pulses used for the DD sequences feature, like in the previous section, a duration of  $\tau = 10 \mu\text{s}$ , a Rabi frequency of  $\Omega \approx 2\pi \cdot 50 \text{ kHz}$ , and are applied resonant to the relevant ground state hyperfine transition.

Figure 6.8 depicts the EIT-LS efficiency  $\eta_{\text{EXP}}$  versus the total storage time  $\Delta T$ , for different DD sequences applied with cycling times  $\tau_c$  of 15  $\mu\text{s}$  (a), 25  $\mu\text{s}$  (b), and 50  $\mu\text{s}$  (c). The light storage efficiency  $\eta_{\text{EXP}}$ , takes into account the efficiency of the DD sequences and decoherence processes in the system, compare with Section 2.3.3. We perform measurements for several time separated UR sequences. We compare UR DD with CPMG DD, and a KDD in XY4 sequence [147], which is often considered the state of the art DD sequence to preserve an arbitrary quantum state. UR, and KDD in XY4 lead to a higher light storage efficiency  $\eta_{\text{EXP}}$  in comparison to CPMG DD, for storage times  $\Delta T$  up to about 20 – 30 ms depending on the cycling time  $\tau_c$ , and the order of the UR sequence, see Figure 6.8. For  $\tau_c = 15 \mu\text{s}$  (a), we find that with higher order UR sequences longer storage times can be achieved, and the crossing of CPMG DD and UR DD is shifted from about 10 ms for UR8 towards 30 ms for UR16.



Moreover, we find that UR12 and UR16 show even a better performance than the KDD in XY4 sequence. For long total storage times  $\Delta T > 30$  ms CPMG DD performs best. However, note that CPMG DD is not for quantum storage in situation including pulse errors, and might thus not preserve the initially prepared spin wave  $S(z)$  with its  $z$ -dependent phase, compare with Sections 2.3.3 and 5.1.4. CPMG DD might modify  $S(z)$ , and for long total storage times only preserve coherences of specific phases, i.e. optimal for the CPMG DD. Thus, the spin wave  $S(z)$  might be only preserved at specific positions  $z$  along the propagation axis of the probe pulse. In addition, we saw in the previous section that CPMG DD, for large number of decoupling cycles  $N$ , partially maps coherence with non-optimal phases  $\gamma$  onto the axis of rotation, i.e. the phase  $\phi$ , of the decoupling pulses. Thus, the spin wave  $S(z)$  might feature a rendered phase distribution along the  $z$ -axis for long storage times  $\Delta T$ , such that upon readout the individual coherences might partially interfere destructively, which leads to a reduced, non-maximal signal pulse. With an increase of the cycling time  $\tau_c$  we find for CPMG DD, KDD in XY4, UR12, and UR16 DD slightly faster decays of the light storage efficiency  $\eta_{\text{EXP}}$ . In contrast, the UR4 and UR8 DD feature a increase of the decay time, for larger cycling times  $\tau_c$ . This behavior might be due to decoherence during a single DD cycle, and pulse errors. For UR16 with a cycling time of  $50 \mu\text{s}$  a single DD cycle features a duration of  $800 \mu\text{s}$ , while UR8 has only a cycle duration of  $400 \mu\text{s}$ . Thus, phase fluctuations due to system-environment interactions effect higher order, i.e. longer DD sequences much stronger than shorter DD sequences. This especially becomes important for longer cycling times  $\tau_c$ . For example we find at  $\tau_c = 50 \mu\text{s}$  the best result to be achieved by UR12 DD, instead of UR16 DD. Thus, there is a trade-off between higher order sequences which compensate pulse errors better, and lower order sequence that suffer less from decoherence. As there exists an analytic for-

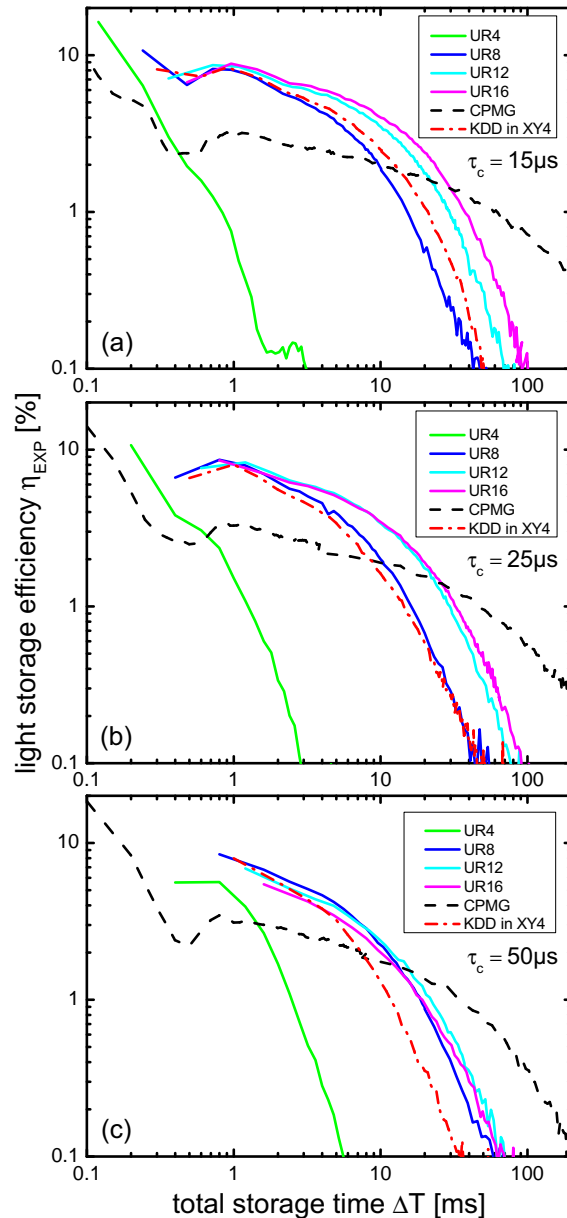


Figure 6.8: EIT-LS efficiency  $\eta_{\text{EXP}}$  versus the total storage time  $\Delta T$  for cycling times of  $15 \mu\text{s}$  (a),  $25 \mu\text{s}$  (b), and  $50 \mu\text{s}$  (c), of different time separated DD sequences.



mula to calculate the phases of any order UR DD sequence it becomes possible to adjust the order, and the cycling time  $\tau_c$  to the experimental setup and the system-environment interactions, to achieve an optimal decoupling.

With UR DD we could achieve up to factor of 2 longer total storage times (1/e-times) compared to KDD in XY4. The light storage efficiency  $\eta_{\text{EXP}}$  increased by up a factor of 4.5, compared to KDD in XY4 at a  $\Delta T \sim 26$  ms. In addition, we found that at short total storage times of about 1 ms UR DD can achieve about a factor of 3 higher storage efficiencies. Thus, UR DD clearly outperform CPMG DD, and KDD in XY4 sequences for dynamic decoherence control. A comparison with [23] shows that our memory features quite well storage times, taken into account that no static decoherence control techniques, like ZEFOZ [22] were applied.

## 6.4 Conclusion

In this chapter we investigated composite pulses for robust dynamic decoherence control in PrYSO. In particular, we investigated the performance of universal composite pulses (UCP), and universal robust (UR) sequences applied as dynamical decoupling sequences. We further compared with well known DD sequences, such as the CPMG DD, KDD, and KDD in XY4. First, we performed systematic measurements on CPMG DD for different RF prepared coherences. We found a strong dependence of coherence lifetime with respect to the phase  $\gamma$  of the prepared coherence. We investigated the influence of different cycling times  $\tau_c$ . As expected, we found for shorter cycling times  $\tau_c$  longer coherence lifetimes, i.e. a better decoupling of the system from the environment. However, we also found that pulse errors can strongly reduce the coherence lifetime if the phase  $\gamma$  of the coherence is chosen such that pulse errors can accumulate. Second, we applied UCP as non-time separated DD sequences, and compared with CPMG DD at equal cycling times. We found UCP to be able to compensate for pulse area errors. Up to about  $N = 20$  DD cycles UCP do not show a phase sensitivity. At long total storage times UCP sequences also depend on the phase  $\gamma$  of the coherence. Third, we performed measurements of time separated DD sequences such as KDD, and UR DD. We found that with a time separation the phase dependence is reduced, however also the coherence lifetime becomes about a factor of 2 shorter compared to the best results achieved by CPMG DD.

Finally we applied time separated sequences for DD of coherences prepared by the EIT-LS protocol. Time separated UR DD, and KDD in XY4 for dynamical decoupling of EIT-LS coherences for different cycling times  $\tau_c$  were investigated. We achieved about a factor of 3 higher storage efficiencies at short storage times of about 1 ms compared to the best results by CPMG DD. In addition, we found that high order UR DD perform better than the state of the art KDD in XY4 sequence. Overall, we could achieve about a factor of 4.5 higher storage efficiencies at long storage times, and about a factor of 2 longer coherence lifetimes. Future investigations will focus on higher order DD sequences, in combination with ZEFOZ, also applied in other storage media, e.g. EuYSO.

## Conclusion and Prospects for Future Work

The present work deals with techniques to improve the EIT-based light storage in an all solid-state memory, i.e. a rare-earth ion-doped PrYSO crystal. The performance of such a memory can be defined by its capability to store light pulses with high efficiency and for long storage durations. In general, the storage efficiency is theoretically limited by the EIT-LS protocol efficiency, while the storage duration is limited by decoherence processes in the solid-state memory. Thus, we first optimized the EIT-LS efficiency at short storage durations. We then investigated the performance of composite and adiabatic techniques for efficient and robust rephasing and finally applied composite techniques for DDC to extend the coherence lifetime in our storage medium.

**Optimization of the EIT Light Storage Efficiency:** In order to optimize the EIT-LS protocol we performed systematic measurements of the EIT-LS efficiency in a PrYSO crystal featuring an optical depth  $d$  of 6. The optical depth sets the theoretical limit of the EIT-LS protocol efficiency. We experimentally optimized the efficiency by systematic variations of the control pulse power and the probe pulse duration. Furthermore, we applied an iterative algorithm, to optimize the temporal shape of the probe pulse. We found a maximal protocol efficiency  $\eta_{\text{EIT}} = 36\%$ , comparable to the theoretical limit. In order to increase the optical depth  $d$ , we developed a multipass setup for the probe beam, consisting of a ringlike arrangement, which is compatible with the geometrical constraints given by the existing setup. This multipass setup allows the simple variation of the number of probe passes  $N$  through the crystal and thus enables a flexible change of the effective optical depth  $d_N = d \cdot N$ . With this setup we achieved up to 16 probe passes through the PrYSO crystal, which corresponds to an increase of the effective optical depth  $d_N$  from 6 to 96. We experimentally optimized the EIT-LS efficiency at variable optical depths. At  $N = 14$ , i.e. an effective optical depth of about 84, we achieved an EIT-LS efficiency of  $\eta_{\text{EIT}} = (76.3 \pm 3.5)\%$  in forward retrieval configuration, reaching previous values in an EIT-driven memory of cold atoms [89] and achieving the highest ever obtained EIT-LS efficiency in a solid-state memory [23]. However, due to losses at the optical components, the setup efficiency  $\eta_{\text{setup}}$  was limited to about 25.2% at  $N = 2$ . As future work will focus on the storage of few photons, it will thus be necessary to improve the optical components, to achieve adequate detection efficiencies. It might also be useful, to further investigate possibilities for backward readout configurations combined with a multipass probe setup.

**Composite and Adiabatic Rephasing of Atomic Coherences:** In order to extend the EIT-LS duration of our memory towards the coherence lifetime, we implemented composite and adiabatic rephasing techniques, exhibiting an improved robustness regarding variations and fluctuations of experimental parameters. We investigated their performance regarding experimental variations, in an application

for rephasing of atomic coherences in the inhomogeneously broadened hyperfine transition of PrYSO. First, we applied universal composite pulses (UCP). UCP were originally designed for robust and high-fidelity population inversion in a two-state system, compensating simultaneous variations in *any* type of experimental parameter. We have experimentally shown that UCP exhibit an enhanced robustness to variations in several experimental parameters. Using UCP we could increase the higher rephasing efficiency about 25 %, compared to diabatic  $\pi$  pulses. UCP can be useful whenever significant unknown experimental variations or fluctuations prevent the application of diabatic  $\pi$  pulses. Second, we demonstrated a first experimental implementation of composite adiabatic passage (CAP) [25]. Essentially, CAP is a composite version of RAP, consisting of a sequence of RAP pulses with appropriately chosen relative phases. CAP was proposed to improve RAP in situations of fairly fulfilled adiabaticity. We compared the performance of CAP and RAP at different degrees of adiabaticity. In particular, we systematically investigated their performance with respect to variations in pulse duration and static detuning. We found CAP to be able to compensate for weak adiabaticity, leading to constant and high rephasing efficiency, irrespectively of the exact choice of the experimental parameters. These properties of CAP can be of interest whenever robust state manipulations are required, while sufficient adiabaticity cannot be provided, e.g. due to experimental restrictions. Third, we performed a first experimental demonstration of single-shot shaped pulses (SSSP), derived from techniques on shortcuts to adiabaticity. We demonstrated the capability of SSSP for efficient and robust rephasing and compared our results with diabatic  $\pi$  pulses. A further comparison with other adiabatic techniques might be necessary to provide a broader insight on SSSP. All three presented techniques can be used to improve the robustness of an population inversion or rephasing process. However, different requirements on the control of the experimental parameters have to be fulfilled. UCP, and CAP rely on identical pulses and a precise relative phase control, i.e. within a few degrees. CAP in addition needs a simple control of the time-dependent detuning. The complex time-dependent Rabi frequency and detuning of SSSP require a much more sophisticate control of experimental parameters. Thus, the choice of an adequate technique strongly depends on the actual experimental situation, i.e. on the experimentally controllable parameters.

**Composite Pulses for Dynamic Decoherence Control:** We investigated the performance of UCP and universal robust (UR) sequences for DDC of directly RF-prepared coherences. We compared our results with well known CPMG DD and KDD sequences. We performed systematic measurements with respect to the cycling time, the phase of the coherence and the order of UCP and UR DD sequence. We found time separated UR DD sequences to be robust with respect to the phase of the coherence. We applied these DD sequences on EIT-LS coherences and compared with CPMG DD and KDD in XY4 [147]. Our experiments showed that our UR DD sequences can outperform the often considered state-of-the-art KDD in XY4 sequence, yielding about a factor of 2 longer coherence lifetimes. Combining our results on optimized EIT-LS with advanced composite DD sequences and static decoherence control by ZEFOZ might provide a major step towards the development of an all solid-state quantum memory.

## Zusammenfassung

Diese Dissertation ist Teil eines Projektes, mit dem Ziel der Entwicklung eines zuverlässigen und effizienten Quantendatenspeichers zur optischen Quanteninformationsverarbeitung [1]. Die Verarbeitung von Quanteninformationen bietet die Chance die klassische Datenverarbeitung und moderne Kommunikationsnetze, mit ihren beschränkten Möglichkeiten zur Steigerung von Rechenleistung und Speicherkapazität, ablösen zu können. Ein häufig diskutierter Ansatz stellt die Wechselwirkung von Photonen als Informationsträger mit atomaren Systemen dar, deren Eigenschaften durch quantenmechanische Gesetze bestimmt sind und damit die Fähigkeit besitzen quantenmechanische Superpositionszustände tragen zu können. Zur Realisierung einer vollständig quanten-optischen Informationsverarbeitung wird daher ein optischer Quanten-Datenspeicher benötigt.

Die vorliegende Arbeit beschäftigt sich mit der Entwicklung und Optimierung eines solchen optischen Quanten-Datenspeichers, auf Basis eines seltenerd-dotierten Kristalls. Als Speichermedien besitzen seltenerd-dotierte Kristalle vorteilhafte spektroskopische Eigenschaften, insbesondere geringe Wechselwirkungen und damit schmale homogene Linienbreiten, ähnlich kalter atomarer Gase. Sie zeichnen sich darüber hinaus durch ihre einfache Handhabung und ihre Skalierbarkeit aus und eignen sich daher gut für den Einsatz in Anwendungen außerhalb der Grundlagenforschung. In den letzten Jahrzehnten wurde eine Vielzahl unterschiedlicher Protokolle zur Speicherung quanten-optischer Information [5–7] entwickelt. In dieser Arbeit kommt ein Protokoll, basierend auf dem Effekt der elektromagnetisch induzierten Transparenz (EIT), zum Einsatz. Dieses ermöglicht es einen Informationen tragenden Lichtpuls (Speicherpuls) in eine kollektive atomare Kohärenz des Speichermediums zu übertragen. Speichereffizienz und maximale Speicherzeit werden im Allgemeinen durch das verwendete Speicherprotokoll und das Speichermedium definiert. Das Ziel dieser Arbeit war die Optimierung eines solchen EIT-basierten quanten-optischen Datenspeichers realisiert in einem Praseodym-dotierten Yttrium-ortho-Silikat (PrYSO) Kristall.

Zunächst wurde die Speichereffizienz des EIT Lichtspeicherprotokolls optimiert. Hierzu wurden systematische Untersuchungen der EIT Speichereffizienz durchgeführt. Die EIT Speichereffizienz wird im Allgemeinen durch die optische Dichte des Speichermediums begrenzt. Seltenerd-dotierte Kristalle zur Datenspeicherung besitzen in der Regel relativ geringe Dotierungsgrade und damit geringe optische Dichten um spannungsinduzierte Linienverbreiterungen zu minimieren. Der hier verwendete PrYSO Kristall wies eine optische Dichte von 6 auf. Bei gegebener optischer Dichte wird die Speichereffizienz durch die Parameter von Kontroll- und Speicherpuls bestimmt. Es wurden daher zunächst die experimentellen Parameter von Kontroll- und Speicherpuls systematisch variiert und die Lichtspeichereffizienz optimiert. Die maximal erreichte EIT Speichereffizienz

betrug  $\eta_{\text{EIT}} = 36 \%$  und ist vergleichbar mit theoretisch ermittelten maximalen Speichereffizienzen bei optischen Dichten  $\sim 6$ . Um die Speichereffizienz weiter steigern zu können wurden verschiedene Ansätze zur Erhöhung der optischen Dichte diskutiert. Es wurde ein optischer Ring entwickelt um den Speicherpuls mehrfach durch den PrYSO Kristall leiten zu können. Dieser erlaubt eine variable Einstellung der Anzahl der Durchläufe  $N$  des Speicherpulses durch den PrYSO Kristall. Es ergibt sich eine effektive optische Dichte  $d_N = d \cdot N$ . Die EIT Speichereffizienz wurde für verschiedene effektive optische Dichten optimiert. Für  $N = 14$  und einer effektiven optischen Dichte von 84 wurde eine EIT Speichereffizienz von  $\eta_{\text{EIT}} = (76.3 \pm 3.5) \%$  erreicht. Dies entspricht aktuell der höchsten Speichereffizienz realisiert mittels EIT in einem Festkörper [23].

Im zweiten Teil dieser Arbeit wurden komposite und adiabatische Techniken zur Verlängerung der Speicherzeit untersucht. In PrYSO wird die maximale Speicherzeit durch die Lebensdauer der atomaren Kohärenzen bestimmt. In der Regel liegen die erreichbaren Speicherzeiten einige Größenordnungen unter dem theoretischen Maximum. Die atomaren Kohärenzen werden in einem inhomogen verbreiterten Hyperfeinübergang präpariert. Dies führt zu unterschiedlicher Phasenevolution der einzelnen Kohärenzen. Dieser Effekt ist als Dephasierung bekannt und verhindert ein effektives Auslesen der Information für Speicherzeiten länger als die Dephasierungszeit. Häufig werden diabatische  $\pi$ -Pulse zur Rephasierung eingesetzt. Diese benötigen jedoch für eine effiziente Rephasierung präzise definierte Pulsparameter und verfügen lediglich über eine geringe Stabilität gegenüber Variationen experimenteller Parameter. In der Kern-Spin-Resonanz werden komposite Pulse seit langem eingesetzt um Pulsfehler und Inhomogenitäten zu kompensieren [72]. Allerdings können die meisten kompositen Pulse lediglich spezielle Formen von Pulsfehlern kompensieren.

In dieser Arbeit wurden zunächst *universal composite pulses* (UCP) zur Rephasierung atomarer Kohärenzen untersucht. UCP zeichnen sich dadurch aus, dass sie in der Lage sind jede Art von Inhomogenität oder Variation von Pulsparametern kompensieren zu können. In systematischen Messungen konnte gezeigt werden, dass UCP, im Vergleich zu  $\pi$ -Pulsen, eine deutlich höhere Stabilität gegen Variationen von experimentellen Parametern aufweisen. Insbesondere konnte gezeigt werden, dass UCP zur gleichzeitigen Kompensation verschiedener Arten von Pulsfehlern eingesetzt werden können. Die Rephasierungseffizienz konnte im Vergleich zu einfachen  $\pi$ -Pulsen um bis zu 25 % gesteigert werden.

Weiterhin wurden zwei adiabatische Techniken zur Rephasierung atomarer Kohärenzen untersucht. Diese weisen, solange die Adiabatiebedingung ausreichend erfüllt ist, eine hohe Stabilität gegenüber Schwankungen von experimentellen Parametern auf. Allerdings werden dazu häufig relativ lange Wechselwirkungszeiten benötigt. Kann die Adiabatiebedingung nur unzureichend erfüllt werden, nimmt ihre Stabilität gegenüber experimentellen Schwankungen deutlich ab. Um adiabatische Prozesse unter solchen Bedingungen verwenden zu können wurde von Torosov *et al.* [25] die Verwendung eines kompositen adiabatischen Prozesses, *composite adiabatic passage* (CAP), vorgeschlagen. CAP ist eine komposite Erweiterung von *rapid adiabatic passage* (RAP) und wurde zur Optimierung unzureichend adiabatischer Prozesse entwickelt. In dieser Arbeit wurde eine erste



experimentelle Implementierung von CAP vorgestellt. Es wurden systematische Messungen zur Rephasierungseffizienz von RAP und CAP bei unterschiedlich erfüllter Adiabatiebedingung durchgeführt. Es konnte gezeigt werden, dass CAP auch bei unzureichender Adiabatie eine hohe und stabile Rephasierungseffizienz liefert, unabhängig von der genauen Wahl der Pulsparameter. Des Weiteren wurden *single-shot shaped pulses* (SSSP) zur Rephasierung eingesetzt. Diese Pulse basieren auf der Idee, einer Reduzierung der Wechselwirkungsdauer adiabatischer Prozesse. Es konnte gezeigt werden, dass SSSP zur Rephasierung eingesetzt werden können und im Vergleich zu  $\pi$ -Pulsen, ein robusteres Verhalten aufweisen. Ein weiterer Vergleich mit RAP und CAP steht noch aus.

Die in dieser Arbeit untersuchten Rephasierungstechniken unterscheiden sich insbesondere in der benötigten Kontrolle über die verschiedenen experimentellen Parameter. Zur Implementierung von UCP werden lediglich identische Pulse und eine relative Phasenkontrolle zwischen den Pulsen, mit einer Genauigkeit von wenigen Grad, vorausgesetzt. Die relativen Phasenänderungen sollten möglichst instantan umgesetzt werden können. Die zeitliche Pulsform spielt hier keine Rolle. Für CAP ist neben der Phasenkontrolle zusätzlich eine zeitlich variable Verstimmung erforderlich. Für SSSP muss ein komplexer zeitlicher Verlauf der Rabi-Frequenz und der Verstimmung experimentell umgesetzt werden können. Hierfür wird eine möglichst exakte und schnelle Kontrolle der experimentellen Parameter benötigt. Die Wahl einer bestimmten Rephasierungstechnik, wird daher neben den zu kompensierenden Inhomogenitäten des Systems, entscheidend von der möglichen Kontrolle der verschiedenen experimentellen Parameter bestimmt.

Neben der reversiblen Dephasierung treten in PrYSO stochastische Phasenänderungen einzelner Kohärenzen auf, die durch eine einfache Rephasierung nicht kompensiert werden können. Diese begrenzen die Kohärenzzeit in der Regel auf  $500 \mu\text{s}$ . Solche Phasenänderungen können nicht unterdrückt werden, allerdings ist es möglich statische und dynamische Techniken anzuwenden, die den Einfluss dieser Phasenänderungen auf die Kohärenzzeit minimieren [22]. Die dynamische Dekohärenzkontrolle basiert auf der schnellen und häufigen Wechselwirkung von Invertierungspulsen mit den präparierten Kohärenzen. Meistens werden dazu identische  $\pi$ -Pulse verwendet, die mit einer Wiederholrate größer als die Zeitskala der stochastischen Phasenänderungen eingestrahlt werden. Pulsfehler der eingestrahlten  $\pi$ -Pulse können die Effizienz der dynamischen Dekohärenzkontrolle reduzieren. Es wurden daher in dieser Arbeit komposite Pulse zur dynamischen Dekohärenzkontrolle eingesetzt. Insbesondere wurden UCP und *universal robust* (UR) Sequenzen untersucht und die Ergebnisse mit bekannten Sequenzen zur dynamischen Entkopplung, wie CPMG, KDD und KDD in XY4, verglichen. Die hier vorgestellten UR Sequenzen konnten die erreichten Speicherzeiten, im Vergleich zu KDD in XY4 [147], nochmals um einen Faktor 2 steigern.

Die Kombination, der in dieser Arbeit vorgestellten Ergebnisse, hoher EIT Lichtspeichereffizienzen und moderner Techniken zur dynamischen Dekohärenzkontrolle, mit statischer Dekohärenzkontrolle soll in Zukunft eingesetzt werden um Lichtpulse mit wenigen Photonen speichern zu können. Die Ergebnisse dieser Arbeit stellen somit einen wichtigen Schritt zur Entwicklung eines Festkörperbasierten Quantendatenspeichers dar.



## Appendix A

### Additional Experimental Results on SSSP

Figure A.1 shows additional experimental results, regarding the robustness of SSSP, as introduced in Section 5.4, with respect to variations of static detuning and Rabi frequency. We measured the rephasing efficiency  $\eta_{reph}$ , normalized to the efficiency of a  $\pi$  pulse rephasing, with respect to the static detuning  $\delta$  and the peak Rabi frequency  $\Omega_{max}$  for a diabatic pulse (a) with a duration of  $\tau = 4 \mu s$  and the SSSP (b) defined by the coefficients of Table 5.3 with a pulse duration of  $T = 48 \mu s$ . The SSSP features a enhanced robustness with respect to variations of peak Rabi frequency  $\Omega_{max}$ , compared to the diabatic pulse. We find a slight shift, of both the rephasing profiles, towards positive static detunings for high peak Rabi frequencies, which might be due to a small Stark shift induced by the driving fields. However, further investigations are needed in order to determine the origin of this shift.

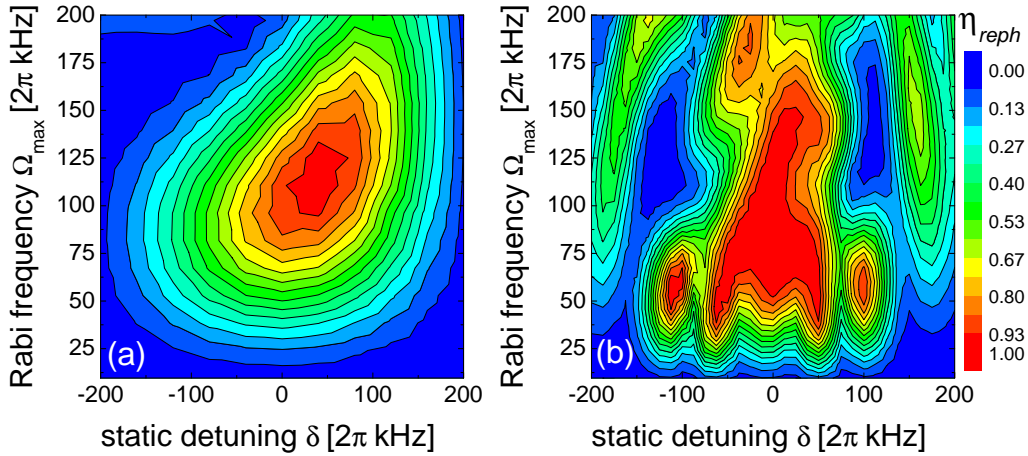


Figure A.1: Rephasing efficiency  $\eta_{reph}$  versus static detuning  $\delta$  and peak Rabi frequency  $\Omega_{max}$  for a diabatic pulse of duration  $\tau = 4 \mu s$  (a) and the SSSP (b) as defined by the coefficients of Table 5.3.

Table A.1: Coefficients  $C_n$  and  $\theta_m$  from the numerical optimization, defining the single-shot shaped pulse, optimized for variations  $\alpha = [-0.5...0.5]$ , and  $\delta = [-0.375\Omega_{\max}...0.375\Omega_{\max}]$ , with  $\Omega_{\max}$  the peak Rabi frequency of the pulse.

$C_1$	$C_2$	$C_3$	$C_4$	$C_5$	pulse area [in units of $\pi$ ]
2.0624	-1.7585	0	0	0	4.06
$\theta_1$	$\theta_2$	$\theta_3$	$\theta_4$	$\theta_5$	fidelity $\bar{J}$
-0.1074	-0.0991	-0.0129	-0.0389	0	0.88

Besides the measurements on the SSSP defined by the coefficients of Table 5.3, we also performed experiments on an SSSP with an even lower pulse area of only  $4\pi$ . This SSSP was derived by the optimization procedure introduced in Section 5.4, with an additional constraint on the peak Rabi frequency  $\Omega_{\max}$ . Table A.1 depicts the coefficients defining this SSSP. Figure A.2 depicts the obtained experimental results for this SSSP. We measured the rephasing efficiency  $\eta_{reph}$  with regard to the peak Rabi frequency  $\Omega_{\max}$ , the pulse duration  $T$  (a), and the static detuning  $\delta$  (b). The pulse features a comparable rephasing profile as the SSSP investigated in Section 5.4.2. However, we find a slightly reduced robustness regarding variations of the experimental parameters.

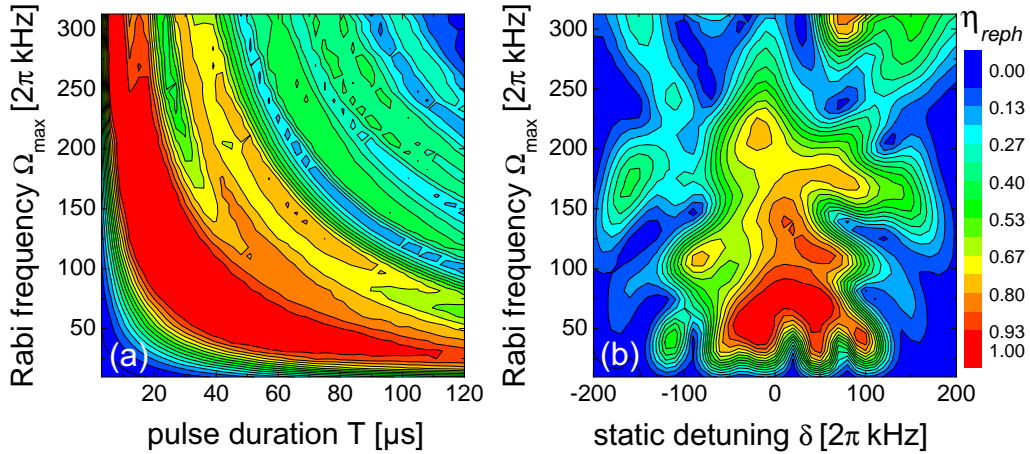


Figure A.2: Rephasing efficiency  $\eta_{reph}$  versus pulse duration  $T$  and peak Rabi frequency  $\Omega_{\max}$  (a), and versus static detuning  $\delta$  and peak Rabi frequency  $\Omega_{\max}$  with  $T = 48 \mu s$  (b) for the SSSP defined by the coefficients of Table A.1.

## Appendix B

### Investigations on Stimulated Photon Echos

Most diabatic  $\pi$ -pulses suffer due to pulse area errors. If these errors become large, for example in a strongly inhomogeneous broadened transition, it might be that an applied  $\pi$ -pulse actually acts as a  $\pi/2$ -pulse for far detuned ensembles. For a HSE sequences with  $N \geq 2$  rephasing cycles, the retrieved RHD signal can thus feature contributions from an stimulated photon echo (SPE) process [150]. SPE maps the prepared coherence by an  $\pi/2$ - pulse onto a population distribution. After a storage time another  $\pi/2$ -pulse maps this population distribution back into a coherence which then rephases and produces an simulated photon echo signal. For  $N = 2$  rephasing cycles it is possible to distinguish between HSE and SPE. Figure B.1 depicts the schematic timing sequences for  $N = 2$  rephasing cycles, with an additional time shift of the initial  $\pi/2$ -pulse. This asymmetric sequence allows us to distinguish between HSE and SPE signal. We used this asymmetric

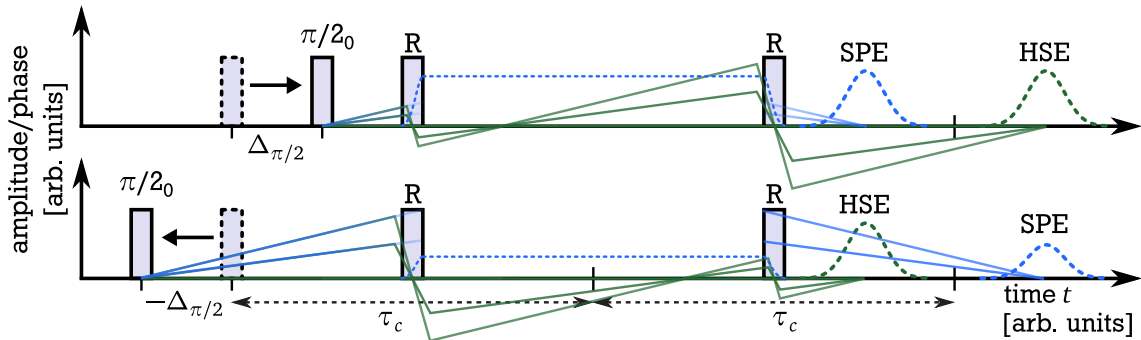


Figure B.1: Schematic pulse timing sequences to distinguish between HSE and SPE, with R the rephasing  $\pi$ -pulses for HSE, and the mapping  $\pi/2$ -pulses for SPE. (Top) The initial  $\pi/2$ -pulse is applied with a time shift of  $\Delta_{\pi/2}$  compared to a symmetric HSE sequence. Thus the HSE signal is also shifted by  $\Delta_{\pi/2}$ , while the SPE signal is shifted by  $-\Delta_{\pi/2}$ . (Bottom) Here the initial  $\pi/2$ -pulse is applied with a time shift of  $-\Delta_{\pi/2}$ . The retrieved SPE signal is smaller, due to a stronger dephasing before the mapping  $\pi/2$ -pulse. Signals are depicted in arbitrary units.

echo sequence to measure the contribution of stimulated photon echo (SPE) to the Hahn spin echo (HSE) signal measured in a symmetric rephasing sequence. HSE and SPE signals are detected by RH detection, see Section 2.4. We applied all pulses with a rectangular temporal shape and a Rabi frequency of  $\Omega = 2\pi \cdot 50$  kHz, which corresponds to a  $\pi/2$ -pulse duration of  $5 \mu\text{s}$ , and a  $\pi$ -pulse duration of  $10 \mu\text{s}$ . The cycling time  $\tau_c$  was  $350 \mu\text{s}$ . Figure B.2 shows the time dependent RH signal versus a static detuning  $\Delta$  of the R-pulses, see Figure B.1, for different timings  $\Delta_{\pi/2}$  of the initial  $\pi/2$ -pulse. Note that the initial  $\pi/2$ -pulse is always

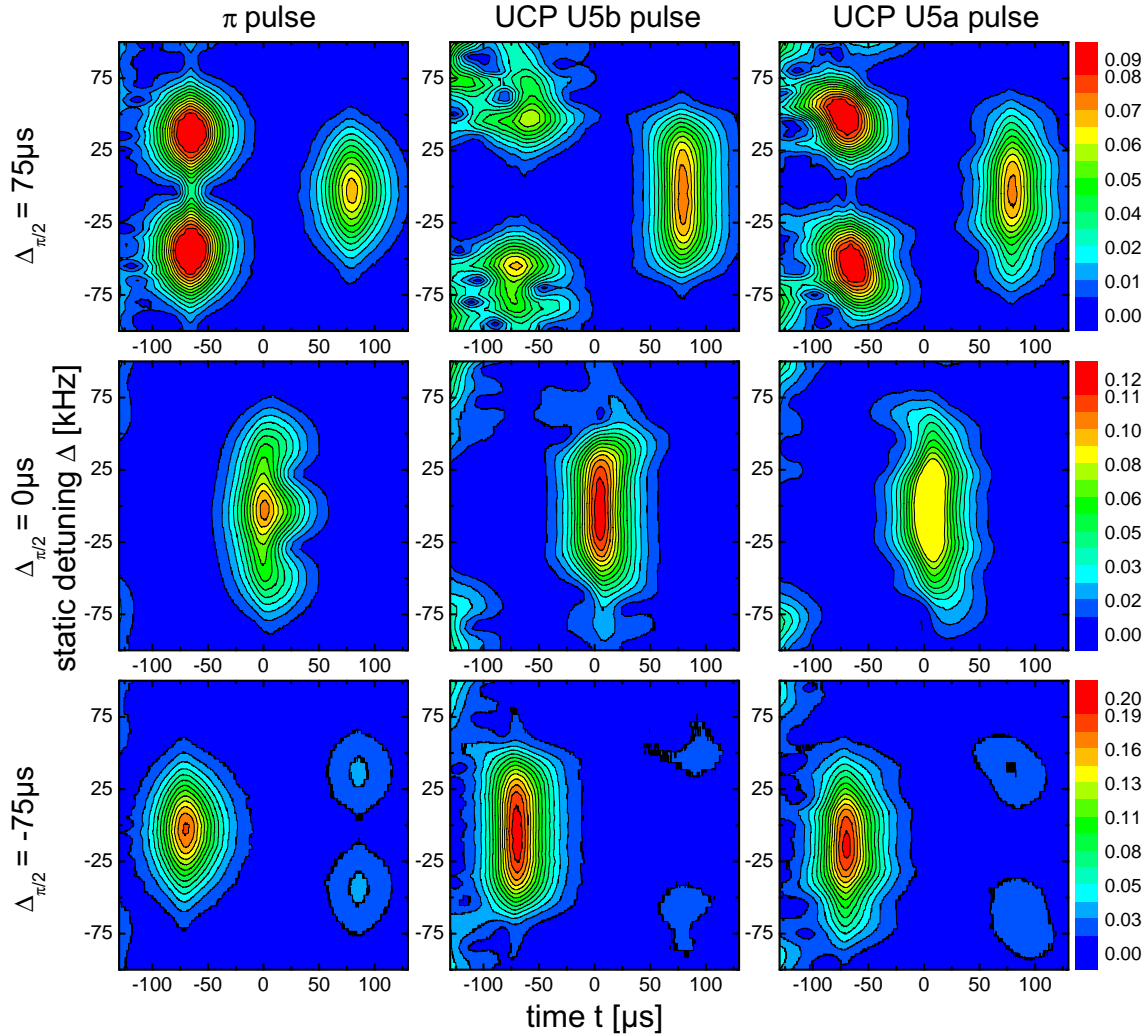


Figure B.2: Time dependent RH signal versus a static detuning of the rephasing pulses for different timings  $\Delta_{\pi/2}$  of the initial  $\pi/2$ -pulse, and three different types of rephasing pulses, i.e.  $\pi$ , UCP U5b, and UCP U5a. See also labels on Figure. Color code in arbitrary units.

applied with  $\Delta = 0$  kHz, i.e. on resonance with the transition. For  $\Delta_{\pi/2} = 75 \mu s$  we find strong SPE signals at about  $-75 \mu s$  if the R-pulses are applied detuned by about  $\pm 50$  kHz. Here the R-pulses act as  $\pi/2$ -pulses, thus mapping the coherence onto a population and generating the SPE signal. However, also for  $\Delta = 0$  kHz we find a small SPE contribution in the case of  $\pi$ -pulse rephasing. In contrast UCP U5b and U5a suppress the SPE signal on resonance, and feature a good robustness of the HSE signal with respect the variations of the static detuning  $\Delta$ . Especially with UCP U5b the SPE signal is fully suppressed for static detunings in range of  $\pm 25$  kHz. For  $\Delta_{\pi/2} = 0 \mu s$ , i.e. a symmetric sequence, HSE and SPE signals coincide at  $t = 0 \mu s$ . The SPE signal is reduced compared to the HSE signal, due to a longer dephasing duration before the mapping process. This becomes even more pronounced for  $\Delta_{\pi/2} = -75 \mu s$ . We find the ratio of the integrated SPE to the integrated HSE signals at  $\Delta = 0$  kHz to drop from 26 % to 1.8 % for the  $\pi$ -pulse, and from 3.2 % to 0 % for the UCP U5b pulse., if  $\Delta_{\pi/2}$  becomes  $-75 \mu s$ .

## Appendix C

### Determination of HF Transition Frequencies

Figure C.1 depicts the time dependent magnitude  $R$  and the phase  $\theta$  determined by the lock-in amplifier of a RF prepared coherence after two HSE rephasing cycles with a cycling time  $\tau_c = 250 \mu\text{s}$ . The RF pulse parameters are:  $\Omega = 2\pi \times 50 \text{ kHz}$ ,  $\tau_\pi = 10 \mu\text{s}$ ,  $\tau_{\pi/2} = 5 \mu\text{s}$ . The driving frequencies are 10.2 MHz (a) and 10.191 MHz (b) for all applied RF pulses. These frequencies are also used as demodulation frequencies of the lock-in amplifier. In both cases we find strong HSE signals at  $t = 0 \mu\text{s}$ , with their origin from the two times rephased coherence prepared by the initial  $\pi/2$  pulse. We further find smaller echo signals at about  $t = 115 \mu\text{s}$ . These arise from a coherence prepared due to the imperfect first rephasing  $\pi$  pulse, which is then rephased by the second  $\pi$  pulse. The time where this small echo signal appears fits very well to the expected time of  $t = 120 \mu\text{s}$ . In Figure C.1 (a) we find a strong linear change of the phase  $\theta$  during the HSE signal, which originates from a constant difference between HSE and demodulation frequency of the lock-in amplifier. Thus, although the coherence is prepared and rephased by pulses of a driving frequency of 10.2 MHz, we find that the generated HSE signal features a frequency which is different and independent from this driving frequency. From the demodulation frequency and the linear change of the phase  $\theta$  we can determine the frequency of the HSE, i.e. the transition frequency of the  $|\pm 3/2\rangle \leftrightarrow |\pm 1/2\rangle$  transition of the ground state  $^3\text{H}_4$  of PrYSO. Figure C.1 (b) depicts the experimental results with the driving frequency adjusted to 10.191 MHz. We find a almost constant phase close to the center of the HSE signal, which indicates that the driving frequency matches the transition frequency of the hyperfine (HF) states. Note, the second HSE signal is phase shifted by  $\pi$  compared to the first HSE signal, which confirms its origin from imperfect rephasing pulses.

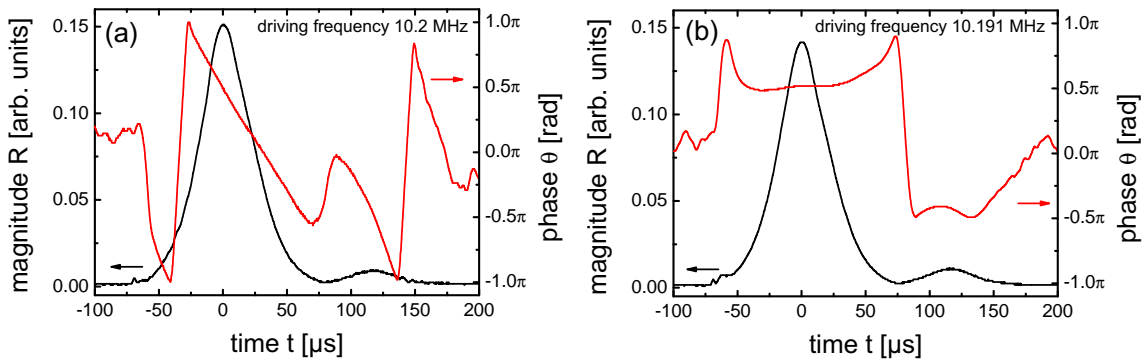


Figure C.1: Time dependent magnitude  $R$  and the phase  $\theta$  of an RF coherence after two HSE rephasing cycles with driving frequencies of the applied pulses of 10.2 MHz (a), and 10.191 MHz.

## Appendix D

### Derivation of the Linear Susceptibility $\chi^{(1)}$

The derivation of the linear susceptibility  $\chi^{(1)}$  (Equation 2.20) is structured as follows: First, we solve the equations of motion for the three-state system density operator. Second, we calculate the polarization  $\vec{P}$ , and determine  $\chi^{(1)}$ .

We calculate the equations of motion for the density operator using the Liouville-von-Neumann Equation 2.11, the three state RWA Hamiltonian (see Equation 2.16), and the dissipator  $\hat{D}$ , as given by Equation 2.19, neglecting spontaneous decay ( $\Gamma_{ij} = 0$ ). We find for the diagonal elements of  $\dot{\rho}$ :

$$\begin{aligned}\dot{\rho}_{11} &= \frac{i}{2}\Omega_p(\rho_{12} - \rho_{21}) \\ \dot{\rho}_{22} &= -\frac{i}{2}\Omega_p(\rho_{12} - \rho_{21}) - \frac{i}{2}\Omega_c(\rho_{32} - \rho_{23}) \\ \dot{\rho}_{33} &= \frac{i}{2}\Omega_c(\rho_{32} - \rho_{23})\end{aligned}\tag{D.1}$$

The off-diagonal elements are given by:

$$\begin{aligned}\dot{\rho}_{21}^* = \dot{\rho}_{12} &= -\gamma_{12}\rho_{12} - \frac{i}{2}\Omega_p(\rho_{22} - \rho_{11}) + \frac{i}{2}\Omega_c\rho_{13} + i\Delta_p\rho_{12} \\ \dot{\rho}_{31}^* = \dot{\rho}_{13} &= -\gamma_{13}\rho_{13} - \frac{i}{2}\Omega_p\rho_{23} + \frac{i}{2}\Omega_c\rho_{12} + i\delta\rho_{13} \\ \dot{\rho}_{32}^* = \dot{\rho}_{23} &= -\gamma_{23}\rho_{23} - \frac{i}{2}\Omega_p\rho_{13} - \frac{i}{2}\Omega_c(\rho_{33} - \rho_{22}) - i\Delta_p\rho_{23} + i\delta\rho_{23}\end{aligned}\tag{D.2}$$

If we assume the population initially in state  $|1\rangle$ , i.e.  $\rho_{11} = 1$ , and  $\rho_{22} = \rho_{33} = 0$ , a strong control field, and a weak probe field the population will primarily stay in state  $|1\rangle$ , with only minor population excited into states  $|2\rangle$ , and  $|3\rangle$ . We thus can assume  $\dot{\rho}_{jj} = 0$ . These approximations simplify the equations of motion to:

$$\begin{aligned}\dot{\rho}_{21}^* = \dot{\rho}_{12} &= (-\gamma_{12} + i\Delta_p)\rho_{12} + \frac{i}{2}\Omega_p + \frac{i}{2}\Omega_c\rho_{13} \\ \dot{\rho}_{31}^* = \dot{\rho}_{13} &= (-\gamma_{13} + i\delta)\rho_{13} - \frac{i}{2}\Omega_p\rho_{23} + \frac{i}{2}\Omega_c\rho_{12} \\ \dot{\rho}_{32}^* = \dot{\rho}_{23} &= (-\gamma_{23} + i\delta)\rho_{23} - \frac{i}{2}\Omega_p\rho_{13} - i\Delta_p\rho_{23}\end{aligned}\tag{D.3}$$

With the weak probe field assumption we further drop any terms proportional to  $\Omega_p^2$ . We find that  $\rho_{23}$  is proportional to  $\Omega_p$ , thus the term  $\frac{i}{2}\Omega_p\rho_{23}$  can be neglected, and the equations of motion reduces to a coupled pair of differential equations:

$$\begin{aligned}\dot{\rho}_{21}^* = \dot{\rho}_{12} &= (-\gamma_{12} + i\Delta_p)\rho_{12} + \frac{i}{2}\Omega_p + \frac{i}{2}\Omega_c\rho_{13} \\ \dot{\rho}_{31}^* = \dot{\rho}_{13} &= (-\gamma_{13} + i\delta)\rho_{13} + \frac{i}{2}\Omega_c\rho_{12}\end{aligned}\tag{D.4}$$



Solving this system of equations we find the steady state solution:

$$\begin{aligned}\rho_{12} &= -\frac{(-2i\gamma_{13} - 2\delta)\Omega_p}{4(\gamma_{12}\gamma_{13} - i\gamma_{12}\delta - i\gamma_{13}\Delta_p - \delta\Delta_p) + \Omega_c^2} \\ \rho_{13} &= -\frac{\Omega_c\Omega_p}{4(\gamma_{12}\gamma_{13} - i\gamma_{12}\delta - i\gamma_{13}\Delta_p - \delta\Delta_p) + \Omega_c^2}\end{aligned}\quad (\text{D.5})$$

The expectation value of the atomic polarization on the probe transition is given by  $\vec{P} = \varrho\mu_{12}\rho_{12}$ . The linear susceptibility  $\chi^{(1)}$  can thus be calculated using  $\vec{P} = \epsilon_0\chi^{(1)}\vec{\mathcal{E}}_p = \epsilon_0\chi^{(1)}\vec{\mathcal{E}}_p^0/2$ , compare with Equation 2.15. We find:

$$\chi^{(1)} = \frac{2|\mu_{12}|^2\varrho}{\epsilon_0\hbar} \frac{2i\gamma_{13} + 2\delta}{4(\gamma_{12}\gamma_{13} - \delta\Delta_p - i\gamma_{12}\delta - i\gamma_{13}\Delta_p) + \Omega_c^2}\quad (\text{D.6})$$

We note, that this definition of  $\chi^{(1)}$  slightly differs from the definition given in [70]. We here used for the decoherence rates  $\gamma_{ij} = \frac{1}{2}(\sum_k \Gamma_{ik} + \sum_k \Gamma_{jk}) + \gamma'_{ij}$  with  $\gamma'_{ij} = 0$ , while in [70],  $\gamma_{ij} = \Gamma_j$ , with  $\Gamma_j$  the total decay from state  $j$ .

---

## Bibliography

- [1] M. A. Nielsen and I. L. Chuang. *Quantum Computation and Quantum Information*. Cambridge University Press, Cambridge (2010)
- [2] H.-J. Briegel, W. Dür, J. I. Cirac, and P. Zoller. *Quantum Repeaters: The Role of Imperfect Local Operations in Quantum Communication*. *Physical Review Letters* **81**(26) 5932 (1998). URL <http://dx.doi.org/10.1103/PhysRevLett.81.5932>
- [3] C. Elliott. *Building the quantum network*. *New Journal of Physics* **4** 346 (2002). URL <http://dx.doi.org/10.1088/1367-2630/4/1/346>
- [4] H. J. Kimble. *The quantum internet*. *Nature* **453**(7198) 1023 (2008). URL <http://dx.doi.org/10.1038/nature07127>
- [5] A. I. Lvovsky, B. C. Sanders, and W. Tittel. *Optical quantum memory*. *Nature Photonics* **3**(12) 706 (2009). URL <http://dx.doi.org/10.1038/nphoton.2009.231>
- [6] C. Simon, M. Afzelius, J. Appel, A. Boyer de la Giroday, S. J. Dewhurst, N. Gisin, C. Y. Hu, F. Jelezko, S. Kröll, J. H. Müller, J. Nunn, E. S. Polzik, J. G. Rarity, H. De Riedmatten, W. Rosenfeld, A. J. Shields, N. Sköld, R. M. Stevenson, R. Thew, I. A. Walmsley, M. C. Weber, H. Weinfurter, J. Wrachtrup, and R. J. Young. *Quantum memories*. *The European Physical Journal D* **58**(1) 1 (2010). URL <http://dx.doi.org/10.1140/epjd/e2010-00103-y>
- [7] H. de Riedmatten and M. Afzelius. *Quantum Light Storage in Solid State Atomic Ensembles*. In A. Predojević and M. W. Mitchell, eds., *Engineering the Atom-Photon Interaction*, 241–273. Springer (2015). URL [http://dx.doi.org/10.1007/978-3-319-19231-4\\_9](http://dx.doi.org/10.1007/978-3-319-19231-4_9)
- [8] M. Afzelius, C. Simon, H. de Riedmatten, and N. Gisin. *Multimode quantum memory based on atomic frequency combs*. *Physical Review A* **79**(5) 052329 (2009). URL <http://dx.doi.org/10.1103/PhysRevA.79.052329>
- [9] M. P. Hedges, J. J. Longdell, Y. Li, and M. J. Sellars. *Efficient quantum memory for light*. *Nature* **465**(7301) 1052 (2010). URL <http://dx.doi.org/10.1038/nature09081>
- [10] M. Hosseini, B. Sparkes, G. Campbell, P. Lam, and B. Buchler. *High efficiency coherent optical memory with warm rubidium vapour*. *Nature Communications* **2** 174 (2011). URL <http://dx.doi.org/10.1038/ncomms1175>

- [11] S. E. Harris, J. E. Field, and A. Imamoglu. *Nonlinear optical processes using electromagnetically induced transparency*. Physical Review Letters **64**(10) 1107 (1990). URL <http://dx.doi.org/10.1103/PhysRevLett.64.1107>
- [12] K.-J. Boller, A. Imamoglu, and S. E. Harris. *Observation of electromagnetically induced transparency*. Physical Review Letters **66**(20) 2593 (1991). URL <http://dx.doi.org/10.1103/PhysRevLett.66.2593>
- [13] M. Fleischhauer and M. D. Lukin. *Dark-State Polaritons in Electromagnetically Induced Transparency*. Physical Review Letters **84**(22) 5094 (2000). URL <http://dx.doi.org/10.1103/PhysRevLett.84.5094>
- [14] D. F. Phillips, A. Fleischhauer, A. Mair, R. L. Walsworth, and M. D. Lukin. *Storage of Light in Atomic Vapor*. Physical Review Letters **86**(5) 783 (2001). URL <http://dx.doi.org/10.1103/PhysRevLett.86.783>
- [15] C. Liu, Z. Dutton, C. H. Behroozi, and L. V. Hau. *Observation of coherent optical information storage in an atomic medium using halted light pulses*. Nature **409**(6819) 490 (2001). URL <http://dx.doi.org/10.1038/35054017>
- [16] L. V. Hau, S. E. Harris, Z. Dutton, and C. H. Behroozi. *Light speed reduction to 17 metres per second in an ultracold atomic gas*. Nature **397**(6720) 594 (1999). URL <http://dx.doi.org/10.1038/17561>
- [17] P. R. Hemmer, A. V. Turukhin, M. S. Shahriar, and J. A. Musser. *Raman-excited spin coherences in nitrogen-vacancy color centers in diamond*. Optics Letters **26**(6) 361 (2001). URL <http://dx.doi.org/10.1364/OL.26.000361>
- [18] J. R. Petta, A. C. Johnson, J. M. Taylor, E. A. Laird, A. Yacoby, M. D. Lukin, C. M. Marcus, M. P. Hanson, and A. C. Gossard. *Coherent Manipulation of Coupled Electron Spins in Semiconductor Quantum Dots*. Science **309**(5744) 2180 (2005). URL <http://dx.doi.org/10.1126/science.1116955>
- [19] B. Urbaszek, X. Marie, T. Amand, O. Krebs, P. Voisin, P. Maletinsky, A. Högele, and A. Imamoglu. *Nuclear spin physics in quantum dots: An optical investigation*. Reviews of Modern Physics **85**(1) 79 (2013). URL <http://dx.doi.org/10.1103/RevModPhys.85.79>
- [20] A. V. Turukhin, V. S. Sudarshanam, M. S. Shahriar, J. A. Musser, B. S. Ham, and P. R. Hemmer. *Observation of Ultraslow and Stored Light Pulses in a Solid*. Physical Review Letters **88**(2) 023602 (2001). URL <http://dx.doi.org/10.1103/PhysRevLett.88.023602>
- [21] M. Zhong, M. P. Hedges, R. L. Ahlefeldt, J. G. Bartholomew, S. E. Beavan, S. M. Wittig, J. J. Longdell, and M. J. Sellars. *Optically addressable nuclear spins in a solid with a six-hour coherence time*. Nature **517**(7533) 177 (2015). URL <http://dx.doi.org/10.1038/nature14025>

- [22] G. Heinze, C. Hubrich, and T. Halfmann. *Stopped Light and Image Storage by Electromagnetically Induced Transparency up to the Regime of One Minute*. Physical Review Letters **111**(3) 033601 (2013). URL <http://dx.doi.org/10.1103/PhysRevLett.111.033601>
- [23] Y.-W. Cho, G. T. Campbell, J. L. Everett, J. Bernu, D. B. Higginbottom, M. T. Cao, J. Geng, N. P. Robins, P. K. Lam, and B. C. Buchler. *Highly efficient optical quantum memory with long coherence time in cold atoms*. Optica **3**(1) 100 (2016). URL <http://dx.doi.org/10.1364/OPTICA.3.000100>
- [24] G. T. Genov, D. Schraft, T. Halfmann, and N. V. Vitanov. *Correction of Arbitrary Field Errors in Population Inversion of Quantum Systems by Universal Composite Pulses*. Physical Review Letters **113**(4) 043001 (2014). URL <http://dx.doi.org/10.1103/PhysRevLett.113.043001>
- [25] B. T. Torosov, S. Guérin, and N. V. Vitanov. *High-Fidelity Adiabatic Passage by Composite Sequences of Chirped Pulses*. Physical Review Letters **106**(23) 233001 (2011). URL <http://dx.doi.org/10.1103/PhysRevLett.106.233001>
- [26] D. Daems, A. Ruschhaupt, D. Sugny, and S. Guérin. *Robust Quantum Control by a Single-Shot Shaped Pulse*. Physical Review Letters **111**(5) 050404 (2013). URL <http://dx.doi.org/10.1103/PhysRevLett.111.050404>
- [27] B. S. Ham, M. S. Shahriar, M. K. Kim, and P. R. Hemmer. *Frequency-selective time-domain optical data storage by electromagnetically induced transparency in a rare-earth-doped solid*. Optics Letters **22**(24) 1849 (1997). URL <http://dx.doi.org/10.1364/OL.22.001849>
- [28] J. J. Longdell and M. J. Sellars. *Experimental demonstration of quantum-state tomography and qubit-qubit interactions for rare-earth-metal-ion-based solid-state qubits*. Physical Review A **69**(3) 032307 (2004). URL <http://dx.doi.org/10.1103/PhysRevA.69.032307>
- [29] M. Nilsson, L. Rippe, N. Ohlsson, T. Christiansson, and S. Kröll. *Initial Experiments Concerning Quantum Information Processing in Rare-Earth-Ion Doped Crystals*. Physica Scripta **T102**(1) 178 (2002). URL <http://dx.doi.org/10.1238/Physica.Topical.102a00178>
- [30] N. Ohlsson, R. Krishna Mohan, and S. Kröll. *Quantum computer hardware based on rare-earth-ion-doped inorganic crystals*. Optics Communications **201**(1) 71 (2002). URL [http://dx.doi.org/10.1016/S0030-4018\(01\)01666-2](http://dx.doi.org/10.1016/S0030-4018(01)01666-2)
- [31] J. Wesenberg and K. Mølmer. *Robust quantum gates and a bus architecture for quantum computing with rare-earth-ion-doped crystals*. Physical Review A **68**(1) 012320 (2003). URL <http://dx.doi.org/10.1103/PhysRevA.68.012320>

- [32] J. H. Wesenberg, K. Mølmer, L. Rippe, and S. Kröll. *Scalable designs for quantum computing with rare-earth-ion-doped crystals*. Physical Review A **75**(1) 012304 (2007). URL <http://dx.doi.org/10.1103/PhysRevA.75.012304>
- [33] S. Chu. *Cold atoms and quantum control*. Nature **416**(6877) 206 (2002). URL <http://dx.doi.org/10.1038/416206a>
- [34] I. Bloch and W. Zwerger. *Many-body physics with ultracold gases*. Reviews of Modern Physics **80**(3) 885 (2008). URL <http://dx.doi.org/10.1103/RevModPhys.80.885>
- [35] I. Bloch, J. Dalibard, and S. Nascimbène. *Quantum simulations with ultracold quantum gases*. Nature Physics **8**(4) 267 (2012). URL <http://dx.doi.org/10.1038/nphys2259>
- [36] I. B. Mekhov and H. Ritsch. *Quantum optics with ultracold quantum gases: towards the full quantum regime of the light–matter interaction*. Journal of Physics B: Atomic, Molecular and Optical Physics **45**(10) 102001 (2012). URL <http://dx.doi.org/10.1088/0953-4075/45/10/102001>
- [37] L. Childress, M. V. Gurudev Dutt, J. M. Taylor, A. S. Zibrov, F. Jelezko, J. Wrachtrup, P. R. Hemmer, and M. D. Lukin. *Coherent Dynamics of Coupled Electron and Nuclear Spin Qubits in Diamond*. Science **314**(5797) 281 (2006). URL <http://dx.doi.org/10.1126/science.1131871>
- [38] P. Neumann, J. Beck, M. Steiner, F. Rempp, H. Fedder, P. R. Hemmer, J. Wrachtrup, and F. Jelezko. *Single-Shot Readout of a Single Nuclear Spin*. Science **329**(5991) 542 (2010). URL <http://dx.doi.org/10.1126/science.1189075>
- [39] G. de Lange, Z. H. Wang, D. Riste, V. V. Dobrovitski, and R. Hanson. *Universal Dynamical Decoupling of a Single Solid-State Spin from a Spin Bath*. Science **330**(6000) 60 (2010). URL <http://dx.doi.org/10.1126/science.1192739>
- [40] P. C. Maurer, G. Kucsko, C. Latta, L. Jiang, N. Y. Yao, S. D. Bennett, F. Pastawski, D. Hunger, N. Chisholm, M. Markham, D. J. Twitchen, J. I. Cirac, and M. D. Lukin. *Room-Temperature Quantum Bit Memory Exceeding One Second*. Science **336**(6086) 1283 (2012). URL <http://dx.doi.org/10.1126/science.1220513>
- [41] M. W. Doherty, J. Michl, F. Dolde, I. Jakobi, P. Neumann, N. B. Manson, and J. Wrachtrup. *Measuring the defect structure orientation of a single NV<sup>-</sup> centre in diamond*. New Journal of Physics **16**(6) 063067 (2014). URL <http://dx.doi.org/10.1088/1367-2630/16/6/063067>
- [42] D. D. B. Rao, S. Yang, and J. Wrachtrup. *Generation of entangled photon strings using NV centers in diamond*. Physical Review B **92**(8) 081301 (2015). URL <http://dx.doi.org/10.1103/PhysRevB.92.081301>

- [43] J. Wrachtrup and F. Jelezko. *Processing quantum information in diamond*. Journal of Physics: Condensed Matter **18**(21) S807 (2006). URL <http://dx.doi.org/10.1088/0953-8984/18/21/S08>
- [44] F. H. L. Koppens, C. Buizert, K. J. Tielrooij, I. T. Vink, K. C. Nowack, T. Meunier, L. P. Kouwenhoven, and L. M. K. Vandersypen. *Driven coherent oscillations of a single electron spin in a quantum dot*. Nature **442**(7104) 766 (2006). URL <http://dx.doi.org/10.1038/nature05065>
- [45] M. Veldhorst, J. C. C. Hwang, C. H. Yang, A. W. Leenstra, B. de Ronde, J. P. Dehollain, J. T. Muhonen, F. E. Hudson, K. M. Itoh, A. Morello, and A. S. Dzurak. *An addressable quantum dot qubit with fault-tolerant control-fidelity*. Nature Nanotechnology **9**(12) 981 (2014). URL <http://dx.doi.org/10.1038/nnano.2014.216>
- [46] D. Loss and D. P. DiVincenzo. *Quantum computation with quantum dots*. Physical Review A **57**(1) 120 (1998). URL <http://dx.doi.org/10.1103/PhysRevA.57.120>
- [47] S. Hufner. *Optical Spectra of Transparent Rare Earth Compounds*. Academic Press (1978)
- [48] R. M. Macfarlane and R. M. Shelby. *Coherent Transient and Holeburning Spectroscopy of Rare Earth Ions in Solids*. In A. A. Kaplyanskii and R. M. Macfarlane, eds., *Spectroscopy of Solids Containing Rare Earth Ions*, 51–184. Elsevier, Amsterdam (1987). URL <http://dx.doi.org/10.1016/B978-0-444-87051-3.50009-2>
- [49] R. Hull, J. Parisi, R. M. Osgood, H. Warlimont, G. Liu, and B. Jacquier, eds. *Spectroscopic Properties of Rare Earths in Optical Materials*, volume 83 of *Springer Series in Materials Science*. Springer-Verlag, Berlin/Heidelberg (2005). URL <http://link.springer.com/10.1007/3-540-28209-2>
- [50] K. Xia, R. Kolesov, Y. Wang, P. Siyushev, R. Reuter, T. Kornher, N. Kukharchyk, A. D. Wieck, B. Villa, S. Yang, and J. Wrachtrup. *All-Optical Preparation of Coherent Dark States of a Single Rare Earth Ion Spin in a Crystal*. Physical Review Letters **115**(9) 093602 (2015). URL <http://dx.doi.org/10.1103/PhysRevLett.115.093602>
- [51] R. Yano, M. Mitsunaga, and N. Uesugi. *Ultralong optical dephasing time in  $\text{Eu}^{3+}:\text{Y}_2\text{SiO}_5$* . Optics Letters **16**(23) 1884 (1991). URL <http://dx.doi.org/10.1364/OL.16.001884>
- [52] R. Equall, Y. Sun, R. Cone, and R. Macfarlane. *Ultraslow optical dephasing in  $\text{Eu}^{3+}:\text{Y}_2\text{SiO}_5$* . Physical Review Letters **72**(14) 2179 (1994). URL <http://dx.doi.org/10.1103/PhysRevLett.72.2179>
- [53] E. Fraval, M. J. Sellars, and J. J. Longdell. *Method of extending hyperfine coherence times in  $\text{Pr}^{3+}:\text{Y}_2\text{SiO}_5$* . Physical Review Letters **92**(7) 077601 (2004). URL <http://dx.doi.org/10.1103/PhysRevLett.92.077601>



- [54] C. H. Macgillavry and G. D. Rieck, eds. *International Tables for x-ray crystallography Volume III: Physical and Chemical Tables*. The Kynoch Press (1968)
- [55] W. Y. Ching, L. Ouyang, and Y.-N. Xu. *Electronic and optical properties of  $Y_2SiO_5$  and  $Y_2Si_2O_7$  with comparisons to  $\alpha-SiO_2$  and  $Y_2O_3$* . Physical Review B **67**(24) 245108 (2003). URL <http://dx.doi.org/10.1103/PhysRevB.67.245108>
- [56] R. W. Equall, R. L. Cone, and R. M. Macfarlane. *Homogeneous broadening and hyperfine structure of optical transitions in  $Pr^{3+}:Y_2SiO_5$* . Physical Review B **52**(6) 3963 (1995). URL <http://dx.doi.org/10.1103/PhysRevB.52.3963>
- [57] P. Becker, N. Olsson, and J. Simpson. *Rare Earth Ions — Introductory Survey*. In *Erbium-Doped Fiber Amplifiers*, 87–129. Elsevier (1999). URL <http://dx.doi.org/10.1016/B978-012084590-3/50006-5>
- [58] S. Mieth. *Preserving Atomic Coherences for Light Storage in  $Pr^{3+}:Y_2SiO_5$  Driven by an OPO Laser System*. Ph. d. thesis, Technische Universität Darmstadt (2015)
- [59] F. Könz, Y. Sun, C. W. Thiel, R. L. Cone, R. W. Equall, R. L. Hutcheson, and R. M. Macfarlane. *Temperature and concentration dependence of optical dephasing, spectral-hole lifetime, and anisotropic absorption in  $Eu^{3+}:Y_2SiO_5$* . Physical Review B **68**(8) 085109 (2003). URL <http://dx.doi.org/10.1103/PhysRevB.68.085109>
- [60] N. Lorenz. *Optimizing EIT Light Storage Efficiency in  $Pr^{3+}:Y_2SiO_5$* . M.sc. thesis, Technische Universität Darmstadt (2014)
- [61] M. Lovrić, P. Glasenapp, D. Suter, B. Tumino, A. Ferrier, P. Goldner, M. Sa-booni, L. Rippe, and S. Kröll. *Hyperfine characterization and spin coherence lifetime extension in  $Pr^{3+}:La_2(WO_4)_3$* . Physical Review B **84**(10) 104417 (2011). URL <http://dx.doi.org/10.1103/PhysRevB.84.104417>
- [62] R. M. Shelby, C. S. Yannoni, and R. M. Macfarlane. *Optically Detected Coherent Transients in Nuclear Hyperfine Levels*. Physical Review Letters **41**(25) 1739 (1978). URL <http://dx.doi.org/10.1103/PhysRevLett.41.1739>
- [63] K. Holliday, M. Croci, E. Vauthey, and U. P. Wild. *Spectral hole burning and holography in an  $Y_2SiO_5:Pr^{3+}$  crystal*. Physical Review B **47**(22) 14741 (1993). URL <http://dx.doi.org/10.1103/PhysRevB.47.14741>
- [64] M. Nilsson, L. Rippe, S. Kröll, R. Klieber, and D. Suter. *Hole-burning techniques for isolation and study of individual hyperfine transitions in inhomogeneously broadened solids demonstrated in  $Pr^{3+}:Y_2SiO_5$* . Physical Review B **70**(21) 214116 (2004). URL <http://dx.doi.org/10.1103/PhysRevB.70.214116>

- [65] M. Nilsson, L. Rippe, S. Kröll, R. Klieber, and D. Suter. *Erratum: Hole-burning techniques for isolation and study of individual hyperfine transitions in inhomogeneously broadened solids demonstrated in  $\text{Pr}^{3+}:\text{Y}_2\text{SiO}_5$*  [*Phys. Rev B* **70**, 214116 (2004)]. *Physical Review B* **71**(14) 149902 (2005). URL <http://dx.doi.org/10.1103/PhysRevB.71.149902>
- [66] R. Yano, M. Mitsunaga, and N. Uesugi. *Stimulated-photon-echo spectroscopy. I. Spectral diffusion in  $\text{Eu}^{3+}\text{YAlO}_3$* . *Physical Review B* **45**(22) 12752 (1992). URL <http://dx.doi.org/10.1103/PhysRevB.45.12752>
- [67] J. Huang, J. M. Zhang, A. Lezama, and T. W. Mossberg. *Excess dephasing in photon-echo experiments arising from excitation-induced electronic level shifts*. *Physical Review Letters* **63**(1) 78 (1989). URL <http://dx.doi.org/10.1103/PhysRevLett.63.78>
- [68] B. W. Shore. *The Theory of Coherent Atomic Excitation*. John Wiley & Sons (1990)
- [69] R. W. Boyd. *Quantum-Mechanical Theory of the Nonlinear Optical Susceptibility*. In *Nonlinear Optics*, 135–206. Elsevier (2008). URL <http://dx.doi.org/10.1016/B978-0-12-369470-6.00003-4>
- [70] M. Fleischhauer, A. Imamoglu, and J. P. Marangos. *Electromagnetically induced transparency: Optics in coherent media*. *Reviews of Modern Physics* **77**(2) 633 (2005). URL <http://dx.doi.org/10.1103/RevModPhys.77.633>
- [71] A. Redfield, S. D. Kunz, and E. Ralph. *Dynamic range in Fourier transform proton magnetic resonance*. *Journal of Magnetic Resonance* (1969) **19**(1) 114 (1975). URL [http://dx.doi.org/10.1016/0022-2364\(75\)90035-9](http://dx.doi.org/10.1016/0022-2364(75)90035-9)
- [72] M. H. Levitt and R. Freeman. *NMR population inversion using a composite pulse*. *Journal of Magnetic Resonance* (1969) **33**(2) 473 (1979). URL [http://dx.doi.org/10.1016/0022-2364\(79\)90265-8](http://dx.doi.org/10.1016/0022-2364(79)90265-8)
- [73] M. H. Levitt. *Composite pulses*. *Progress in Nuclear Magnetic Resonance Spectroscopy* **18**(2) 61 (1986). URL [http://dx.doi.org/10.1016/0079-6565\(86\)80005-X](http://dx.doi.org/10.1016/0079-6565(86)80005-X)
- [74] M. H. Levitt. *Composite Pulses*. In R. K. Harris and R. L. Wasylishen, eds., *Encyclopedia of Magnetic Resonance*. John Wiley & Sons, Ltd, Chichester, UK (2007). URL <http://dx.doi.org/10.1002/9780470034590.emrstm0086>
- [75] S. H. Autler and C. H. Townes. *Stark Effect in Rapidly Varying Fields*. *Physical Review* **100**(2) 703 (1955). URL <http://dx.doi.org/10.1103/PhysRev.100.703>
- [76] P. M. Anisimov, J. P. Dowling, and B. C. Sanders. *Objectively Discerning Autler-Townes Splitting from Electromagnetically Induced Transparency*. *Physical Review Letters* **107**(16) 163604 (2011). URL <http://dx.doi.org/10.1103/PhysRevLett.107.163604>

- [77] J. P. Marangos and T. Halfmann. *Electromagnetically Induced Transparency*. In M. Bass, ed., *Handbook of Optics Volume IV*. McGraw-Hill Professional, 3rd edition (2009)
- [78] J. Gea-Banacloche, Y.-q. Li, S.-z. Jin, and M. Xiao. *Electromagnetically induced transparency in ladder-type inhomogeneously broadened media: Theory and experiment*. *Physical Review A* **51**(1) 576 (1995). URL <http://dx.doi.org/10.1103/PhysRevA.51.576>
- [79] I. Novikova, R. Walsworth, and Y. Xiao. *Electromagnetically induced transparency-based slow and stored light in warm atoms*. *Laser & Photonics Reviews* **6**(3) 333 (2012). URL <http://dx.doi.org/10.1002/lpor.201100021>
- [80] S. E. Harris, J. E. Field, and A. Kasapi. *Dispersive properties of electromagnetically induced transparency*. *Physical Review A* **46**(1) R29 (1992). URL <http://dx.doi.org/10.1103/PhysRevA.46.R29>
- [81] A. V. Gorshkov, A. André, M. Fleischhauer, A. S. Sørensen, and M. D. Lukin. *Universal Approach to Optimal Photon Storage in Atomic Media*. *Physical Review Letters* **98**(12) 123601 (2007). URL <http://dx.doi.org/10.1103/PhysRevLett.98.123601>
- [82] A. V. Gorshkov, A. André, M. D. Lukin, and A. S. Sørensen. *Photon storage in  $\Lambda$ -type optically dense atomic media. II. Free-space model*. *Physical Review A* **76**(3) 033805 (2007). URL <http://dx.doi.org/10.1103/PhysRevA.76.033805>
- [83] K. Heshami, D. G. England, P. C. Humphreys, P. J. Bustard, V. M. Acosta, J. Nunn, and B. J. Sussman. *Quantum memories: emerging applications and recent advances*. *Journal of Modern Optics* 1–24 (2016). URL <http://dx.doi.org/10.1080/09500340.2016.1148212>
- [84] M. Fleischhauer and M. D. Lukin. *Quantum memory for photons: Dark-state polaritons*. *Physical Review A* **65**(2) 022314 (2002). URL <http://dx.doi.org/10.1103/PhysRevA.65.022314>
- [85] G. Nikoghosyan and G. Grigoryan. *Influence of relaxation on propagation, storage, and retrieving of light pulses in a medium with electromagnetically induced transparency*. *Physical Review A* **72**(4) 043814 (2005). URL <http://dx.doi.org/10.1103/PhysRevA.72.043814>
- [86] A. V. Gorshkov, A. André, M. D. Lukin, and A. S. Sørensen. *Photon storage in  $\Lambda$ -type optically dense atomic media. I. Cavity model*. *Physical Review A* **76**(3) 033804 (2007). URL <http://dx.doi.org/10.1103/PhysRevA.76.033804>
- [87] I. Novikova, A. V. Gorshkov, D. F. Phillips, A. S. Sørensen, M. D. Lukin, and R. L. Walsworth. *Optimal Control of Light Pulse Storage and Retrieval*.

- Physical Review Letters **98**(24) 243602 (2007). URL <http://dx.doi.org/10.1103/PhysRevLett.98.243602>
- [88] I. Novikova, N. B. Phillips, and A. V. Gorshkov. *Optimal light storage with full pulse-shape control*. Physical Review A **78**(2) 021802 (2008). URL <http://dx.doi.org/10.1103/PhysRevA.78.021802>
- [89] Y.-H. Chen, M.-J. Lee, I.-C. Wang, S. Du, Y.-F. Chen, Y.-C. Chen, and I. A. Yu. *Coherent Optical Memory with High Storage Efficiency and Large Fractional Delay*. Physical Review Letters **110**(8) 083601 (2013). URL <http://dx.doi.org/10.1103/PhysRevLett.110.083601>
- [90] L. Viola, E. Knill, and S. Lloyd. *Dynamical Decoupling of Open Quantum Systems*. Physical Review Letters **82**(12) 2417 (1999). URL <http://dx.doi.org/10.1103/PhysRevLett.82.2417>
- [91] L. Viola. *Advances in decoherence control*. Journal of Modern Optics **51**(16-18) 2357 (2004). URL <http://dx.doi.org/10.1080/09500340408231795>
- [92] W. Yang, Z.-Y. Wang, and R.-B. Liu. *Preserving qubit coherence by dynamical decoupling*. Frontiers of Physics **6**(1) 2 (2011). URL <http://dx.doi.org/10.1007/s11467-010-0113-8>
- [93] A. M. Souza, G. A. Alvarez, and D. Suter. *Robust dynamical decoupling*. Philosophical Transactions of the Royal Society A: Mathematical, Physical and Engineering Sciences **370**(1976) 4748 (2012). URL <http://dx.doi.org/10.1098/rsta.2011.0355>
- [94] J. Mlynek, N. C. Wong, R. G. DeVoe, E. S. Kintzer, and R. G. Brewer. *Raman Heterodyne Detection of Nuclear Magnetic Resonance*. Physical Review Letters **50**(13) 993 (1983). URL <http://dx.doi.org/10.1103/PhysRevLett.50.993>
- [95] N. C. Wong, E. S. Kintzer, J. Mlynek, R. G. DeVoe, and R. G. Brewer. *Raman heterodyne detection of nuclear magnetic resonance*. Physical Review B **28**(9) 4993 (1983). URL <http://dx.doi.org/10.1103/PhysRevB.28.4993>
- [96] T. Blasberg and D. Suter. *Determination of oscillator strengths in  $Pr^{3+}:YAlO_3$  by Raman heterodyne and hole burning spectroscopy*. Journal of Luminescence **65**(4) 199 (1995). URL [http://dx.doi.org/10.1016/0022-2313\(95\)00065-2](http://dx.doi.org/10.1016/0022-2313(95)00065-2)
- [97] G. Heinze, C. Hubrich, and T. Halfmann. *Coherence time extension in  $Pr^{3+}:Y_2SiO_5$  by self-optimized magnetic fields and dynamical decoupling*. Physical Review A **89**(5) 053825 (2014). URL <http://dx.doi.org/10.1103/PhysRevA.89.053825>
- [98] S. Mieth, A. Henderson, and T. Halfmann. *Tunable, continuous-wave optical parametric oscillator with more than 1W output power in the orange visible spectrum*. Optics Express **22**(9) 11182 (2014). URL <http://dx.doi.org/10.1364/OE.22.011182>

- [99] R. W. P. Drever, J. L. Hall, F. V. Kowalski, J. Hough, G. M. Ford, A. J. Munley, and H. Ward. *Laser phase and frequency stabilization using an optical resonator*. Applied Physics B Photophysics and Laser Chemistry **31**(2) 97 (1983). URL <http://dx.doi.org/10.1007/BF00702605>
- [100] E. A. Donley, T. P. Heavner, F. Levi, M. O. Tataw, and S. R. Jefferts. *Double-pass acousto-optic modulator system*. Review of Scientific Instruments **76**(6) 063112 (2005). URL <http://dx.doi.org/10.1063/1.1930095>
- [101] D. Schraft. *Entwicklung eines evolutionären Verfahrens zur Optimierung quantenoptischer Prozesse*. M.sc. thesis, Technische Universität Darmstadt (2010)
- [102] G. Heinze. *Kohärente magnetische Hochfrequenzanregungen eines seltenerd-dotierten Festkörpers*. Diploma thesis, Technische Universität Kaiserslautern (2008)
- [103] J. Mispelter, M. Lupu, and A. Briguët. *NMR Probeheads for Biophysical and Biomedical Experiments*. Imperial College Press (2015). URL <http://dx.doi.org/10.1142/p759>
- [104] M. Sabooni, Q. Li, S. Kröll, and L. Rippe. *Efficient Quantum Memory Using a Weakly Absorbing Sample*. Physical Review Letters **110**(13) 133604 (2013). URL <http://dx.doi.org/10.1103/PhysRevLett.110.133604>
- [105] J. J. Longdell, E. Fraval, M. J. Sellars, and N. B. Manson. *Stopped Light with Storage Times Greater than One Second Using Electromagnetically Induced Transparency in a Solid*. Physical Review Letters **95**(6) 063601 (2005). URL <http://dx.doi.org/10.1103/PhysRevLett.95.063601>
- [106] G. Heinze. *Kohärente optische Datenspeicherung mittels EIT in einem  $\text{Pr}^{3+}:\text{Y}_2\text{SiO}_5$ -Kristall*. Ph. d. thesis, Technische Universität Darmstadt (2013). URL <http://tuprints.ulb.tu-darmstadt.de/id/eprint/3686>
- [107] F. Beil, J. Klein, G. Nikoghosyan, and T. Halfmann. *Electromagnetically induced transparency and retrieval of light pulses in a  $\Lambda$ -type and a V-type level scheme in  $\text{Pr}^{3+}:\text{Y}_2\text{SiO}_5$* . Journal of Physics B: Atomic, Molecular and Optical Physics **41**(7) 074001 (2008). URL <http://dx.doi.org/10.1088/0953-4075/41/7/074001>
- [108] E. L. Hahn. *Spin Echoes*. Physical Review **80**(4) 580 (1950). URL <http://dx.doi.org/10.1103/PhysRev.80.580>
- [109] R. Tycko, H. Cho, E. Schneider, and A. Pines. *Composite pulses without phase distortion*. Journal of Magnetic Resonance (1969) **61**(1) 90 (1985). URL [http://dx.doi.org/10.1016/0022-2364\(85\)90270-7](http://dx.doi.org/10.1016/0022-2364(85)90270-7)
- [110] F. Schmidt-Kaler, H. Häffner, M. Riebe, S. Gulde, G. P. T. Lancaster, T. Deuschle, C. Becher, C. F. Roos, J. Eschner, and R. Blatt. *Realization of the Cirac–Zoller controlled-NOT quantum gate*. Nature **422**(6930) 408 (2003). URL <http://dx.doi.org/10.1038/nature01494>



- [111] M. Riebe, T. Monz, K. Kim, A. S. Villar, P. Schindler, M. Chwalla, M. Hennrich, and R. Blatt. *Deterministic entanglement swapping with an ion-trap quantum computer*. *Nature Physics* **4**(11) 839 (2008). URL <http://dx.doi.org/10.1038/nphys1107>
- [112] T. Monz, K. Kim, W. Hänsel, M. Riebe, A. S. Villar, P. Schindler, M. Chwalla, M. Hennrich, and R. Blatt. *Realization of the Quantum Toffoli Gate with Trapped Ions*. *Physical Review Letters* **102**(4) 040501 (2009). URL <http://dx.doi.org/10.1103/PhysRevLett.102.040501>
- [113] M. Pons, V. Ahufinger, C. Wunderlich, A. Sanpera, S. Braungardt, A. Sen(De), U. Sen, and M. Lewenstein. *Trapped Ion Chain as a Neural Network: Error Resistant Quantum Computation*. *Physical Review Letters* **98**(2) 023003 (2007). URL <http://dx.doi.org/10.1103/PhysRevLett.98.023003>
- [114] N. Timoney, V. Elman, S. Glaser, C. Weiss, M. Johanning, W. Neuhauser, and C. Wunderlich. *Error-resistant single-qubit gates with trapped ions*. *Physical Review A* **77**(5) 052334 (2008). URL <http://dx.doi.org/10.1103/PhysRevA.77.052334>
- [115] C. Piltz, B. Scharfenberger, A. Khromova, A. F. Varón, and C. Wunderlich. *Protecting Conditional Quantum Gates by Robust Dynamical Decoupling*. *Physical Review Letters* **110**(20) 200501 (2013). URL <http://dx.doi.org/10.1103/PhysRevLett.110.200501>
- [116] C. Hardy, W. Edelstein, and D. Vatis. *Efficient adiabatic fast passage for NMR population inversion in the presence of radiofrequency field inhomogeneity and frequency offsets*. *Journal of Magnetic Resonance* (1969) **66**(3) 470 (1986). URL [http://dx.doi.org/10.1016/0022-2364\(86\)90190-3](http://dx.doi.org/10.1016/0022-2364(86)90190-3)
- [117] A. Tannús and M. Garwood. *Adiabatic pulses*. *NMR in Biomedicine* **10**(8) 423 (1997). URL [http://dx.doi.org/10.1002/\(SICI\)1099-1492\(199712\)10:8<423::AID-NBM488>3.0.CO;2-X](http://dx.doi.org/10.1002/(SICI)1099-1492(199712)10:8<423::AID-NBM488>3.0.CO;2-X)
- [118] M. Garwood and L. DelaBarre. *The Return of the Frequency Sweep: Designing Adiabatic Pulses for Contemporary NMR*. *Journal of Magnetic Resonance* **153**(2) 155 (2001). URL <http://dx.doi.org/10.1006/jmre.2001.2340>
- [119] N. V. Vitanov, T. Halfmann, B. W. Shore, and K. Bergmann. *Laser-Induced Population Transfer by Adiabatic Passage Techniques*. *Annual Review of Physical Chemistry* **52**(1) 763 (2001). URL <http://dx.doi.org/10.1146/annurev.physchem.52.1.763>
- [120] J. Klein, F. Beil, and T. Halfmann. *Rapid adiabatic passage in a  $Pr^{3+}:Y_2SiO_5$  crystal*. *Journal of Physics B: Atomic, Molecular and Optical Physics* **40**(11) S345 (2007). URL <http://dx.doi.org/10.1088/0953-4075/40/11/S08>



- [121] R. Lauro, T. Chanelière, and J.-L. Le Gouët. *Adiabatic refocusing of nuclear spins in  $Tm^{3+}$ :YAG*. *Physical Review B* **83**(3) 035124 (2011). URL <http://dx.doi.org/10.1103/PhysRevB.83.035124>
- [122] S. Mieth, D. Schraft, T. Halfmann, and L. P. Yatsenko. *Rephasing of optically driven atomic coherences by rapid adiabatic passage in  $Pr^{3+}$ : $Y_2SiO_5$* . *Physical Review A* **86**(6) 063404 (2012). URL <http://dx.doi.org/10.1103/PhysRevA.86.063404>
- [123] M. F. Pascual-Winter, R. C. Tongning, R. Lauro, A. Louchet-Chauvet, T. Chanelière, and J.-L. Le Gouët. *Adiabatic passage with spin locking in  $Tm^{3+}$ :YAG*. *Physical Review B* **86**(6) 064301 (2012). URL <http://dx.doi.org/10.1103/PhysRevB.86.064301>
- [124] M. F. Pascual-Winter, R.-C. Tongning, T. Chanelière, and J.-L. L. Gouët. *Securing coherence rephasing with a pair of adiabatic rapid passages*. *New Journal of Physics* **15**(5) 055024 (2013). URL <http://dx.doi.org/10.1088/1367-2630/15/5/055024>
- [125] X. Chen, I. Lizuain, A. Ruschhaupt, D. Guéry-Odelin, and J. G. Muga. *Shortcut to Adiabatic Passage in Two- and Three-Level Atoms*. *Physical Review Letters* **105**(12) 123003 (2010). URL <http://dx.doi.org/10.1103/PhysRevLett.105.123003>
- [126] E. Torrontegui, S. Ibáñez, S. Martínez-Garaot, M. Modugno, A. del Campo, D. Guéry-Odelin, A. Ruschhaupt, X. Chen, and J. G. Muga. *Shortcuts to Adiabaticity*. In *Advances in Atomic, Molecular, and Optical Physics*, 117–169. Elsevier (2013). URL <http://dx.doi.org/10.1016/B978-0-12-408090-4.00002-5>
- [127] M. Ndong, G. Djotyan, A. Ruschhaupt, and S. Guérin. *Robust coherent superposition of states by single-shot shaped pulse*. *Journal of Physics B: Atomic, Molecular and Optical Physics* **48**(17) 174007 (2015). URL <http://dx.doi.org/10.1088/0953-4075/48/17/174007>
- [128] C. P. Lindsey and G. D. Patterson. *Detailed comparison of the Williams–Watts and Cole–Davidson functions*. *The Journal of Chemical Physics* **73**(7) 3348 (1980). URL <http://dx.doi.org/10.1063/1.440530>
- [129] W. B. Mims. *Phase Memory in Electron Spin Echoes, Lattice Relaxation Effects in  $CaWO_4$ : Er, Ce, Mn*. *Physical Review* **168**(2) 370 (1968). URL <http://dx.doi.org/10.1103/PhysRev.168.370>
- [130] C. Thiel, T. Böttger, and R. Cone. *Rare-earth-doped materials for applications in quantum information storage and signal processing*. *Journal of Luminescence* **131**(3) 353 (2011). URL <http://dx.doi.org/10.1016/j.jlumin.2010.12.015>

- [131] H. Y. Carr and E. M. Purcell. *Effects of Diffusion on Free Precession in Nuclear Magnetic Resonance Experiments*. *Physical Review* **94**(3) 630 (1954). URL <http://dx.doi.org/10.1103/PhysRev.94.630>
- [132] S. Meiboom and D. Gill. *Modified Spin-Echo Method for Measuring Nuclear Relaxation Times*. *Review of Scientific Instruments* **29**(8) 688 (1958). URL <http://dx.doi.org/10.1063/1.1716296>
- [133] J.-C. Diels and W. Rudolph. *Ultrashort Laser Pulse Phenomena*. Elsevier (2006). URL <http://www.sciencedirect.com/science/book/9780122154935>
- [134] M. M. T. Loy. *Observation of Population Inversion by Optical Adiabatic Rapid Passage*. *Physical Review Letters* **32**(15) 814 (1974). URL <http://dx.doi.org/10.1103/PhysRevLett.32.814>
- [135] U. Gaubatz, P. Rudecki, S. Schiemann, and K. Bergmann. *Population transfer between molecular vibrational levels by stimulated Raman scattering with partially overlapping laser fields. A new concept and experimental results*. *The Journal of Chemical Physics* **92**(9) 5363 (1990). URL <http://dx.doi.org/10.1063/1.458514>
- [136] K. Bergmann, H. Theuer, and B. W. Shore. *Coherent population transfer among quantum states of atoms and molecules*. *Reviews of Modern Physics* **70**(3) 1003 (1998). URL <http://dx.doi.org/10.1103/RevModPhys.70.1003>
- [137] B. T. Torosov and N. V. Vitanov. *Smooth composite pulses for high-fidelity quantum information processing*. *Physical Review A* **83**(5) 053420 (2011). URL <http://dx.doi.org/10.1103/PhysRevA.83.053420>
- [138] N. V. Vitanov and K.-A. Suominen. *Nonlinear level-crossing models*. *Physical Review A* **59**(6) 4580 (1999). URL <http://dx.doi.org/10.1103/PhysRevA.59.4580>
- [139] G. Dridi, S. Guérin, V. Hakobyan, H. R. Jauslin, and H. Eleuch. *Ultrafast stimulated Raman parallel adiabatic passage by shaped pulses*. *Physical Review A* **80**(4) 043408 (2009). URL <http://dx.doi.org/10.1103/PhysRevA.80.043408>
- [140] S. Guérin, V. Hakobyan, and H. R. Jauslin. *Optimal adiabatic passage by shaped pulses: Efficiency and robustness*. *Physical Review A* **84**(1) 013423 (2011). URL <http://dx.doi.org/10.1103/PhysRevA.84.013423>
- [141] C. Brif, R. Chakrabarti, and H. Rabitz. *Control of quantum phenomena: past, present and future*. *New Journal of Physics* **12**(7) 075008 (2010). URL <http://dx.doi.org/10.1088/1367-2630/12/7/075008>
- [142] J. Werschnik and E. K. U. Gross. *Quantum optimal control theory*. *Journal of Physics B: Atomic, Molecular and Optical Physics* **40**(18) R175 (2007). URL <http://dx.doi.org/10.1088/0953-4075/40/18/R01>

- [143] N. Khaneja, T. Reiss, C. Kehlet, T. Schulte-Herbrüggen, and S. J. Glaser. *Optimal control of coupled spin dynamics: design of NMR pulse sequences by gradient ascent algorithms*. *Journal of Magnetic Resonance* **172**(2) 296 (2005). URL <http://dx.doi.org/10.1016/j.jmr.2004.11.004>
- [144] T. E. Skinner and N. I. Gershenzon. *Optimal control design of pulse shapes as analytic functions*. *Journal of Magnetic Resonance* **204**(2) 248 (2010). URL <http://dx.doi.org/10.1016/j.jmr.2010.03.002>
- [145] A. Maudsley. *Modified Carr-Purcell-Meiboom-Gill sequence for NMR fourier imaging applications*. *Journal of Magnetic Resonance* (1969) **69**(3) 488 (1986). URL [http://dx.doi.org/10.1016/0022-2364\(86\)90160-5](http://dx.doi.org/10.1016/0022-2364(86)90160-5)
- [146] G. S. Uhrig. *Keeping a Quantum Bit Alive by Optimized  $\pi$ -Pulse Sequences*. *Physical Review Letters* **98**(10) 100504 (2007). URL <http://dx.doi.org/10.1103/PhysRevLett.98.100504>
- [147] A. M. Souza, G. A. Álvarez, and D. Suter. *Robust Dynamical Decoupling for Quantum Computing and Quantum Memory*. *Physical Review Letters* **106**(24) 240501 (2011). URL <http://dx.doi.org/10.1103/PhysRevLett.106.240501>
- [148] G. Heinze, S. Mieth, and T. Halfmann. *Control of dark-state polariton collapses in a doped crystal*. *Physical Review A* **84**(1) 013827 (2011). URL <http://dx.doi.org/10.1103/PhysRevA.84.013827>
- [149] G. T. Genov, D. Schraft, N. V. Vitanov, and T. Halfmann. *Universally robust, arbitrarily accurate sequences for dynamical decoupling* (2016)
- [150] T. W. Mossberg, R. Kachru, S. R. Hartmann, and A. M. Flusberg. *Echoes in gaseous media: A generalized theory of rephasing phenomena*. *Physical Review A* **20**(5) 1976 (1979). URL <http://dx.doi.org/10.1103/PhysRevA.20.1976>

## Publications and Conference Contributions

### Publications in peer-reviewed Journals

- G. T. Genov, D. Schraft, N. V. Vitanov, and T. Halfmann  
*Universally robust, arbitrarily accurate sequences for dynamical decoupling*  
submitted to Physical Review Letters
- L. Van-Damme, D. Schraft, G. T. Genov, D. Sugny, T. Halfmann, and S. Guérin  
*Robust NOT-gate by single-shot shaped pulses: Demonstration by rephasing of atomic coherences*  
submitted to Physical Review Letters
- D. Schraft, M. Hain, N. Lorenz, and T. Halfmann  
*Stopped Light at High Storage Efficiency in a  $\text{Pr}^{3+}:\text{Y}_2\text{SiO}_5$  Crystal*  
[Phys. Rev. Lett. 116, 073602 \(2016\)](#)
- G. T. Genov, D. Schraft, T. Halfmann, and N. V. Vitanov  
*Correction of arbitrary field errors in population inversion of quantum systems by universal composite pulses*  
[Phys. Rev. Lett. 113, 043001 \(2014\)](#)
- D. Schraft, G. T. Genov, N. V. Vitanov, and T. Halfmann  
*Experimental demonstration of composite adiabatic passage*  
[Phys. Rev. A. 88, 063406 \(2013\)](#)
- S. Mieth, D. Schraft, L. P. Yatsenko, and T. Halfmann  
*Rephasing of optically driven atomic coherences by rapid adiabatic passage in  $\text{Pr}^{3+}:\text{Y}_2\text{SiO}_5$*   
[Phys. Rev. A 86, 063404 \(2012\)](#)

### Talks at National and International Conferences

- M. Hain, N. Lorenz, D. Schraft, and T. Halfmann  
*Stopped Light at High Storage Efficiency in a  $\text{Pr}^{3+}:\text{Y}_2\text{SiO}_5$  Crystal*  
Workshop on Control of Quantum Dynamics of Atoms, Molecules and Ensembles by Light (CAMEL XII) – Nessebar (Bulgaria), June 2016

- G. Genov, D. Schraft, T. Halfmann, and N. V. Vitanov  
*Universal Arbitrarily Accurate Pulse Error Compensating Sequences for Rephasing and Dynamical Decoupling*  
Workshop on Control of Quantum Dynamics of Atoms, Molecules and Ensembles by Light (CAMEL XII) – Nessebar (Bulgaria), June 2016
- M. Hain, N. Lorenz, D. Schraft, and T. Halfmann  
*Light storage by EIT, using multi-pass configurations in doped solid to reach efficiencies up to 76 %*  
Conference on Quantum Light-Matter Interaction in Solid State Systems (QLIMS) – Marie Curie Initial Training Network – Coherent Information Processing in Rare-Earth Ion Doped Solids (CIPRIS) – Barcelona (Spain), November 2015
- D. Schraft, G. T. Genov, S. Guérin, and T. Halfmann  
*Single-shot shaped pulses for robust rephasing of atomic coherences*  
Workshop on Control of Quantum Dynamics of Atoms, Molecules and Ensembles by Light (CAMEL XI) – Nessebar (Bulgaria), June 2015
- D. Schraft, G. T. Genov, T. Halfmann, and N. V. Vitanov  
*Universal composite pulses for robust rephasing of atomic coherences in a doped solid*  
DPG Spring Meeting of the Section AMOP – Heidelberg (Germany), March 2015
- D. Schraft, G. T. Genov, N. V. Vitanov, and T. Halfmann  
*Universal composite pulses for rephasing of atomic coherences in a doped solid*  
3rd mini school – Marie Curie Initial Training Network – Coherent Information Processing in Rare-Earth Ion Doped Solids (CIPRIS) – Lund (Sweden), August 2014
- D. Schraft, G. T. Genov, N. V. Vitanov, and T. Halfmann  
*Universal composite pulses for rephasing of atomic coherences in a doped solid*  
Workshop on Control of Quantum Dynamics of Atoms, Molecules and Ensembles by Light (CAMEL X) – Nessebar (Bulgaria), June 2014
- D. Schraft, and T. Halfmann  
*Rephasing of atomic coherences by composite sequences in a doped solid*  
2nd mini school – Marie Curie Initial Training Network – Coherent Information Processing in Rare-Earth Ion Doped Solids (CIPRIS) – Paris (France), August 2013
- D. Schraft, and T. Halfmann  
*Rephasing of atomic coherences by composite sequences in a doped solid*  
Workshop on Control of Quantum Dynamics of Atoms, Molecules and Ensembles by Light (CAMEL IX) – Nessebar (Bulgaria), June 2013

## Posters at National and International Conferences

- G. Genov, D. Schraft, T. Halfmann, and N.V. Vitanov  
*Correction of arbitrary field errors in population inversion by universal composite pulses*  
European Conference on Atoms Molecules and Photons (ECAMP) Frankfurt am Main (Germany), September 2016
- M. Hain, D. Schraft, N. Lorenz, and T. Halfmann  
*Stopped Light at High Storage Efficiency in a  $Pr^{3+}:Y_2SiO_5$  Crystal*  
European Conference on Atoms Molecules and Photons (ECAMP) Frankfurt am Main (Germany), September 2016
- N. Rentzsch, G. Heinze, D. Schraft, and T. Halfmann  
*Multiplexed image storage by EIT in a doped solid*  
DPG Spring Meeting of the Section AMOP – Stuttgart (Germany), March 2012
- D. Schraft, F. Beil, G. Heinze, T. Halfmann  
*Feedback-controlled optimization of light storage by EIT in a doped crystal*  
Workshop on Control of Quantum Dynamics of Atoms, Molecules and Ensembles by Light (CAMEL VII) – Nessebar (Bulgaria), June 2011



## Supervisions and Contributions to Teaching

### Master Thesis

- Marcel Hain, *Increasing the EIT Light Storage Efficiency in  $Pr^{3+}:Y_2SiO_5$  Using Multipass Configurations*, Technische Universität Darmstadt, 2016
- Nikolaus Lorenz, *Optimising EIT Light Storage Efficiency in  $Pr^{3+}:Y_2SiO_5$* , Technische Universität Darmstadt, 2014
- Torsten Abel, *Lokalisierte Lichtspeicherung in einem seltenerd-dotierten Festkörper*, Technische Universität Darmstadt, 2013
- Daniel Englisch, *Optische Rephasierung zur Lichtspeicherung in  $Pr^{3+}:Y_2SiO_5$* , Technische Universität Darmstadt, 2013

### Bachelor Thesis

- Daniel Preißler, *Implementierung von Methoden zur Bestimmung der EIT-Lichtspeichereffizienz in  $Pr^{3+}:Y_2SiO_5$* , Technische Universität Darmstadt, 2015
- Alexander Bruns, *Anwendung und Simulation geformter Einzelschuss-Pulse zur Rephasierung atomarer Kohärenzen*, Technische Universität Darmstadt, 2015
- Jonas Zessin, *Geformte Einzelschuss-Pulse zur Rephasierung atomarer Kohärenzen*, Technische Universität Darmstadt, 2014
- Maximilian Georg Meier, *Stabilisierung eines kommerziellen Systems zur Laserlinienbreitenbestimmung*, Technische Universität Darmstadt, 2014
- Oliver Diemel, *Optimierung der Lichtspeicherung durch evolutionäre Algorithmen*, Technische Universität Darmstadt, 2012
- Moritz Kick, *Optische Rephasierung von atomaren Kohärenzen in  $Pr^{3+}:Y_2SiO_5$* , Technische Universität Darmstadt, 2012

### Contributions to Teaching

- Supervision of the advanced lab course:  
*4.10. Akusto-optischer Modulator*, WS 2011/2012 - WS 2015/2016
- Support of lectures:  
*experimental physics II course*, SS 2016  
*experimental physics III course*, WS 2016/2017
- Supervision of student exercises: *specialist course optics*, WS 2012/2013
- Supervision of student seminar presentations:  
*Akusto-Optik*, WS 2014/2015  
*Erzeugung kurzer Laserpulse/Akusto- und Elektro-Optik*, WS 2013/2014

# Curriculum Vitæ

of Daniel Schraft,  
born November 8, 1983 in Frankfurt am Main  
currently living in Darmstadt.

---

## Education

1990 - 1994	Attendance of the Waldenser Elementary School in Mörfelden-Walldorf
1994 - 2000	Attendance of the Bertha-von-Suttner High School in Mörfelden-Walldorf
2000 - 2003	Attendance of the High School in Groß-Gerau
06/2003	A-levels at the High School Groß-Gerau

---

## University Education

2003 - 2007	Physics Studies (B.Sc) at TU Darmstadt
04/2007	Bachelor of Science Degree in Physics, <i><sup>2</sup>H-NMR-Untersuchungen der modifizierten Defektdynamik in dotiertem Eis</i> , TU Darmstadt (Nuclear Magnetic Resonance (Prof. Fujara) group)
2007 - 2010	Physics Studies (M.Sc) at TU Darmstadt
11/2010	Master of Science Degree in Physics, <i>Entwicklung eines evolutionären Verfahrens zur Optimierung quantenoptischer Prozesse</i> , TU Darmstadt (Nonlinear/Quantum Optics group)
since 06/2011	Doctoral Studies at the Department of Physics, TU Darmstadt (Nonlinear/Quantum Optics group)

---

## Working Experience

05/2004 - 06/2009	Student employee at the GSI Helmholtzzentrum für Schwerionenforschung (PHELIX/plasma physics division), Darmstadt
-------------------	---

Darmstadt, September 2016

## Acknowledgment

Diese letzten Seiten möchte ich nutzen um all denen meinen herzlichsten Dank auszusprechen, die maßgeblich zum Gelingen dieser Arbeit beigetragen haben.

**Thomas**, mehr als 5 Jahre war ich nun ein Teil Deiner Arbeitsgruppe NLO/QO. Zunächst als Masterstudent, später als Doktorand, habe ich mich jeden Tag aufs Neue auf interessante Aufgaben und Herausforderungen gefreut. Ich möchte Dir für Dein Vertrauen, Deine Unterstützung, und die Möglichkeit mit Dir zusammen in diesem außergewöhnlichen Team gearbeitet haben zu dürfen, danken. Ich wünsche Dir für die Zukunft persönlich alles Gute und wissenschaftlich weiterhin viele Erfolge. Lieber Thomas, für diese schöne und spannende Zeit Danke ich Dir ganz herzlichst.

**Professor Walther**, für die Übernahme der Zweitkorrektur, trotz Ihres sicherlich immer dichten Terminkalenders, möchte ich mich bei Ihnen ganz herzlich bedanken. Auch als es am Ende meiner Arbeit mit der Einreichung nochmal eng wurde, und Termine und Fristen eingehalten werden mussten, haben Sie sich davon nicht beeindruckt lassen. Vielen Dank für Ihre Unterstützung.

This thesis is significantly based on the ideas of some clever theory guys to whom I am truly grateful. Here, I want to take the opportunity to thank these people. **Nikolay** without all your ideas on composite pulses - diabatic, adiabatic, robust or even universal - this work could not have been completed. Thank you very much for all your helpful input and support. **Stephane** thank you very much for your ideas on single-shot shaped pulses, and that you gave me the chance to first test these type of pulses experimentally. **Leonid** and **Bruce** thank you for all the fruitful discussions on coherent interactions, your support, and your interest in my work. It was my pleasure to have met all of you.

**PrYSO/EuYSO-Team**, vielen Dank für die ausnahmslos gute Atmosphäre und die Motivation, mit der wir zusammen an den unterschiedlichsten Problemen gearbeitet haben und für die unzähligen Messnächte die wir zusammen im Labor verbracht, - gemessen, diskutiert und gelacht haben.

Lieber **Simon**, ich erinnere mich an den Tag im Oktober vor „einigen“ Jahren als wir zusammen in der AG unsere Masterarbeit begonnen haben. Seit damals ist viel passiert und wenn ich über diese gemeinsame Zeit nachdenke, so tue ich dies immer mit einem Lachen. Auch wenn ich die ein oder andere Narbe davongetragen habe :-)) möchte ich diese Zeit mit Dir nicht missen. Ich bin dankbar, dass ich mich immer auf Dich verlassen konnte. Es war einfach genial.

Dear **Genko**, a few years ago you started your Postdoc as the first fully theoretical physicist in the group, however it did not take us very long and you also became an quite experienced experimentalist :-)). Thank you for your outstanding support on theory of composite pulses, single-shot shaped pulses, and for adding all types

of inhomogeneities to our simulations in order to finally match the experimental results. I wish **Kami** and you all the best for the future. I am sure we will meet again, no matter if in Germany or Bulgaria.

**Georg**, ich war keine drei Wochen in der AG da hast Du mich mit deinem Crosser auf den Frankenstein gejagt und es wurde mir schlagartig klar, dass dies wohl nicht nur dein Tempo auf dem Rad sein wird. Mit deinem Einsatz im Labor warst Du für Simon und mich immer ein Vorbild. Deine Meinung und dein Rat habe ich während meiner Masterarbeit und auch während meiner Promotion immer sehr geschätzt. Später konnte ich Dich dann doch noch von einem „richtigen“ Rad überzeugen. Ich erinnere mich immer gerne an unsere gemeinsamen Touren egal ob hier um Darmstadt, in Oberstdorf oder Mittenwald. Danke auch für diese schönen Momente neben der Physik.

**Fabian**, als mein Betreuer während meiner Masterarbeit hast Du mir mit deiner lockeren Art und deinem Humor das PrYSO-Projekt näher gebracht. Ich erinnere mich an einige legendäre Tischtennisspiele und viel BestWorschtinTown während unserer Messnächte. Vielen Dank für diese gute Zeit.

Ein besonderer Dank natürlich auch an meine BSc- und MSc-Studenten, die ich während meiner Promotion betreuen durfte, **Moritz Kick, Oliver Diemel, Maximilian Meier, Jonas Zessin, Alexander Bruns, Daniel Preissler, Daniel Englisch, Torsten Abel, Nikolaus Lorenz und Marcel Hain.**

**Marcel und Thomas W.** nun ist es an Euch das **PrYSO/EuYSO-Team** zu führen. Ich bin mir sicher, dass Ihr diese Aufgabe mit Bravour meistern werdet. Ich hoffe Ihr werdet bei allen experimentellen und theoretischen Problemen immer mit Spaß, Freude und Begeisterung an diesem Projekt arbeiten. Ich wünsche Euch für Eure Promotion die nötige Motivation, jede Menge Durchhaltevermögen und natürlich ganz viel Erfolg.

Der gesamten aktuellen und früheren **AG Halfmann**, danke für diese wunderbare Zeit, die ausgesprochen gute und angenehme Arbeitsatmosphäre, die ausgelassenen Runden am Kaffeetisch, die sportlichen Gruppenausflüge zum Wandern, Klettern, Radfahren, Paintball, Tischtennis, die geselligen Runden bei Weihnachtsfeiern und Grillabenden. Dies alles werde ich sehr vermissen. Mein Dank geht dabei insbesondere an meine Mitpromovenden und Kollegen, die mich über diese lange Zeit begleitet haben, **Patric, Frank, Uwe, Christian, Lacho und Thorsten.** Liebe **Damaris**, auch Dir ein herzliches Danke für all die Unterstützung mit Verträgen, Bestellungen, Dienstreiseanträgen und, und, und.

Zu guter Letzt geht ein ganz großer Dank an meine **Familie: Jutta, Michael, Benjamin und Nafise.** Euch allen ein herzliches Dankeschön für eure vielseitige Unterstützung, euer Verständnis, wenn neben der Promotion mal wieder nur sehr wenig Zeit für anderes blieb, und die Kraft, die Ihr mir gegeben habt, um dieses Projekt erfolgreich abzuschließen zu können. **Vielen Dank.**

Daniel Schraft

Darmstadt, Frühjahr 2017



# Erklärung zur Dissertation

Hiermit versichere ich, die vorliegende Dissertation ohne Hilfe Dritter nur mit den angegebenen Quellen und Hilfsmitteln angefertigt zu haben. Alle Stellen, die aus Quellen entnommen wurden, sind als solche kenntlich gemacht. Diese Arbeit hat in gleicher oder ähnlicher Form noch keiner Prüfungsbehörde vorgelegen.

Darmstadt, den 19. Oktober 2016

---

(Daniel Schraft)